

AD-A276 382



DOCUMENTATION PAGE

OMB No 0704-0188

Do not estimate the average number of responses, including the time for reviewing instructions, searching existing data sources, gathering and reviewing the collection of information. Send comments regarding this burden estimate or any other aspect of this collection of information, including suggestions for reducing this burden, to Washington Headquarters Services, Directorate for Information Operations and Reports, 1215 Jefferson Ave., Suite 1204, Washington, DC 20543-0188, and to the Office of Management and Budget, Paperwork Reduction Project (0704-0188), Washington, DC 20503.

2 REPORT DATE
9/30/93

3 REPORT TYPE AND DATES COVERED
Final Report: 1/1/89-6/30/93

4 TITLE AND SUBTITLE
PROCESS PARAMETER-GROWTH ENVIRONMENT-FILM PROPERTY RELATIONSHIPS FOR REACTIVE SPUTTER DEPOSITED METAL (V, Nb, Zr, Y, Au) OXIDE, NITRIDE, AND OXYNITRIDE FILMS

5 FUNDING NUMBERS
DAAL03-89-K-0022

6 AUTHOR(S)
Professor Carolyn Rubin Aita

7 PERFORMING ORGANIZATION NAME(S) AND ADDRESS(ES)
Materials Department
University of Wisconsin-Milwaukee
PO Box 784
Milwaukee, WI 53201

DTIC
SELECTED
FEB 24 1994
C D

8 PERFORMING ORGANIZATION NUMBER

9 SPONSORING/MONITORING AGENCY NAME(S) AND ADDRESS(ES)
U. S. Army Research Office
P. O. Box 12211
Research Triangle Park, NC 27709-2211

10 SPONSORING/MONITORING AGENCY REPORT NUMBER
ARO 26427.12-MS

11 SUPPLEMENTARY NOTES
The view, opinions and/or findings contained in this report are those of the author(s) and should not be construed as an official Department of the Army position, policy, or decision, unless so designated by other documentation.

12a DISTRIBUTION/AVAILABILITY STATEMENT
Approved for public release; distribution unlimited.

12b DISTRIBUTION CODE
94-05979

13 ABSTRACT (Maximum 200 words)
The research developed process parameter-growth environment-film property relations [phase maps] for model sputter-deposited transition metal oxides, nitrides, and oxynitrides grown by reactive sputter deposition at low temperature. Optical emission spectrometry was used for plasma diagnostics. The results summarized here include the role of sputtered metal-oxygen molecular flux in oxide film growth; structural differences in highest valence oxides including conditions for amorphous growth; and using fundamental optical absorption edge features to probe short range structural disorder. Eight appendices containing sixteen journal articles are included.

DTIC QUALITY INSPECTED 2

14 SUBJECT TERMS
Sputter deposition; Glow discharge; discharge diagnostics; transition metal oxides; zirconia; yttria; niobia; vanadia; gold oxide; optical emission spectrometry.

15 NUMBER OF PAGES
100

16 PRICE CODE

17 SECURITY CLASSIFICATION OF REPORT
UNCLASSIFIED

18 SECURITY CLASSIFICATION OF THIS PAGE
UNCLASSIFIED

19 SECURITY CLASSIFICATION OF ABSTRACT
UNCLASSIFIED

20 LIMITATION OF ABSTRACT
UL

**PROCESS PARAMETER-GROWTH ENVIRONMENT-
FILM PROPERTY RELATIONSHIPS FOR REACTIVE SPUTTER
DEPOSITED METAL (V, Nb, Zr, Y, Au) OXIDE, NITRIDE,
AND OXYNITRIDE FILMS**

1/1/89-6/30/93

FINAL REPORT

CAROLYN RUBIN AITA

9/30/93

Accession For	
NTIS CRA&I	<input checked="" type="checkbox"/>
DTIC TAB	<input type="checkbox"/>
Unannounced	<input type="checkbox"/>
Justification	
By	
Distribution /	
Availability Codes	
Dist	Avail and/or Special
A-1	

U.S. Army Research Office Contract No. 26427-MS/ DAAL03-89-K-0022

Materials Department and the Laboratory for Surface Studies

University of Wisconsin-Milwaukee

P.O. Box 784 Milwaukee, Wisconsin 53201

aita@csd4.csd.uwm.edu

APPROVED FOR PUBLIC RELEASE

DISTRIBUTION UNLIMITED

**THE VIEWS, OPINIONS, AND/OR FINDINGS CONTAINED IN THIS REPORT ARE THOSE OF THE
AUTHOR(S) AND SHOULD NOT BE CONSTRUED AS AN OFFICIAL DEPARTMENT OF THE ARMY
POSITION, POLICY, OR DECISION, UNLESS SO DESIGNATED BY OTHER DOCUMENTATION.**

FOREWORD

The major theme of this research was to develop process parameter-growth environment-film property relations for model sputter-deposited transition metal oxides, nitrides, and oxynitrides grown by reactive sputter deposition at low temperature.

Four PhD and three MS degrees were awarded to students whose theses were based on this theme. Twenty-one refereed publications, twenty-eight talks at national/international meetings, and a patent disclosure resulted from this research. If one likes to count, a good case can be made for the work's success on the basis of numbers.

I, myself, have a different measure of success. How did our work extend the collective knowledge in the field? What myths did we debunk? What *next* questions are contained in our answers? How can our results be used?

In Sec. II of the Report that follows, we address the first three questions by presenting and discussing important general results. The last question launched us into two new areas of research: nanolaminates for transformation-toughening coatings, currently supported under US ARO Grant No. DAAH04-93-G-0238, and self-sealing insulators for corrosion-resistant coatings [Appendix VIII], which received support under a University of Wisconsin-System Applied Research Grant.

Much of the "finished" areas in this work involve oxide deposition, with nitrides and oxynitrides taking a backseat largely due to time constraints. Therefore, the results highlighted in this Report concern oxide growth and characterization. However, results concerning other than pure oxide systems are still being evaluated and will eventually be written-up as journal articles.

I thank Robert R. Reeber [US ARO], George S. Baker [UW-MKE], Wai-Yim Ching [U. Missouri-Kansas City], Michel E. Marhic [Northwestern U], and Michael Aita [CardioGenesis] for many fruitful discussions regarding this research; Elzbieta Kolawa and Marc-A. Nicolet for generously carrying out Rutherford backscattering measurements and analysis, and for providing a "home" for at Caltech during the summers of 1990 and 1991.

Carolyn Rubin Aita
Milwaukee, Wisconsin
September, 1993

TABLE OF CONTENTS

Section	Page
Foreword	i
List of Appendices	iii
I. Statement of Problem Studied	1
II. Summary of Most Important Results	
A. Role of metal-oxygen molecular flux in oxide growth.	3
B. Structural differences in highest valence oxides.	
1. Conditions for amorphous oxide growth.	5
2. Amorphous versus crystalline growth of the same metal oxide: the role of substrate temperature and growth rate.	6
C. Using fundamental optical edge features to probe short-range structural disorder in vanadia, zirconia, and yttria.	7
III. Publications and Presentations	
A. Refereed Publications	10
B. National/International Conference Presentations	11
IV. Students Supported and Degrees Obtained	14
V. Invention Disclosure Title	14
VI. Bibliography	15
Appendices I through VIII	

LIST OF APPENDICES

APPENDIX I

- A. "Near band gap optical behavior of sputter deposited α - and $\alpha+\beta$ -ZrO₂ films." C.-K. Kwok and C.R. Aita, J. Appl. Phys. 66, 2756-2758 (1989).
- B. "The indirect band gap in α -ZrO₂." C.-K. Kwok and C.R. Aita, J. Vac. Sci. Technol. A 8, 3345-3346 (1990).

APPENDIX II

- A. "Process parameter/growth environment/film property relationships for the sputter deposited yttrium-oxygen system." C.-K. Kwok, C.R. Aita, and E. Kolawa, J. Vac. Sci. Tech. A 8, 1330-1334 (1990).
- B. "Near-ultraviolet optical absorption in sputter deposited cubic yttria." C.-K. Kwok, C.R. Aita, and E. Kolawa, J. Appl. Phys. 68, 2945-2950 (1990).
- C. "High temperature air-annealing behavior of sputter deposited amorphous yttria films on fused silica." S.N. Mukherjee and C.R. Aita, J. Vac. Sci. Technol. A 10, 2723-8 (1992).
- D. "Kinetics of morphological change during annealing of amorphous yttria." S.N. Mukherjee and C.R. Aita, J. Vac. Sci. Technol. A 10, 3362-4 (1992).
- E. "Cyclic annealing-induced microstructural and crystallographic changes in crystalline yttria films on silica." S.N. Mukherjee and C.R. Aita, J. Vac. Sci. Technol. A 10, 3356-8 (1992).

APPENDIX III

- A. "Cathode voltage-gas composition-film crystallography relationships for sputter deposited vanadia." C.R. Aita, Li-Jong Liou, C.-K. Kwok, R.C. Lee, and E. Kolawa, Thin Solid Films 193/194, 18-26 (1990).
- B. "Annealing response of disordered sputter deposited vanadium pentoxide (V₂O₅)." John Luksich and C.R. Aita, J. Vac. Sci. Technol. A 9, 542-546 (1991).
- C. "Electronic transition-related optical absorption in vanadia films." A.M. Abuhadba and C.R. Aita, Proc. Materials Research Soc. 242, 731-736 (1992).

APPENDIX IV

- A. "A phase map for sputter deposited niobium oxides." R. C. Lee and C.R. Aita, J. Appl. Phys. 70, 2094-2103, (1991).
- B. "Growth conditions for sputter deposited niobium oxides." R.C. Lee and C.R. Aita, J. Vac. Sci. Technol. A 10, 1777-80 (1992).

APPENDIX V

"The relationship of phase formation in sputter deposited metal-oxygen systems to metal, metal-oxygen, and oxygen flux." C.R. Aita, J. Vac. Sci. Technol. A, 11 1540-7 (1993). INVITED

APPENDIX VI

"Core level and valence band x-ray photoelectron spectroscopy of gold oxide." C.R. Aita and N. C. Tran, J. Vac. Sci. Technol. A 9, 1498-1500 (1991).

APPENDIX VII

"Sputter deposition of highly <100+001> textured tetragonal barium titanate grown on unheated silica using a neon discharge." C.R. Aita and N.M. Abuhadba, J. Appl. Phys. 71, 3054-3046 (1992).

APPENDIX VIII

"Nanocrystalline aluminum nitride: growth by sputter deposition, optical absorption, and corrosion protection behavior." C.R. Aita and W.S. Tait, Nanostructured Mater. 1, 269-80 (1992). REVIEW

I. STATEMENT OF PROBLEM STUDIED

Reactive sputter deposition is extensively used to grow films in which one or more of the constituent elements is volatile. The process involves non-equilibrium growth at a solid surface (substrate) in contact with a low pressure glow discharge. The growth environment is complex, does not easily lend itself to even rudimentary *in situ* discharge diagnostics, and has not been a topic of active study. Historically, research was geared to developing process parameter-film property relations with an eye towards making a film with desired behavior. However, even the most detailed parametric study is phenomenological and machine-specific unless it contains growth environment information.

The research we undertook here was a step towards remedying this situation. We studied the low temperature growth (140-375 °C) of a series of model metal oxide, nitride, and oxynitride materials systems. We worked towards three general goals:

- 1) Relate deposition process parameters to important features of the growth environment for each model system.
- 2) Determine the effect of these growth environment features on film phase formation for each model system.
- 3) *Understand* similarities and differences between model systems and develop general tenets that enable prediction of growth characteristics in other materials systems.

The experimental program was three-fold: film growth by reactive sputter deposition, *in situ* discharge diagnostics, film characterization. A radio frequency diode apparatus was used to grow films on Suprasil fused silica, <111>-cut Si, and carbon foil substrates. The substrates were not externally heated, but did heat above room temperature due to contact with the plasma.

The discharge contained a rare gas+ a reactive gas. The targets (cathodes) were vanadium, niobium, zirconium, yttrium, and gold. As a group, these elements have a broad range of oxidation and nitridation behavior. Furthermore, the transition metals form a sequence down column VB of the periodic table and across the second long period. Therefore, differences in oxide/nitride growth between materials systems can be discussed in terms of sequential changes in cation bonding characteristics.

The following independent process parameters were varied: nominal reactive gas content, rare gas type, and cathode voltage. Discharge power, substrate temperature, and growth rate depend upon combinations of these parameters.

The primary *in situ* discharge diagnostic technique was optical emission spectrometry, although mass spectrometry was used as an adjunct source of plasma chemistry information. The five features at the substrate of most concern here were the flux and type of a) sputtered atoms, b) sputtered molecules, c) reactive gas species, the temperature, and the growth rate.

Film characterization involved direct methods to determine chemistry, short range order, long range order, and morphology. Adjunct methods involving behavior from which structural and chemical information was extracted (e.g. electrical resistivity, ultraviolet-visible optical absorption, corrosion resistance) were also used.

Process parameter-growth environment-film property data were combined in a "phase map" for each materials system [Appendix V].¹ Because of its graphic nature, the phase map is a convenient scientific tool to use to accomplish goal (3) [i.e. to understand and generalize the data collected under goals (1) and (2)]. In addition, the phase map has a technological benefit: is an easy way for other investigators to get information regarding phase formation that is not specific to a particular experimental set-up.

II. SUMMARY OF MOST IMPORTANT RESULTS

In keeping with the suggested US ARO guidelines for this Report, results for specific materials systems already appearing in the semiannual progress reports are not repeated here. Many specific results are also given in the published work contained in the Appendices. Here, we highlight three general important results that best represent the spirit of the work. As mentioned in the Foreword, our effort went largely into metal-oxygen systems, and consequently, the following discussion and conclusions concern conditions for metal oxide film growth and characteristics.

A. Role of metal-oxygen molecular flux in oxide growth

A metal target surface sputtered in a rare gas containing a small nominal amount of C_{60} getters oxygen (all types) from the discharge. As the nominal gas O_2 content is increased, an oxide forms on the target surface, gettering reaches a steady state, and excess oxygen appears in the discharge available for reaction at the substrate. The sputtered flux from an oxidized target surface in general² consists of metal atoms, M, and metal bonded to oxygen in molecular form(s), collectively denoted "M-O". Earlier studies suggested that the fraction of total flux sputtered as molecules was proportional to the M-O bond strength.³⁻⁵ However, recent data show that even molecules with a positive free energy of formation, such as AuO and AuO₂, are sputtered intact.⁶

Therefore we felt that the two important features of growth environment chemistry to be monitored here as a function of process parameter were:

- a) the fractional flux of M and M-O species to the growth interface, called f^M and f^{M-O} respectively where $f^M + f^{M-O} = 1$;
- b) the availability of oxygen for reaction at the substrate.⁷

The common effect of these features on phase formation in the transition metal oxygen-systems studied here is as follows [Appendix V]:¹

1) A large f^{M-O} (small f^M) and oxygen available for reaction at the substrate resulted in high valence oxide growth, e.g. amorphous niobia, crystalline niobia, crystalline yttria, crystalline biphasic monoclinic+tetragonal zirconia, crystalline monophasic monoclinic zirconia, amorphous vanadia, and crystalline vanadia.

2) 1) A large f^M (small f^{M-O}) and oxygen available for reaction at the substrate resulted in high valence oxide growth, but with structural disorder, e.g. crystalline site-disordered yttria, amorphous yttria, crystalline vanadia with contracted interlayer spacing.

3) A large f^{M-O} but insufficient oxygen at the growth interface resulted in suboxide growth, e.g. zirconium monoxide, "x-niobia", mixed vanadium suboxides.

4) A large f^M and insufficient oxygen at the substrate resulted in O-doped metal and suboxide growth, e.g. O-doped yttrium, O-doped niobium, niobium monoxide, niobium dioxide and mixed vanadium suboxides.

We conclude:

1) Metal-oxygen molecular flux must be taken into account when modelling oxide growth by reactive sputter deposition.

2) Without exception, growth of well-ordered highest valence oxide films with bulk structure depends upon a reaction between sputtered metal-oxygen molecules and oxygen at the substrate.

3) A reaction at the substrate between sputtered metal atoms and oxygen leads to a disordered structure even though oxidation is complete (e.g. a disordered highest valence oxide is grown).

The first conclusion is an extremely important contribution to the "debunking myths" criterion for measuring research success (see Foreword). Without scientific

basis, the reactive sputter deposition community currently ignores the existence of a sputtered metal-oxygen molecular flux, which is actually often the majority flux, and models oxide growth on the basis of a reaction between a sputtered metal atomic flux and oxygen at the substrate. Our results have shown that this approach is entirely wrong.

Although metal targets were used in this study, the above conclusions are relevant for a ceramic oxide target as well. Consider the case of sputter deposition of zinc oxide from a ZnO target.^{8,9} Old results showed target dissociation produced a mixed Zn+ZnO flux to the substrate. Highly aligned single basal orientation growth was obtained when the fractional ZnO flux was maximized; and disrupted when the fractional Zn flux was increased. This result was found even when a pure O₂ discharge was used to provide plenty of oxygen available for reaction at the substrate. The zinc oxide growth situation is actually analogous to crystalline site-disordered yttria growth in the present study [Appendix II.B].^{10,11}

We decided to test the importance of molecular flux in promoting crystallographic order with respect to deposition from a binary oxide target and chose barium titanate (BaTiO₃) as the model. The result showed that a highly oriented <110+001> texture were indeed associated with a large molecular fractional flux. Crystallographic order deteriorated with increasing atomic Ti and Ba flux, even through there was sufficient oxygen available for reaction at the substrate [Appendix VII].^{12,13}

B. Structural differences in highest valence oxides

1. Conditions for amorphous oxide growth

For several of the model systems, we found that large phase fields of amorphous¹⁴ structures were formed under conditions also associated with the best-ordered crystalline growth (a large f_{M-O} and oxygen available for reaction at

the substrate). These systems are ones in which there is "structural complexity" in the corresponding bulk oxides. By structural complexity, we mean either: ¹⁵ 1) the cation forms mixed valence compounds so that a vernier or infinitely adaptive physical structure accomodates electronic changes associated with changing stoichiometry; 2) structural flexibility in metal-oxygen bonding giving rise to polymorphs with the same chemistry *and* very similar free energies of formation.

Bulk niobium oxides have both types of structural complexity and bulk vanadium oxides have the first type. Therefore, it is not surprising that large phase fields of amorphous niobia and vanadia form under the growth conditions of unity f_{M-O} and available oxygen.

The bulk zirconium-oxygen and yttrium-oxygen systems do not have structural complexity. However, recently¹⁶ sputter deposition was used to grow a continuous series of crystalline yttrium suboxide films based on an orthorhombic structure with adjustable lattice parameters depending upon the amount of O sublattice vacancies. In our study, no amorphous phases were formed in the zirconium-oxygen and yttrium-oxygen systems under growth conditions of a large f_{M-O} + available oxygen. However, amorphous yttria was produced under unusual conditions for highest valence oxide growth: a large flux of Y atoms to the substrate+available oxygen. Keeping in mind the adjustable orthorhombic structure mentioned above, it is possible that nuclei of these suboxides initially form during growth of amorphous yttria and are subsequently oxidized to produce stoichiometric yttria but without the large atomic motion required for long range order (crystallization) able to occur.

2. Amorphous versus crystalline growth of the same metal oxide: the role of substrate temperature and growth rate.

In the case of niobia and vanadia, *both* amorphous and crystalline

stoichiometric oxides were formed under the conditions of a large f^{M-O} and oxygen available for reaction at the substrate. The crystalline form replaced the amorphous one as the gas O_2 content and the cathode voltage were increased.

These results can be understood by considering the effect of both substrate temperature and growth rate [e.g. Fig. 4 of Appendix V]. A lower arrival (hence, growth) rate and a higher temperature promote crystallinity via increased surface diffusion before the next monolayer of flux arrives to quench adatom motion, a trend expected from growth by evaporation studies.¹⁷

C. Using fundamental optical edge features to probe short-range structural disorder in vanadia, zirconia, and yttria

All of the metals in this study [including gold (Appendix VI)] bond to oxygen via metal (n-1)d and ns electron interactions with O 2p electrons. Vanadia, niobia, yttria, and zirconia are wide band gap semiconductors. The lower part of the conduction band in these oxides consists of two split-off subbands formed from empty (n-1)d electron states. These subbands fill in the visible-ultraviolet spectral region, thereby lending themselves nicely to conventional UV-vis spectrophotometry analysis.

The question is: what kind of information can be obtained? Disruptions in short-range order (nearest and next-nearest neighbor involvement) cause changes in the crystal field around the metal (cation). As is characteristic for d electrons, the charge density redistribution coincidental with short-range order disturbances remains fairly localized at the site of the cation. Here, we used near UV-visible spectrophotometry as a sensitive probe of short-range disorder, even in crystalline films for which x-ray diffraction data showed long-range order indistinguishable from bulk material, i.e. no gross defects in the crystal "skeleton" (lattice) were detected.

The major procedural problem involved determining what the fundamental optical absorption edge of a well-ordered specimen of these oxides should look like. In all cases, there were no standard transmission spectra or even definitive theoretical band structure calculations from which we could deduce optical features. We relied heavily on existing (and often conflicting) theory, on published bulk ceramic reflectivity spectra, and on spectra from films grown as a part of this study that were believed to represent well-ordered crystals. Three main results obtained from spectrophotometry of several oxides are given next.

1. Zirconia: Monoclinic zirconia [$m\text{-ZrO}_2$] is the only bulk zirconium oxide at STP. However, a high temperature tetragonal polymorph [$t\text{-ZrO}_2$] formed in addition to $m\text{-ZrO}_2$ under some conditions in sputter deposited films.¹⁸ The absorption edge of films of $m\text{-ZrO}_2$ and biphasic $m+t\text{-ZrO}_2$ was studied and related to band structure calculations for each polymorph [Appendix I.A&B].^{11,19,20} The fact that single-[111] orientation $m\text{-ZrO}_2$ could be produced allowed easy spectrophotometric analysis of this material without internal scattering from {111-111} twin boundaries prevalent in bulk material. An initial indirect transition across the energy band gap of $m\text{-ZrO}_2$ at 4.70 eV and two direct transitions at 5.17 and 5.93 eV were identified and associated with two split-off Zr 4d subbands.

2. Yttria: Yttria with a bcc bixbyite structure is the only bulk yttrium oxide at STP. The 80-atom unit cell has a distorted fluorite structure with vacancies on 1/4 of the anionic sites. Y occupies two *structurally nonequivalent but chemically equivalent* sites within the unit cell: Y second-nearest neighbors are different at each type of site. The fundamental optical absorption edge was found to consist of two direct interband transitions, at 5.07 and 5.73 eV [Appendices II.B & V].^{1,10,11} This edge structure resulted from two split-off Y 4d subbands at the bottom of the yttria conduction band and was "sharp" in well-ordered yttria [see Appendix V, Fig. 9]. However, there were also crystalline yttria films in which the distinction

between subbands was obscured, denoted "smeared edge"[see Appendix V, Fig. 10], similar to that found in amorphous yttria [Appendix II A,B, &C].^{10,21,22} The proposed reason for edge smearing was Y atom site-disorder (affecting the Y *next-nearest* neighbor environment as described above) which created additional electronic states within the energy gap between the subbands.

3. Vanadia: We refined the optical absorption edge picture to include a structure at energy higher than the band gap, identifiable with two split-off 3d subbands [Appendix III.C].^{23,24} We showed that the subband was dependent upon V *nearest* neighbor environment only, in particular that V be in distorted octahedral coordination with six O, as in the bulk material, but was *independent of long range order*.

These examples demonstrate the influence of d electron behavior (i.e. local chemistry around a cation; i.e., short-range structural order) on fundamental optical absorption edge characteristics. It is important to understand the connection, since interest in these oxides as optical materials lies in their near ultraviolet-visible spectral behavior, which *we know how to control*.

III. PUBLICATIONS AND PRESENTATIONS

A. REFEREED PUBLICATIONS:

1. "Near band gap optical behavior of sputter deposited α - and $\alpha+\beta$ -ZrO₂ films." C.-K. Kwok and C.R. Aita, J. Appl. Phys. 66, 2756-2758 (1989). [APPENDIX I.A]
2. "Process parameter/growth environment/film property relationships for the sputter deposited yttrium-oxygen system." C.-K. Kwok, C.R. Aita, and E. Kolawa, J. Vac. Sci. Tech. A 8, 1330-1334 (1990).
3. "The indirect band gap in α -ZrO₂." C.-K. Kwok and C.R. Aita, J. Vac. Sci. Technol. A 8, 3345-3346 (1990). [APPENDIX II.A]
4. "Near-ultraviolet optical absorption in sputter deposited cubic yttria." C. -K. Kwok, C.R. Aita, and E. Kolawa, J. Appl. Phys. 68, 2945-2950 (1990). [APPENDIX II.B]
5. "Cathode voltage-gas composition-film crystallography relationships for sputter deposited vanadia." C.R. Aita, Li-Jong Liou, C.-K. Kwok, R C. Lee, and E. Kolawa, Thin Solid Films 193/194, 18-26 (1990). [APPENDIX III.A]
6. "The fundamental optical absorption edge of sputter deposited zirconia and yttria." C.R. Aita and C.-K. Kwok, J. Amer. Ceram. Soc. 73, 3209-14 (1990).
7. "Core level and valence band x-ray photoelectron spectroscopy of gold oxide." C.R. Aita and N. C. Tran, J. Vac. Sci. Technol. A 9, 1498-1500 (1991). [APPENDIX VI]
8. "Annealing response of disordered sputter deposited vanadium pentoxide (V₂O₅)." John Luksich and C.R. Aita, J. Vac. Sci. Technol. A 9, 542-546 (1991). [APPENDIX III.B]
9. "A phase map for sputter deposited niobium oxides." R. C. Lee and C.R. Aita, J. Appl. Phys. 70 2094-2103, (1991).
10. "Sputter deposition of highly $\langle 100+001 \rangle$ textured tetragonal barium titanate grown on unheated silica using a neon discharge." C.R. Aita and N.M. Abuhadba, J. Appl. Phys. 71, 3054-3046 (1992). [APPENDIX VII]
11. "Cathode voltage-gas composition-film crystallography relationships for vanadia sputter deposited in Ne/O₂ discharges." N.M. Abuhadba and C.R. Aita, Surface Modification Technologies V (edited by T.S. Sudharshan and J.F. Braza, The Institute of Metals, UK, 1992) pp. 517-526.
12. "Sputter deposition and *in situ* discharge diagnostics of tetragonal barium titanate on unheated substrates using Ar/O₂ and Ne/O₂ discharges." N.M. Abuhadba and C.R. Aita, Mater. Manuf. Processes 7, xxx (1992).

-also printed in: Proc. Fifth International Conference on Surface Modification Technologies, The Institute of Metals, UK, 1992) pp. 195-204.

13. "Phase maps for sputter deposited refractory metal oxide ceramic coatings: A review of Nb-oxide, Y-oxide, and Zr-oxide growth." C.R. Aita, *Mater. Sci. Technol.* 8, 666-672 (1992). INVITED

-also printed in: *Surface Modification Technologies V* (edited by T.S. Sudharshan and J.F. Braza, The Institute of Metals, UK, 1992) pp. 541-555.

14. "High temperature air-annealing behavior of sputter deposited amorphous yttria films on fused silica." S.N. Mukherjee and C.R. Aita, *J. Vac. Sci. Technol. A* 10, 2723-8 (1992).

[APPENDIX II.C]

15. "Growth conditions for sputter deposited niobium oxides." R.C. Lee and C.R. Aita, *J. Vac. Sci. Technol. A* 10, 1777-83 (1992).

[APPENDIX IV.A]

16. "Phase mapping sputter deposited wide band-gap metal oxides." C.R. Aita, R.C. Lee, C.-K. Kwok, and E.A. Kolawa, *Proc. Materials Research Soc.* 242, 737-42 (1992).

17. "Electronic transition-related optical absorption in vanadia films." A.M. Abuhadba and C.R. Aita, *Proc. Materials Research Soc.* 242, 731-6 (1992).

[APPENDIX III.C]

18. "Kinetics of morphological change during annealing of amorphous yttria." S.N. Mukherjee and C.R. Aita, *J. Vac. Sci. Technol. A* 10, 3362-4 (1992).

[APPENDIX II.D]

19. "Annealing-induced microstructural and crystallographic changes in crystalline yttria films on silica." S.N. Mukherjee and C.R. Aita, *J. Vac. Sci. Technol. A* 10, 3356-8 (1992).

[APPENDIX II.E]

20. "Nanocrystalline aluminum nitride: growth by sputter deposition, optical absorption, and corrosion protection behavior." C.R. Aita and W.S. Tait, *Nanostructured Mater.* 1, 269-80 (1992). REVIEW

[APPENDIX VIII]

21. "The relationship of phase formation in sputter deposited metal-oxygen systems to metal, metal-oxygen, and oxygen flux." C.R. Aita, *J. Vac. Sci. Technol. A*, 11 1540-7 (1993). INVITED

[APPENDIX V]

B. INVITED AND CONTRIBUTED NATIONAL SYMPOSIA PAPERS

[Presenting author underlined>

1. "Process parameter-growth environment-film property relationships for the sputter deposited yttrium-oxygen system." C.-K. Kwok and C.R. Aita, American Vacuum Society 36th National Symposium, Boston, MA, 1989.

2. "The effect of microcrystallinity on interband optical transitions in sputter deposited ZrO₂ films." C.-K. Kwok, C.R. Aita, and E. Kolawa, Materials Research Society 1989 Fall Meeting, Boston, MA, 1989.

3. "Modelling interband optical spectra of microcrystalline wide band gap semiconductors using the coherent potential approximation." C.R. Aita, Materials Research Society 1989 Fall Meeting, Boston, MA, 1989.
4. "Sputter deposition of yttria." C.-K. Kwok, C.R. Aita, and E. Kolawa, 19th Annual Symposium on Applied Vacuum Science and Technology, Clearwater Beach, FL, 1990.
5. "Near-ultraviolet interband optical transitions in sputter deposited yttria films." C.-K. Kwok, C.R. Aita, and E. Kolawa, American Physical Society 1990 March Meeting, Anaheim, CA, 1990.
6. "Cathode voltage-gas composition-crystallography relationships for sputter deposited vanadium pentoxide." C.R. Aita and L.-J. Liou, American Vacuum Society 8th International Conference on Thin Films & 17th International Conference on Metallurgical Coatings, San Diego, CA, 1990.
7. "The fundamental optical absorption edge of sputter deposited zirconia and yttria." C.-K. Kwok and C.R. Aita, American Ceramic Society 92nd Annual Meeting, Dallas, TX, 1990.
8. "The effect of structural disorder on optical absorption edge disorder in sputter deposited zirconia and yttria." C.R. Aita and C.-K. Kwok, 5th International Conference on Solid films and Surfaces, Providence, RI, 1990.
10. "Crystallite-size effects on near ultraviolet interband optical transitions in sputter-deposited zirconia." C.R. Aita and C.-K. Kwok, American Vacuum Society 37th National Symposium, Toronto, Ontario, Canada, 1990.
11. "Annealing response of disordered sputter deposited vanadium pentoxide." I. Luksich and C.R. Aita, American Vacuum Society 37th National Symposium, Toronto, Ontario, Canada, 1990.
12. "Optical absorption edge disorder in sputter deposited cubic yttria: relationship to Y:Y-oxide flux and implications for short range structural disorder." C.-K. Kwok, C.R. Aita, and E. Kolawa, American Vacuum Society 37th National Symposium, Toronto, Ontario, Canada, 1990.
13. "The valence band of gold-oxide, studied by x-ray photoelectron spectroscopy." C.R. Aita and N.C. Tran, American Vacuum Society 37th National Symposium, Toronto, Ontario, Canada, 1990.
14. "Phase maps of sputter deposited ceramic films." C.R. Aita, 20th Annual Symposium on Applied Vacuum Science and Technology, Clearwater Beach, FL, 1991. INVITED
15. "Phase maps for sputter deposited refractory metal oxide ceramic coatings (V-, Y-, Zr-, and Nb-oxides)." C. Aita, 5th International Conference on Surface Modification Technologies, Birmingham, UK, Sept. 2-4, 1991. INVITED
16. "Optical and structural properties of vanadium pentoxide sputter deposited in neon/oxygen discharges." N. Abuhadba and C. Aita, 5th International Conference on Surface Modification Technologies, Birmingham, UK, Sept. 2-4, 1991.

17. "Sputter deposition and in situ discharge diagnostics of tetragonal barium titanate on unheated substrates using Ar/O₂ and Ne/O₂ plasmas." N. Abuhadba and C. Aita, 5th International Conference on Surface Modification Technologies, Birmingham, UK, Sept. 2-4, 1991.
18. "Changes in optical properties, morphology, and chemistry upon natural aging and annealing of yttria coatings on silica." S.N. Mukherjee and C.R. Aita, Atomic Structure, Bonding, and Properties of Ceramics Meeting, American Ceramic Society, Marco Island, FL, Oct. 15-18, 1991.
19. "The effect of the growth environment on the crystallography and optical behavior of barium titanate coatings sputter deposited on fused silica." N.M. Abuhadba and C.R. Aita, Atomic Structure, Bonding, and Properties of Ceramics Meeting, American Ceramic Society, Marco Island, FL, Oct. 15-18, 1991.
20. "The fundamental optical absorption edge of sputter deposited vanadia: relationship to atomic disorder." N.M. Abuhadba and C.R. Aita, Atomic Structure, Bonding, and Properties of Ceramics Meeting, American Ceramic Society, Marco Island, FL, Oct. 15-18, 1991.
21. "The annealing stability of yttria (Y₂O₃) coatings on fused silica studied by x-ray photoelectron spectroscopy." S. Mukherjee and C.R. Aita, American Vacuum Society 38th National Symposium, Seattle, WA, Nov. 11-15, 1991.
22. "The effect of the growth environment on the phase boundaries in the sputter deposited niobium-oxygen system." R.C. Lee and C.R. Aita, American Vacuum Society 38th National Symposium, Seattle, WA, Nov. 11-15, 1991.
23. "Electronic transition-related optical absorption in vanadium pentoxide." N. M. Abuhadba and C. R. Aita, Materials Research Society 1991 Fall Meeting, Boston, MA, Dec. 2-6, 1991.
24. "Phase mapping sputter deposited wide band-gap metal oxides." C.R. Aita, R.C. Lee, and C.K. Kwok, Materials Research Society 1991 Fall Meeting, Boston, MA, Dec. 2-6, 1991.
25. "The effect of temperature and time on the annealing stability of sputter deposited amorphous yttria." S.N. Mukherjee and C.R. Aita, American Ceramic Society 93rd Annual Meeting, Minneapolis, MN, April 12-16, 1992.
26. "The relationship of phase formation in sputter deposited metal-oxygen systems to metal, metal-oxygen, and oxygen flux to the substrate." C.R. Aita, American Vacuum Society 39th National Symposium, Chicago, IL Nov. 9-13, 1992, INVITED.
27. "Optical behavior of <010>-orthorhombic and amorphous sputter deposited V₂O₅ thin films." N. M. Abuhadba and C.R. Aita, American Vacuum Society 39th National Symposium, Chicago, IL Nov. 9-13, 1992.
28. "Development of phase and texture in sputter deposited ZrO₂ and ZrO₂- Al₂O₃ nanolaminates." C.R. Aita, M.D. Wiggins, and C.M. Scanlan, Materials Research Society 1993 Fall Meeting, Boston, MA, Nov. 29-Dec. 3, 1993. [To be presented]

IV. STUDENTS SUPPORTED/DEGREES OBTAINED

1. Chee-Kin Kwok, PhD-12/89, "Process parameter-growth environment-film property relationships for reactive sputter deposited zirconium-oxygen and yttrium-oxygen films."
2. Shibnath Mukherjee, PhD-5/91, "Natural aging and annealing characteristics of sputter deposited yttria."
3. Nada. M. Abuhadba (O'Brien), PhD-5/92, "Process parameter-growth environment-film property relationships for radio frequency reactive sputter deposited vanadium oxides in rare gas/oxygen discharges."
4. Ray C. Lee, PhD-5/92, "Process parameter-growth environment-film property relationships for the sputter deposited Nb-O and Nb-N systems."
5. Li-Jong Liou, MS-5/90, "Cathode voltage-gas composition-film crystallography relationships for sputter deposited vanadia."
6. John Luksich, MS-12/90, "Annealing response of sputter deposited vanadium pentoxide."
7. Thomas P. James, MS-8/93, "Corrosion behavior of radio frequency sputter deposited vanadium and vanadium pentoxide thin films on 1010 steel substrates."

V. INVENTION DISCLOSURE TITLE

A Transformation-Toughening Ceramic Nanolaminate Coating

First record of intention: June 15, 1992.

Disclosure process initiated: September 20, 1993.

VI. BIBLIOGRAPHY

1. C.R. Aita, J. Vac. Sci. Technol. A, 11 1540 (1993). [APPENDIX V]
2. C.R. Aita, J. Vac. Sci. Technol. A3, 625 (1985) and refs. within.
3. J.W. Coburn, E. Taglauer, and E. Kay, J. Appl. Phys. 45, 1779 (1974).
4. J.W. Coburn, E. Taglauer, and E. Kay, J. Vac. Sci. Technol. 12, 151 (1975).
5. Y. Okajima, J. Appl. Phys. 55, 230 (1984).
6. C.R. Aita, J. Appl. Phys. 61, 5182 (1987).
7. We know that the plasma chemistry indices chosen here give an incomplete picture. Other indigenous species, including rare gas and "activated" oxygen carrying internal and/or kinetic energy whose bombardment of the substrate *potentially* have a strong influence on phase formation. However, we concluded that the influence of these species was secondary, their presence is more likely to influence long range structural order than control stoichiometry and hence the position of the phase boundaries. Thermodynamics drives each of the model metal-oxygen systems towards forming the high valence oxide, using whatever type of oxygen is available.
8. C.R. Aita, A.J. Purdes, R.J. Lad, and P.D. Funkenbusch, J. Appl. Phys. 51, 5533 (1980).
9. C.R. Aita, R.J. Lad, and T.C. Tisone, J. Appl. Phys. 51, 6405-6410 (1980).
10. C.-K. Kwok, C.R. Aita, and E. Kolawa, J. Appl. Phys. 68, 2945 (1990).
[APPENDIX II.B]
11. C.R. Aita and C.-K. Kwok, J. Amer. Ceram. Soc. 73, 3209 (1990).
12. C.R. Aita and N.M. Abuhadba, J. Appl. Phys. 71, 3054 (1992). [APPENDIX VII]
13. N.M. Abuhadba and C.R. Aita, Proc. Fifth International Conference on Surface Modification Technologies, (The Institute of Metals, UK, 1992) pp. 195-204.
14. The term "amorphous" is used here to describe a material that has no long range order. The material may or may not be vitreous, i.e., have the nearest

neighbor configuration of oxygen around metal is the same throughout the material.

15. F.P. Fehlner, Low Temperature Oxidation (Wiley-Interscience, New York, NY, 1981) pp. 31-49.
16. A.F. Jankowski, L.R. Schrawyer, and J.P. Hayes, *J. Vac. Sci. Technol. A* 11, 1548 (1993).
17. E. Krikorian and R.J. Sneed, *J. Appl. Phys.* 37, 3665 (1966).
18. C.-K. Kwok and C.R. Aita, *J. Vac. Sci. Technol. A*, 7, 1235 (1989).
19. C.-K. Kwok and C.R. Aita, *J. Vac. Sci. Technol. A*, 8, 3345 (1990). [Appendix I.B]
20. C.-K. Kwok and C.R. Aita, *J. Appl. Phys.* 66, 2756 (1989). [Appendix I.A]
21. C.-K. Kwok, C.R. Aita, and E.A. Kolawa, *J. Vac. Sci. Technol. A* 8, 1330 (1990). [Appendix II.A]
22. S.N. Mukherjee and C.R. Aita, *J. Vac. Sci. Technol. A* 10, 2723-8 (1992). [Appendix II.C]
23. N.M. Abuhadba and C.R. Aita, *Surface Modification Technologies V* (edited by T.S. Sudharshan and J.F. Braza, The Institute of Metals, UK, 1992) pp. 517-526.
24. N.M. Abuhadba and C.R. Aita, *Proc. Materials Research Soc.* 242, 731-6 (1992). [APPENDIX III.C]

APPENDIX I

- A. "Near band gap optical behavior of sputter deposited α - and $\alpha+\beta$ -ZrO₂ films." C.-K. Kwok and C.R. Aita, J. Appl. Phys. 66, 2756-2758 (1989).
- B. "The indirect band gap in α -ZrO₂." C.-K. Kwok and C.R. Aita, J. Vac. Sci. Technol. A 8, 3345-3346 (1990).

Near-band gap optical behavior of sputter deposited α - and $\alpha + \beta$ -ZrO₂ films

Chee-Kin Kwok and Carolyn Rubin Aita

*Materials Department and the Laboratory for Surface Studies, University of Wisconsin-Milwaukee,
P. O. Box 784, Milwaukee, Wisconsin 53201*

(Received 27 February 1989; accepted for publication 24 May 1989)

The functional dependence of the optical absorption coefficient on photon energy in the 4.9–6.5 eV range was determined for α - and $\alpha + \beta$ -ZrO₂ films grown by reactive sputter deposition on fused silica. Two allowed direct interband transitions in α -ZrO₂ were identified, with energies equal to 5.20 and 5.79 eV. Modification of these transitions in $\alpha + \beta$ -ZrO₂ is reported.

Monoclinic α -ZrO₂ is the only stable form for an infinite-size ZrO₂ crystal at standard temperature and pressure. However, it is well known^{1–4} that when the crystallite size is small, α -ZrO₂ and one of its high-temperature polymorphs, tetragonal β -ZrO₂, coexist. β -ZrO₂ in the composite is not a metastable phase nor the result of stabilization by impurities. It is a consequence of the dominance of the surface energy contribution to the Gibbs free energy of formation when the

crystallite surface area-to-volume ratio exceeds a critical value.⁴

We previously reported⁵ that phase transition from α -Zr to α -ZrO₂ in the sputter-deposited Zr-O system involves the formation of $\alpha + \beta$ -ZrO₂ structures. The shape of the fundamental optical absorption edge was found to be different for films that contain a β -ZrO₂ component compared to films that are single-phase α -ZrO₂. The functional depen-

dence of the absorption coefficient α on the incident photon energy $h\nu$ is reported here. Two optical transitions across the band gap of α -ZrO₂ are identified. Modification of these transitions in $\alpha + \beta$ -ZrO₂ films is reported.

Films were grown on Suprasil II fused silica in a hot-oil pumped rf diode sputter deposition system using a 13-cm-diam, 99.8% pure Zr target and discharges containing 2% O₂ in a rare gas, Ne (film A), Ar (film B), or Kr (film C). The discharge was operated at a cathode voltage of -1.3 kV ($p-p$) and a total pressure of 1×10^{-2} Torr. Further details of the deposition process are given in Ref. 6, as well as a discussion of the changes in growth environment and target oxidation state that accompany a change in rare gas type.

Film thickness was measured post-deposition from a masked step using a profilometer. Growth rate was calculated from this measurement. Crystallinography was determined by double-angle x-ray diffraction (XRD) using unresolved 1.5418 -Å CuK α radiation. Calibration was done using the $\{10\bar{1}1\}$ peak of an α -quartz standard at $2\theta = 2.66 \pm 0.02^\circ$, with a full width at half maximum (FWHM) intensity of 0.18° .

A Perkin-Elmer Model 330 UV-Visible-NIR double-beam spectrophotometer with a specular reflection attachment was used to measure the transmittance T and reflectance R of 0.19 - 0.25 μm (6.5 - 4.9 eV) near-normal incidence radiation at room temperature in laboratory air. For a film of thickness x , α is related to T and R ,

$$T = [(1 - R)^2 \exp(-\alpha x)] / [1 - R^2 \exp(-2\alpha x)]. \quad (1)$$

Film thickness and growth rate are recorded in Table I. The major XRD peaks are shown in Fig. 1. No adjustment in intensity was made for thickness difference between samples. The XRD pattern of Film A consists of a single peak at $2\theta = 28.1^\circ$ attributed to $\{11\bar{1}\}$ α -ZrO₂ planes.⁸ The pattern of Film B consists of a peak at $2\theta = 28.2^\circ$ attributed to $\{11\bar{1}\}$ α -ZrO₂ planes, and a broad asymmetric peak attributed to $\{111\}$ β -ZrO₂ planes at $2\theta = 30.3^\circ$ and $\{111\}$ α -ZrO₂ planes at $2\theta = 31.6^\circ$. The pattern of Film C has a third peak, attributed to five sets of closely spaced α - and β -ZrO₂ planes whose indices are given in Fig. 1. The sloping baseline on all patterns was caused by diffraction from the microcrystallites of the fused silica substrate.

High-resolution patterns were taken of the $\{11\bar{1}\}$ α -ZrO₂ peak of all films and the FWHM was used to calculate the minimum dimension d of a $\{11\bar{1}\}$ -oriented α -ZrO₂ crystallite in a direction perpendicular to the substrate, after separating out the instrument contribution to peak broadening.⁹ Values of d are recorded in Table I. Calculations⁴ based

TABLE I Film thickness (x), growth rate (r), minimum crystallite diameter (d), and the energy of two optical transitions (E_1 and E_2) in α - and $\alpha + \beta$ -ZrO₂ films sputter deposited on fused silica.

Film	Gas	x (kÅ) ^a	r (Å/min) ^a	d (Å)	E_1 (eV)	E_2 (eV)
A	Ne-2%O ₂	10 ± 0.2	15.6 ± 3	126	5.20	5.79
B	Ar-2%O ₂	2.4 ± 0.4	37 ± 6	88	5.14	
C	Kr-2%O ₂	3.3 ± 0.3	51 ± 5	70	5.12	

^a $\pm 10\%$

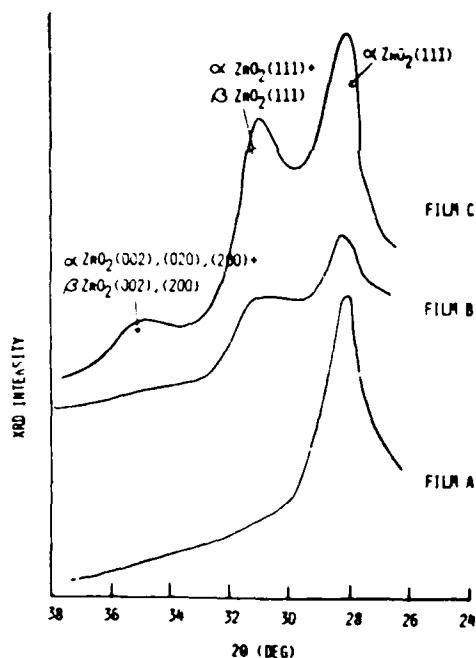


FIG. 1. X-ray diffraction patterns for α -ZrO₂ (film A) and $\alpha + \beta$ -ZrO₂ (films B and C) sputter deposited on fused silica.

on a balance between the surface and volume contributions to the Gibbs free energy of formation of the α and β phases predict a crystallite diameter of 306 Å at which the two phases coexist. The value obtained from our experimental data is ~ 0.3 of the predicted value.

Figure 2 shows α as a function of $h\nu$. For all films, the

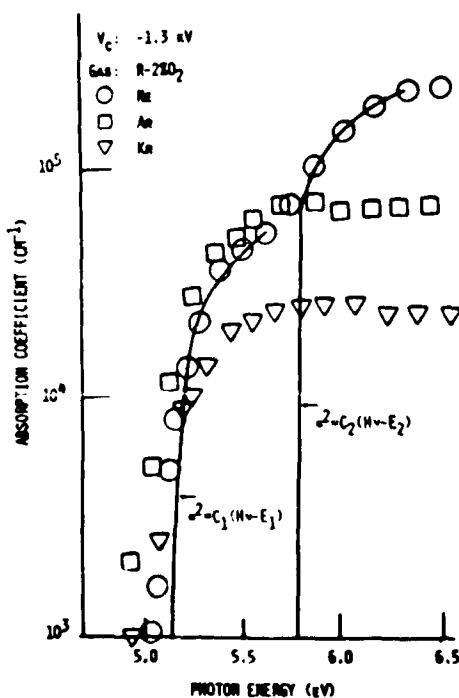


FIG. 2. The absorption coefficient as a function of incident photon energy for α -ZrO₂ and $\alpha + \beta$ -ZrO₂ films sputter deposited on fused silica. The solid curves represent Eqs. (2) and (3) applied to film A.

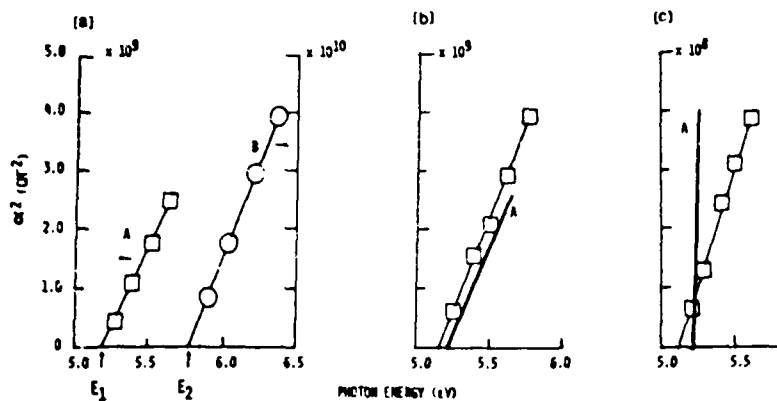


FIG. 3 The square of the absorption coefficient, as a function of incident photon energy for (a) film A showing two linear regions, (b) film B, and (c) film C. The first linear region for film A is reproduced in the appropriate scale for comparison in (b) and (c).

dependence of α on $h\nu$ is logarithmic at the onset of absorption. The inverse slope of the exponential increase of α with $h\nu$ is on the order of kT^{-1} for many crystalline semiconductors and insulators.¹⁰ Here, $d(\ln \alpha)/d(h\nu)$ is equal to $(2.5 kT)^{-1}$ for film A, $(4.6 kT)^{-1}$ for film B, and $(3.6 kT)^{-1}$ for film C.

For film A, the dependence of α on $h\nu$ takes the form

$$\alpha^2 = C_1(h\nu - E_1) \quad (2)$$

between $h\nu = 5.28$ – 5.64 eV, and

$$\alpha^2 = C_2(h\nu - E_2) \quad (3)$$

between $h\nu = 5.90$ – 6.37 eV. For films B and C, the dependence of α on $h\nu$ initially follows Eq. (2). However, α saturates with increasing $h\nu$. The higher energy optical transition that occurs in Film A given by Eq. (3) does not occur in films B and C. Figure 3 shows α^2 as a function of $h\nu$. E_1 and E_2 were obtained from the value of $h\nu$ at which $\alpha = 0$ and are recorded in Table I.

From the functional dependence of α on $h\nu$ for film A, we identify here, for the first time, two allowed direct interband transitions⁷ that occur in α -ZrO₂. The energies of the transitions, E_1 and E_2 , are 5.20 and 5.79 eV, respectively. Band calculations for α -ZrO₂ have yet to be carried out. Therefore, we cannot yet associate these optical transitions with specific electronic transitions. The coexistence of α - and β -ZrO₂ phases results in the following modifications:

(1) elimination of the high-energy transition; (2) a shift of E_1 to lower energy (5.20 eV for film A to 5.14 eV for film B to 5.12 eV for film C); and (3) ultimately, a decrease in the value of α over the entire absorption edge. The reasons for these modifications in terms of changes in short-range Zr-O order will be the subject of future research.

This work was supported under U. S. Army Research Office Grant No. DAAG03-89-K-0022 and by a gift from Johnson Controls, Inc. to the Wisconsin Distinguished Professorship (CRA).

¹J. P. Abriata and J. Garces, *Bull. Alloy Phase Diag.* **7**, 116 (1986).

²R. C. Garvie, *J. Phys. Chem.* **69**, 1238 (1965).

³E. C. Subbarao, H. S. Matti, and K. K. Srivastava, *Phys. Status Solidi A* **221**, 9 (1974).

⁴R. C. Garvie, *J. Phys. Chem.* **82**, 218 (1978).

⁵M. Rühle, *J. Vac. Sci. Technol. A* **3**, 749 (1985).

⁶C. K. Kwok and C. R. Aita, *J. Vac. Sci. Technol. A* **7**, 1235 (1989).

⁷See, for example, J. I. Pankove, *Optical Processes in Semiconductors* (Prentice-Hall, Englewood Cliffs, NJ, 1971).

⁸ASTM Joint Committee on Powder Diffraction Standards, 1974, *Powder Diffraction File Nos. 13-307 (α -ZrO₂) and 14-534 (β -ZrO₂)*.

⁹L. V. Azaroff, *Elements of X-Ray Crystallography* (McGraw-Hill, New York, 1968), pp. 549–558. The term "minimum dimension" is used here to acknowledge that we are assuming the limiting case of peak broadening due to finite crystalline size with no contribution from random lattice strain.

¹⁰F. Urbach, *Phys. Rev.* **92**, 1324 (1953).

Indirect band gap in α -ZrO₂

Chee-Kin Kwok and Carolyn Rubin Aita^{*)}

Materials Department and the Laboratory for Surface Studies, University of Wisconsin-Milwaukee, Milwaukee, Wisconsin 53201

(Received 13 December 1989; accepted 17 February 1990)

Measurements of the absorption coefficient on the fundamental optical absorption edge of α -ZrO₂ show that an indirect interband transition at 4.70 eV precedes two previously reported direct transitions. This result is in agreement with recent theoretical calculations of the α -ZrO₂ band structure

For three decades, there have been reports of the position of the fundamental optical absorption edge of polycrystalline bulk and thin film α -ZrO₂.¹⁻⁹ With one exception,⁷ all investigators agree that the edge is near 5 eV. However, only recently have features on the edge been investigated and two direct interband transitions identified.^{10,11} Here, we extend our previous work¹⁰ to identify an indirect interband transition at lower energy.

The material studied here is in the form of a thin film grown on fused silica by sputter deposition from a 12.7-cm diam Zr target using a rf excited Ar-20% O₂ discharge operated at -1.9 kV cathode voltage. The deposition was carried out in the manner previously described in a process parameter-growth environment: film property study of the Zr-O system.⁹ The crystal structure was determined from x-ray diffraction to be monoclinic α -ZrO₂ with {111} planes oriented parallel to the substrate. The minimum crystallite dimension in a direction perpendicular to the substrate, de-

termined from the {111} diffraction peak half-width using the Scherrer equation,¹² is 16 nm. This value is larger than the critical value, 13 nm, at which we observe growth of solely the monoclinic α phase in sputter deposited ZrO₂ films.¹⁰

Double-beam spectrophotometry was used to measure the transmittance T and reflectance R of near-normal incidence radiation in the 0.19-0.80 μ m spectral region (6.53-1.55 eV). An aluminum mirror was used as the reflectance standard. The absorption coefficient α was calculated from the relationship:¹³

$$T = [(1 - R)^2 \exp(-\alpha x)] / [(1 - R^2) \exp(-2\alpha x)], \quad (1)$$

where x is the film thickness, 1.2 kÅ.

Figure 1 shows α versus incident photon energy E . The data enclosed within the box in Fig. 1 have the functional form $\alpha^{1/2} = C(E - E_0)$, as shown in Fig. 2. The straight line shown in Fig. 2 is the best fit through the data points. The functionality of α versus E is indicative of an indirect

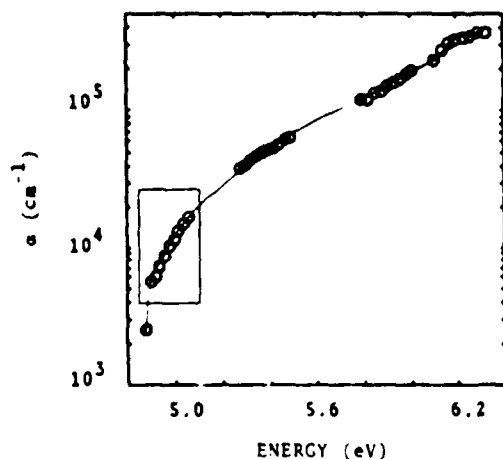


Fig. 1 The absorption coefficient α as a function of incident photon energy E for sputter deposited α -ZrO₂. The data enclosed within the box are of the functional form $\alpha^{1/2} = C(E - E_0)$, as shown in Fig. 2, indicative of an indirect interband transition at energy E_0 .

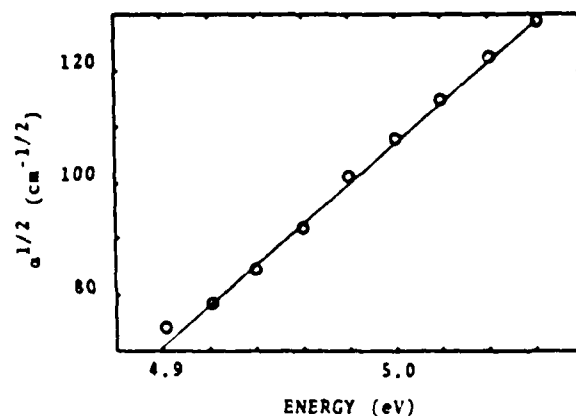


Fig. 2 $\alpha^{1/2}$ vs E for 4.90-5.06 eV. The straight line is the best fit through the data and when extrapolated to $\alpha = 0$ yields $E = 4.70$ eV, the indirect band gap of α -ZrO₂.

interband transition that occurs at energy $E_i = 4.70$ eV, determined by extrapolation of the straight line through the data to $\alpha = 0$. $C_1 = 355$ (cm² eV)⁻¹.

The behavior of α versus E for $E < \sim 5.3$ eV observed here is the same as previously reported¹⁰ for α -ZrO₂ sputter deposited in Ne-2% O₂ at -1.3 kV cathode voltage and will not be discussed in detail. In brief, the dependence of α on E takes the form of $\alpha^2 = C_1(E - E_1)$ for $E > \sim 5.3$ eV and $\alpha^2 = C_2(E - E_2)$ for $E > \sim 6.0$ eV. E_1 and E_2 are the energies of two direct interband transitions, determined by extrapolation of a graph α^2 versus E to $\alpha = 0$ in each region. E_1 and E_2 are equal to 5.20 and 5.95 eV, respectively, in reasonable agreement with the previously reported results, 5.20 and 5.79 eV. C_1 and C_2 are equal to 1.5×10^{10} and 3.3×10^{11} (cm² eV)⁻¹, respectively.

A recent theoretical determination of the band structure of α -ZrO₂ by Zandiehnam *et al.*¹⁴ predicts an indirect gap at 4.51 eV, close to our experimental result of 4.70 eV. In terms of the Brillouin zone symmetry lines for the monoclinic lattice, the transition across the indirect gap is from a point along Γ at the top of the valence band to a point along the BD axis at the bottom of the conduction band. Furthermore, the joint density of states is double peaked near the absorption edge, consistent with the two direct near-edge transitions observed here.

Acknowledgments: We acknowledge fruitful conversations with Dr. R. H. French and Professor W. Y. Ching. This work was supported under USARO Grant No. DAAL-03-

89-K-0022 and by a gift from Johnson Controls, Inc. to the Wisconsin Distinguished Professorship of CRA.

* Author to whom all correspondence should be addressed.

¹ R. E. Salomon, W. M. Graven, and G. B. Adams, Jr., *J. Chem. Phys.* **32**, 310 (1960).

² J. G. Bendoraitis and R. E. Salomon, *J. Phys. Chem.* **65**, 3666 (1965).

³ R. S. Sokolova, *Sov. J. Appl. Phys.* **41**, 454 (1974).

⁴ M. Abou Sekkina, *Ind. J. Phys.* **52A**, 244 (1978).

⁵ W. T. Pawlewicz, D. D. Hays, and P. M. Martin, *Thin Solid Films* **73**, 169 (1980).

⁶ K. V. S. R. Apparao, N. K. Sahoo, and T. C. Bagchi, *Thin Solid Films* **129**, L71 (1985).

⁷ R. Rujkorakarn and J. R. Sites, *J. Vac. Sci. Technol. A* **4**, 568 (1986).

"Band gap" reported at 3.8 eV

⁸ M. A. Russak, C. V. Jahnes, and E. P. Katz, *J. Vac. Sci. Technol. A* **7**, 1248 (1989).

⁹ C.-K. Kwok and C. R. Aita, *J. Vac. Sci. Technol. A* **7**, 1235 (1989).

¹⁰ C.-K. Kwok and C. R. Aita, *J. Appl. Phys.* **66**, 2756 (1989).

¹¹ R. H. French, 91st Annual Meeting of the American Ceramic Society, Indianapolis, IN, April 1989 (unpublished). Kramers-Kronig analysis of reflectance measurements on single crystal α -ZrO₂ show direct transitions at 5.3 and 6.2 eV.

¹² L. V. Azaroff, *Elements of X-Ray Crystallography* (McGraw-Hill, New York, 1968), pp. 549-558. The term "minimum dimension" is used here to acknowledge that we are assuming the limiting case of peak broadening due to finite crystallite size with no contribution from random lattice strain.

¹³ See, for example, J. I. Pankove, *Optical Process in Semiconductors* (Prentice-Hall, Englewood Cliffs, NJ, 1971).

¹⁴ F. Zandiehnam, R. A. Murray, and W. Y. Ching, *Physica B* **150**, 19 (1988).

APPENDIX II

- A. "Process parameter/growth environment/film property relationships for the sputter deposited yttrium-oxygen system." C.-K. Kwok, C.R. Aita, and E. Kolawa, *J. Vac. Sci. Tech. A* 8, 1330-1334 (1990).
- B. "Near-ultraviolet optical absorption in sputter deposited cubic yttria." C.-K. Kwok, C.R. Aita, and E. Kolawa, *J. Appl. Phys.* 68, 2945-2950 (1990).
- C. "High temperature air-annealing behavior of sputter deposited amorphous yttria films on fused silica." S.N. Mukherjee and C.R. Aita, *J. Vac. Sci. Technol. A* 10, 2723-8 (1992).
- D. "Kinetics of morphological change during annealing of amorphous yttria." S.N. Mukherjee and C.R. Aita, *J. Vac. Sci. Technol. A* 10, 3362-4 (1992).
- E. "Annealing-induced microstructural and crystallographic changes in crystalline yttria films on silica." S.N. Mukherjee and C.R. Aita, *J. Vac. Sci. Technol. A* 10, 3356-8 (1992).

Process parameter-growth environment-film property relationships for the sputter deposited yttrium-oxygen system

Chee-Kin Kwok and Carolyn Rubin Aita

Materials Department and the Laboratory for Surface Studies, University of Wisconsin-Milwaukee, Milwaukee, Wisconsin 53201

Elzbieta Kolawa

California Institute of Technology, Pasadena, California 91125

(Received 31 October 1989; accepted 6 November 1989)

In this study, a Y target was sputtered in radio frequency (rf)-excited, rare gas discharges (Ne, Ar) containing 0%–40% O_2 , operated at cathode voltage from -1.0 to -1.7 kV. *In situ* optical emission spectrometry was used to monitor two neutral excited Y atom transitions ($\lambda = 0.6191, 0.6793 \mu\text{m}$) and an excited O atom transition ($\lambda = 0.7774 \mu\text{m}$) as a function of changing process parameter. Films were grown on fused SiO_2 substrates, and their crystallography, optical behavior, and electrical resistivity was determined. A "phase diagram" for Y-O not grown under conditions of equilibrium thermodynamics was constructed, and included hexagonal Y, cubic Y_2O_3 , and Y and Y_2O_3 that had no long range crystallographic order. Two direct optical transitions across the energy band gap of cubic Y_2O_3 , at 5.07 and 5.73 eV, were identified. Combining discharge diagnostics, growth rate, and film property results, it was concluded that Y_2O_3 was formed at the substrate concurrent with the complete oxidation of the target surface. Even after target oxidation, the discharge contained atomic Y. On the basis of fundamental optical absorption edge characteristics, cubic Y_2O_3 that more closely resembled the bulk material was obtained when the Y-oxide molecule/Y atom flux to the substrate was high.

I. INTRODUCTION

The purpose of this study is to investigate process parameter-growth environment-film property relationships for the reactive sputter deposited Y-O materials system. Films were prepared by sputtering a Y target using O_2 -bearing discharges. The transition from Y to Y_2O_3 growth was studied as a function of three process parameters: (1) the cathode voltage, (2) the O_2 content of the sputtering gas, and (3) the type of rare gas used in conjunction with O_2 . These parameters can be independently varied, and combined, they determine other important parameters such as discharge power and growth rate.

The experimental program included optical emission spectrometry for *in situ* discharge diagnostics. Two optical transitions of the neutral Y atom from a low-lying excited state to the ground state were used to monitor the Y atomic population in the discharge as a function of changing process parameter. In addition, an optical transition of the neutral O atom was used to monitor target surface oxidation. The film properties that were investigated are crystallography, visible/near-ultraviolet optical behavior, and electrical resistivity.

Thin film yttria is of interest as a capacitor material and although there have been only a few reports of its fabrication, these reports cover a wide variety of techniques including post deposition oxidation of Y films,^{1,2} physical vapor and inductively coupled plasma deposition using a Y-O powder source,^{3,4} and rf- and ion-beam sputter deposition from a Y₂O₃ target.^{5,6} Reactive sputter deposition using a metal target and an O_2 -bearing discharge is an important method for near room temperature metal oxide film growth. We hope that the results presented below will enable other inves-

tigators to reproducibly grow yttria films with desired properties by this method.

II. EXPERIMENTAL PROCEDURE

Films were grown in a radio frequency (rf) diode sputter deposition apparatus. A 13 cm diameter 99.8% Y target was thermally bonded to a water-cooled Cu cathode. Supersil fused silica substrates were placed on a water-cooled Y-coated Cu pallet covering the anode. The anode-cathode spacing was 7 cm.

The chamber was evacuated to $< 5 \times 10^{-7}$ Torr with a liquid N_2 -trapped, hot Si-base oil diffusion pump and back-filled with the sputtering gas to a total pressure of 1×10^{-2} Torr. The sputtering gas consisted of a rare gas, Ne (99.996%) or Ar (99.999%), containing from 0% to 40% O_2 (99.99%). Each component was separately admitted into the chamber using an MKS Instruments Baratron Series 260 pressure/flow control system.

Two presputters preceded each deposition. The first presputter was carried out in pure rare gas for 30 min, and its purpose was to remove the oxide layer that had formed on the target surface upon exposure to air. The second presputter was carried out in the rare gas- O_2 mixture used to deposit the film and its purpose was to allow time for discharge and target surface reactions to reach dynamic equilibrium. The movable shutter that covered the substrates was then removed and the films were deposited according to the conditions listed in Table I. Values of cathode voltage from 1.0 to 1.7 kV peak-to-peak were used. The anode was kept at ground potential.

A model HR320 Instruments SA optical spectrometer with 1200 and 2400 groove/mm holographic gratings capa-

TABLE I. Deposition parameters, film thickness, growth rate, and resistivity of Y and Y₂O₃ films sputter deposited on fused SiO₂.

Film	Rare gas	%O ₂	V _d (-kV)	Power (W)	x (10 ² nm)	G (nm/min)	ρ ^a (μΩ cm)
1	Ar	0	1.7	310	25.7 ± 0.7	32.0 ± 0.9	254 ± 19
2	Ar	2	1.7	340	24.2 ± 0.6	28.4 ± 0.7	2411 ± 74
3	Ar	4	1.7	670	4.9 ± 0.6	5.3 ± 0.7	nc
4	Ar	0	1.5	280	6.5 ± 0.3	28.4 ± 1.2	196 ± 13
5	Ar	2	1.5	350	12.0 ± 0.4	28.6 ± 0.9	364 ± 44
6	Ar	4	1.5	600	3.3 ± 0.2	5.0 ± 0.3	nc
7	Ar	20	1.5	620	1.7 ± 0.1	4.5 ± 0.3	nc
8	Ar	0	1.3	170	5.5 ± 0.1	21.1 ± 0.5	200 ± 8
9	Ar	2	1.3	390	2.2 ± 0.2	4.2 ± 0.4	nc
10	Ar	20	1.3	400	1.9 ± 0.2	3.2 ± 0.3	nc
11	Ar	40	1.3	400	2.4 ± 0.2	2.8 ± 0.3	nc
12	Ne	0	1.7	360	12.2 ± 0.7	10.1 ± 0.6	248 ± 22
13	Ne	2	1.7	450	1.4 ± 0.2	2.0 ± 0.3	nc
14	Ne	4	1.7	460	1.6 ± 0.1	1.8 ± 0.1	nc
15	Ne	20	1.7	630	1.7 ± 0.1	2.2 ± 0.1	nc
16	Ne	0	1.5	290	5.9 ± 0.4	7.4 ± 0.5	193 ± 19
17	Ne	2	1.5	405	1.2 ± 0.1	2.0 ± 0.1	nc
18	Ne	4	1.5	405	2.1 ± 0.4	2.3 ± 0.5	nc
19	Ne	20	1.5	450	1.2 ± 0.1	2.0 ± 0.2	nc
20	Ne	40	1.5	580	1.8 ± 0.1	2.2 ± 0.2	nc
21	Ne	0	1.3	180	1.9 ± 0.2	9.3 ± 0.1	503 ± 40
22	Ne	2	1.3	270	1.0 ± 0.3	1.7 ± 0.5	nc
23	Ne	20	1.3	330	1.1 ± 0.1	1.8 ± 0.2	nc
24	Ne	40	1.3	430	1.5 ± 0.2	2.4 ± 0.3	nc
25	Ne	20	1.0	170	1.4 ± 0.2	1.2 ± 0.2	nc
26	Ne	40	1.0	190	1.4 ± 0.2	1.2 ± 0.2	nc

^aρ for bulk Y = 57 μΩ cm.

ble of 0.05 nm resolution was used for *in situ* optical emission diagnostics of the discharge. Radiation emitted from the region between the anode and cathode was sampled as a function of wavelength through an optical window with a transmission cutoff of 0.32 μm. The window was shuttered when not in use, and was also periodically removed from the chamber and its transmission characteristics were checked by spectrophotometry to monitor and correct for intensity changes caused by coating with sputtered flux in the course of the experiment.

The emission intensity $I(Y^*)$ from two optical transitions of the neutral Y atom, at $\lambda = 0.6191$ and 0.6793 μm,¹⁰ was monitored. The lower level of the transitions is the Y atom ground state Y⁰. The glow discharges studied here are not in thermal equilibrium. Therefore, the number of atoms at the upper and lower levels of the transition, $n(Y^*)$ and $n(Y^0)$ respectively, are not directly related through the statistical weight of each level and the Boltzmann factor. However, if the discharge is optically thin,¹⁰ changes in $n(Y^*)$ are directly proportional to changes in $I(Y^*)$ and can be used to estimate changes in $n(Y^0)$.¹¹ Emission from neutral atomic O, $\lambda = 0.7774$ μm, was used to detect the presence of oxygen in the discharge.¹²

Film thickness x was measured postdeposition with a Tenacor Alpha-Step 200 model profilometer. The growth rate, G , was determined from this measurement. Electrical resistivity ρ was measured using a four-point probe. Crystallography was determined by double-angle x-ray diffraction (XRD) using Cu K α radiation ($\lambda = 0.15418$ nm). Peak

position (2θ), relative intensity, and full width at one-half of the maximum intensity (FWHM) were determined. The diffractometer was calibrated using the (01.1) diffraction peak of a quartz standard at $2\theta = 26.66 \pm 0.02^\circ$, whose width is 0.18° . Rutherford backscattering spectroscopy (RBS) was carried out on selected films to determine the relative atomic concentration of Y and O. 2 MeV He⁺ ions were used as the bombarding species.

A Perkin-Elmer Model 330 UV-visible-IR double beam spectrophotometer with a specular reflection attachment was used to determine the transmittance T and reflectance R of near-normal incident radiation. Measurements were made in laboratory air at room temperature. The absorption coefficient α was calculated from¹¹

$$T = [(1 - R)^2 \exp(-\alpha x)] / [1 - R^2 \exp(-2\alpha x)]. \quad (1)$$

III. RESULTS AND DISCUSSION

Film thickness, growth rate, and resistivity are recorded in Table I. Crystallographic parameters are recorded in Table II. Films grown in Ar-O₂ discharges show two phases, hexagonal close-packed Y and body-centered-cubic Y₂O₃. There are two additional structures present in films grown in Ne-O₂ discharges, metallic (Film No. 21) and insulating (Film Nos. 22, 25, and 26) phases that have no long range crystallographic order detectable by XRD. RBS results show that the nonmetallic phase is chemically identifiable as Y₂O₃, and is denoted here as "a-Y₂O₃." Figure 1 shows the

TABLE II. Major diffraction planes in Y and Y₂O₃ films.

Film	2θ (deg)	Plane	FWHM (deg)	Rel. I	d _{hkl} (nm) ^a
1	30.92	00.2 α-Y	0.46	100	0.289
	64.49	00.4 α-Y	0.93	3	0.145
2	30.86	00.2 α-Y	0.42	100	0.290
	64.32	00.4 α-Y	0.76	3	0.145
3	29.02	222 c-Y ₂ O ₃	0.70	100	0.308
	48.14	440 c-Y ₂ O ₃	1.10	21	0.189
4	30.96	00.2 α-Y	0.38	100	0.289
	64.49	00.4 α-Y	0.82	2	0.145
5	30.81	00.2 α-Y	0.46	100	0.290
	64.11	00.4 α-Y	0.50	2	0.145
6	29.01	222 c-Y ₂ O ₃	0.76	100	0.308
	28.94	222 c-Y ₂ O ₃	0.68	100	0.309
8	30.96	00.2 α-Y	0.38	100	0.289
	28.98	222 c-Y ₂ O ₃	0.78	100	0.308
10	28.97	222 c-Y ₂ O ₃	0.77	100	0.308
	28.96	222 c-Y ₂ O ₃	0.80	100	0.308
12	27.89	10.0 α-Y	0.42	32	0.320
	30.44	00.2 α-Y	0.64	10	0.294
13	31.95	10.1 α-Y	0.59	6	0.280
	49.16	11.0 α-Y	0.64	100	0.185
14	28.96	222 c-Y ₂ O ₃	0.82	100	0.308
	28.93	222 c-Y ₂ O ₃	0.78	100	0.309
15	28.94	222 c-Y ₂ O ₃	0.71	100	0.309
	49.09	11.0 α-Y	0.62	100	0.186
16	27.86	10.0 α-Y	0.41	26	0.320
	30.38	00.2 α-Y	0.60	6	0.294
17	31.88	10.1 α-Y	0.63	21	0.281
	28.95	222 c-Y ₂ O ₃	0.83	100	0.308
18	28.97	222 c-Y ₂ O ₃	0.75	100	0.308
	28.97	222 c-Y ₂ O ₃	0.75	100	0.308
20	28.89	222 c-Y ₂ O ₃	0.67	100	0.309
	no diffraction peaks				
21	no diffraction peaks				
22	no diffraction peaks				
	28.94	222 c-Y ₂ O ₃	0.83	100	0.309
23	28.96	222 c-Y ₂ O ₃	0.77	100	0.308
	no diffraction peaks				
24	no diffraction peaks				
25	no diffraction peaks				
26	no diffraction peaks				

^ad_{hkl} for bulk unstressed material (in nm): hexagonal α-Y (10.0)-0.315, (00.2)-0.286, (10.1)-0.280, (11.0)-0.182; cubic c-Y₂O₃ (222)-0.306, (440)-0.187.

fields over which all phases exist as a function of cathode voltage and gas O₂ content for (a) Ar-O₂ and (b) Ne-O₂ discharges.

In terms of visual appearance, all Y₂O₃ films are transparent and colorless. Figure 2 shows the optical absorption coefficient calculated from Eq. (1) as a function of incident photon energy, *E*, for two films that represent the extremes in yttria optical behavior observed here: Film No. 7, which is c-Y₂O₃, and Film No. 22, which is α-Y₂O₃. Two optical transitions across the energy band gap occur in Film No. 7. There is a direct dependence of α² on *E* for both transitions, as shown in Fig. 3, indicating direct transitions.¹¹ Extrapolation of the data in Fig. 3 to α = 0 yields *E*_{g1} = 5.07 eV and *E*_{g2} = 5.73 eV. Two optical absorption studies of single crystal Y₂O₃ place the band gap at ~5.6 eV¹⁴ and ~6.1 eV,¹⁵ measured from the short wavelength limit of transmission. The value of *E*_{g2} obtained here is in good agreement with the single crystal values.

It can be seen from Fig. 2 that the α versus *E* data for Film No. 22 lacks the fine structure present in Film No. 7. How-

ever, a change of slope in the curve for Film No. 22 occurs in the vicinity of the onset of the higher energy transition in Film No. 7. At high photon energy, the curves for Film Nos. 7 and 22 converge indicating similar Y-O short range order.

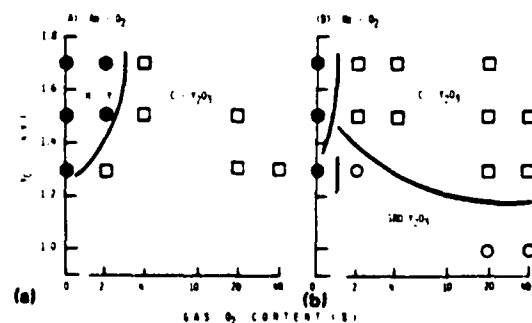


FIG. 1. A "phase diagram" for sputter deposited Y-O films. The crystal structure as a function of the cathode voltage and gas O₂ content. ●—hexagonal Y, ●—short range order Y, □—cubic Y₂O₃, ○—short range order Y₂O₃. (a) Ar-O₂, and (b) Ne-O₂.

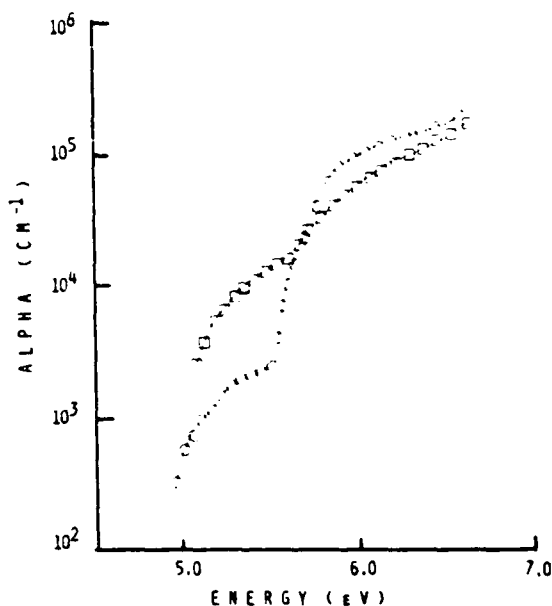


FIG. 2 The optical absorption coefficient as a function of the incident photon energy for two representative films \circ - c - Y_2O_3 , \square - a - Y_2O_3 .

The fundamental optical absorption edges of c - Y_2O_3 , Film Nos. 10, 11, and 20 are coincident with that of Film No. 7. The edges of a - Y_2O_3 , Film Nos. 25 and 26 are coincident with that of Film No. 22. However, all other c - Y_2O_3 films have edges whose features are less sharp than those of Film No. 7, indicating a greater amount of disorder, and yet not as featureless as the edge of Film No. 22. We will relate this phenomenon to the growth environment below.

With respect to discharge characteristics, the optical emission intensity from Y^* atoms is recorded in Table III. All values are relative to the intensity of the transition in a pure rare gas discharge operated at the same cathode voltage. There apparently is a resonance between the Y transition at $0.6191 \mu\text{m}$ (2.006 eV) and a strong O transition at $0.6157 \mu\text{m}$ (2.017 eV) that enhances $I(Y_{0.6191}^*)$ in Ne- O_2 discharges under some conditions, as indicated in Table III, and these data are not representative of a change $\pi(Y^*)$.

The relative arrival rate A is also included in Table III. This quantity is the growth rate relative to its value in a pure rare gas discharge operated at the same cathode voltage corrected for the difference in density between Y (4.47 g/cm^3) and Y_2O_3 (5.01 g/cm^3) when applicable. Bulk values for density are used here. It is well known that the metal target surface reacts with oxygen during reactive sputtering and the sputtered flux will consist of both metal and metal-oxide species. The relative arrival rate is assumed here to be proportional to the flux of Y to the substrate both in atomic form and bonded to O in a gaseous Y-oxide molecule of unknown chemistry.

Using a comparison of $I(Y^*)$ and A in Ar- O_2 discharges operated at -1.5 and -1.7 kV as an example, we can define three types of behavior as the sputtering gas O_2 content is increased. Type I: $I(Y^*)$ decreases faster than A as $2\% O_2$ is added to the discharge, indicating that some form of Y-oxide is being formed at and sputtered from the target surface as a molecule, along with atomic Y. Films grown under

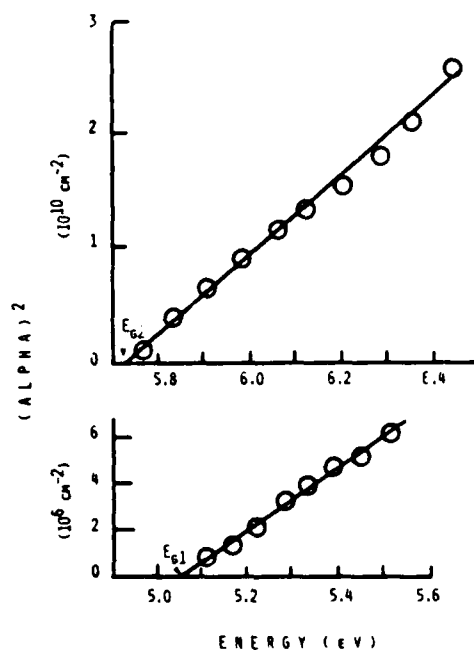


FIG. 3 The square of the absorption coefficient as a function of the incident photon energy for c - Y_2O_3 . Extrapolation of the data to $\alpha^2 = 0$ yields $E_{G2} = 5.07 \text{ eV}$ and $E_{G1} = 5.73 \text{ eV}$ for two direct transitions across the energy band gap.

these conditions are metallic but have a resistivity that is higher than that of films grown in pure rare gas operated at the same cathode voltage, suggesting the incorporation of O. Type II: Both $I(Y^*)$ and A decrease to $\sim 20\%$ of their value in pure rare gas as the gas O_2 content is increased to 4% . Concurrently, (1) an emission line at $0.7774 \mu\text{m}$ signals the presence of O in the discharge, and (2) the discharge power nearly doubles. O in the discharge indicates that the target is no longer gettering oxygen. Y_2O_3 is a better electron emitter than Y, and the increase in discharge power indicates that a complete oxide layer has formed at the target surface. Films grown under these conditions are c - Y_2O_3 , but have a fundamental optical absorption edge that lacks the sharpness of the representative curve for c - Y_2O_3 , shown in Fig. 2. Type III: $I(Y^*)$ decreases further and A remains constant as the gas O_2 content is increased to 20% , indicating that there is a larger flux of Y arriving at the substrate in a form other than atomic Y, compared to Type II. Type III behavior is earmarked by a value of $I(Y^*)$ that is less than A . The resulting films are c - Y_2O_3 , with an optical absorption edge represented by the curve shown for c - Y_2O_3 in Fig. 2.

Type III behavior occurs in Ar- O_2 discharges containing $\sim 2\% O_2$, operated at -1.3 kV , and in Ne- $40\% O_2$, operated at -1.5 kV . Type II behavior occurs in Ne- O_2 discharges operated at all values of V_c for gas O_2 content between 2 and $20\% O_2$. Type II behavior represents a relatively large metal flux associated with an oxidized target surface, which can come about either by dissociation of the Y-oxide at the target surface upon sputtering, or by dissociation of the sputtered gaseous Y-oxide molecule in the negative glow. With respect to process parameters, high cathode voltage, low gas

TABLE III. Relative intensity of Y optical emission transitions monitored in Ar-O₂ and Ne-O₂ discharges during Y and Y₂O₃ film growth, and the relative Y arrival rate.

Rare gas	%O ₂	V _d (-kV)	I(0.6191 μm)	I(0.6793 μm)	A
Ar	0	1.7	100	100	100
Ar	2	1.7	70	70	89
Ar	4	1.7	19	12	15
Ar	0	1.5	100	100	100
Ar	2	1.5	60	60	100
Ar	4	1.5	15	15	16
Ar	20	1.5	3	2	14
Ar	0	1.3	100	100	100
Ar	2	1.3	6	5	18
Ar	20	1.3	7	4	13
Ar	40	1.3	7	3	12
Ne	0	1.7	100	100	100
Ne	2	1.7	59	52	18
Ne	4	1.7	38	38	16
Ne	20	1.7	53 ^a	31	19
Ne	0	1.5	100	100	100
Ne	2	1.5	62	65	24
Ne	4	1.5	66	60	27
Ne	20	1.5	85 ^a	25	24
Ne	40	1.5	226 ^a	20	26
Ne	0	1.3	100	100	100
Ne	2	1.3	110 ^a	100	16
Ne	4	1.3	113 ^a	83	...
Ne	20	1.3	114 ^a	26	17

^aRelative to the value in a pure rare gas discharge operated at the same value of V_d.

^bValue is enhanced by resonance with a strong O transition at 0.6157 μm, and not representative of changes in n(Y^{II}).

O₂ content, and Ne rather than Ar as the rare gas component encourages Type II behavior. The latter result is in contrast to findings for the Zr-O system,¹⁶ in which the use of Ne reduced the metal/metal oxide flux in the negative glow. Clearly, Ne is acting upon oxidized Y either at the target surface or in the negative glow in a much different way than it acts upon oxidized Zr. This interesting phenomenon will be an area for future research.

IV. SUMMARY

Reactive sputter deposition of Y and Y₂O₃ films using a Y target and O₂-bearing discharges was studied as a function of three process parameters: cathode voltage, discharge O₂ content, and type of rare gas used in conjunction with O₂. *In situ* optical emission spectrometry was used to monitor changes in the Y and O atomic population in the negative glow as a function of changing process parameter. The range of parameters over which hexagonal Y, cubic Y₂O₃, and Y and Y₂O₃ structures with no long range crystallographic order were deposited was determined. Two direct optical transitions across the energy band gap of c-Y₂O₃, at 5.07 and 5.73 eV, were identified. Combining discharge diagnostics, growth rate, and film property results, it was concluded that Y₂O₃ was formed at the substrate concurrent with the complete oxidation of the target surface. Furthermore, based on fundamental optical absorption edge characteristics, c-Y₂O₃ that more closely resembled the bulk material was obtained when the Y-oxide/Y flux to the substrate was high.

ACKNOWLEDGMENTS

This work was supported under US ARO Grant No. DAAL03-89-K-0022 and through a gift by Johnson Controls, Inc. to the Wisconsin Distinguished Professorship of CRA.

- ¹J. R. Rauden, *J. Electrochem. Soc.* **114**, 75 (1966).
²M. Gursvitch, I. Manchanda, and J. M. Gibson, *Appl. Phys. Lett.* **51**, 919 (1987).
³T. Tsutsumi, *Jpn. J. Appl. Phys.* **9**, 735 (1970).
⁴D. F. Bezuidenhout and R. Pretorius, *Thin Solid Films* **139**, 121 (1986).
⁵M. Sayer, M. S. Martin, and N. J. Hellicar, *Thin Solid Films* **6**, R61 (1970).
⁶B. D. Merkle, R. N. Kniseley, and F. A. Schmidt, *J. Appl. Phys.* **62**, 1017 (1987).
⁷R. M. Goldstein and S. C. Wigginton, *Thin Solid Films* **3**, R41, (1969).
⁸R. W. Tustison, F. F. Varitimos, D. G. Montanari, and J. M. Wahl, *J. Vac. Sci. Technol. A* **7**, 2256 (1989).
⁹A. N. Zaidel, V. K. Prokofev, S. M. Karskin, V. A. Slavnyi, and E. Ya. Shreider, *Tables of Spectral Lines* (Plenum, New York, 1970).
¹⁰H. G. Kuhn, *Atomic Spectra* (Academic, New York, 1963), p. 80.
¹¹J. E. Greene, *J. Vac. Sci. Technol.* **15**, 1718 (1978).
¹²C. R. Alta and M. E. Marhic, *J. Appl. Phys.* **52**, 1807 (1981); *J. Vac. Sci. Technol. A* **1**, 69 (1983).
¹³See, for example, J. I. Pankove, *Optical Processes in Semiconductors* (Prentice-Hall, Englewood Cliffs, NJ, 1971).
¹⁴Y. Nigara, *Jpn. J. Appl. Phys.* **7**, 404 (1968).
¹⁵V. N. Abramov and A. I. Kuznetsov, *Sov. Phys. Solid State* **20**, 399 (1978).
¹⁶C. K. Kwok and C. R. Alta, *J. Vac. Sci. Technol. A* **7**, 1235 (1989).

Near-ultraviolet optical absorption in sputter-deposited cubic yttria

Chee-Kin Kwok, Carolyn Rubin Aita,^{a)} and Elzbieta Kolawa^{b)}

Materials Department and the Laboratory for Surface Studies, University of Wisconsin-Milwaukee, P.O. Box 784, Milwaukee, Wisconsin 53201

(Received 5 April 1990; accepted for publication 6 June 1990)

Cubic yttria films were sputter deposited on unheated fused silica substrates. *In situ* optical spectrometry was used to monitor emission from six *YI* transitions in the discharge. A simple formalism was developed for estimating the ratio of yttrium arriving at the substrate in atomic form to yttrium bonded to oxygen in an unspecified molecular form. The optical absorption coefficient ($\alpha = \sim 10^3 - 10^7 \text{ cm}^{-1}$) of the films was determined, post-deposition, over the energy range 5.0–6.2 eV. The results show that a large atomic yttrium flux to the substrate during deposition resulted in a "disordered" optical absorption edge. A large flux of yttrium bonded to oxygen resulted in an edge with two direct interband transitions separated by 0.66 eV, in good agreement with the bulk single crystal ϵ_2 data and a recent theoretical energy band calculation for cubic yttria.

I. INTRODUCTION

Yttria, chemically Y_2O_3 , in bulk form at room temperature has a bixbyite-type body-centered cubic lattice structure consisting of an eighty-atom unit cell in which Y is in sixfold coordination with O.¹ In a previous study,² a "phase diagram" for the sputter deposited Y-O system, shown in Fig. 1, was developed in which film crystallography was presented as a function of three independent process parameters: (1) cathode voltage; (2) O_2 content of the sputtering gas; and (3) type of rare gas used in conjunction with O_2 . From Fig. 1, it can be seen that both cubic- (c-) and short-range order (a-) yttria structures occur in sputter deposited films. Preliminary results comparing the optical absorption edge of a single film of each type showed differences in the optical absorption edge, as expected.

The purpose of this study is threefold: (1) to expand preliminary near-ultraviolet optical absorption results² by sampling films throughout the c-yttria phase field; (2) to compare the results with those reported for bulk single-crystal c yttria¹ and to a recent theoretical calculation of the electronic band structure,⁴ and (3) to relate electronic disorder in the vicinity of the band gap (evidenced by changes in near-ultraviolet absorption) to the film growth environment.

II. EXPERIMENTAL PROCEDURE

The experimental program consisted of film growth by reactive sputter deposition, *in situ* sputtering discharge diagnostics using optical emission spectrometry, and post-deposition film characterization using visible-near-ultraviolet spectrophotometry to determine the structure of the fundamental optical absorption edge. Infrared spectrophotometry and Rutherford backscattering spectroscopy were carried out on selected samples to obtain lattice absorption data and chemistry.

A. Film growth

Films were grown in an rf diode apparatus by sputtering a 13-cm-diam, 99.8% pure Y target bonded to a water-cooled Cu cathode. Supersil fused silica, (111)-cut Si, and carbon foil substrates were placed on a water-cooled Y-coated Cu pallet covering the anode. The anode-cathode spacing was 7 cm. The chamber was evacuated to $< 5 \times 10^{-7}$ Torr with a liquid- N_2 trapped, hot Si-base oil diffusion pump and backfilled with the sputtering gas to a total pressure of 1×10^{-2} Torr. The sputtering gas consisted of a rare gas, Ne (99.996% pure) or Ar (99.999% pure), and O_2 (99.99% pure). Each component was separately admitted into the chamber using an MKS Instruments Baratron Series 260 pressure/flow control system.

Two presputters preceded each deposition. The first presputter was carried out in pure rare gas for 30 min, and its purpose was to remove the oxide layer that had formed on the target surface upon exposure to air. The second presputter was carried out in the rare gas- O_2 mixture used to deposit the film and its purpose was to allow time for discharge and target surface reactions to reach dynamic equilibrium. The

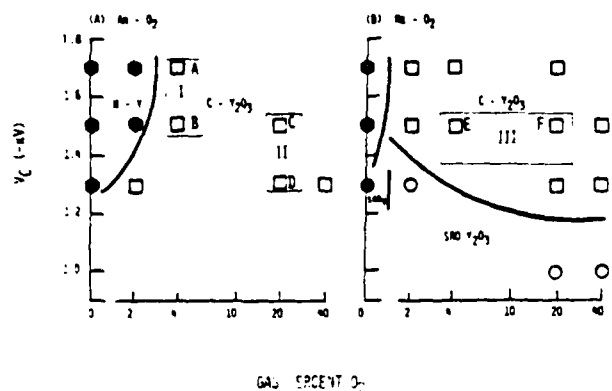


FIG. 1. A "phase diagram" for sputter deposited Y-O films, adapted from Ref. 2, indicating films A-F studied.

^{a)} Send all correspondence to this author.

^{b)} Permanent address: California Institute of Technology, 116-21, Pasadena, CA 91125.

TABLE I. Growth parameters, film thickness, growth rate, and Y:O atomic concentration for sputter deposited *c*-yttria films.

Film	Gas	V (-kV)	Power (W)	x (kÅ) ^a	G (Å/min)	Y:O ^b	x' (kÅ) ^b
A	Ar-4% O ₂	1.7	670	4.9 ± 0.6	53 ± 7
B	Ar-4% O ₂	1.5	600	3.3 ± 0.2	50 ± 3	2:3.0	3.30
C	Ar-20% O ₂	1.5	620	1.7 ± 0.1	45 ± 3
D	Ar-20% O ₂	1.3	400	1.9 ± 0.2	32 ± 3	2:3.0	1.97
E	Ne-4% O ₂	1.5	405	2.1 ± 0.4	23 ± 5
F	Ne-20% O ₂	1.5	450	1.2 ± 0.1	20 ± 2

^a Profilometer measurement of yttria on fused silica.

^b RBS measurement of yttria on carbon foil.

movable shutter that covered the substrates was then removed and the films were grown according to the conditions listed in Table I. The cathode voltage *V_c* recorded in Table I was measured peak-to-peak during a 13.56-MHz rf cycle. The anode was kept at ground potential. The films studied are designated by the letters A-F on Fig. 1.

B. Discharge characterization

The rf forward power in the discharge was determined as a function of nominal sputtering gas composition and cathode voltage. This set of data, combined with optical emission data, allows us to determine when target surface oxidation has occurred.

A model HR320 Instruments SA optical spectrometer with 1200 and 2400 groove/mm holographic gratings capable of 0.5 Å resolution was used to measure the optical emission intensity *I*(λ) as a function of nominal sputtering gas composition and cathode voltage. *I*(λ) corresponding to six de-excitations of the neutral yttrium atom (YI) to ground state were monitored, at λ = 3621, 4128, 4143, 4236, 6191, and 6793 Å.⁵ Radiation emitted from the region between the anode and cathode was sampled through an optical window with a transmission cutoff of 3.2 kÅ. The window was shuttered when not in use, and was also periodically removed from the chamber and its transmission characteristics checked by spectrophotometry to detect intensity changes caused by coating with sputtered flux during the course of the experiment.

C. Film characterization

Crystallographic data for the films are reported in Ref. 2 and recorded in Table II. In summary, all films are polycrystalline *c*-yttria. Film A has a preferred {222} orientation. Films B-F have only {222} planes oriented parallel to the substrate. In all films, the interplanar spacing *d*₍₂₂₂₎ is larger than the bulk value, and the full width at one-half maximum diffraction peak intensity Δ*d*₍₂₂₂₎ is greater than the value due to instrument effects alone.

Film thickness *x* was measured post-deposition with a Tencor Alpha-Step 200 model profilometer from a step produced by masking part of the fused silica substrate during

deposition. The growth rate *G* was determined by dividing film thickness by deposition time. We wanted to calculate the growth rate relative to its value in a pure rare gas discharge operated at a particular cathode voltage *G*' = [*G*(rare gas + O₂)/*G*(rare gas)]. Films were grown in pure rare gas for this purpose. As discussed in Sec. IV, *G*' was used to estimate the arrival flux of Y/Y-oxide gaseous species to the substrate.

A Perkin-Elmer Model 330 UV-visible-IR double beam spectrophotometer with a specular reflection attachment was used to measure the transmittance *T* and reflectance *R* of near-normal incident radiation of films grown on fused silica. Measurements were made in laboratory air at room temperature. The absorption coefficient α was calculated from the expression,⁶

$$T = [(1 - R)^2 \exp(-\alpha x)] / [1 - R^2 \exp(-2\alpha x)]. \tag{1}$$

A Nicolet Model MX-1 FT IR spectrometer was used to obtain the infrared absorption spectra of films grown on (111) Si using the same discharge conditions used to grow

TABLE II. Crystallographic parameters of sputter-deposited *c* yttria on fused silica (from Ref. 2).

Film	2θ (deg) ^a	Plane	Rel. <i>I</i> ^b	<i>d</i> _{hkl} (Å) ^b	Δ <i>d</i> (deg) ^c
A	29.02	222 <i>c</i> -Y ₂ O ₃	100	3.077	0.70
	48.14	440 <i>c</i> -Y ₂ O ₃	21	1.890	1.10
B	29.01	222 <i>c</i> -Y ₂ O ₃	100	3.078	0.76
C	28.94	222 <i>c</i> -Y ₂ O ₃	100	3.085	0.68
D	28.97	222 <i>c</i> -Y ₂ O ₃	100	3.082	0.77
E	28.97	222 <i>c</i> -Y ₂ O ₃	100	3.082	0.75
F	28.97	222 <i>c</i> -Y ₂ O ₃	100	3.082	0.75

^a Unresolved CuKα radiation used, λ = 1.5418 Å; error in single measurement = ± 0.02°.

^b Rel. *I* and *d*_{hkl} for bulk unstressed *c*-Y₂O₃: (222)-100, 3.060 Å, (440)-46, 1.874 Å; error in single *d*_{hkl} measurement = ± 0.002 Å.

^c Δ*d* 0.18 (± 0.04)° for the (011) diffraction peak of the quartz standard at 2θ = 26.66°.

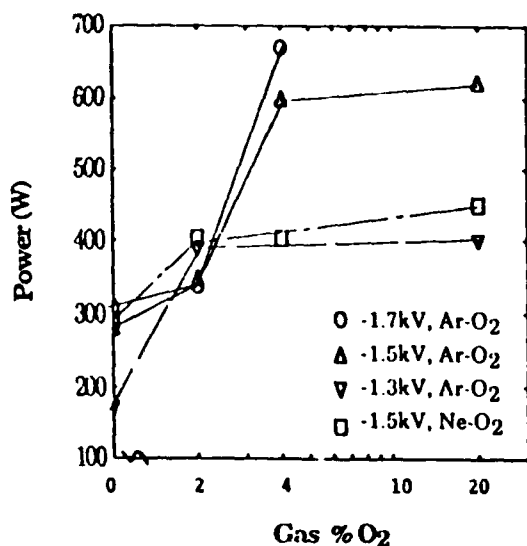


FIG. 2. The power as a function of gas O₂ content for Ar-O₂ discharges operated at -1.3, -1.5, and -1.7 kV (*p-p*), and Ne-O₂ discharges operated at -1.5 kV (*p-p*).

films B and D. These films are denoted B' and D'. The instrument was calibrated using a polystyrene standard to an accuracy of $\pm 4 \text{ cm}^{-1}$ in the wave number region of interest, 400–4000 cm^{-1} (25.0–2.5 μm).

Rutherford backscattering spectroscopy (RBS) of films grown on carbon foil using the same conditions used to grow films B and D was carried out with 2 MeV He⁺ ions

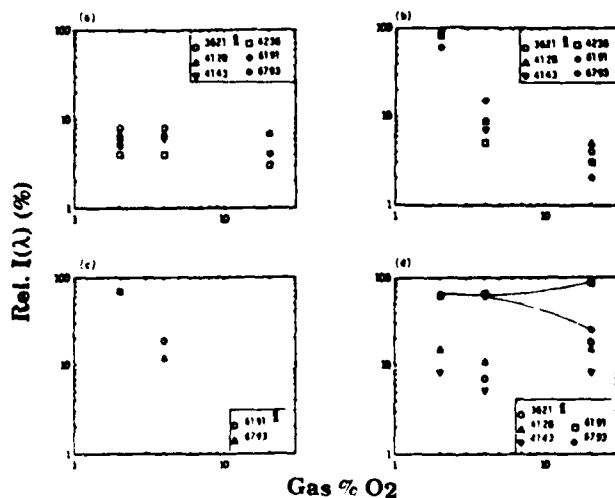


FIG. 3. Rel. $I(\lambda)$ as a function of gas O₂ content for (a) -1.3 kV, Ar-O₂ discharges, (b) -1.5 kV, Ar-O₂ discharges, (c) -1.7 kV, Ar-O₂ discharges, and (d) -1.5 kV, Ne-O₂ discharges (curves are drawn through red transition data for an easier comparison with UV transitions).

as the bombarding species. Y:O atomic concentration ($\pm < 10\%$) and film thickness using bulk *c*-yttria density were determined.

III. RESULTS

Figure 2 shows the rf forward power as a function of nominal sputtering gas composition and cathode voltage. The emission intensity relative to its value in a pure rare gas discharge operated at a particular cathode voltage, Rel. $I(\lambda)$, is shown in Fig. 3.

Film thickness, growth rate, and Y:O atomic concentration are recorded in Table I. The Y:O atomic concentration in films B and D is 2:3. Profilometer and RBS measurements of thickness are in agreement.

In terms of visual appearance, all films are transparent and colorless in transmitted light. Figure 4 shows the optical absorption coefficient as a function of incident photon energy E for films grown in three regions of the phase diagram, as shown in Fig. 1. (a) Films A and B were grown in Ar-O₂ discharges, using conditions near the yttrium:*c*-yttria phase boundary (region I). (b) Films C and D were grown in Ar-O₂ discharges, using conditions far from the yttrium:*c*-yttria phase boundary (region II). (c) Films E and F were grown in Ne-O₂ discharges, using conditions across the *c*-yttria phase field (region III), specifically at the same nominal O₂ content (4% and 20%) and V_c (-1.5 kV) used to grow films B and D.

In general, α varies as $C(E - E_g)^{1/2}$ for direct transitions ($\Delta k = 0$) across the band gap. We previously identified² two direct interband transitions in a film grown under region II conditions, with optical gaps $E_{g1} = 5.07 \text{ eV}$ and $E_{g2} = 5.73 \text{ eV}$. Figure 5 shows α^2 versus E for films C and D. It can be seen that these data are in good agreement with curves from Ref. 2, included in Fig. 5.

The infrared spectra of B' and D' have a vibrational band characteristic of bulk *c*-yttria short range order.^{7,8} The frequency at maximum band intensity ν and the full width at one-half maximum intensity $\Delta\nu$ are recorded in Table III. Bulk *c*-yttria powder has a strong vibrational band at $\nu = 561 \text{ cm}^{-1}$,⁸ single-crystal data places ν at 580 cm^{-1} ,⁷ and at 542 cm^{-1} for polycrystalline, multiorientation, and evaporated *c*-yttria films.⁹ Films B and D have identical ν values, within experimental error, and lie between bulk polycrystalline and single-crystal values. $\Delta\nu$ values, which represent the statistical distribution of the vibrational frequency about the average value, are identical for films B and D. These results show that *c*-yttria films representing regions I and II in the phase diagram are indistinguishable in terms of average Y-O short-range order.

IV. DISCUSSION

In the case of Ar-O₂ discharges, the sudden increase in power and decrease in Rel. $I(\lambda)$ at a critical gas O₂ content indicates that an oxide has formed on the target surface, and that this oxide is a better secondary electron emitter than yttrium metal. Target surface oxidation occurs at 4% O₂ for discharges operated at -1.7 and -1.5 kV, and at 2% O₂ for a -1.3-kV discharge. Yttrium atoms in the discharge result from target surface oxide dissociation upon sputtering

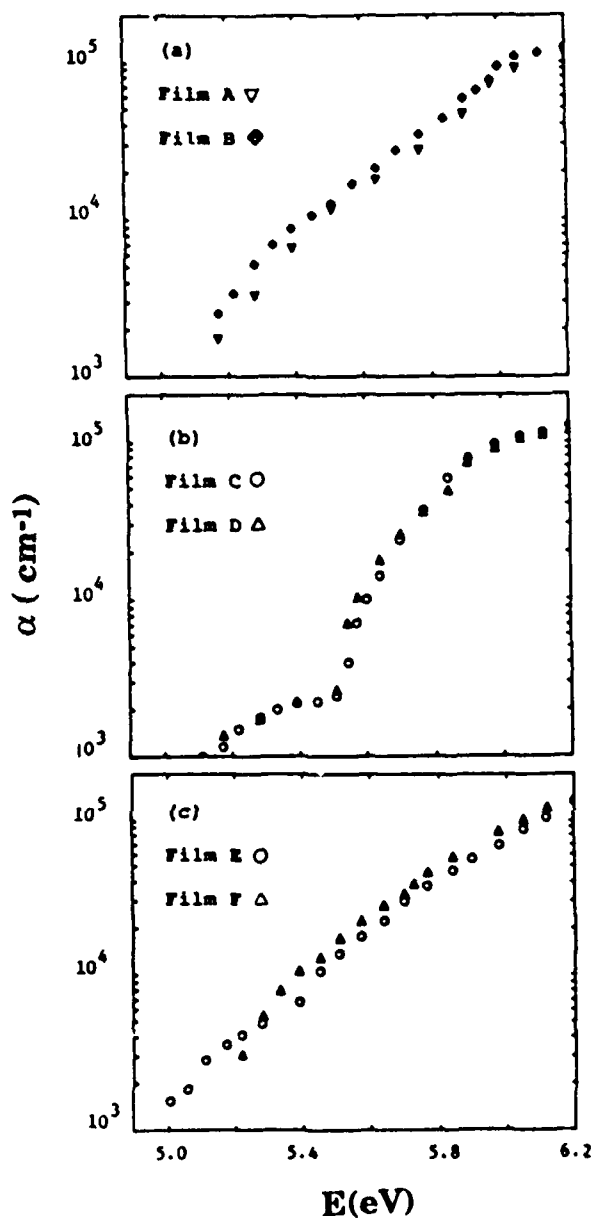


FIG. 4. The optical absorption coefficient α as a function of incident photon energy E for (a) films A and B (region I), (b) films C and D (region II), and (c) films E and F (region III).

or from dissociation of sputtered Y-oxide molecules in the plasma volume. In the case of Ne-O₂ discharges operated at -1.5 kV, the increase in power and decrease in $I(\lambda)$ from all ultraviolet transitions indicates an oxidized target surface at 2% O₂. Hence, all films studied are sputtered from an oxidized target surface. $I(6191 \text{ \AA})$ and $I(6793 \text{ \AA})$ are not reduced in -1.5 kV, Ne-O₂ discharges even though the target surface is oxidized. There appears to be selective enhancement of the upper-level population associated with

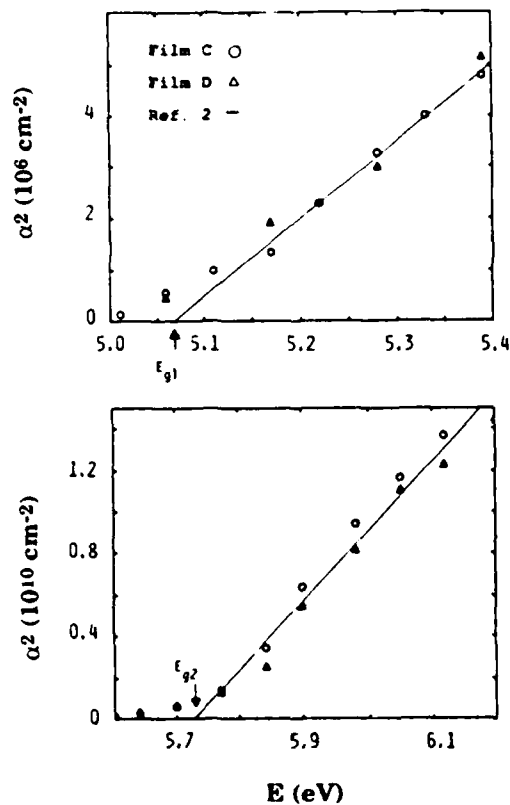


FIG. 5. α^2 vs E for films C and D. The solid line represents data taken from Ref. 2. Two direct transitions across the energy band gap occur at $E_{g1} = 5.07 \text{ eV}$ and $E_{g2} = 5.73 \text{ eV}$.

these red transitions due to a plasma volume reaction(s).

Optical absorption measurements yielding edge structure have yet to be made on bulk single-crystal *c* yttria. The α versus E spectrum, however, will be similar to ϵ_2 versus E . The only reported determination of ϵ_2 versus E for single-crystal *c* yttria, a Kramers-Kronig analysis of reflectance data,¹ shows an initial double-peaked structure similar to that observed in films C and D, with α at 6 eV calculated to be $1.9 \times 10^5 \text{ cm}^{-1}$, in good agreement with our data [$\alpha(6 \text{ eV}) = 1 \times 10^5 \text{ cm}^{-1}$]. A recent theoretical calculation⁴ of the *c*-yttria energy band structure shows two direct transitions along Γ ($k = 0$) to bands separated by $< 1 \text{ eV}$ in the

TABLE III. Infrared absorption of *c*-yttria films sputter deposited on (111) Si.

Film	ν (cm^{-1}) ^a	$\Delta\nu$ (cm^{-1})
B	561	22
D	559	20

^a $\times 4 \text{ cm}^{-1}$.

lower part of the conduction band. The energy separation $\Delta E = 0.66$ eV between the two direct transitions that comprise the edge of films C and D is in excellent agreement with theory.

α versus E curves for films A, B, E, and F lack the fine structure present in the curves for films C and D. The energy separation between the two transitions disappears, and in fact, α does not vary directly with $E^{1/2}$ anywhere on the edge, indicating a modified joint density of states.

Differences in the optical absorption edge structure of films grown in different regions of the *c*-yttria phase field cannot be attributed to gross differences in chemistry, crystallography, or short-range Y-O order. Furthermore, process parameters such as growth rate and discharge power do not systematically affect the edge structure. We can, however, relate the edge structure of region I and II films to the Y-oxide/Y flux incident on the substrate as follows.

Based on mass spectrometry studies of other target materials,¹⁰ the flux arriving at the substrate is expected to consist of yttrium atoms + some form of Y-oxide molecule that has been sputtered intact. If \mathcal{F} equals the total flux of yttrium in all forms arriving at the substrate relative to its value in rare gas, then,

$$\mathcal{F} = \mathcal{F}(Y) + \mathcal{F}(Y\text{-oxide}), \quad (2)$$

where $\mathcal{F}(Y)$ and $\mathcal{F}(Y\text{-oxide})$ are the relative flux of atomic yttrium and yttrium bonded to oxygen in some form,¹¹ respectively. Assuming unity sticking coefficient, then,

$$\mathcal{F} = G'[\rho(Y)/\rho(Y_2O_3)], \quad (3)$$

where G' is the relative growth rate defined in Sec. II C and the bulk atomic densities are $\rho(Y) = 4.47$ g/cm³ and $\rho(Y_2O_3) = 5.01$ g/cm³. In general, for an optically thin plasma in local thermal equilibrium,¹²

$$I(\lambda) = hcA_{ki}N_k/4\pi\lambda, \quad (4)$$

where A_{ki} is the Einstein coefficient of the optical transition associated with de-excitation of an atom in an upper state k to a lower state i resulting in emission of radiation at λ , N_k is the number of atoms in the upper state, h is Planck's constant, and c is the speed of light in vacuum. N_k is proportional to N_i , the number of ground state atoms. Hence, Rel. $I(\lambda)$, defined in Sec. III, is given by

$$\text{Rel. } I(\lambda) = \text{Rel. } N_k = \text{Rel. } N_i \mathcal{F}(Y), \quad (5)$$

where Rel. N_k and Rel. N_i are the number of atoms in excited and ground states k and i relative to their number in a pure rare gas discharge operated at the same cathode voltage. Using Eq. (2),

$$\begin{aligned} \mathcal{F}(Y\text{-oxide}) &= \mathcal{F} - \mathcal{F}(Y) \\ &= G'[\rho(Y)/\rho(Y_2O_3)] - \text{Rel. } I(\lambda), \end{aligned} \quad (6)$$

and the Y-oxide/Y flux to the substrate is given by

$$\begin{aligned} \mathcal{F}(Y\text{-oxide})/\mathcal{F}(Y) &= \{G'[\rho(Y)/\rho(Y_2O_3)] \\ &\quad - \text{Rel. } I(\lambda)\}/\text{Rel. } I(\lambda). \end{aligned} \quad (7)$$

The right-hand side of Eq. (7) contains quantities we have measured. The values for $\{G'[\rho(Y)/\rho(Y_2O_3)]\}$, Rel. $I(\lambda)$, and $\mathcal{F}(Y\text{-oxide})/\mathcal{F}(Y)$ for films A-D are re-

TABLE IV. Values used to calculate $\mathcal{F}(Y\text{-oxide})/\mathcal{F}(Y)$ [Eq. (7)].

Film	$\{G'[\rho(Y)/\rho(Y_2O_3)]\}$ (%)	Rel. $I(\lambda)$ (%)	$\mathcal{F}(Y\text{-oxide})/\mathcal{F}(Y)$
A	15	15.5 ± 3.5	-0
B	16	10.0 ± 4.5	0.6
C	14	3.7 ± 1.3	2.8
D	13	4.5 ± 1.8	1.9

Calculated by taking the average value of all wavelengths shown for a particular deposition condition in Fig. 3.

^bCalculated using the average value of Rel. $I(\lambda)$.

corded in Table IV. $\mathcal{F}(Y\text{-oxide})/\mathcal{F}(Y) = 0-0.6$ for region I films, and is at least $3.2-4.6\times$ larger for region II films. Under region I conditions, yttrium is delivered to the substrate predominantly in atomic form, whereas under region II conditions, yttrium is delivered to the substrate predominantly in a form bonded to O. A large atomic yttrium flux results in a "disordered" optical absorption edge (films A and B), whereas a large Y-oxide flux results in an edge with the characteristic features of bulk *c* yttria (films C and D).

The above analysis cannot be applied to films E and F (region III). There is selective enhancement of N_k of the two red transitions in Ne-O₂ discharges operated at -1.5 kV, and Eq. (5) does not hold. Rel. $I(\lambda)$ is the same for both red transitions in Ne-5-4% O₂, suggesting a yet to be identified broad band excitation source [$E_{6191\text{ \AA}} - E_{6191\text{ \AA}} = (2.006 - 1.823)$ eV = 0.183 eV]. In Ne-20% O₂, $I(6793\text{ \AA})$ is reduced to the level of the ultraviolet transitions, the upper population of this transition no longer enhanced, whereas $I(6191\text{ \AA})$ does not decrease, indicating its excitation source has changed. $I(6191\text{ \AA})$ enhancement in Ne-20% O₂ is most likely caused by a resonance with an atomic O transition at 6157 \AA [$E_{6157\text{ \AA}} - E_{6191\text{ \AA}} = (2.017 - 2.006)$ eV = 0.011 eV], known to be strong in Ne-O₂ sputtering discharges.¹³ Films grown under region III conditions, in which the flux of yttrium atoms excited to ~2 eV is high, have disordered absorption edges. The precise connection between this excited yttrium population and the creation of electronic disorder on the edge awaits further investigation.

V. SUMMARY

Cubic yttria films were sputter deposited on unheated fused silica substrates. *In situ* optical spectrometry was used to monitor emission from six YI transitions in the discharge. A simple formalism was developed for estimating the ratio of yttrium arriving at the substrate in atomic form to yttrium bonded to oxygen in an unspecified molecular form. The optical absorption coefficient ($\alpha = \sim 10^3-10^5$ cm⁻¹) of the films was determined, post-deposition, over the energy range 5.0-6.2 eV.

From the results presented above, we conclude:

(1) The absorption edge structure varies with nominal sputtering gas composition (O₂ content, type of rare gas used in conjunction with O₂) and cathode voltage, even though the films produced have similar stoichiometry, crys-

tallographic parameters, and lattice absorption behavior.

(2) A large atomic yttrium flux to the substrate results in cubic yttria with a "disordered" optical absorption edge.

(3) A large flux of yttrium bonded to oxygen to the substrate results in cubic yttria whose edge consists of two direct interband transitions separated by 0.66 eV, in good agreement with the bulk single-crystal ϵ_2 data¹ and a recent theoretical energy band calculation for cubic yttria.⁴

ACKNOWLEDGMENTS

This work was supported under U.S. ARO Grant No. DAAL03-89-K-0022 and through a gift by Johnson Controls Inc. to the Wisconsin Distinguished Professorship of CRA.

¹R. C. Anderson, in *High Temperature Oxides Part II*, edited by A. M. Alper (Academic, New York, 1970), pp. 1-3; R. W. G. Wyckoff, *Crystal Structures* (Interscience, New York, 1964), Vol. 2, p. 4; O. N. Carlson, *Bull. Alloy Phase Diag.* **11**, 61 (1990).

²C.-K. Kwok, C. R. Aita, and E. Kolawa, *J. Vac. Sci. Technol. A* **8**, 1330 (1990).

³V. N. Abramov and A. I. Kuznetsov, *Sov. Phys. Solid State* **20**, 399 (1978).

⁴W.-Y. Ching (private communication).

⁵A. N. Zaidel, V. K. Prokofev, S. M. Karskin, V. A. Slavnyi, and E. Ya. Shreider, *Tables of Spectral Lines* (IFI/Plenum, New York, 1970).

⁶See, for example, J. I. Pankove, *Optical Processes in Semiconductors* (Prentice-Hall, Englewood Cliffs, NJ, 1971), pp. 93-95.

⁷Y. Nigara, *Jpn. J. Appl. Phys.* **7**, 404 (1968).

⁸N. T. McDevitt and W. L. Baun, *Spectrochim. Acta* **20**, 799 (1964).

⁹D. F. Bezuidenhout and R. Pretorius, *Thin Solid Films* **139**, 121 (1986).

¹⁰C. R. Aita, *J. Vac. Sci. Technol. A* **3**, 625 (1985).

¹¹YO, a prominent feature in the spectra of M-type stars, has been detected in gas experiments using selective excitation spectrometry: T. C. Steimle and Y. Al-Ramadin, *J. Mol. Spectrosc.* **122**, 103 (1987); A. Bernard, R. Bacis, and P. Luc, *Astrophys. J.* **227**, 338 (1979); C. Linton, *J. Mol. Spectrosc.* **69**, 351 (1978); K. Liu and J. M. Parson, *J. Chem. Phys.* **67**, 1814 (1977), and in atmospheric-pressure inductively coupled plasmas using emission spectrometry: B. D. Merkle, R. N. Kniseley, and F. A. Schmidt, *J. Appl. Phys.* **62**, 1017 (1987); R. S. Houk, *Anal. Chem.* **58**, 97A (1985).

¹²H. G. Kuhn, *Atomic Spectra* (Academic, New York, 1963), p. 79-83.

¹³C. R. Aita and M. E. Marhic, *J. Vac. Sci. Technol. A* **1**, 69 (1983).

High temperature air-annealing behavior of sputter deposited amorphous yttria films on fused silica

S. N. Mukherjee and C. R. Aita

Materials Department, University of Wisconsin-Milwaukee, P.O. Box 784, Milwaukee, Wisconsin 53201

(Received 11 November 1991; accepted 16 December 1991)

This article addresses the response of amorphous yttria films grown on fused silica substrates to high temperature (900 °C) cyclic annealing in air for up to 145.5 h. Surface science and bulk analytical techniques were applied to determine and correlate changes in microstructure, crystallization, optical behavior, and chemistry (atomic concentration and bonding) concurrent with annealing. Limited crystallization occurred after short-term annealing, resulting in regions of nanocrystallinity in an amorphous matrix. X-ray photoelectron spectroscopy data showed an accompanying loss of resolution of Y $3d_{3/2} - 3d_{5/2}$ spin states, but no change in the fundamental optical absorption edge was observed. Long-term annealing resulted in granularization of the matrix itself, with a large increase in optical absorption in the 3–5 eV range. X-ray photoelectron spectroscopy data showed a broadening of the O 1s peak. No evidence of Si diffusion from the interfacial region into the yttria film was seen, even after long-term annealing, demonstrating amorphous yttria's potential use as a high temperature diffusion barrier for metal-on-Si-based ceramic applications.

I. INTRODUCTION

Yttria, Y_2O_3 , is a wide energy band gap, refractory material. The standard temperature and pressure structure is bixbyite-type cubic, stable up to 2325 °C. Previously, we constructed a phase map for the sputter deposited yttrium-oxygen system, and showed that both crystalline and high density amorphous yttria films can be produced near room temperature in a controlled manner on many types of substrates.^{1–4}

Amorphous yttria is an important material because of its use as a high temperature diffusion barrier.⁵ It also has potential use as a corrosion-inhibiting coating, which, as in the case of aluminum nitride,^{6,7} may be enhanced when long range crystalline order is suppressed. Its high dielectric constant $\epsilon = 14-17$ makes amorphous yttria a good capacitor material for very large scale integration applications.⁸ Last, its wide band gap giving transparency throughout the near infrared-visible region and its refractory nature make amorphous yttria a potential candidate as a protective coating on high power laser mirrors and lenses.

The present paper addresses the stability of amorphous yttria films deposited on fused silica substrates and subjected to high temperature cyclic annealing.⁹ The goal of the study was to understand the material's response to the type of annealing that it may encounter when in use in the field. Using a battery of bulk analytical techniques, we report changes in microstructure, crystallization, and optical absorption that accompany annealing. X-ray photoelectron spectroscopy was used to obtain information about chemical species and bonding that was central to our understanding of the relationship between these changes for a given annealing time at temperature.

II. EXPERIMENTAL PROCEDURE

The films studied here were grown on unheated Suprasil fused silica substrates by radio-frequency (rf) diode sput-

tering a 99.8% Y target in Ne- O_2 atmospheres, as previously described.^{1–4} The as-deposited films were 100 nm thick, amorphous, stoichiometric Y_2O_3 . These films had "naturally aged" for one year at room temperature in laboratory air before the current annealing study was begun.

In order to study the effect of cumulative time-at-temperature, a naturally aged film was annealed in air at 900 °C for sequential periods of time of 0.5, 1, 24, 48, and 72 h. After each time period, the film was withdrawn from the furnace, cooled in air, and examined as described below. Two additional films were annealed in laboratory air at 900 °C for time periods of 1 and 72 h, respectively, solely for the purpose of x-ray photoelectron spectroscopy analysis.

Characterization of the films after each processing step included the following measurements. Electrical resistivity of all films was measured with a four-point probe, and found to be greater than $10^{10} \mu\Omega \text{ cm}$.

Microstructural changes commensurate with annealing were determined using both optical and scanning electron microscopy. Crystallography was determined by double-angle x-ray diffraction (XRD) using unresolved Cu K_α radiation with wavelength $\lambda = 0.1542 \text{ nm}$. The diffractometer was calibrated using the {01.1} diffraction peak of a polycrystalline quartz standard at $2\theta = 26.66 \pm 0.02^\circ$. XRD peak intensity, position ($2\theta \pm 0.02^\circ$), and full width at one half of the maximum intensity were measured. From these measurements, the interplanar spacing d was calculated from the Bragg relationship for first order diffraction: $\lambda = 2d \sin \theta$. The minimum crystallite size D was determined using the Scherrer equation¹⁰ $D = 0.9\lambda/B \cos \theta$, where B is the peak width corrected for instrumental broadening contributions.

A Perkin-Elmer Model 330 ultraviolet-visible-infrared double beam spectrophotometer was used to determine the optical reflectance R and transmittance T of near-normal

incident radiation through the film – substrate composite. Measurements were made in laboratory air at room temperature over the wavelength range of 183 to 1000 nm (6.6 to 1.2 eV). An Al mirror was used for the background correction in the reflectance mode, and the film reflectance was measured relative to the Al mirror. A bare fused silica substrate was placed in the reference beam path during transmittance measurements. In this manner, transmittance through the silica substrate, even though > 90% throughout the wavelength region of interest, was subtracted from the value for the film – substrate composite.

The optical absorption coefficient α was calculated as a function of incident photon energy E from these spectrophotometric measurements and a knowledge of film thickness $x = 100$ nm using the following expression¹¹

$$T = \frac{(1 - R)^2 \exp(-\alpha x)}{1 - R^2 \exp(-2\alpha x)}. \quad (1)$$

Information regarding the joint density of electronic states (valence – conduction band states) in the vicinity of band gap was obtained from the functional dependence of the absorption coefficient on the incident photon energy.

A VG Instruments Model Mark II Auger electron spectroscopy/electron spectroscopy for chemical analysis (AES/ESCA) system with a 1253.6 eV Mg K_{α} radiation source was used for x-ray photoelectron spectroscopy (XPS). The instrument was calibrated using a gold foil standard, to the Au $4f_{7/2}$ electron binding energy at 83.8 ± 0.2 eV with a full width at one half-maximum intensity (FWHM) of 1.2 eV. XPS depth profiling using a 5 keV Ar⁺ ion beam as the sputter etching agent was carried out to obtain chemical information from layers below the film surface. The sputter etching rate was estimated to be 1.2 ± 0.2 nm/min.

III. RESULTS AND DISCUSSION

A. Microstructure

Optical microscopy of the naturally aged film revealed a featureless structure. However, after annealing for 0.5 h, globules with dimensions of 2–4 μm were observed in the featureless matrix [Fig. 1(a)]. The average interglobular spacing was 4 μm . The size and dispersion of these globules did not change even after a cumulative anneal time of 145.5 h.

However, annealing at 900 °C beyond 1.5 h resulted in a transition in the matrix itself. The featureless matrix was replaced by "grains" with conspicuous boundaries. The average grain diameter was 0.6 μm . A scanning electron micrograph (SEM) of this structure, taken after a cumulative anneal of 145.5 h, is shown in Fig. 1(b).

B. Crystallography

X-ray diffraction measurements showed that, as expected, the as-grown amorphous films did not undergo crystallization after natural aging. However, after annealing for 0.5 h, a transition to a nanocrystalline structure occurred, evidenced by two weak, broad diffraction peaks corresponding to {222} and {440} planes of the cubic bixbyite-type yttria lattice. These peaks were of equal in-

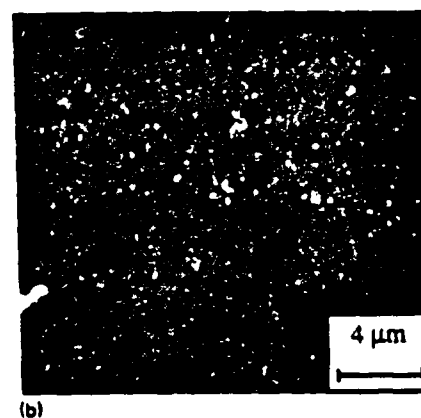
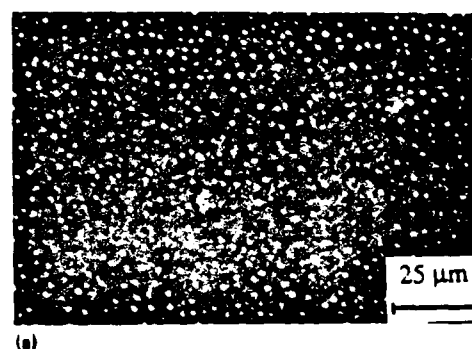


FIG. 1 (a) Optical micrograph of a yttria film annealed in air at 900 °C for 0.5 h. (b) Scanning electron micrograph of a yttria film after a 145.5 h anneal.

tensity. The interplanar spacings $d\{222\} = 0.304$ nm and $d\{440\} = 0.187$ nm were the same as those for unstressed bulk cubic yttria. Neither peak intensity nor diffraction angle (hence interplanar spacing) was affected by increasing the cumulative annealing time to 145.5 h. The nanocrystallite size calculated from {222} reflections after a 0.5 h anneal was equal to 50 nm, and increased twofold after 145.5 h at temperature.

A comparison of XRD and microstructural data shows that partial crystallization is accompanied by the formation of "globules," which we conclude to contain clusters of nanocrystallites.

C. Optical absorption coefficient

With respect to visual appearance, films in all processing conditions were colorless in transmitted light. The optical absorption coefficient, calculated using Eq. (1), is shown in Fig. 2 as a function of incident photon energy. It can be seen that natural aging shifted the low energy region of the absorption curve to higher energy, while the high energy absorption coefficient remained unchanged. The precise reason for the change in the shape of the low energy portion of the α versus E curve with natural aging is as yet unknown, but the fact that the high energy portion did not

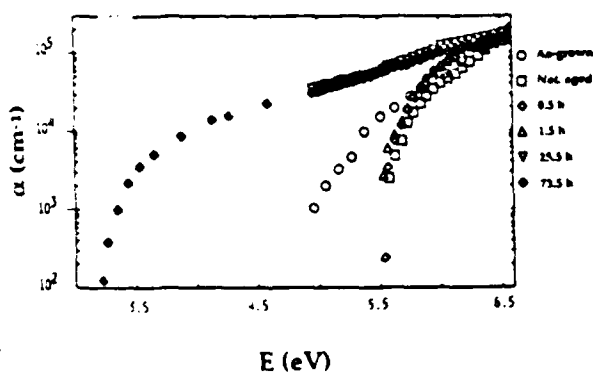


FIG. 2 The optical absorption coefficient as a function of incident photon energy for different processing conditions of a yttria film

change with aging signifies that nearest-neighbor Y-O bonding remained unchanged.¹²

Annealing for up to 1.5 h did not affect the fundamental optical absorption edge. Apparently, the formation of nanocrystallites concentrated in globular regions whose dimensions are an order of magnitude larger than the incident radiation does not affect the edge position or shape. With further annealing, however, a large shift to lower energy occurred, as can be seen from the α versus E curve for 25.5 h, and this trend continued with increasing annealing time. The increased optical absorption is commensurate with the granularization of the matrix and is most likely caused by scattering of the incident light of wavelength that is the same order of magnitude as the diameter of a grain.

D. Chemistry

The relative atomic concentration of each element for a film annealed for 72 h, was calculated using XPS peak height sensitivity factors¹³ for Y, Si, and O. The depth profiles thus obtained are shown in Fig. 3. There is an outermost-surface layer of Y₂O₃ in a 1:3 ratio characteristic of Y(OH)₃. With subsequent etching, the Y and O concentrations reach a ratio of 2:3, characteristic of Y₂O₃. This ratio remains constant to the film/substrate interface, at a depth of 100 nm.

Figure 3 shows that a small Si signal (< 1 at. %) first appears after etching to a depth of 60 nm from the film/air interface. This signal increases to a value of ~ 5 at. % after etching to a depth of 100 nm, which corresponds to the film thickness. Si had the same profile and amplitude in the unannealed and annealed conditions, and its presence in the spectra is attributed to either smearing of the interface during film growth, a common occurrence during sputter deposition, or an artifact of the sputter-etching process required for depth profiling. It is therefore concluded that Si does not diffuse from the interfacial region into the film upon high temperature annealing. This result is technologically important because yttria is a candidate for a high temperature diffusion barrier layer for metal-on-Si-based ceramic systems.

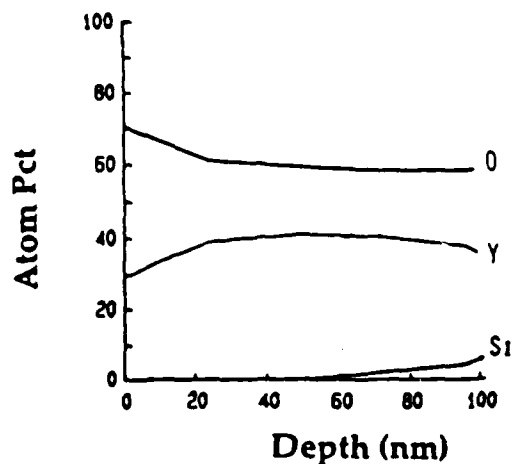


FIG. 3. The relative atomic concentration of O, Y, and Si species in a yttria film air annealed at 900 °C for 72 h as a function of the depth from the film/air interface.

We next compare the Y 3d and O 1s photoelectron peak shape for the naturally aged condition with material annealed for 1 and 72 h. Figures 4-6 show spectra taken at a depth of (a) 12 nm (i.e., near the film/air interface) and (b) 72 nm (i.e., near the film/substrate interface) for each annealing time. Yttria is a good insulator as shown by electrical resistivity measurements cited above. As expected, there was considerable charge shifting of the photoelectron binding energy peaks in all films. The usual method we use for charge shift correction, referencing to the C 1s photoelectron binding energy peak at 284.6 eV, cannot be used here. Adventitious carbon simply did not exist in the interior of the films. Although the C 1s photoelectron binding energy at the film surface before sputter etching can be used to estimate the amount of charge shifting, 5.1-6.5 eV, this value cannot be used as a correction factor to obtain an absolute photoelectron binding energy. The abscissa shown in Figs. 4-6 is therefore uncorrected for sample charging and does not represent true Y 3d or O 1s photoelectron binding energy.

Figure 4 shows the Y 3d and O 1s photoelectron peaks of naturally aged material. Comparing Figs. 4(a) and 4(c), it can be seen that the Y 3d peaks for both depths within the naturally aged film are identical in shape. Multiplet splitting of core-level peaks is observed in systems having unpaired electrons in the valence level, due to spin-orbit ($j-j$) coupling.¹⁴ For yttrium atoms, the areal ratio of the doublets due to $3d_{3/2} - 3d_{5/2}$ line splitting is in the ratio of their respective degeneracies ($2j + 1$) and equal to 1.5. In the naturally aged condition, the 5/2-3/2 spin-orbit split components of the Y 3d peak were in the areal ratio of 1.3, close to the theoretical value. The doublets were separated by 2.0 eV, close to the value reported for Y₂O₃.¹⁵ Figure 4(b) shows that the O 1s photoelectron spectrum near the film/air interface consists of a main peak with a shoulder centered at 2.6 eV higher binding energy. The main O 1s peak is attributed to O bonded to Y in amorphous yttria and the shoulder is attributed to physisorbed

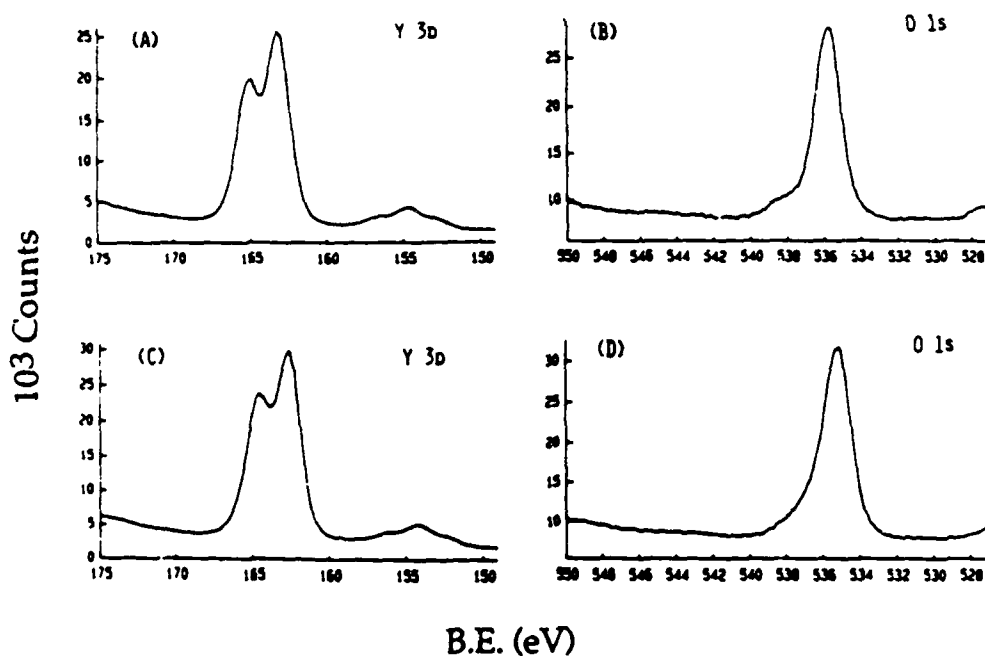


FIG. 4. Core electron binding energy spectra for a naturally aged yttria film: (a) Y 3d and (b) O 1s photoelectron peaks, taken at 12 nm from the film/air interface; (c) Y 3d and (d) O 1s photoelectron peaks, taken at 72 nm from the film/air interface.

O₂ and hydrated O species bonded to Y, as in Y(OH)₃.¹⁶ Figure 4(d) shows that the O 1s peak shoulder intensity has decreased, indicating that the number of physisorbed and hydrated oxygen species have decreased.

Figures 5 and 6 show the Y 3d and O 1s photoelectron peaks of material annealed for 1 and 72 h, respectively. From Figs. 5(a) and 5(c), it can be seen that at both depths within the film, the 5/2 and 3/2 components of the Y 3d peak show a loss of resolution compared to the naturally aged material. XRD and microscopy data show that a partial phase change occurs after short term annealing (0.5 h), resulting in a two-phase material: an amorphous matrix + a nanocrystalline second phase. The loss of resolution observed in the Y 3d components after a 1 h anneal is attributed to the fact that both crystalline and amorphous yttria have a Y 3d doublet, but at slightly different energies. A comparison of Figs. 6(a) and 6(c) with 5(a) and 5(c) shows that there is no further loss of resolution in the Y 3d peak components with increasing annealing time. This result is consistent with XRD results showing no further crystallization after a 0.5 h anneal.

A comparison of Fig. 4(b) with 5(b) and Fig. 4(d) with 5(d) shows that the O 1s peak shape does not change with annealing for 1 h at either 12 or 72 nm from the film/air interface. However, a large change in the O 1s peak shape occurs at both depths within the film after annealing for 72 h, as seen by comparing Figs. 5(b) and 5(d) with Figs. 6(b) and 6(d). The full width at one half-maximum intensity of the main O 1s peak doubles and the shoulder disappears. The fact that no Si appears in the spectrum at 12 nm from the film/air interface leads us to conclude that Si diffusion from the film/substrate interface

and the consequent formation of Si oxides and/or yttrium silicates are not the cause of O 1s peak broadening.

Instead, we looked at the microstructural transformation of the matrix itself into granular regions to explain O 1s peak broadening. There was a large grain boundary area created by this transformation, with a surface area-to-volume ratio of 10 μm^{-1} . O bonding at the grain surface may be different from that in the grain interior,¹⁷ giving rise to the increase in the range of O 1s photoelectron binding energy values observed here.

IV. SUMMARY

We have studied the response of amorphous yttria films grown on fused silica substrates to high temperature (900 °C) cyclic annealing for up to 145.5 h. We combined applied surface science and bulk analytical techniques to determine changes in microstructure, crystallization, optical absorption behavior, and chemistry concurrent with annealing. The following conclusions are drawn from this time-at-temperature study:

(1) Short-term annealing resulted in limited crystallization. Nanocrystallites were formed in localized clusters (globules) within the amorphous yttria matrix after 0.5 h at 900 °C. No change in the fundamental optical absorption edge occurred at this stage of annealing because the globule dimensions were an order of magnitude larger than the wavelength of the incident radiation. XPS data showed a loss of resolution of the 5/2-3/2 spin states of the Y 3d photoelectron peak. This result was attributed to the superposition of different contributions from the amorphous and nanocrystalline components in the film. No further

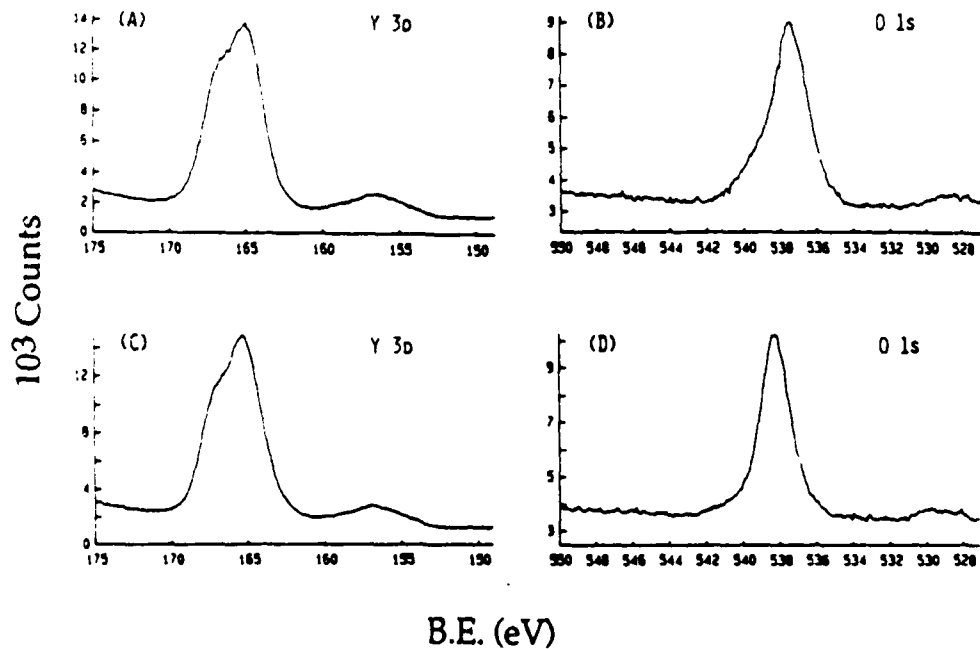


FIG. 5. Core electron binding energy spectra for a yttria film air annealed for 1 h at 900 °C: (a) Y 3d and (b) O 1s photoelectron peaks, taken at 12 nm from the film/air interface; (c) Y 3d and (d) O 1s photoelectron peaks, taken at 72 nm from the film/air interface.

crystallization was observed after a cumulative anneal for 1.5 h.

(2) Annealing for longer than 1.5 h resulted in a change in the microstructure of the matrix itself: granular regions with distinct boundaries developed. A large increase in op-

tical absorption in the 3–5 eV range (413–248 nm) accompanied granularization. This effect was attributed to scattering by the grains, whose diameter was the same order of magnitude as the wavelength of the incident radiation. XPS data showed that there was no further change in the

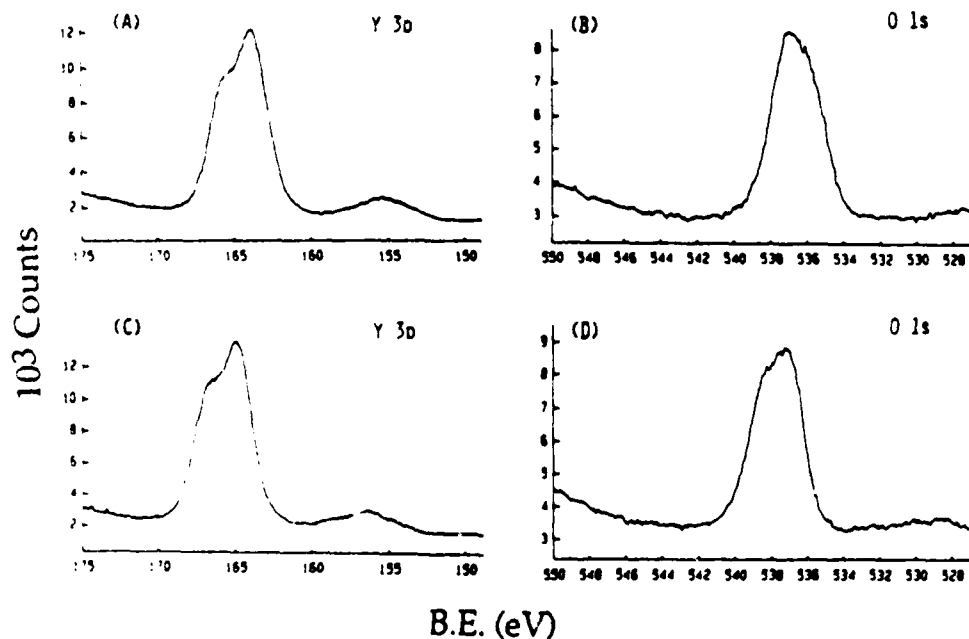


FIG. 6. Core electron binding energy spectra for a yttria film air annealed for 72 h at 900 °C: (a) Y 3d and (b) O 1s photoelectron peaks, taken at 12 nm from the film/air interface; (c) Y 3d and (d) O 1s photoelectron peaks, taken at 72 nm from the film/air interface.

Y 3d photoelectron binding energy peak shape. However, the width of the O 1s photoelectron binding energy peak doubled. A large grain boundary area was created by the granularization of the matrix. We suggest that O bonding at the grain surface may be different from that in the grain interior, giving rise to the increase in the range of O 1s photoelectron binding energy values.

(3) An important technological result that emerged from this study was that Si did not diffuse from the interfacial region into the film, even after long-term annealing, demonstrating yttria's potential use as a high temperature diffusion barrier for metal-on-Si-based ceramic applications.

ACKNOWLEDGMENTS

The authors would like to thank Professor T. L. Barr and Professor G. S. Baker for helpful discussions. This work was supported under USARO Grant No. DAAL-03-89-K-0022, by the Wisconsin Distinguished Professorship of C. R. A., and by gifts from Johnson Controls, Inc. and Schunk Graphite Technology.

C. K. Kwok, C. R. Aita, and E. Kolawa, *J. Vac. Sci. Technol. A* 8, 1330 (1990).

C. K. Kwok, C. R. Aita, and E. Kolawa, *J. Appl. Phys.* 68, 2945 (1990).

C. R. Aita and C. K. Kwok, *J. Am. Ceram. Soc.* 74, 3209 (1991).

C. R. Aita, *J. Mater. Sci. Technol.* (in press).

R. L. Mehan, M. R. Jackson, and M. D. McConnell, *J. Mater. Sci.* 18, 3195 (1983).

W. S. Tait, C. O. Huber, B. C. Begnoche, J. R. Sielmann, and C. R. Aita, *J. Vac. Sci. Technol. A* 6, 924 (1988).

W. S. Tait and C. R. Aita, *Corrosion* 46, 115 (1990).

M. Gurvitch, L. Manchanda, and J. M. Gibson, *Appl. Phys. Lett.* 51, 919 (1987).

S. N. Mukherjee, Ph.D. thesis, University of Wisconsin-Milwaukee, May 1991.

See, for example, L. V. Azaroff, *Elements of X-ray Crystallography* (McGraw-Hill, New York, 1968), pp. 551-8. The term "minimum size" is used here because we are assuming the limiting case of XRD peak broadening due to finite crystallite size effects, with no contribution from random lattice strain.

J. I. Pankove, *Optical Processes in Semiconductors* (Prentice-Hall, Englewood Cliffs, NJ, 1971), pp. 93-95.

R. Zallen, *Physics of Amorphous Solids* (Wiley, New York, 1983), pp. 252-274.

D. Briggs and M. P. Seah, *Practical Surface Analysis by Auger and Photoelectron Spectroscopy* (Wiley, New York, 1983), pp. 511-512.

D. Briggs and J. C. Riviere, in *Practical Surface Analysis by Auger and Photoelectron Spectroscopy*, edited by D. Briggs and M. P. Seah (Wiley, New York, 1983), pp. 88, 89, 113, 128-130.

C. D. Wagner, W. M. Riggs, L. E. Davis, J. F. Moulder, and G. E. Muilenberg, *Handbook of X-ray Photoelectron Spectroscopy* (Perkin-Elmer, Eden Prairie, MN, 1978), pp. 98-99.

T. L. Barr, *Electron spectroscopy for Chemical Analysis Examination of Rare Earth and Near Rare Earth Species*, Special Technical Publication 643 (ASTM, Philadelphia, PA, 1978), pp. 83-104.

See, for example, J. C. Phillips, in *Solid State Physics*, edited by H. Ehrenreich, F. Seitz, and D. Turnbull (Academic, New York, 1982), p. 128, in which a similar issue is addressed for GeO₂.

RAPID COMMUNICATIONS

This section is reserved for short submissions which contain important new results and are intended for accelerated publication.

Kinetics of morphological change during annealing of amorphous yttria

S. N. Mukherjee and C. R. Aita

Materials Department, University of Wisconsin-Milwaukee, Milwaukee, Wisconsin 53201

(Received 30 December 1991; 29 February 1992)

We report a time-at-temperature study of air annealing at 700 °C of amorphous yttria films sputter deposited on fused silica. The results show that crystallization was limited (7%). A striking morphological change involved the formation of 2.5 μm -maximum diameter globules. By comparing changes in globule number with maximum diameter, the time-at-temperature ranges for which nucleation + growth and growth + coarsening processes occurred was determined. The globule formation rate initially followed an Arrhenius curve: $dN_V/dt = (4 \times 10^3/\text{cc s})\exp[-0.28 \times 10^{-3}/\text{s}t]$. The activation energy estimated for globule formation was close to that for Y diffusion in yttria.

Technological interest in amorphous yttria films is based on their diverse use as capacitors, protective coatings for high power density laser optics, corrosion-inhibiting linings for magnetic fusion reactors, and high temperature diffusion barrier layers for metal-on-silicon-based ceramic systems.¹⁻⁴ In all of these applications, the film is subjected to cyclic heating. It is therefore important to understand the material's time-at-temperature response to annealing, with particular attention to stability of morphology and resistance to crystallization.

In a recent article,⁵ we reported the high temperature (900 °C) air-annealing behavior of yttria films on silica. Two major morphological changes occurred. (1) Spherical precipitates (globules) formed in the amorphous yttria matrix after a short time at temperature. (2) Further annealing caused roughening or "granularization" of the matrix, i.e., breaking up into regions separated by distinct boundaries. In the present article, we examine the effect of lowering the annealing temperature on crystallization and morphological changes.

A 140 nm-thick amorphous yttria film was grown on unheated Suprasil fused silica substrates by rf diode sputtering a 99.8% Y target in a Ne-20% O₂ discharge operated at 1.0 kV_{pp} as previously described.⁶ The film "aged" for one year at room temperature in laboratory air before air annealing at 700 °C for cumulative lengths of time, t , of 0.5, 1.5, 25.5, 73.5, and 145.5 h. After each anneal, the film was withdrawn from the furnace, cooled in air, and examined as follows. Morphology was observed with an optical microscope with a resolution of ~ 100 nm. Crystallography was determined by double-angle x-ray diffraction (XRD) using unresolved CuK α radiation ($\lambda = 0.1542$ nm). XRD peak intensity, position ($2\theta \pm 0.02^\circ$), and full width at one half of the maximum intensity were measured. The interplanar spacing d was calculated from the Bragg relationship for first order diffraction: $\lambda = 2d \sin \theta$.

Crystallization: After annealing for 0.5 h, two weak, broad diffraction peaks were detected, corresponding to {222} and {440} planes of the cubic bixbyte-type yttria lattice. Peak intensity was 7% of that obtained from a crystalline yttria film of the same thickness. Interplanar spacing was found to be $d\{222\} = 0.304$ nm and $d\{440\} = 0.187$ nm, equal to that for unstressed bulk cubic yttria.⁷ There was no further change in intensity or angle upon subsequent annealing, even after a cumulative time of 145.5 h, showing that crystallization was limited.

Morphology: Before annealing, the films were featureless down to the resolving power of the microscope. After 0.5 h at temperature, globules formed in the featureless matrix. A micrograph taken after a 25.5 h anneal is shown in Fig. 1. Unlike a 900 °C anneal,⁵ no granularization or other features were observed in the matrix, even after 145.5 h.

An areal counting method was used to measure the number of globules/area [N_A] and the diameter of the largest globule $2R_{\text{max}}$, was measured by linear intercept. The number/volume [N_V] was obtained using the following expression:⁸

$$N_V = N_A/2R_{\text{max}} \quad (1)$$

$2R_{\text{max}}$ is shown as a function of $\log t$ in Fig. 2. N_V , calculated from Eq. (1), is shown in Fig. 3 as a function of t . The point on this curve lying against the y axis corresponds to 0.5 h (1.8×10^3 s). A logarithmic time scale was not used here because we wanted to show the functionality of $N_V(t)$. It can be seen that the number of globules initially increases rapidly as a function of annealing time, then less rapidly, and finally decreases. The functionality of $N_V(t)$ is characteristic of a distribution of second phase particles which nucleate, grow, and finally coarsen at the expense of smaller neighbors.⁹ The dominant operative processes before the N_V versus t curve reaches its maxi-



FIG. 1. An optical micrograph of a yttria film annealed in air at 700 °C for 25.5 h.

mum are nucleation and growth of nuclei to supercritical size. After the maximum, growth and coarsening dominate. A comparison of Figs. 2 and 3 shows that $R_{max}(t)$ increases sharply as $N_V(t)$ decreases, suggesting that coarsening is occurring.

The globule formation rate, dN_V/dt , was determined by taking the instantaneous slope at five points on the N_V versus t curve for $t < 55.5$ h (2×10^5 s), i.e., in the region in

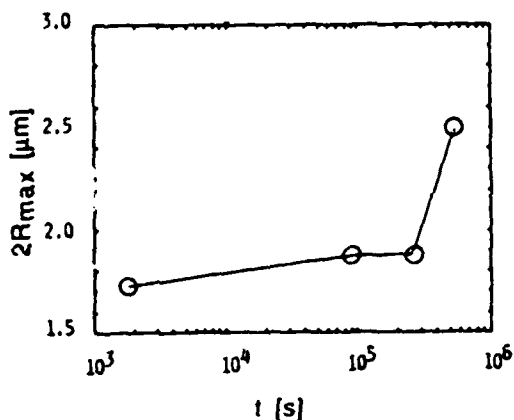


FIG. 2. The diameter of the largest globule $2R_{max}$ as a function of annealing time t .

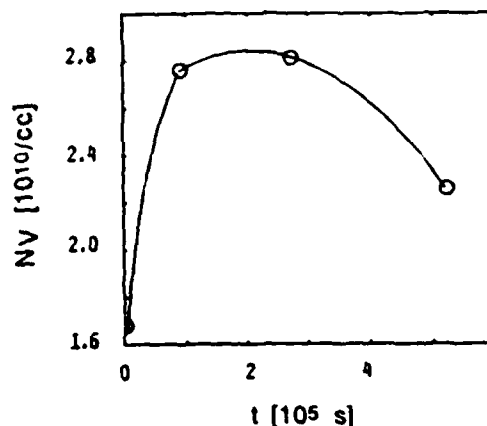


FIG. 3. The number of globules/volume N_V as a function of annealing time t .

which the number of supercritical size globules increases with t . These data, shown in Fig. 4(a) as a function of t , follow an Arrhenius curve typical of diffusion-controlled kinetics¹⁰

$$dN_V/dt = A \exp(-kt). \tag{2}$$

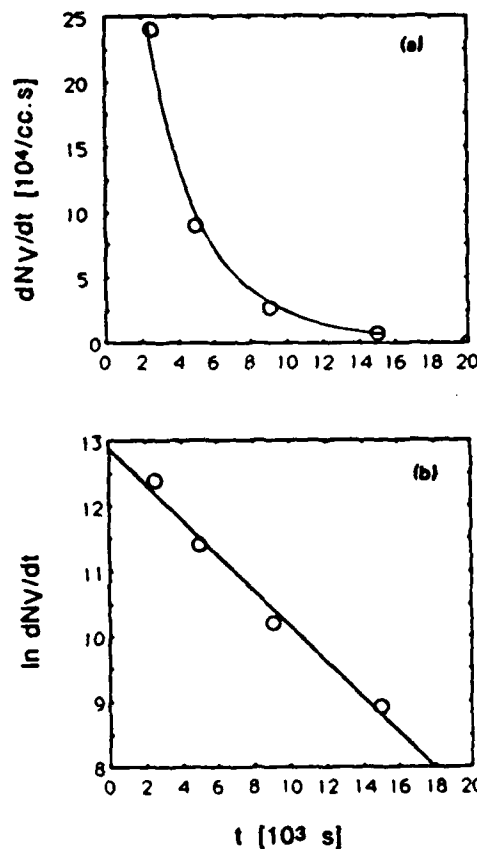


FIG. 4. (a) Globule formation rate dN_V/dt as a function of annealing time, t . The solid curve represents $dN_V/dt = (4 \times 10^3/\text{cc.s}) \times \exp\{-0.28 \times 10^{-3}/s)t\}$ determined from (b) $\ln(dN_V/dt)$ vs t .

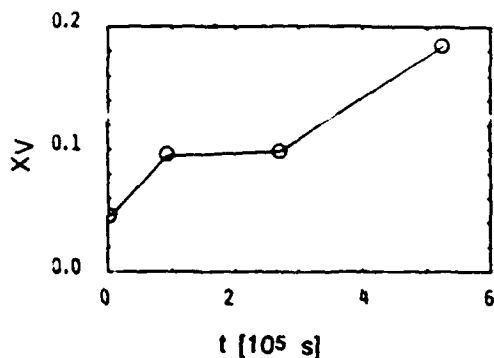


FIG. 5. The maximum volume fraction of material transformed into globules X_V vs annealing time t .

A graph of $\ln [dN_V/dt]$ versus t , shown in Fig. 4(b), yields $A = 4 \times 10^5/\text{cc s}$ and $k = 0.28 \times 10^{-3}/\text{s}$.

The activation energy Q for globule formation was estimated by combining data for 700 and 900 °C (Ref. 11) and using the following¹²:

$$- [Q/R] \{ (1/T_1) - (1/T_2) \} = \ln(t_2/t_1), \quad (3)$$

where $T_1 = 900$ °C (1173 K) and $T_2 = 700$ °C (973 K). t_1 and t_2 are the times at which N_V reaches a maximum at each temperature: $t_1 < 0.5$ h (1.8×10^3 s) at 900 °C,¹¹ and $t_2 = \sim 55.5$ h (2×10^5 s) at 700 °C (Fig. 3). Substitution of these values into Eq. (3) yields $Q = 53$ kcal/mol (2.31 eV) using $t_1 = 0.5$ h; and using a very small value for t_1 : 0.05 h, $Q = 79$ kcal/mol (3.45 eV). If globule formation is controlled by diffusion of a single species, then, from the above

calculation, we conclude that the activation energy is close to that for Y diffusion in bulk crystalline yttria, $Q = 3.48$ eV.¹³

Last, the maximum volume fraction of material transformed into globules X_V was determined using $X_V = (4\pi R_{\text{max}}^3/3)N_V$. These data, presented in Fig 5 as a function of t , show that 18% of the matrix was transformed into globules after 145.5 h at temperature.

Acknowledgments: The authors thank Professor G. S. Baker for many helpful discussions. This work was supported under USARO Grant No. DAAL-03-89-K-0022, and by the Wisconsin Distinguished Professorship of CRA.

¹M. Gurvitch, L. Manchanda, and J. M. Gibson, *Appl. Phys. Lett.* **51**, 919 (1987).

²A. A. Kaminski, in *Laser Crystals* (Springer, Berlin, 1981).

³R. L. Mehan, M. R. Jackson, and M. D. McConnell, *J. Mater. Sci.* **18**, 3195 (1983).

⁴A. B. Hull (unpublished).

⁵S. N. Mukherjee and C. R. Aita, *J. Vac. Sci. Technol. A* **10**, 2723 (1992).

⁶C.-K. Kwok, C. R. Aita, and E. Kolawa, *J. Vac. Sci. Technol. A* **8**, 1330 (1990); *J. Appl. Phys.* **68**, 2945 (1990).

⁷JCPDS File No. 20-1412, 1972.

⁸J. D. Verhoeven, *Fundamentals of Physical Metallurgy* (Wiley, New York, 1975), p. 345.

⁹See for example, M. G. Lagally, Y.-W. Mo, R. Kariotis, B. S. Swartzentruber, and M. B. Webb, in *Kinetics of Ordering and Growth at Surfaces*, edited by M. G. Lagally (Plenum, New York, 1990), pp. 145-155.

¹⁰J. D. Verhoeven, in Ref. 9, p. 159.

¹¹S. N. Mukherjee, Ph.D. thesis, University of Wisconsin-Milwaukee, May 1991.

¹²J. D. Verhoeven, in Ref. 9, pp. 140-142.

¹³W. D. Kingery, H. K. Bowen, and D. R. Uhlmann, *Introduction to Ceramics* (Wiley, New York, 1976), p. 240.

Cyclic annealing-induced microstructural and crystallographic changes in crystalline yttria films on silica

S. N. Mukherjee and C. R. Aita

Materials Department, University of Wisconsin-Milwaukee, Milwaukee, Wisconsin 53201

(Received 30 March 1992; accepted 9 May 1992)

A cyclic air-annealing study of crystalline yttria films sputter deposited on fused silica is reported here. The results show major microstructural instability after a short time (0.5 h) at temperature (700 °C), involving localized stress relief as the film undergoes biaxial compression → tension during a heating → cooling cycle. Long-term cyclic annealing causes delamination by interfacial bubble formation and explosion. Accompanying crystallographic changes are discussed. The results are compared with those for amorphous yttria-on-silica, in which stress relief is entirely by hillock formation, growth, and coalescence.

Very large scale integration (VLSI) architecture calls for high dielectric constant (ϵ) thin film insulators.¹ Yttria, with $\epsilon = 13\text{--}17$,^{2,3} compared to 3.9 for SiO₂, is a good candidate. Processing of insulating films in VLSI applications often involves heating, as both postdeposition annealing in a controlled environment to further increase ϵ ,⁴ and cyclic heating during device operation. Therefore, microstructural and crystallographic integrity of a prospective insulator is of major concern.

Amorphous stoichiometric yttria films sputter deposited on silica were found to be stable after cyclic air annealing at 500 °C.⁵ Cyclic air-annealing at higher temperature, in the 700–900 °C range,^{6,7} showed that crystallization was limited. However, several microstructural changes occurred, the most pronounced of which was the nucleation, growth, and coalescence of globules in an otherwise smooth matrix of material. An Arrhenius curve for the globule formation rate yielded an activation energy in the range of 2.31–3.45 eV.

Here, we report the effect of cyclic air annealing on crystalline yttria-on-silica for up to 145.5 h (5.24×10^5 s) at 700 °C. This temperature was chosen because it is intermediate between one (500 °C) at which no microstructural change occurred and another (900 °C) at which there was total disintegration of the film even after short term annealing.⁵ The microstructural changes reported below associated with stress relief in crystalline yttria are different than those in the initially amorphous material, and involve hillock formation, tearing, interfacial bubble formation, and bubble explosion.

The crystalline yttria films were grown as previously described^{8–10} near-room temperature on Suprasil II fused silica substrates. A rf diode apparatus was used to sputter a 99.8% Y target in a 1×10^{-2} Torr, Ar–20%O₂ discharge operated at ~1.5 kV (peak-to-peak). The films had "aged" for one year at room temperature in laboratory air before the annealing study was begun.

The films were annealed in air at 700 °C for cumulative time periods of 0.5 h (1.8×10^3 s), 1.5 h (5.4×10^3 s), 25.5 h (9.18×10^4 s), 73.5 h (2.65×10^5 s) and 145.5 h (5.24×10^5 s). After each period, the film was withdrawn from the furnace, cooled in air, and examined. Optical (OM) and scanning electron (SEM) microscopy were

used to observe microstructural changes. Because of the insulating nature of both film and substrate, sample charging was a major problem in the SEM. The samples were therefore coated with carbon to improve conduction before examination.

Crystallography was determined by double-angle x-ray diffraction (XRD) using unresolved CuK α radiation ($\lambda = 0.1542$ nm). The diffractometer was calibrated using the (01.1) diffraction peak of a polycrystalline quartz standard at $2\Theta = 26.66 \pm 0.02^\circ$ whose width was 0.26° . XRD maximum peak intensity, position ($2\Theta \pm 0.02^\circ$), and full width at one-half of the maximum intensity (FWHM) were measured. The interplanar spacing d was calculated from the Bragg relationship for first order diffraction: $\lambda = 2d \sin \Theta$. The minimum crystallite size D was calculated using the Scherrer equation:¹¹ $D = 0.9\lambda/B \cos \Theta$, where B is the peak width corrected for instrumental broadening.

Microstructure: Before annealing, the film had a smooth, featureless surface. Annealing for 0.5 h resulted in the formation of holes over the entire surface, as shown in Fig. 1. Adjacent to many of the holes were flakes, irregularly shaped pieces of material that appeared to have been pushed out of the film, as shown in the insert in Fig. 1. The density of holes + flakes was $\sim 5 \times 10^6/\text{cm}^2$. This mor-

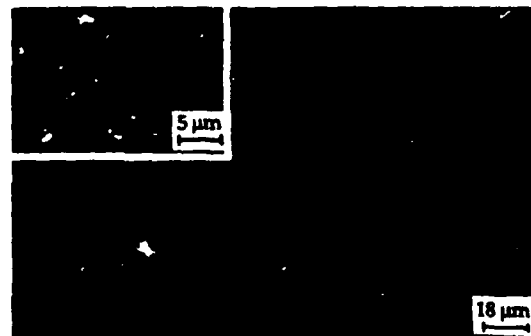


FIG. 1. OM image of a crystalline yttria film on fused silica annealed in air at 700 °C for 0.5 h. Insert shows SEM image of the hole + flake morphology.



FIG. 2. OM image of a crystalline yttria film on fused silica annealed in air at 700 °C for 25.5 h showing a circular region in which delamination has assumed.

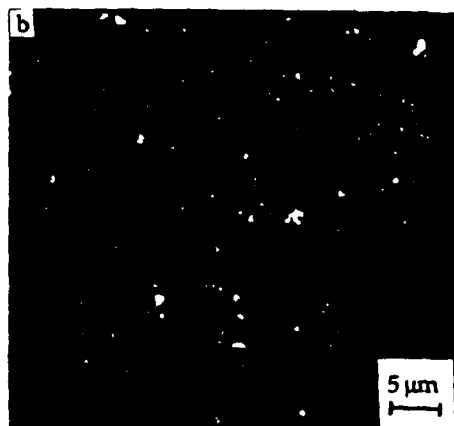


FIG. 3. (a) OM image of a crystalline yttria film on fused silica annealed in air at 700 °C for 145.5 h showing enlargement and explosion of the circular region. (b) SEM image showing exploded morphology.

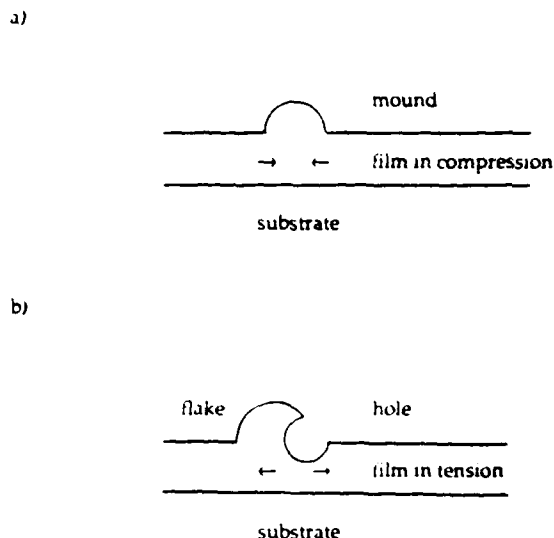


FIG. 4. A drawing showing the effect of cyclic annealing on biaxial stress in the film, and the formation of (a) mounds upon heating from 25 to 700 °C, and (b) holes + flakes upon cooling down 700 to 25 °C.

phology did not change after a 1.5 h anneal. Increasing the annealing time to 25.5 h brought about an additional change: large circular regions ($\sim 140 \mu\text{m}$ average) formed in which the film delaminated from the substrate (Fig. 2). After 145.5 h, the circular regions enlarged ($\sim 160 \mu\text{m}$ average) and exploded [Figs. 3(a) and 3(b)].

The hole + flake morphology can be understood in terms of the difference in the thermal expansion coefficients of yttria [$8 \times 10^{-6} \text{ mm}/(\text{mm } ^\circ\text{C})$] and fused silica [$0.55 \times 10^{-6} \text{ mm}/(\text{mm } ^\circ\text{C})$]. A thin film with a larger coefficient of thermal expansion than that of the substrate is subjected to biaxial compression parallel to the substrate plane during heating. The residual stress in the film upon heating from 25 to 700 °C was calculated from¹²

$$\varphi_Y = E_S E_Y \Delta \alpha \Delta T / \{(1 - \nu) \{E_S + 2E_Y(t_Y/t_S)\}\}. \quad (1)$$

where E_S and E_Y are the Young's moduli of fused silica and yttria, respectively, $\Delta \alpha$ is the difference between the thermal expansion coefficients of yttria and fused silica, ΔT is the difference between annealing temperature and room temperature, ν is the Poisson's ratio of yttria, and t_Y and t_S are the thickness of the film (70 nm) and substrate, respectively. The bulk material constants at ambient temperature were used. The calculated residual stress in the film is huge, $\sim 1250 \text{ MPa}$.

Stress relaxation occurs upon heating, but this can be on a local scale, analogous to hillock formation in low melting point metal films heated from liquid nitrogen at room temperature.¹³ Localized stress relaxation is the driving force for atomic flux to regions of lower compressive stress. A mound forms, as schematically shown in Fig. 4(a). Mounds are stress-free or tensile-stressed regions present in the films at 700 °C.

During the rapid cooling part of the cycle, the film is under biaxial tension because it shrinks faster than the

TABLE I. X-ray diffraction for annealed yttria-on-silica.

Cycle	Anneal time (h)	d_{222} (nm) ^a	I_{max} ^b	FWHM ^c (deg)	Crystallite size ν (nm)
1	0	0.307	100±27	0.91	12.7±0.4
2	0.5	0.306	160±7	0.65	21.1±1.1
3	1.5	0.306	186±24	0.65	21.2±1.1
4	25.5	0.306	199±23	0.59	24.9±1.6
5	73.5	0.306	182±8	0.58	25.7±1.7
6	145.5	0.305	192±14	0.57	25.7±1.7

^a±0.001 nm.^bArbitrary units.^c±0.02°.

substrate. The mound, because of its reduced compressive stress at higher temperature, is in a greater state of tension than the surrounding matrix upon cooling. Tearing (hole formation) either within the mound or at the mound/matrix interface occurs, as schematically shown in Fig. 4(b). We propose that the flakes associated with holes in the room temperature microstructure after cyclic annealing are debris formed from the mounds themselves.

The process of mound formation at high temperature described here is equivalent to the previously described globule formation in amorphous yttria.⁷ Even the density of holes in amorphous yttria and globules in crystalline yttria is approximately the same. In amorphous yttria, however, no film tearing occurs upon cooling, and the globules, or hillocks, grow during the next temperature cycle. Globule growth appears to be frustrated in crystalline yttria by tearing of the film upon cooling; stress relief during extended heating occurs by delamination.

Crystallography: X-ray diffraction data presented in Table I show that the naturally aged film had a preferred (111) orientation, as evidenced by a single diffraction peak corresponding to {222} planes of the cubic bixbyite-type yttria lattice. The interplanar lattice spacing (d) was 0.307±0.001 nm, greater than that (0.304 nm) for unstressed bulk yttria.¹⁴

There was no change in the preferred (111) orientation after annealing for 145.5 h. The maximum intensity of the

{222} diffraction peak increased after annealing for 0.5 h, indicating better alignment with the substrate normal, and then became constant within experimental error. Annealing had no effect on the lattice spacing up to 73.5 h which equaled the bulk value after 145.5 h. The peak width (FWHM) decreased significantly from 0.91° to 0.65° after a 0.5 h anneal. Subsequent annealing resulted in a marginal decrease of FWHM. The minimum crystallite size, calculated from {222} reflections was 12.7±0.4 nm before annealing and increased to 21.1±1.1 nm after a 0.5 h anneal. Increasing the annealing time up to 145.5 h resulted in a minimum crystallite size of 25.7±1.7 nm. A comparison of microstructural and crystallographic changes shows that the orientation of crystallites improves as a response to annealing, at the expense of the film's mechanical integrity.

Acknowledgments: This work was supported under USARO Grant No. DAAL-03-89-K-0022.

¹G. S. Oehrlein, F. M. D'heurle, and A. Reisman, *J. Appl. Phys.* 55, 3715 (1984).²T. Tsutsumi, *Jpn. J. Appl. Phys.* 9, 735 (1970).³T. S. Kalkur, R. Y. Kwor, and C. A. Paz de Araujo, *Thin Solid Films* 170, 185 (1989).⁴R. N. Sharma, S. T. Lakshmi Kumar, and A. C. Rastogi, *Thin Solid Films* 199, 1 (1991).⁵S. N. Mukherjee, PhD thesis, University of Wisconsin-Milwaukee, May 1991.⁶S. N. Mukherjee and C. R. Aita, *J. Vac. Sci. Technol. A* 10, 2723 (1992).⁷S. N. Mukherjee and C. R. Aita, *J. Vac. Sci. Technol. A* 10, 3356 (1992).⁸C.-K. Kwok, C. R. Aita, and E. A. Kolawa, *J. Vac. Sci. Technol. A* 8, 1330 (1990).⁹C.-K. Kwok, C. R. Aita, and E. A. Kolawa, *J. Appl. Phys.* 68, 2945 (1990).¹⁰C. R. Aita and C.-K. Kwok, *J. Amer. Ceram. Soc.* 74, 3209 (1991).¹¹L. V. Azaroff, *Elements of X-ray Crystallography* (McGraw-Hill, New York, 1968), pp. 551-559. The term "minimum size" is used to denote the limiting case of peak broadening due to finite crystallite site effects only, with no contribution from random lattice strain.¹²A. V. Virkar, J. L. Huang, and R. A. Cutler, *J. Am. Ceram. Soc.* 70, 3, 164 (1987).¹³K. N. Tu, J. W. Mayer, and L. C. Feldman, *Electronic Thin Film Science of Electrical Engineers in Material Sciences* (Macmillan, New York, 1992), pp. 373-374.¹⁴ASTM JCPDS Film No. 20-1412 (1972).

APPENDIX III

- A. "Cathode voltage-gas composition-film crystallography relationships for sputter deposited vanadia." C.R. Aita, Li-Jong Liou, C.-K. Kwok, R C. Lee, and E. Kolawa, *Thin Solid Films* 193/194, 18-26 (1990).

- B. "Annealing response of disordered sputter deposited vanadium pentoxide (V_2O_5)." John Luksich and C.R. Aita, *J. Vac. Sci. Technol. A* 9, 542-546 (1991).

- C. "Electronic transition-related optical absorption in vanadia films." A.M. Abuhadba and C.R. Aita, *Proc. Materials Research Soc.* 242, 731-736 (1992).

CATHODE VOLTAGE-GAS COMPOSITION-FILM CRYSTALLOGRAPHY RELATIONSHIPS FOR SPUTTER-DEPOSITED VANADIA (V_2O_5)

CAROLYN RUBIN AITA, LI-JONG LIU, CHEE-KIN KWOK, RAY C. LEE AND ELZBIETA KOLAWA*

Materials Department, University of Wisconsin—Milwaukee, PO Box 784, Milwaukee, WI 53201 (U.S.A.)

Films were grown by r.f.-excited reactive sputter deposition on $\langle 111 \rangle$ -cut silicon substrates using a vanadium target and O_2 -bearing discharges containing 0%–98% argon operated at four values of cathode voltage. The 4111.6 Å emission line intensity from neutral excited vanadium atoms in the discharge was monitored by optical spectrometry, and these data were used to detect target surface oxidation. The region of cathode voltage–gas O_2 content space over which crystalline vanadia was produced was defined. All crystalline vanadia grew with vanadyl oxygen layers oriented parallel to the substrate (b axis normal). The interlayer spacing b varied from less than to greater than b_0 , the value for bulk vanadia. An oxidized target surface was a requirement for an interlayer spacing $b > b_0$ but not a guarantee of it. As the cathode voltage decreased, the critical gas O_2 content at which the target surface became oxidized was shifted to lower values and the critical gas O_2 content at which $b > b_0$ was shifted to higher values, opening up a region in which crystalline vanadia with $b \leq b_0$ and short-range order vanadia were produced from an oxidized target surface.

1. INTRODUCTION

Vanadia, chemically V_2O_5 , is a wide band gap semiconductor at room temperature with an orthorhombic lattice structure with bulk parameters $a_0 = 11.519$ Å, $b_0 = 4.373$ Å and $c_0 = 3.564$ Å¹. The extended space lattice consists of alternating layers of vanadium plus oxygen atoms and oxygen atoms (vanadyl oxygen) alone oriented parallel to the b axis or $\langle 010 \rangle$ crystallographic direction^{2–7} as shown in Fig. 1. Bonding along the $\langle 010 \rangle$ direction is weak⁸. The interlayer spacing b of sputter-deposited vanadia was previously found to vary as a function of Ar– O_2 discharge composition^{9–11} and this variation was related to defects in the vanadyl oxygen layer¹².

Vanadia is an interesting technological material. Differences in the interlayer spacing, reflecting differences of atomic arrangement in the vanadyl oxygen layer,

* Permanent address: California Institute of Technology, Pasadena, CA 91125, U.S.A.

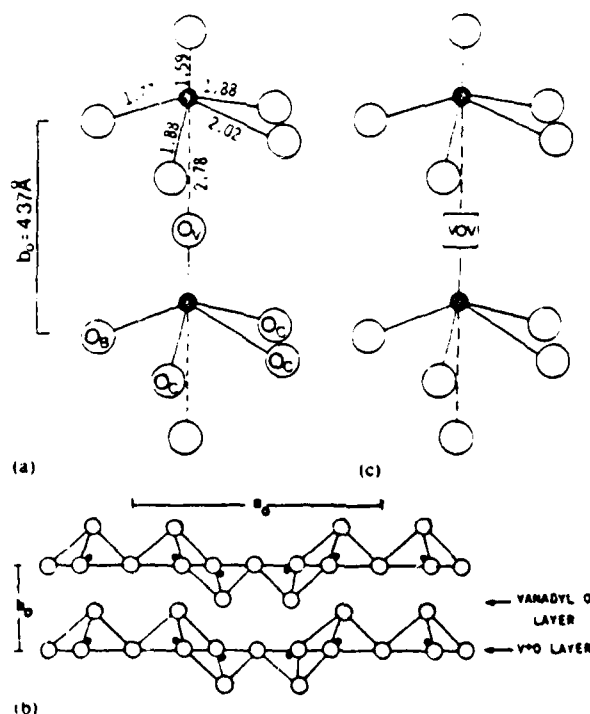


Fig. 1. (a) The effective fivefold coordination of vanadium with oxygen in the perfect vanadia lattice. Dark circles represent vanadium atoms; white circles represent oxygen atoms. O_v, vanadyl oxygen; O_c, chain oxygen; O_b, bridge oxygen. Bond lengths are shown in angstroms. (b) A projection of the '001' plane. (c) One possible type of atomic disorder that affects the interlayer spacing b : a vanadyl oxygen vacancy (From ref. 12.)

lead to materials for different applications. Bulk and thin film vanadia with vanadyl oxygen vacancies ($b < b_0$) have historically been used as an oxidation catalyst¹³⁻¹⁶. The optical transmission characteristics of thin film vanadia with $b > b_0$ ^{9,10} make it a candidate for a solar cell window. In addition, vanadia, like other vanadium oxides, undergoes a semiconductor \rightarrow metal phase transition, apparently independent of crystallographic order. A transition was measured in amorphous vanadia films from a resistivity change at 525-535 μK and thermally activated electronic switches were fabricated¹⁷. Very recently⁸, a semiconductor \rightarrow metal phase transition was measured in crystalline vanadia films at 531 K (film 6 in the present study).

We examine below the effect of Ar-O₂ gas composition at four values of cathode voltage on the crystallography of sputter-deposited vanadia. Gas composition and cathode voltage are independent process parameters. The goal is to determine (1) the field in cathode voltage-gas composition space within which vanadia with long-range crystallographic order is produced and (2) the change in vanadia interlayer spacing within this field.

2. EXPERIMENTAL PROCEDURE

2.1. Film growth

A liquid-N₂-cold-trapped, hot-oil-diffusion-pumped, r.f.-excited planar diode sputter deposition system was used to grow the films. The target was a 99.7% vanadium disc 12.7 cm in diameter bonded to a water-cooled copper cathode. The substrates were <111>-cut silicon wafers placed on a water-cooled copper anode. The anode-cathode spacing was 5 cm.

The chamber was evacuated to 6.65×10^{-6} Pa (5×10^{-7} Torr) before back-filling with sputtering gas. With a shutter covering the substrates, a two-step pre-sputter procedure was carried out in which the target was sputtered in argon for 20 min and then for an additional 20 min in the Ar-O₂ gas mixture used for the actual deposition, after which the shutter was opened. The total gas pressure was measured with a capacitance manometer and kept constant at 1.33 Pa (1×10^{-2} Torr). 99.999% pure argon and 99.997% pure O₂ were used. Each component was introduced separately into the sputtering chamber. Ar:O₂ ratios from 0:100 to 98:2 were established using an MKS Baratron Series 260 control system, Model 258 flow transducers and Model 248A solenoid control valves. The peak-to-peak cathode voltage V_c was varied from -1.4 to -2.0 kV. Specific deposition conditions are recorded in Table I.

In a separate experiment a model HR320 Instruments SA optical spectrometer capable of 0.5 Å resolution was used for optical emission discharge diagnostics. Radiation emitted from the region between the anode and cathode was sampled as a function of wavelength through a window with a transmission cut-off of 3.2 kÅ. The window was shuttered when not in use and was also periodically removed from the chamber and its transmission characteristics checked by spectrophotometry for intensity changes caused by coating with sputtered flux during the experiment. The emission intensity $I(V^*)$ from an optical transition of the neutral vanadium atom at $\lambda = 4111.6$ Å was monitored¹⁹. Changes in $I(V^*)$ are related to changes in the number of vanadium atoms in the discharge and to the formation of an oxide layer at the target surface⁹.

2.2. Post-deposition film analysis

The film thickness was determined using a profilometer to measure the height of a step produced by masking a region of the substrate during deposition. The growth rate was determined by dividing thickness by deposition time. Film thickness and growth rate are recorded in Table I.

The crystallography was determined by double-angle X-ray diffraction (XRD) using Cu K α radiation ($\lambda = 1.5418$ Å). The peak position (2θ), intensity and full width at half maximum intensity (FWHM) were measured. The diffractometer was calibrated using the {0101} diffraction peak of a quartz standard at $2\theta = 26.66 \pm 0.02^\circ$ whose width is 0.18° . Rutherford backscattering spectroscopy (RBS) using 2 MeV He²⁺ ions was carried out on selected films to determine the relative atomic concentration of vanadium and oxygen ($\pm 10\%$).

TABLE I
CONDITIONS USED TO SPUTTER DEPOSIT VANADIA AND VANADIUM OXIDE FILMS ON $\langle 111 \rangle$ -Si

Film	Cathode voltage (-kV)	Gas O_2 (%)	Growth rate ($\text{\AA}/\text{min}^{-1}$)	Thickness (k \AA)
1	20	2	67	3.0
2	20	4	65	2.9
3	20	6	56	2.5
4	20	10	53	2.4
5	20	15	44	2.0
6	20	25	41	1.9
7	20	100	34	1.6
8	18	2	61	2.8
9	18	4	47 ± 9	2.1 ± 0.4
10	18	6	51	2.3
11	18	10	44	2.0
12	18	15	39	1.7
13	18	25	27	1.2
14	18	100	23	1.0
15	1.6	2	54 ± 5	2.4 ± 0.2
16	1.6	4	47	2.1
17	1.6	6	40	1.8
18	1.6	10	38	1.7
19	1.6	15	33	1.5
20	1.6	25	24	1.1
21	1.6	100	20	0.9
22	1.4	2	-	-
23	1.4	4	-	-
24	1.4	6	-	-
25	1.4	10	-	-
26	1.4	15	-	-
27	1.4	25	-	-
28	1.4	100	-	-

3. RESULTS

The r.f. forward power and growth rate are shown as a function of gas O_2 content in Figs. 2(a) and 2(b) respectively. Figure 2(c) shows $I(V^*)$ as a function of gas O_2 content for different values of V_c .

Two types of crystallographic results were obtained by XRD. Films either showed diffraction only from $\{010\}$ vanadia planes (b axis normal to the substrate) or did not produce a diffraction pattern. The latter films were designated "short-range order (SRO) vanadium oxide". The region of cathode voltage-gas O_2 content space over which each type of film was produced is shown in Fig. 3. The results previously obtained¹¹ by sputtering a vanadium target 7.6 cm in diameter at -2.2 kV are included in Fig. 3. The interlayer spacing b of the crystalline films was calculated by substituting the vanadia $\{010\}$ XRD peak position into the Bragg equation for first-order diffraction, $\lambda = 2b\sin\theta$. b , FWHM and the intensity of the vanadia $\{010\}$ XRD peak are shown in Figs. 4(a)-4(c) respectively as a function of gas O_2 content.

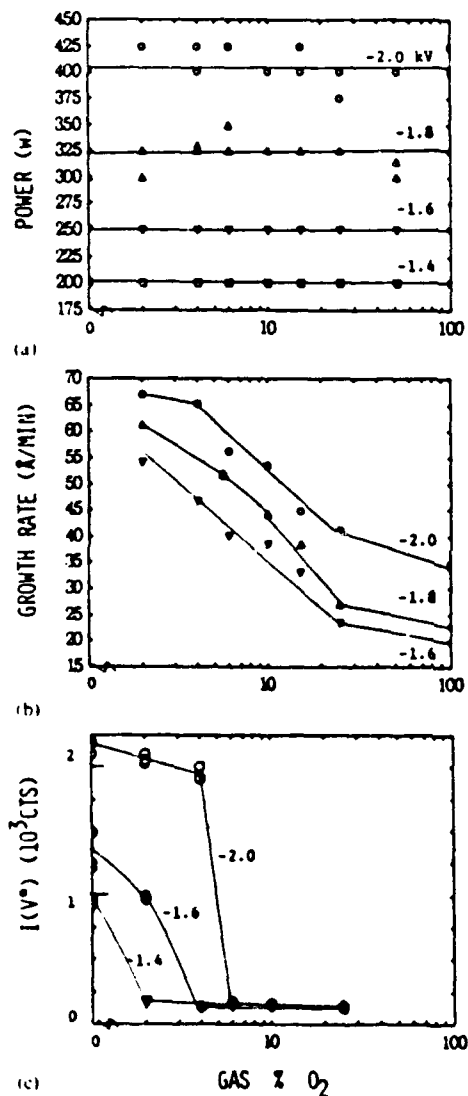


Fig. 2. (a) The rf forward power in the discharge, (b) the film growth rate and (c) the optical emission intensity at 4111.6 \AA from excited neutral vanadium atoms in the discharge as a function of gas O_2 content for different values of cathode voltage.

In a preliminary examination of the film chemistry, RBS was carried out on four films grown at -1.6 kV : films 15 and 17, which are SRO vanadium oxide, and films 18 and 20, which contain crystalline vanadia. The results show that within experimental uncertainty all of these films are chemically V_2O_5 .

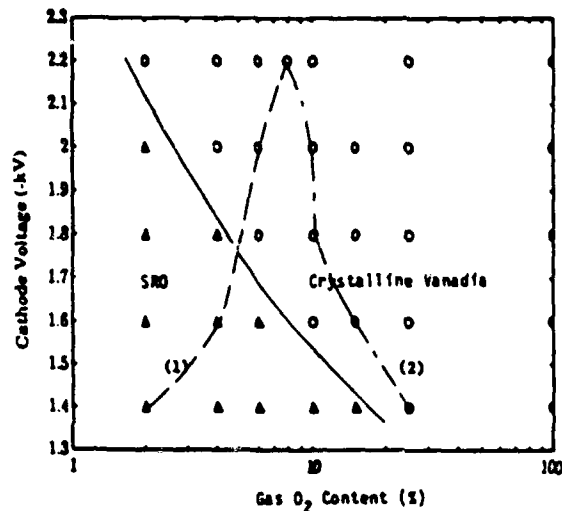


Fig. 3. A "phase diagram" in gas O_2 content-cathode voltage space showing regions in which short-range order vanadium oxide (triangles) and crystalline vanadia (ovals) with the b axis normal to the substrate plane are formed. The solid line defines the boundary between crystalline and non-crystalline phase regions. Curve (1) represents the gas O_2 content-cathode voltage coordinates at which the target surface becomes oxidized. Curve (2) represents the lowest gas O_2 content for a particular cathode voltage for which $b > b_0$.

4. DISCUSSION

4.1. Growth parameters and discharge characteristics

It is well known that when a metal target is sputtered in an O_2 -bearing discharge the target surface may become oxidized. In general, the flux sputtered from an oxidized target surface consists of both uncharged metal atoms and metal oxide molecules sputtered intact²⁰. In the case of the V-O system studied here, the reduction of $I(V^*)$ to a value equal to the background noise (approximately 120 counts) at a critical gas O_2 content, as shown in Fig. 2(c), indicates that vanadium atoms are no longer detectable in the sputtered flux. Vanadium is transferred from the oxidized target surface to the substrate in molecular form bonded to oxygen. It can also be seen from Fig. 2(c) that the critical gas O_2 content at which $I(V^*)$ vanishes increases with increasing V_c . This phenomenon has been reported for other target materials sputtered in argon containing small amounts of O_2 ²¹ and is attributed to increased dissociation of the target surface oxide under bombardment by more energetic Ar^+ ions (the majority sputtering species) as V_c is increased.

It can be seen from Fig. 2(a) that the discharge power is constant for all values of V_c from 100% argon to 100% O_2 , indicating that the deposition apparatus impedance remains unchanged even after a target surface oxide has formed. The criterion of a target surface oxide with metallic behavior is easy to satisfy in the V-O system. Several vanadium oxide phases are metallic conductors (VO , V_2O_3 , V_6O_{13}) at room temperature²², and even semiconductor phases VO_2 and V_2O_5 undergo

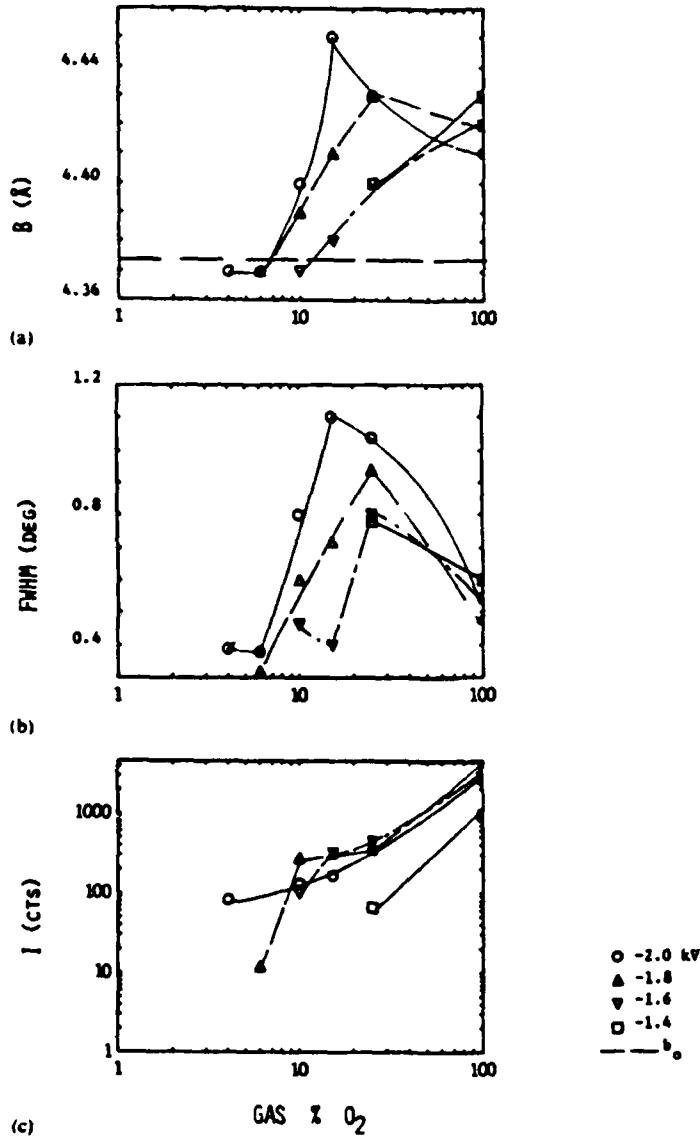


Fig. 4. Vanadia crystallography: (a) interlayer spacing b , (b) $\{010\}$ diffraction peak FWHM and (c) $\{010\}$ peak maximum intensity as a function of gas O₂ content for different values of cathode voltage.

metallic transitions at relatively low temperatures (341 K¹⁷ and approximately 530 K^{17,18} respectively) compared to the temperature probably attained locally at the target surface due to the sputtering process.

It can be seen from Fig. 2(b) that a significant decrease in growth rate occurs as

the sputtering gas O_2 content is increased from 2% to 25%, the precise explanation for which is left for future determination. In general, factors responsible may include: (1) a decrease in the sputtering yield due to the formation of a target surface oxide that is a better "barrier" to sputtering by Ar^+ than vanadium metal²³⁻²⁵ or has a lower density than vanadium metal²³; (2) a decrease in the number of Ar^+ species in the discharge²⁶; and (3) the more efficient sputtering ability of Ar^+ compared to O_2^+ .

4.2 Film crystallography

It can be seen from Fig. 3 that the lowest gas O_2 content at which vanadia with long-range crystallographic order is formed increases with decreasing V_c . It can be seen from Fig. 4(a) that the interlayer spacing of vanadia formed at low gas O_2 content is less than b_0 . b increases to above b_0 as the gas O_2 content is increased. The lowest gas O_2 content at which $b > b_0$ is also dependent upon V_c , and in general increases with increasing V_c .

For films grown in gas $Ar \leq 25\% O_2$, an increase in b is accompanied by (1) an increase in FWHM (Fig. 4(b)), indicating an increase in random strain and/or decrease in crystallite size, and (2) an increase in peak intensity (Fig. 4(c)), indicating an increase in the number of $\{010\}$ diffracting planes oriented parallel to the substrate plane. However, in spite of its increase, the peak intensity for these films is low, suggesting (1) poor alignment of $\{010\}$ planes with the substrate plane and (2) the presence of SRO vanadium oxide (amorphous and/or microcrystalline of undetermined orientation) as an additional phase. RBS results show that in films 18 and 20, if SRO vanadium oxide is present in addition to vanadia, its V:O atomic concentration is within $\pm 10\%$ of V_2O_5 . Films grown in 100% O_2 have $b > b_0$ and are crystallographically more ordered than films grown in $Ar \leq 25\% O_2$; their XRD patterns show a large $\{010\}$ peak intensity and a smaller FWHM.

Data from Figs. 2(c) and 4(a) are superimposed on the "phase diagram" in Fig. 3, by curves representing (1) the lowest value of gas O_2 for which $b > b_0$ and (2) the value of gas O_2 at which the target surface becomes oxidized. Previous data from refs. 9 and 11 show that curves (1) and (2) coincide for $V_c = -2.2$ kV. The data presented here show that these curves diverge with decreasing V_c . An oxidized target surface is a requirement for an interlayer spacing $b > b_0$ but not a guarantee of it. As V_c is decreased from -2.2 to -1.4 kV, the critical gas O_2 content at which the target surface is oxidized is shifted to lower values and the critical gas O_2 content at which $b > b_0$ is shifted to higher values, opening up a region in which crystalline vanadia with $b \leq b_0$ and SRO vanadia are produced from an oxidized target surface.

ACKNOWLEDGMENTS

The authors thank M. Aita and M.-A. Nicolet for helpful discussions. This work was supported under USARO Grant No. DAAL-03-89-K-0022 and from a gift by Johnson Controls, Inc. to the Wisconsin Distinguished Professorship of C.R.A.

REFERENCES

- 1 ASTM Joint Commission on Powder Diffraction Standards File No. 9-387, 1974. (b_0 and c_0 are reversed in this reference from the manner in which they appear throughout the literature.)
- 2 H. G. Bachmann, F. R. Ahmed and W. H. Barnes, *Z. Kristallogr.*, **115** (1961) S.11.
- 3 L. Fiermans and J. Vennik, *Surf. Sci.*, **9** (1968) 187.
- 4 A. Mosset, P. Lecante, J. Galy and J. Livage, *Phil. Mag. B*, **46** (1982) 137.
- 5 E. Gillis and E. Boesman, *Phys. Status Solidi*, **14** (1966) 337.
- 6 P. Clauws and J. Vennik, *Phys. Status Solidi B*, **56** (1974) 553.
- 7 W. Lambrecht, B. Djafari-Rouhani and J. Vennik, *J. Phys. C: Solid State Phys.*, **19** (1986) 369.
- 8 A. Bystrom, K.-A. Wilhelm and O. Brotsen, *Acta Chem. Scand.*, **4** (1950) 1119.
- 9 L. E. Orgel, *An Introduction to Transition-Metal Chemistry: Ligand Field Theory*. Methuen, London, 1960, p. 173.
- 10 S. D. Hansen and C. R. Aita, *J. Vac. Sci. Technol. A*, **3** (1985) 660.
- 11 C. R. Aita, Y.-L. Liu, M. L. Kao and S. D. Hansen, *J. Appl. Phys.*, **60** (1986) 749.
- 12 C. R. Aita, C.-K. Kwok and M. L. Kao, *M.R.S. Proc.*, **82** (1987) 435.
- 13 C. R. Aita and M. L. Kao, *J. Vac. Sci. Technol. A*, **5** (1987) 2714.
- 14 L. Fiermans, P. Clauws, W. Lambrecht, L. Vandenbrouche and J. Vennik, *Phys. Status Solidi A*, **59** (1980) 495.
- 15 M. V. Copart, *Z. Physiol. Chem.*, **84** (1973) 150.
- 16 L. Fiermans, L. Vandenbrouche, R. Vandenberghe, J. Vennik and G. Dalmai, *J. Microsc. Spectrosc. Electron.*, **4** (1979) 543.
- 17 J. H. Perlstein, *J. Solid State Chem.*, **3** (1971) 217.
- 18 G. S. Nadkarni and V. S. Shirodkar, *Thin Solid Films*, **105** (1983) 115.
- 19 L. L. Kazmerski, personal communication. (Measurements were made on films grown for the present study.)
- 20 A. N. Zaidel, V. K. Prokofev, S. M. Kaidkii, V. A. Slavnyi and E. Ya. Shreider, *Tables of Spectral Lines*, IFL Plenum, New York, NY, 1970.
- 21 C. R. Aita, *J. Vac. Sci. Technol. A*, **3** (1985) 625.
- 22 Zn O: C. R. Aita, R. J. Lad and T. C. Tisone, *J. Appl. Phys.*, **51** (1980) 6405.
Zr O: C.-K. Kwok and C. R. Aita, *J. Vac. Sci. Technol. A*, **7** (1989) 1235.
Y-O: C.-K. Kwok, C. R. Aita and E. Kolawa, *J. Vac. Sci. Technol. A*, **8** (1990).
- 23 J. B. Goodenough, *Phys. Rev.*, **117** (1960) 1442.
N. F. Mott, *Rev. Mod. Phys.*, **40** (1968) 665.
- 24 P. Sigmund, *Phys. Rev.*, **184** (1969) 383.
- 25 H. Winters, in M. Kaminsky (ed.), *Radiation Effects on Solids, Advances in Chemistry Series*, Vol. 158, American Chemical Society.
- 26 R. Kelley, in M. Kaminsky (ed.), *Radiation Effects on Solids, Advances in Chemistry Series*, Vol. 158, American Chemical Society.
- 27 C. R. Aita and R. J. Lad, *J. Appl. Phys.*, **60** (1986) 837.
C. R. Aita, *J. Appl. Phys.*, **61** (1987) 5182.

Annealing response of disordered sputter deposited vanadium pentoxide (V_2O_5)

John Luksich^{a)} and Carolyn Rubin Aita^{b)}

Materials Department, University of Wisconsin-Milwaukee, P.O. Box 784, Milwaukee, Wisconsin 53201

(Received 22 October 1990; accepted 12 November 1990)

We report the response to isothermal, low temperature (280 °C) annealing in air for up to 60 min, in terms of changes in crystallography and optical absorption coefficient $\alpha(E)$ of two types of sputter deposited, disordered vanadium pentoxide; (1) an amorphous film and (2) a single (010)-crystallographic orientation film in which the interlayer spacing b is slightly greater (0.03%) than b_0 , the ideal value. It was found that low temperature annealing does not crystallize amorphous vanadium pentoxide, and that no change occurs in $\alpha(E)$ in the charge transfer region $E > \sim 2.5$ eV. The Tauc nondirect optical band gap $E' = 2.34$ eV. However, the low energy absorption tail present in the as-grown amorphous film disappears upon annealing, attributed to the elimination of V^{+4} sites. On the other hand, annealing crystalline vanadium pentoxide causes crystallographic changes, the interlayer spacing expands, and concurrently, $\alpha(E)$ in the charge transfer region, $E > 2.6$ eV, increases. In agreement with a recent theoretical band calculation and single crystal data, the indirect optical band gap $E_i = 2.36$ eV for both as-grown and annealed crystalline vanadium pentoxide.

I. INTRODUCTION

Vanadium pentoxide (V_2O_5), is a wide band gap semiconductor at room temperature with an orthorhombic lattice structure with parameters $a_0 = 11.519$, $b_0 = 4.373$, and $c_0 = 3.564$ Å.¹ The extended space lattice consists of alternating layers of V + O atoms and O atoms (vanadyl O) alone oriented parallel to the b axis or (010) crystallographic direction.²⁻⁷ Bonding along the (010) direction is weak.⁸

In a series of experiments⁹⁻¹² in which films were grown from a vanadium target sputtered in Ar- O_2 discharges, we previously related long range atomic disorder in near room-temperature sputter deposited vanadium pentoxide to the process parameters gas O_2 content and cathode voltage V_C . Using optical emission spectrometry for *in situ* discharge diagnostics, we identified key species in the growth environment whose relative flux to the substrate strongly affected film crystallography and stoichiometry. Two important factors in the growth environment were found to be: (1) the V atomic/V-oxide molecular flux that arrived at the substrate, and (2) the amount of oxygen in the discharge after the surface of the target had become oxidized and its ability to getter oxygen from the discharge volume had stopped. In terms of process parameter-film structure relationships, a "phase diagram" for vanadium pentoxide not grown under conditions of thermodynamic equilibrium was developed,¹² in which changes in long range atomic order structure were mapped onto gas O_2 content- V_C space. All crystalline vanadium pentoxide, grown on a variety of substrates including (111)-cut Si, fused SiO_2 , laboratory glass, and (0001)-cut Al_2O_3 , was found to have solely a (010) orientation, that is, the b axis in all crystallites was oriented perpendicular to the substrate plane. The interlayer spacing b however, took on values from 4.36 to 4.45 Å (the deviation from ideal $b_0 = \Delta b = \{(b - b_0)/b_0\} = -0.003$ to $+0.018$). In addition

to disorder in interlayer spacing, films with no long range atomic order were also produced.

Each form of vanadium pentoxide has technological interest. Bulk and thin film vanadium pentoxide with vanadyl O vacancies ($b < b_0$) has historically been used as an important catalyst for the oxidation of hydrocarbons¹³⁻¹⁸ and the reduction of nitric oxides.¹⁹ The optical transmission characteristics of thin film vanadium pentoxide with $b > b_0$ ^{9,10} make it a candidate for a solar cell window. Crystalline vanadium pentoxide films of undetermined interplanar spacing have been used as the intercalation counterelectrode in electrochromic cells.^{20,21} Amorphous vanadium pentoxide has been studied for its semiconducting behavior arising from hopping of unpaired electrons between V atoms in $+5$ and $+4$ valence states.^{22,23} In addition, a phase transition at 250-260 °C, with an accompanying change in electrical resistivity has been reported in amorphous vanadium pentoxide, and thermally activated electronic switches were fabricated.²⁴

We have previously studied²⁵ low temperature (280 °C) oxidation of films in which $b < b_0$ and related changes in crystal structure and optical absorption behavior first to annihilation of V_6O_{13} growth faults, and after a longer time at temperature, of vanadyl O vacancies. In the following paper, we investigate the low temperature, isothermal annealing response, in terms of changes in crystallography and optical absorption behavior, of two types of disordered vanadium pentoxide structure: (1) an amorphous film, and (2) a film in which b , is slightly greater than b_0 ($\Delta b = +0.003$).

II. EXPERIMENTAL PROCEDURE

A. Film growth

A liquid N_2 -cold trapped, hot-oil diffusion pumped, radio-frequency (rf)-excited planar diode sputter deposition

system was used to grow the films. The target was a 12.7 cm diam, 99.7% V disc bonded to a water-cooled Cu cathode. The substrates, laboratory glass slides and carbon ribbon, were placed on a water-cooled Cu anode. The anode-cathode spacing was 5 cm.

The chamber was evacuated to 5×10^{-7} Torr before backfilling with sputtering gas. With a shutter covering the substrates, a two-step presputter procedure was carried out in which the target was sputtered in Ar for 20 min, and then for an additional 20 min in the Ar-O₂ gas mixture used for the actual deposition, after which the shutter was opened. The total gas pressure was measured with a capacitance manometer and kept constant at 1×10^{-2} Torr. 99.999% pure Ar and 99.997% pure O₂ were used. Each component was introduced separately into the sputtering chamber. Ar:O₂ ratios of 98:2 and 90:10 were established using a MKS Baratron Series 260 control system, Model 258 flow transducers, and Model 248A solenoid control valves. The discharge was operated at $V_c = -1.6$ kV ($p-p$), corresponding to 250 W rf forward discharge power.

B. Post-deposition film analysis

Film thickness was determined using a profilometer to measure the height of a step produced by masking a region of the glass substrate during deposition. Growth rate was determined by dividing thickness by deposition time. Film thickness and growth rate are recorded in Table I.

The crystallography of films grown on glass was investigated by double-angle x-ray diffraction (XRD) using Cu K α radiation ($\lambda = 1.5418$ Å). Peak position (2θ) and full width at one-half of the maximum intensity (FWHM) were measured. The diffractometer was calibrated using the {0101} diffraction peak of a quartz standard at $2\theta = 26.66^\circ \pm 0.02^\circ$ whose width is 0.23° . Rutherford backscattering spectroscopy (RBS) using 2 MeV He⁺ ions was carried out on films grown on carbon ribbon to determine the relative atomic concentration of V and O ($\pm 10\%$).

The optical transmittance T and reflectance R of near-normal incident radiation of films grown on glass was measured with a Perkin-Elmer Model 330 ultraviolet (UV)-visible-infrared (IR) double beam spectrophotometer. Measurements were made in laboratory air at room temperature. Reflectance measurements were made relative to a protected Al mirror. The absorption coefficient α was calculated as a function of incident photon energy E from the expression,²⁶

$$T = [(1 - R)^2 \exp(-\alpha x)] / [1 - R^2 \exp(-2\alpha x)]. \quad (1)$$

C. Heat treatment

Samples on glass were annealed in a 46 cm long Lindbergh tube furnace with both ends open to air. A Fluke digital thermometer with a type K thermocouple was used to calibrate the furnace to ± 2.0 °C. Samples were placed in the furnace at 280 °C for 30 and 60 min. Samples were then withdrawn from the furnace and cooled in laboratory air. XRD and optical transmission and reflection data was taken after each anneal.

III. RESULTS

A. Chemistry and crystallography

Rutherford backscattering spectroscopy results, recorded in Table I, show that the V:O atomic ratio in both as-grown films are, within the $\pm 10\%$ accuracy of the measurement, stoichiometric ($0.36 < V/O < 0.44$).

X-ray diffraction results are recorded in Table II. Film A as-grown and annealed up to 60 min showed no diffraction peaks, indicating an absence of long range atomic order. Film B as-grown and annealed up to 60 min showed diffraction solely from {010} V₂O₅ planes, with Δb increasing from +0.003 to 0.026 as a function of annealing time. An increase in FWHM accompanied the increase in Δb . An increase in FWHM indicates an increase in random strain (larger distribution of b values) and/or a decrease in crystallite size.

B. Optical absorption behavior

The visual appearance in transmitted light of as-grown film A was transparent green. As-grown film B and all annealed states of films A and B were transparent yellow.

The optical absorption coefficient $\alpha(E)$ is shown for values $> 10^3$ cm⁻¹ in Figs. 1 and 2 for all as-grown and annealed films. Values of $\alpha(E) < 10^3$ cm⁻¹ were excluded because they represent possible absorption and scattering due to film morphology, for example, at crystallite boundaries or other internal surfaces, and not representative of changes in V-O bonding that we are attempting to probe by examining changes in $\alpha(E)$.

Included in Figs. 1 and 2 are data for single crystal V₂O₅,²⁷ with the electric field vector E of the incident radiation par-

TABLE I. Deposition parameters, film thickness, and V:O atomic ratio^a for sputter deposited vanadium pentoxide.

Film	Gas %O ₂	V_c (-kV $p-p$)	Power (W)	Rate (Å/min)	Thickness (kÅ)	V/O at. %
A	2	-1.6	250	54 ± 5^b	1.7	0.36
B	10	-1.6	250	38 ± 5	0.6	0.38

^aDetermined by RBS ($\pm 10\%$).

^bError represents two standard deviations from the mean.

TABLE II. XRD peak position (2θ), interlayer spacing (b), Δb ($b - b_0/b_0$), and half-width (FWHM) of as-deposited and annealed sputter deposited vanadium pentoxide.

I. Film A				
1. As deposited: No diffraction peaks				
2. 280 °C/30 min: No diffraction peaks				
3. 280 °C/60 min: No diffraction peaks				
II. Film B				
	2θ (deg) ^a	b (Å) ^a	Δb	FWHM (deg) ^a
1. As deposited:	20.24 ± 0.02	4.387 ± 0.004	+ 0.003	0.48 ± 0.07
2. 280 °C/30 min:	20.00 ± 0.01	4.439 ± 0.002	+ 0.015	0.50 ± 0.03
3. 280 °C/60 min:	19.78 ± 0.03	4.488 ± 0.006	+ 0.026	0.55 ± 0.02

^aError in all values represents two standard deviations from the mean.

allel to the a and c crystal axes. Because of difficulties in growing single crystal V_2O_5 of sufficient thickness parallel to the b crystal axis, no data for $E \parallel b$ were available. The data for all single (010) orientation films in this study were taken with $E \parallel b$, a consequence of the fact that films grow with layers parallel to the substrate. Therefore, when comparing film and single crystal data, the difference in geometry, and hence possible anisotropic optical behavior, must be kept in mind.

IV. DISCUSSION

A comparison of the crystallographic data presented in Table II and optical absorption data presented in Fig. 1 shows that annealing amorphous film A at 280 °C for up to

60 min does not cause crystallization, but does change its optical absorption behavior. It can be seen from Fig. 1 that as-grown film A shows considerable absorption throughout the visible spectral region, with $\alpha(E) = \sim 10^4 \text{ cm}^{-1}$ from 1.5–2.5 eV ($\lambda = 0.7\text{--}0.5 \mu\text{m}$). A sharp increase in $\alpha(E)$ occurs at ~ 2.5 eV. A low energy tail on the optical absorption edge has been previously reported in crystalline sputter deposited V_2O_5 containing V^{+4} .^{10,25} In the case of crystalline V_2O_5 , V^{+4} sites were created during growth, concurrent with creating vanadyl O vacancies. In the case of as-grown film A, it is possible that V^{+4} sites arise from the general disorder of the amorphous material. In fact, $\alpha(E)$ for amorphous, stoichiometric V_2O_5 films grown by a sol-gel technique shows absorption associated with V^{+4} sites throughout the visible and near IR spectral regions.^{22,23} The region

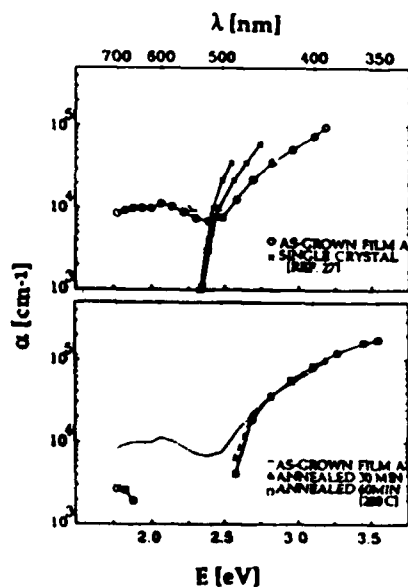


FIG. 1. The optical absorption coefficient $\alpha(E)$ as a function of incident photon energy for film A, as-grown and annealed for 30 and 60 min at 280 °C. Single crystal vanadium pentoxide data for $E \parallel a$ and $E \parallel c$ is from Kenny *et al.*¹⁷

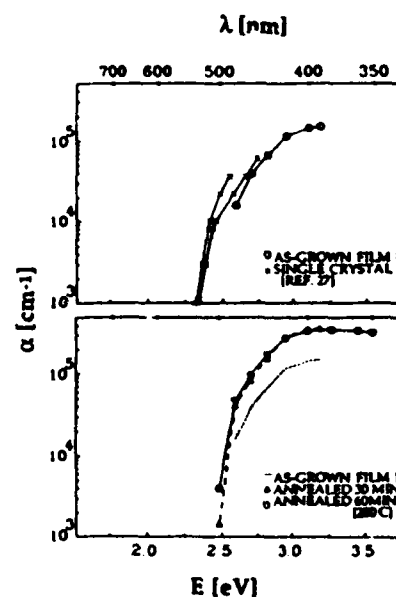


FIG. 2. The optical absorption coefficient $\alpha(E)$ as a function of incident photon energy for film B, as-grown and annealed for 30 and 60 min at 280 °C. Single crystal vanadium pentoxide data for $E \parallel a$ and $E \parallel c$ is from Kenny *et al.*¹⁷

of the $\alpha(E)$ versus E curve above ~ 2.5 eV is the charge transfer region [10] in which optical absorption is due to valence \rightarrow conduction interband electronic transitions. Annealing at 280°C for 30 min eliminates the low energy tail, presumably by elimination of V^{+4} sites, which is observed by the naked eye as a color change of the film from green to yellow. Annealing for 60 min causes a discrete, low intensity band centered at 1.75 eV to develop. Data for film A as-grown and annealed at 260°C are coincident in the charge transfer region.

The data near the onset of the charge transfer region ($E = \sim 2.5$ – 3.2 eV) for all states of film A were analyzed using the Tauc model²⁸ for an amorphous semiconductor to obtain a nondirect optical band gap E' defined by the following equation

$$[\alpha(E)E]^{1/2} = C[E - E'] \quad (2)$$

Extrapolation of the data to $\alpha(E) = 0$, as shown in Fig. 3, yields $E' = 2.34$ eV.

It can be seen from Fig. 2 that, unlike film A, as-grown film B has a sharp optical absorption edge with an onset at 2.5 eV and a change in slope marking the beginning of the charge transfer region at 2.6 eV. Annealing for 30 min at 280°C increases $\alpha(E > 2.6$ eV), indicating an increase in the joint density of states at the band edges. Annealing for 60 min produces no further change.

A recent²⁹ theoretical linear combination of atomic orbitals calculation based on the orthorhombic vanadium pentoxide unit cell predicts an initial indirect interband transition. We therefore fit the data for film B to the following equation, which defines an indirect band gap E_i in a crystalline solid:³⁰

$$\alpha(E)^{1/2} = D[E - E_i] \quad (3)$$

Extrapolation of the data to $\alpha(E) = 0$, as shown in Fig. 4, yields $E_i = 2.36$ eV for both as-grown and annealed film B.

Single crystal data²⁷ for $\alpha(E)$ in an available limited energy range, 2.3–2.8 eV, shows a sharp absorption edge with an onset at 2.3 eV and a change of slope at 2.45 eV. An early calculation based on an initial forbidden direct interband transition (without theoretical basis) was previously used to determine the single crystal band gap, and the values for $E||a$ and $E||c$ were 2.34 and 2.36 eV, respectively. There is an $[\alpha(E)E]^{2/3}$ dependence on E for a forbidden direct transition. Reevaluation of the single crystal data in light of the recent theoretical calculation, using Eq. (2), yields the same

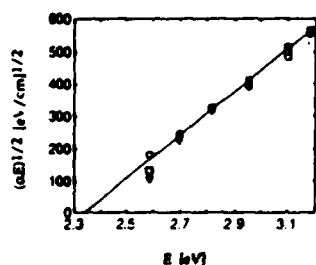


FIG. 3. $\alpha(E)$ data near the onset of the charge transfer region for all states of film A analyzed using the Tauc model²⁸ for an amorphous semiconductor to obtain a nondirect optical band gap E' defined in Eq. (2). Extrapolation to $\alpha(E) = 0$ yields $E' = 2.34$ eV. Circles— as-grown, squares—30 min anneal, triangles—60 min anneal.

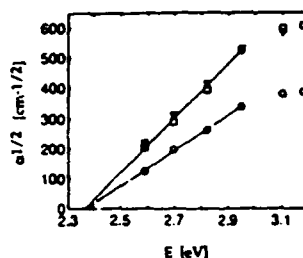


FIG. 4. $\alpha(E)$ data near the onset of the charge transfer region for all states of film B analyzed using Eq. (3) to obtain an indirect optical band gap E_i . Extrapolation to $\alpha(E) = 0$ yields $E_i = 2.36$ eV. Circles— as-grown, squares—30 min anneal, triangles—60 min anneal.

values for E_i , in excellent agreement with both the nondirect gap for all states of film A and the indirect gap for all states of film B.

V. SUMMARY

We investigated the response to isothermal, low temperature (280°C) annealing in air for up to 60 min, in terms of changes in crystallography and optical absorption coefficient $\alpha(E)$ of two types of sputter deposited, disordered vanadium pentoxide: (1) amorphous film A, and (2) single (010)-orientation film B in which the interlayer spacing b is slightly greater (0.03%) than b_0 , the ideal value. It was found that:

(1) Annealing amorphous film A does not cause crystallization. However, a low energy absorption tail disappears, attributed to the elimination of V^{+4} sites. No change occurs in $\alpha(E)$ in the charge transfer region $E > \sim 2.5$ eV. The Tauc nondirect optical band gap, $E' = 2.34$ eV for all states of film A.

(2) Annealing crystalline film B causes b to further expand and $\alpha(E)$ in the charge transfer region, $E > 2.6$ eV, to increase. In agreement with a recent theoretical band calculation and single crystal data for vanadium pentoxide, the indirect optical band gap $E_i = 2.36$ eV for all states of film B.

ACKNOWLEDGMENTS

We thank Professor D. Venugopalan (UW-MKE) for use of the annealing facility, and Dr. E. A. Kolawa, Dr. C.-K. Kwok, and Professor M. A. Nicolet (Caltech) for Rutherford backscattering measurements, useful discussions, and encouragement. This work was supported under US ARO Grant No. DAAL-03-89-K-0022, and through a gift to the Wisconsin Distinguished Professorship of CRA.

²⁷Permanent address: Johnson Controls, Inc., Systems and Services Division, 507 East Michigan Street, Milwaukee, WI 53201.

²⁸Author to whom correspondence should be addressed.

²⁹ASTM Joint Commission on Powder Diffraction Standards File No. 9-387 (1974). b_0 and c_0 are reversed in this reference from the manner in which they appear throughout the literature.

³⁰H. G. Bachmann, F. R. Ahmed, and W. H. Barnes. Z. Kristal. S. 115, 11 (1961).

³¹L. Fiermans and J. Vennik, Surf. Sci. 9, 187 (1969).

³²A. Mosset, P. Lecante, J. Galv. and J. Livage, Philos. Mag. B 46, 137 (1982).

³³E. Gillis and E. Boesman, Phys. Status Solidi 14, 337 (1966).

³⁴P. Clauws and J. Vennik, Phys. Status Solidi B 66, 553 (1974).

³⁵W. Lambrecht, B. Djafari-Rouhani, and J. Vennik, J. Phys. C 19, 369 (1986).

- ¹A. Bystrom, K.-A. Wilhelm, and O. Brotsen, *Acta Chem. Scand.* 4, 1119 (1950).
²L. E. Orgel, *An Introduction to Transition-Metal Chemistry: Ligand Field Theory* (Methuen, London, 1960), p. 173.
³S. D. Hansen and C. R. Aita, *J. Vac. Sci. Technol. A* 3, 660 (1985).
⁴C. R. Aita, Y.-L. Liu, M. L. Kao, and S. D. Hansen, *J. Appl. Phys.* 60, 749 (1986).
⁵C. R. Aita, C. K. Kwok, and M. L. Kao, *Mat. Res. Soc. Proc.* 82, 435 (1987).
⁶C. R. Aita, L. J. Liou, C. K. Kwok, R. C. Lee, and E. Kolawa, *Thin Solid Films*, XXX (1990).
⁷L. Fiermans, P. Clauws, W. Lambrecht, L. Vandenbrouche, and J. Vennik, *Phys. Status Solidi A* 59, 495 (1980).
⁸M. V. Copart, *Z. Physiol. Chem.* 84, 150 (1987).
⁹L. Fiermans, L. Vandenbrouche, R. Vandenberghe, J. Vennik, and G. Dalmai, *J. Microsc. Spectros. Elec. Ion.* 4, 543 (1979).
¹⁰J. H. Perlstein, *J. Solid State Chem.* 3, 217 (1971).
¹¹H. Miyata, M. Kohno, and T. Ono, *J. Chem. Soc. Faraday Trans. 1*, 85, 3663 (1989).
¹²H. Miyata, S. Tokuda, and T. Yoshida, *Appl. Spectrosc.* 43, 522 (1989).
¹³A. Kaiker and A. Wokauun, *Naturwissen Schafter* 76, 168 (1989).
¹⁴S. F. Cogan, N. M. Nguyen, S. J. Perrotti, and R. D. Rauh, *J. Appl. Phys.* 66, 1333 (1989); *SPIE Proc.* 1016, 57 (1988).
¹⁵A. Talledo, A. M. Andersson, and C. G. Grandqvist, *J. Mater. Res.* 5, 1253 (1990).
¹⁶C. Sanchez, F. Babonneau, R. Morineau, and J. Livage, *Philos. Mag.* B 47, 279 (1983).
¹⁷J. Bullo, P. Cordier, O. Gallais, M. Gauthier, and F. Babonneau, *J. Non-Cryst. Solids* 68, 135 (1984).
¹⁸G. S. Nadkarni and V. S. Shirodkar, *Thin Solid Films* 105, 115 (1983).
¹⁹C. R. Aita and M. L. Kao, *J. Vac. Sci. Technol. A* 5, 2714 (1987).
²⁰J. I. Pankove, *Optical Processes in Semiconductors* (Prentice-Hall, Englewood Cliffs, NJ, 1971), pp. 93-95.
²¹N. Kenny, C. R. Kannewurf, and D. H. Whitmore, *J. Phys. Chem. Solids* 2, 1237 (1966).
²²G. Cody, in *Semiconductors and Semimetals*, edited by J. I. Pankove (Academic, New York, 1984), Vol. 21, Part B.
²³Y.-W. Ching (unpublished).
²⁴J. I. Pankove, *op cit.* pp. 37-43.

ELECTRONIC TRANSITION-RELATED OPTICAL ABSORPTION IN VANADIA FILMS

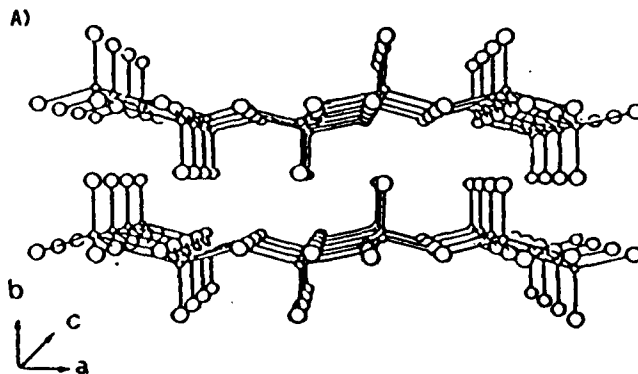
NADA M. ABUHADBA AND CAROLYN R. AITA
Materials Department, University of Wisconsin-Milwaukee, P.O. Box 784, Milwaukee,
Wisconsin 53201

ABSTRACT

Vanadium pentoxide (vanadia) is a wide band gap semiconductor. Its layered orthorhombic structure consists of alternating sublayers of V+O atoms and O atoms (vanadyl O) alone aligned perpendicular to the b-axis. This unique structure makes vanadia a useful host for alkali atom intercalation for electrochromic applications, and therefore, an understanding of its optical properties is important. Here, we study the optical absorption characteristics of vanadia in the incident photon energy range $E=2.5-6.0$ eV ($\lambda=490-200$ nm). The material is in the form of $0.1\mu\text{m}$ thick films sputter deposited in Ne/O₂ discharges. Two types of films were studied: single-oriented films with the b-axis perpendicular to the substrate, and amorphous films with an oxygen deficiency. The optical absorption coefficient, $\alpha(E)$, was determined and interpreted in terms of the structure of the V 3d conduction band. Amorphous, O-deficient vanadia were examined for room temperature aging and were found to oxidize and increase in transmittance in the photon energy range studied.

INTRODUCTION

Vanadia, V₂O₅, is a wide band gap semiconductor at room temperature. It crystallizes in the orthorhombic crystal structure with bulk parameters $a=11.519$ Å, $b=4.373$ Å, and $c=3.564$ Å [1-6]. The crystal structure is shown in Fig. 1a [7]. Perpendicular to the b crystal axis, i.e., in the (010) plane, vanadia has a layered structure consisting of alternating rows of V+O atoms and O atoms alone. In vanadia, a central V atom is bonded to six O atoms in a distorted octahedral symmetry. Four O atoms are coplanar, a fifth O lies 1.59 Å above the central V atom and is referred to as the vanadyl O, and a sixth O atom lies 2.78 Å below the central V. Figure 1b shows the local atomic arrangement. Bonding perpendicular to the layer is weak because of the large separation between a central V atom and the vanadyl O of an adjacent layer.



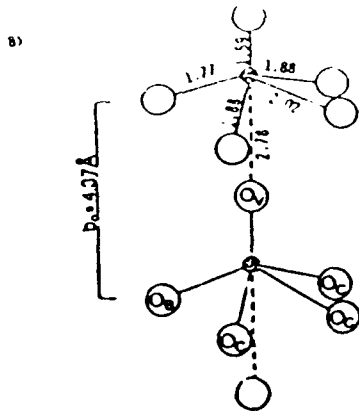


Fig. 1: a) Perspective drawing of the vanadia lattice, with small circles indicating V and larger circles indicating O [from Ref. 7]. b) The local arrangement around a central V atom in distorted octahedral coordination with six O [O_V =vanadyl O, O_C =chain O, O_B =bridge O]

Interest in the optical properties of vanadia originated as a result of a better understanding of the catalytic process of hydrocarbon oxidation [7-11]. The oxygen molecule dissociates at the surface of nonstoichiometric vanadia by trapping an oxygen atom at a vacant vanadyl oxygen site. Optical-related studies showed presence of a broad infrared band centered at about $1\mu\text{m}$, the intensity of which increased or decreased upon reduction or oxidation of vanadia respectively [9,11]. The band was attributed to electronic transitions within occupied V^{+4} 3d band (i.e. $3d^1 \rightarrow 3d^1$).

The wide interlayer spacing allows intercalation of alkali atoms within the vanadia lattice, and that, in turn resulted in the interest in thin films of vanadia in solid state batteries [12] and electrochromic devices for smart windows [13-16]. Intercalation and de-intercalation are associated with reduction and oxidation of the material, and hence the IR band in thin film vanadia has repeatedly been investigated [13,16,18]. However, there have been few studies of optical behavior at energy greater than the band gap, i.e. in the ultraviolet spectral region, which is the subject of the present paper. Aita et al. [17-21] have been studying the effect of various sputter deposition parameters on the vanadia films structural and optical properties grown in Ar/O_2 discharges.

We report here the optical properties of single (110) orientation vanadia and amorphous vanadia films for incident photon energy, $E=2.5-6.0$ eV (wavelength $\lambda=490-200$ nm). Films are grown by radio frequency reactive sputter deposition in Ne/O_2 discharges. The effect of using Ne/O_2 discharges on the films' structural properties is discussed in Ref. 27. Optical absorption characteristics in the ultraviolet region are related to the structure of the vanadia conduction band. The effect of room temperature aging of the amorphous films is discussed in terms of film oxidation.

EXPERIMENT

Film Growth

A liquid N_2 -cold trapped, hot-oil diffusion pumped, rf-excited planar diode sputter deposition system was used to grow the films. The target was a 12.7 cm-diam, 99.7% V disc bonded to a water-cooled cathode. The substrates were pyrex glass slides and fused silica placed on a water-cooled Cu anode. The anode-cathode spacing was 5 cm.

The chamber was evacuated to 6.65×10^{-6} pa (5×10^{-7} torr) before backfilling with sputtering gas. The total gas pressure was measured with a capacitance manometer and kept constant at 1.33 Pa (1×10^{-2} torr). 99.999% pure Ne and 99.997% pure O_2 were used. Each component was introduced separately into the sputtering chamber. Ne: O_2 ratios were

established using an MKS Baratron Series 260 control system, Model 258 flow transducers, and Model 248A solenoid control valves. With a shutter covering the substrates, a two-step pre-sputter procedure was carried out in which the target was sputtered in Ne for 45 minutes, and then for an additional 45 minutes in the Ne/O₂ gas mixture used for the actual deposition, after which the shutter was opened. Peak-to-peak cathode voltage, V_c, was -1.6 kV. Specific deposition conditions are recorded in Table 1.

Ne gas was used as the sputtering rare gas instead of the commonly used Ar for several reasons. A well-known characteristic of reactive sputter deposition from an elemental target is that compound formation at the target surface above a critical reactive gas content, for example oxygen content [21-22]. In that 'mode' of the target, the flux of species sputtered off the target and arriving at the substrate is almost totally in molecular form. It is also known that metastable Ne (Ne^m= 16.62 and 16.71 eV) can Penning ionize ground state O₂ molecules (ionization potential E_i=12.1 eV) whereas Ar metastables (Ar^m=11.55 and 11.72 eV) cannot [23-25]. The product of Penning ionization (Ne^m + O₂ → O₂⁺ + Ne⁰ + 1e) is a positively-charged oxygen species which is readily attracted to the negatively biased target, enhancing target oxidation. The target surface no longer getters all oxygen from the plasma, making it available for reaction with metal or suboxide species at the substrate. While that property of Ne is unattractive for forming metal suboxides by reactive sputtering, it is very convenient for forming high valence metal oxides. In addition, the low mass of Ne⁺ results in a lower sputtering yield and hence lower deposition rate. The mobility of species at the substrate is not only temperature dependent but also time dependent. For both of these reasons, crystalline growth is in general enhanced (disordered or amorphous growth is minimized) when Ne rather than Ar is used as the rare gas component of the discharge, aiding at the formation of highly orientated uniepitaxial films (i.e. polycrystalline with sharp fiber texture) [26-27].

Film Characterization

Film thickness was determined using a Tencor Alpha Step Model 200 profilometer to measure the height of a step produced by masking a region of the substrate during deposition. Growth rate was determined by dividing thickness by deposition time.

Crystallography was determined by double-angle x-ray diffraction (XRD) using Cu K α radiation ($\lambda = 1.5418 \text{ \AA}$) for films grown on glass slides. Peak position (2θ), intensity, and full width at one-half of the maximum intensity (FWHM) were measured. The diffractometer was calibrated using the {01.1} diffraction peak of a quartz standard at $2\theta = 26.66 \pm 0.02^\circ$ whose width is 0.25° . The interplanar spacing, $d\{hkl\}$ was calculated using the Bragg equation for nth order diffraction: $d\{hkl\} = n\lambda/2\sin\theta$.

A Perkin-Elmer Model 330 UV-Visible-Near IR double beam spectrophotometer with a specular reflection attachment was used to measure the transmittance and reflection of near normal incidence radiation in the 200-650 nm range for films on fused silica. Measurements were performed immediately after deposition and then again after a period of nine months. In the transmittance regime, a bare fused silica substrate was placed in the path of the reference beam so that the recorded transmittance is due to the transmission through the film alone. Reflectance measurements were made relative to an Al mirror. No sample was placed in the reference beam path. In the energy region studied here, which is near and above the band gap, the film is highly absorbing so that reflection of the incident beam at the film-substrate interface is minimized, thus allowing the use of Eq. (1) for absorption coefficient calculations [28]:

$$T = [(1-R)^2 \exp(-\alpha x)] / [1 - R^2 \exp(-2\alpha x)]. \quad (1)$$

T is transmittance, R is reflectance, x is film thickness, and α is the absorption coefficient calculated as a function of wavelength.

RESULTS

Film thickness, growth rate, and x-ray diffraction results are given in Table I. Films that showed no x-ray diffraction peaks were green in color and are referred to here as amorphous vanadia. Crystalline films showed two x-ray diffraction peaks attributed to first and second order diffraction of (010) planes of orthorhombic vanadia.

Table I: Film designation, sputtering gas O₂ content (%O₂), film thickness (T), growth rate (G), crystal structure (CS), and interlayer spacing (B).

Film	%O ₂	T (Å)	G (Å/min)	CS	B (Å)
A	2	1300	11	Amorphous	—
B	4	840	14	Amorphous	—
C	10	890	7	(010) orthorhombic	4.405
D	25	1300	11	(010) orthorhombic	4.398

Figure 2 shows the absorption coefficient calculated using Eq. 1 as a function of incident photon energy for Films A, C, and D. The transmittance through as-deposited amorphous Films A and B is compared to that after a period of nine months of aging to test for film stability. The results are shown in Fig. 3.

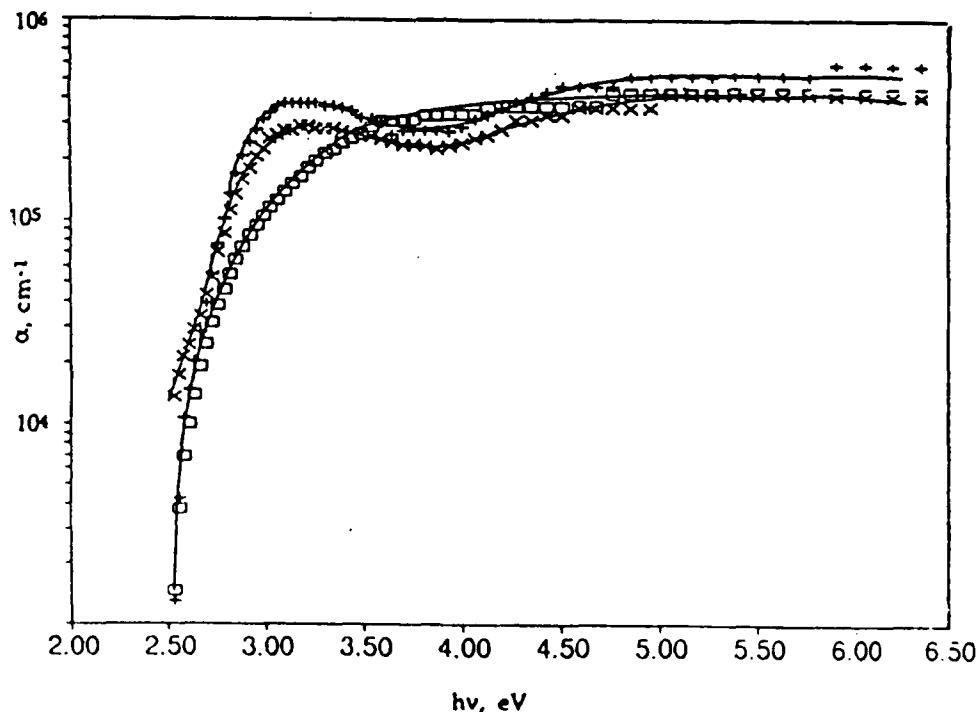


Fig. 2: Absorption coefficient as a function of incident photon energy for crystalline vanadia Film C (+) and Film D (x) and amorphous vanadia Film A (□).

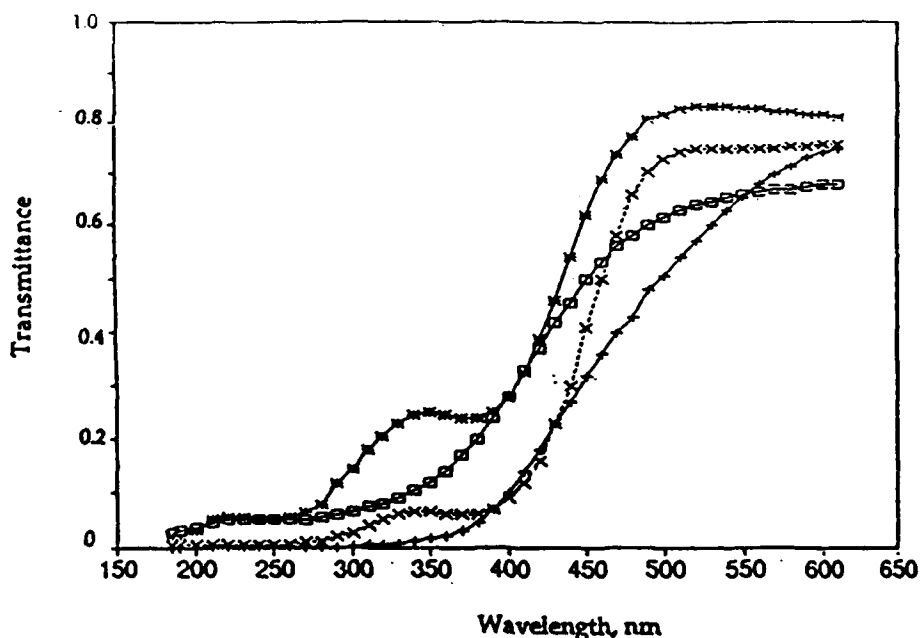


Fig.3: Transmittance through Film A (+), and Film B (o) in as deposited state. In the aged state, Films A and B are designated by (x) and (*) respectively.

DISCUSSION

Vanadia films grown in discharges of O_2 content greater than 4% and at cathode voltage of 1.6kV had a solely $\langle 010 \rangle$ orientation, i.e. the films are uniepitaxial, with the b axis lying perpendicular to the substrate. The interlayer spacing was always greater than the bulk value (4.373Å). No long range order was detected in films grown in O_2 content less than 4%. It was previously reported that the critical O_2 content needed to produce crystalline vanadia in Ne/ O_2 discharges decreased with increasing cathode voltage [27], and is less than the critical O_2 content found in Ar/ O_2 discharges at 1.6 kV, consistent with the previous discussion of Penning ionization of O_2 .

A comparison of the absorption behavior of crystalline vanadia Films C and D and amorphous vanadia Film A in Fig. 2 reveals two main differences:

- 1) an absorption band with an onset at 2.5 eV and centered at 3.2 eV present only in crystalline vanadia, followed by another broader band, the onset of which is at 3.8 eV.
- 2) a shift in the absorption edge for $h\nu > 2.8$ eV toward higher energy in amorphous vanadia.

The structure of the optical absorption curve of crystalline vanadia can be explained as follows. The valance band in vanadia has an O 2p nature. The conduction band consists of two split-off V 3d bands, a feature characteristic of the symmetry of crystalline vanadia. The lower V 3d band was first calculated by Bullet to be 0.4 eV wide, and separated by 0.3 eV from the upper and broader V 3d band [29]. The onset of absorption at 2.5 eV is therefore attributed to electronic transitions from the O 2p to the lower V 3d band. The broader, higher energy band whose onset is 3.8 eV, is attributed to transitions from the O 2p to the upper V 3d band. The first spectroscopic measurements on single crystal V_2O_5 to reveal such a band structure was performed by Mokerov et al. [30]. In the real part, n , and imaginary part, k , of the complex refractive index, a band with a maximum at 2.5 eV and 0.4 eV wide, followed

by a stronger band centered at 2.92 eV for polarized light with E || a, and at 3.15 eV for E || c was reported.

The split-off V 3d bands lose resolution in as-deposited amorphous vanadia films, accompanied by a shift in the absorption edge to higher energy. The latter effect has previously been observed to occur in nanocrystalline vanadia thin films after Li⁺ intercalation to produce V⁺⁴ sites [16], consistent with the substoichiometric nature of the amorphous films. Crystalline films do not age at room temperature, whereas amorphous films do. We attribute this aging to oxidation which annihilates V⁺⁴ defects. A similar result was previously reported for substoichiometric vanadia on sapphire [17].

REFERENCES

1. ASTM Joint Commission on Powder Diffraction Standards File No. 9-387, (1974). b and c are reversed in this reference from the manner in which they appear throughout the literature.
2. H. G. Bachmann, F.R. Ahmed, and W.H. Barnes, *Z. Kristal.* **115**, S.11 (1961).
3. L. Fiermans and J. Vennik, *Surf. Sci.* **9**, 187 (1968).
4. E. Gillis and E. Boesman, *Phys. Status Solidi* **14**, 337 (1966).
5. P. Clauws and J. Vennik, *Phys. Status Solidi B* **66**, 553 (1974).
6. W. Lambrecht, B. Djafari-Rouhani, and J. Vennik, *J. Phys. C* **19**, 369 (1986).
7. R. Ramirez, B. Casal, L. Utera, and E. Ruiz-Hitzky, *J. Chem. Phys.* in press.
8. L. Fiermans, P. Clauws, W. Lambrecht, L. Vandenbrouche, and J. Vennik, *Phys. Status Solidi A* **59**, 495 (1980).
9. L. Fiermans, L. Vandenbrouche, R. Vandenberge, J. Vennik, and G. Dalmai, *J. Microsc. Spectros. Electron.* **4**, 543 (1979).
10. J.H. Perlstein, *J. Solid State Chem.* **3**, 217 (1971).
11. J. Bullot, P. Cordier, O. Gallais, M. Gauthier, and F. Babonneau, *J. Non-cryst. Sol.* **68**, 135 (1984).
12. J.B. Bates, N.J. Dudney, C.F. Luck, and L. Klatt, *Ceramic Transactions* **11**, 35 (1990).
13. S.F. Cogan, N.M. Nguyen, S.J. Perrotti, and R. D. Rauh in *Optical Materials Technology for Energy Efficiency and Solar Energy Conversion VII* (SPIE, **1016**, 1988) pp. 57-62.
14. S.F. Cogan, N.M. Nguyen, S. J. Perrotti, and R. D. Rauh: *J. Appl. Phys.* **66**, 1989, 1333.
15. A. Talledo, A.M. Andersson, C.G. Granqvist: *J. Mater. Res.* **5**, 1253 (1990).
16. A. Talledo, A.M. Andersson, and C.G. Granqvist, *J. Appl. Physics.* **69**, 3261 (1991).
17. S.D. Hansen and C.R. Aita: *J. Vac. Sci. Technol. A* **3**, 660 (1985).
18. C.R. Aita, Y.-L. Liu, M.L. Kao, and S.D. Hansen, *J. Appl. Phys.* **60**, 749 (1986).
19. C.R. Aita, C.-K. Kwok, and M.L. Kao, *Mat. Res. Soc. Proc.* **82**, 435 (1987).
20. C.R. Aita and M.L. Kao, *J. Vac. Sci. Technol. A* **5**, 2714 (1987).
21. C.R. Aita, L.-J. Liou, C-K. Kwok, R.C. Lee, and E. Kolawa, *Thin Solid Films* **193-4**, 18 (1991).
22. R.C. Lee and C.R. Aita, *J. Appl. Phys.* **70**, 2094 (1991).
23. C.R. Aita and Ngoc C. Tran, *J. Appl. Phys.* **56**, 958 (1984).
24. J.W. Coburn and E. Kay, *Appl. Phys. Lett.* **18**, 435 (1971).
25. C.R. Aita and M.E. Marhic, *J. Vac. Sci. Technol. A*, **1**(1), 69 (1983).
26. N.M. Abuhadba and C.R. Aita, *J. Appl. Phys.* **71**, xxx (1992).
27. N.M. Abuhadba and C.R. Aita, *Mater. Sci. Technol.* xxx (1991).
28. J.I. Pankove, *Optical Processes in Semiconductors* (Prentice-Hill, Englewood Cliffs, NJ, 1971), p. 93.
29. D.W. Bullet, *J. Phys. C. Solid St. Phys.* **13**, L595 (1980).
30. V.G. Mokerov, V.L. Makarov, V.B. Tulvinski, and A.R. Begishev, *Opt. Spectrosc.*, **40**, 58 (1976).

APPENDIX IV

- A. "A phase map for sputter deposited niobium oxides." R. C. Lee and C.R. Aita, J. Appl. Phys. 70 2094-2103, (1991).

- B. "Growth conditions for sputter deposited niobium oxides." R.C. Lee and C.R. Aita, J. Vac. Sci. Technol. A 10, 1777-83 (1992).

A phase map for sputter deposited niobium oxides

Ray C. Lee and Carolyn Rubin Aita¹⁾

Materials Department, University of Wisconsin-Milwaukee, P.O. Box 784, Milwaukee, Wisconsin 53201

(Received 11 April 1991; accepted for publication 23 May 1991)

A Nb target was sputtered in radio frequency (rf) Ar/O₂ and Ne/O₂ discharges, and films were grown on unheated fused silica, (111)-cut Si, and carbon ribbon. The transition from Nb metal to niobia film growth was studied as a function of three independent process parameters: cathode voltage, gas O₂ content, and rare gas type. On the basis of x-ray diffraction results, resistivity, optical transmission, refractive index, Nb:O ratio, and infrared absorption characteristics, the following phases were identified in the films: bcc Nb, NbO, NbO₂, x-niobia, amorphous niobia, microcrystalline niobia, and crystalline niobia (where niobia = Nb₂O_{5-x} with 0 < x < 0.2). *In situ* optical spectrometry of the discharge was used to monitor the emission intensity $I(\lambda)$ of four radiative electronic transitions of the neutral excited Nb atom to ground state ($\lambda = 5344, 5079, 4101, \text{ and } 4059 \text{ \AA}$).

Changes in $I(\lambda)$ and the growth rate was used to (1) determine the set of process parameters at which target surface oxidation occurred, and (2) estimate the fractional flux of atomic Nb and Nb bonded to O in an unspecified molecular form (Nb-oxide) incident on the substrate. Film structure was found to depend to some extent upon this fractional flux.

A phase map was constructed in which film structure and the Nb and Nb-oxide fractional flux were graphed onto process parameter space, demonstrating the equivalent effect of different sets of process parameters.

I. INTRODUCTION

Sputter deposition involves film growth in a low-pressure, glow discharge environment, usually far from conditions of thermodynamic equilibrium. A solid target is bombarded by energetic gas ions, and the ejected atoms and molecules are collected on a substrate to form a film. Reactive sputter deposition, used in this study to deposit niobium oxides, involves the inclusion of O₂ in a rare gas discharge. As a result, chemical reactions can potentially occur at the target surface, in the plasma, and at the substrate. Precisely because sputter deposition is governed by kinetics, it is ideally suited for growing metastable phases, composite structures, and high melting point materials near room temperature.

In this paper, we address process parameter-growth environment-film structure relationships for the sputter deposited Nb-O materials system. The experiment consisted of sputtering an Nb target in rf Ar/O₂ and Ne/O₂ discharges and depositing films on unheated fused silica, (111)-cut Si, and carbon ribbon substrates. The transition from Nb metal to niobia film growth was studied as a function of three process parameters: (1) the cathode voltage, (2) the O₂ content of the sputtering gas, and (3) the type of rare gas used in conjunction with O₂. These parameters can be independently varied, and combined, they determine other important parameters such as discharge power, growth rate, and the number of various types of oxygen species in the plasma.^{1,2}

In general, when a target of metal *M* is sputtered in an O₂-bearing discharge, the sputtered target species consist of both *M* atoms and *M* bonded to oxygen in an un-

specified molecular form(s), denoted here "*M*-oxide."³ The flux of target species incident on the growth interface will therefore consist of both *M* and *M*-oxide. When studying other sputter deposited transition metal-oxygen systems grown on unheated substrates, Zr-O,^{4,7} Y-O,⁷⁻⁹ and V-O,¹⁰⁻¹⁵ we found that the relative *M*-oxide: *M* flux was a factor in determining the oxidation state of *M* in the film. For this reason, optical emission spectrometry was used in this study for *in situ* discharge diagnostics, specifically to determine the relative Nb-oxide: Nb flux in the plasma, and hence incident on the growth interface.

Post-deposition film characterization included x-ray diffraction to determine crystallographic parameters, four-point probe measurements to obtain electrical resistivity, Rutherford backscattering (RBS) to determine Nb:O atomic ratio, spectrophotometry in the near-ultraviolet visible-near-infrared spectral region to determine optical transmission and refractive index, and infrared absorption spectrometry to identify Nb-O short-range atomic order.

The experimental data were used to construct a "phase map." First, film structure was graphed onto process parameter space. Then, values of relative Nb-oxide:Nb flux incident on the substrate were overlaid on the process parameter-film structure diagram. The resulting map is a graphical representation of the equivalence of different process parameters on both the film structure and an important aspect of the growth environment, the Nb-oxide:Nb flux.

The scientific purpose of constructing a phase map for any sputter deposited system is to enable us to understand changes in film structure in terms of a changing growth environment, a first step towards modeling metal oxide

¹⁾Author to whom correspondence should be addressed.

growth by sputter deposition. An important technological outcome is that another investigator using the information about the equivalence of process parameters, graphically represented by the phase maps, will be able to make educated decisions when designing an experiment to obtain specific film properties even if no means of *in situ* discharge diagnostics is available.

II. EXPERIMENTAL PROCEDURE

A. Film growth

Films were grown in a radio frequency (rf) diode apparatus operated at 13.56 MHz by sputtering a 13-cm-diam, 99.97% pure Nb target bonded to a water-cooled Cu cathode. Supersil fused silica, <111>-cut Si, and carbon foil substrates, each required for different post-deposition analytical techniques, were placed on a water-cooled Nb-coated Cu pallet covering the anode. The anode-cathode spacing was 6 cm.

The chamber was evacuated to $< 5 \times 10^{-7}$ Torr with a liquid N₂-trapped, hot Si-base oil diffusion pump and back-filled with the sputtering gas to a total pressure of 1×10^{-2} Torr. The sputtering gas consisted of O₂ (99.99%) and a rare gas, Ne (99.996%) or Ar (99.999%). The total gas pressure was measured with a capacitance manometer. Each component of the sputtering gas was introduced separately into the chamber. Rare gas/O₂ ratios were established using an MKS Baratron Series 260 control system, model 258 flow transducers, and model 248A solenoid control valves.

Two presputters preceded each deposition. The first presputter was carried out in rare gas for ~60 min, and its purpose was to remove the oxide layer that had formed on the target surface upon exposure to air. The second presputter was carried out for ~20 min in the rare gas/O₂ mixture used to deposit the film, and its purpose was to allow time for discharge and target surface reactions to reach dynamic equilibrium. The movable shutter that covered the substrates was then removed and films were deposited.

The nominal sputtering gas composition used in this study ranged from 100% rare gas to rare gas/50% O₂, and the cathode voltage, measured peak-to-peak during a 13.56 MHz rf cycle, ranged from -1.3 to -2.2 kV. The largest cathode voltage used to operate Ne/O₂ discharges was -1.9 kV, in comparison to a maximum voltage of -2.2 kV used to operate Ar/O₂ discharges. The reason is that Ne/O₂ discharges became unstable when excited by a voltage greater than -1.9 kV. Specific combinations of process parameters used to grow the films are recorded in Table I.

B. *In situ* discharge diagnostics

An optical spectrometer with 1200 and 2400 groove/mm holographic gratings capable of 0.5 Å resolution in the near-ultraviolet to near-infrared spectrum was used to sample radiation of wavelength λ emitted between the anode and cathode through an optical window with a cutoff wavelength at 3200 Å. The window was shuttered

when not in use, and furthermore, its transmission characteristics were periodically checked for intensity changes caused by coating with sputtered flux during the experiment.

The optical emission intensity, $I(\lambda)$, of four radiative electronic transitions of the excited neutral Nb atom to ground state, at $\lambda = 4059, 4101, 5079,$ and 5344 \AA ,¹⁶ were monitored. Assuming the condition of an optically thin plasma in local thermal equilibrium, $I(\lambda)$ is proportional to the number of ground state Nb atoms in the discharge.^{17,18} As will be shown in Sec. III F, an estimate of the fractional Nb and Nb-oxide flux incident on the growth interface during deposition can be made using $I(\lambda)$ and growth rate data.⁹ Furthermore, changes in $I(\lambda)$ were used to determine: (1) when each step of the presputter process had been completed, and (2) the set of critical process parameters at which an oxide layer was formed at the target surface.^{4,6,10,14}

C. Post-deposition film characterization

The film thickness was measured with a profilometer from a step produced by masking part of the fused silica substrate during deposition. The growth rate was determined by dividing the value of film thickness by the deposition time. The resistivity was measured with a four-point probe, with an upper limit of $10^{10} \mu\Omega \text{ cm}$.

The crystallography of films grown on fused silica and <111>Si was determined by double-angle x-ray diffraction (XRD) using unresolved CuK α radiation ($\lambda = 1.5418 \text{ \AA}$). XRD peak position ($2\theta \pm 0.02^\circ$), maximum peak intensity (I), and full width at one half maximum intensity (FWHM) were measured. The diffractometer was calibrated using the {01.1} diffraction peak of a quartz standard at $2\theta = 26.66 \pm 0.02^\circ$ whose FWHM is 0.18° .

In addition, one or more of the following measurements were made on selected films. Double-beam spectrophotometry was used to determine the optical transmission, $T(\lambda)$, as a function of incident photon wavelength, λ , of films grown on fused silica. For a transparent film of thickness d , the refractive index, $n(\lambda)$, was determined from the spacing of adjacent maxima, at λ_1 and λ_2 , on $T(\lambda)$ vs λ curves using the expression:¹⁹

$$2d = [(n_1/\lambda_1) - (n_2/\lambda_2)]^{-1} \quad (1)$$

Rutherford backscattering spectrometry was used to measure the Nb:O atomic concentration ($\pm < 10\%$) of films grown on carbon foil using 2-MeV He⁺² ions as the bombarding species. Fourier transform infrared spectrometry was used to determine absorption due to lattice vibrations in films grown on <111>Si. This measurement yielded information about short-range Nb-O atomic order.

III. RESULTS AND DISCUSSION

A. Discharge characteristics

Values of rf forward power and growth rate are recorded in Table I, and shown as a function of gas O₂ content for constant values of cathode voltage in Figs. 1 and 2. $I(\lambda)$ relative to its value in a pure rare gas discharge

TABLE I. Cathode voltage (V_c) and nominal gas composition, used to grow Nb-O films, and the resulting rf forward power in the discharge (P), film thickness (d), and growth rate (G), film resistivity (ρ), and visual appearance.

Film	V_c (-kV)	Rare gas	%O ₂	P (W)	d^a (kÅ)	G (Å/min)	ρ^b (10 $\mu\Omega$ cm)	Appearance ^c
1.	2.2	Ar	0	580	7.2	243 ± 9	2.4 ± 0.1	g,r
2.	2.2	Ar	2	560	9.2	272 ± 3	3.9 ± 0.1	g,r
3.	2.2	Ar	4	570	11.2	249 ± 6	13 ± 1.0	g,r
4.	2.2	Ar	6	560	15.5	200 ± 8	44 ± 1.0	c,t
5.	2.2	Ar	8	570	8.4	133 ± 3	nc	c,t
6.	2.2	Ar	10	580	6.5	108 ± 4	nc	c,t
7.	2.2	Ar	50	640	4.9	82 ± 2	nc	c,t
8.	1.9	Ar	0	430	8.4	200 ± 10	2.0 ± 0.1	g,r
9.	1.9	Ar	2	430	18.7	210 ± 10	6.6 ± 0.2	g,r
10.	1.9	Ar	4	430	14.9	219 ± 7	10 ± 1.0	g,r
11.	1.9	Ar	6	440	5.8	82 ± 4	nc	c,t
12.	1.9	Ar	8	450	6.8	85 ± 2	nc	c,t
13.	1.9	Ar	10	450	5.4	76 ± 1	nc	c,t
14.	1.9	Ar	50	480	5.0	56 ± 5	nc	c,t
15.	1.6	Ar	0	320	3.6	156 ± 6	3.6 ± 0.2	g,r
16.	1.6	Ar	2	350	11.6	143 ± 3	24 ± 1.0	g,r
17.	1.6	Ar	4	370	6.1	70 ± 1	nc	c,t
18.	1.6	Ar	6	380	6.1	70 ± 1	nc	c,t
19.	1.3	Ar	0	230	3.2	106 ± 3	2.0 ± 0.1	g,r
20.	1.3	Ar	2	220	4.7	58 ± 1	nc	c,t
21.	1.3	Ar	4	220	3.9	48 ± 1	nc	c,t
22.	1.9	Ne	0	420	2.0	88 ± 6	5.3 ± 0.5	g,r
23.	1.9	Ne	2	420	1.1	53 ± 7	450 ± 120	g,t
24.	1.9	Ne	4	470	nc	c,t
25.	1.9	Ne	6	480	2.8	40 ± 2	nc	c,t
26.	1.9	Ne	8	500	3.2	40 ± 2	nc	c,t
27.	1.9	Ne	10	500	nc	c,t
28.	1.9	Ne	50	480	2.9	44 ± 3	nc	c,t
29.	1.6	Ne	0	240	1.4	61 ± 6	1.1 ± 0.1	g,r
30.	1.6	Ne	2	270	0.9	41 ± 4	nc	c,t
31.	1.6	Ne	4	280	0.9	32 ± 4	nc	c,t
32.	1.6	Ne	50	350	3.0	33 ± 1	nc	c,t
33.	1.3	Ne	0	170	0.9	48 ± 6	2.0 ± 3	g,r
34.	1.3	Ne	2	180	0.4	25 ± 3	nc	c,t
35.	1.3	Ne	4	180	1.2	19 ± 2	nc	c,t
36.	1.3	Ne	50	220	1.7	21 ± 1	nc	c,t

^aMeasured by profilometer from a step on films grown on fused silica. Each value represents a set of measurements. The standard deviation is not shown in the Table. However, it is used to calculate the error in G tabulated here.

^b ρ for bulk Nb metal = 12.7 $\mu\Omega$ cm; nc = nonconductor, exceeds probe limits of 10¹⁰ $\mu\Omega$ cm.

^cg = gray, c = colorless, r = reflecting, t = transparent.

operated at the same cathode voltage is shown in Fig. 3 as a function gas O₂ content.

It can be seen from Fig. 2 that the growth rate rapidly decreases after a small amount of O₂ is added to the discharge, and then either remains constant or decreases more slowly. This phenomenon is well-documented in the sputter deposition literature, and is associated with the formation of an oxide layer at the target surface that offers a barrier to sputtering greater than that offered by the metal.

It can be seen from Fig. 3 that Rel. $I(\lambda)$ either vanishes or decreases to a small value after a small amount of O₂ is added to the discharge. This result indicates that atomic Nb is either no longer present in the plasma or its amount has been greatly reduced; Nb-oxide is sputtered from the oxidized target surface layer.

The gas O₂ content at which both the growth rate decreases and Rel $I(\lambda)$ vanishes or is greatly reduced is denoted "O₂^{*}". In the case of Ar/O₂ discharges, O₂^{*} increases with increasing V_c , and is equal to 2, 4, 6, and 8%

O₂ for -1.3, -1.6, -1.9, and -2.2 kV discharges, respectively. Similar behavior has been reported for other target materials sputtered in Ar/O₂ discharges,^{4,8,10,14} and is attributed to increased dissociation of the target surface oxide under bombardment by more energetic Ar⁺ ions as V_c is increased. O₂^{*} is equal to 2% in the case of Ne/O₂ discharges operated at -1.3, -1.6, and -1.9 kV.

It can be seen from Fig. 1 that the rf forward power does not change abruptly at O₂^{*}. This result indicates that the electrical impedance of the deposition setup does not change significantly upon target surface oxidation. Similar behavior was found when V (Refs. 10 and 14) and Au (Ref. 20) targets were sputtered in O₂-bearing discharges. It was hypothesized that oxides with secondary electron emission characteristics similar to V or Au metal were formed at the target surface. The Y-O system offers a contrast to this behavior. The formation of a target surface layer of yttria, which is a more efficient secondary electron

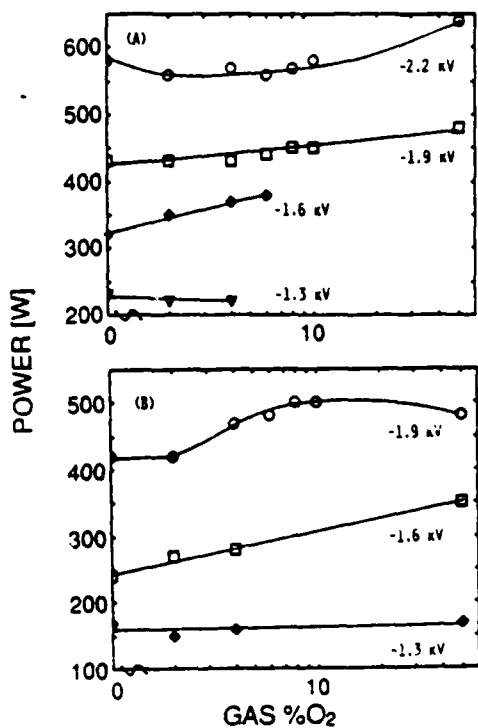


FIG. 1. rf forward power in the discharge as a function of gas O_2 content in (a) Ar/ O_2 and (b) Ne/ O_2 discharges.

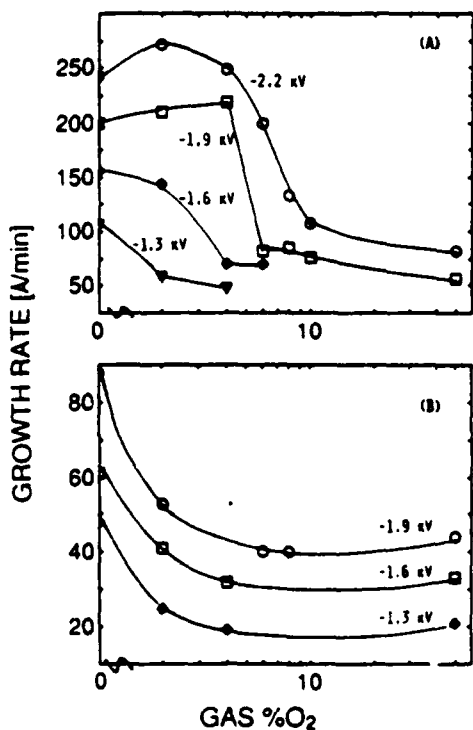


FIG. 2. Film growth rate as a function of gas O_2 content in (a) Ar/ O_2 and (b) Ne/ O_2 discharges.

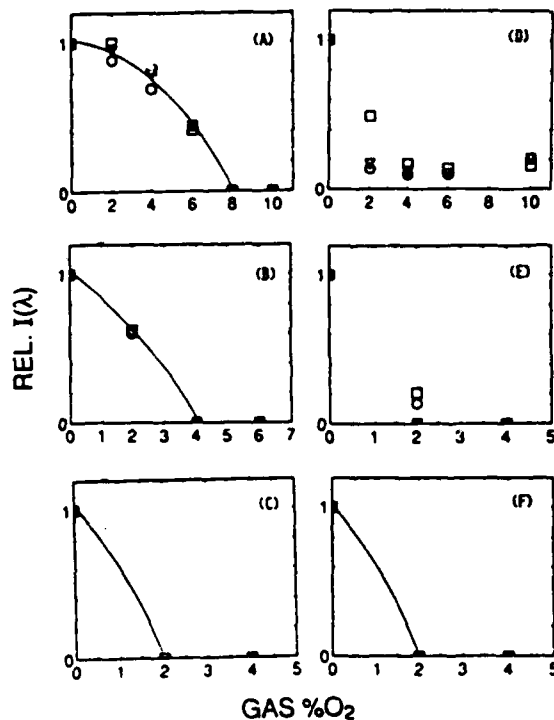


FIG. 3. Relative optical emission intensity from excited Nb atoms in the plasma in (a) -2.2 kV, (b) -1.6 kV, and (c) -1.3 kV Ar/ O_2 discharges, where $\lambda = 5344$ Å (circles), 5079 Å (triangles), and 4059 Å (squares), and (d) -1.9 kV, (e) -1.6 kV, and (f) -1.3 kV Ne/ O_2 discharges, where $\lambda = 5079$ Å (circles), 4101 Å (triangles), and 4059 Å (squares). Each data point represents the average value of at least three measurements.

emitter than yttrium metal, caused the discharge power to double at $O_2^{6,9}$.

B. Film properties

Crystallography: The crystallography of films grown on fused silica, obtained from XRD measurements²¹ is recorded in Table II. Films on $\langle 111 \rangle$ Si using the same growth conditions yielded similar results. Representative diffraction patterns are presented in Figs. 4(a)–4(d), which show how film structure changes as the cathode voltage is decreased [Fig. 4(a)–4(b)–4(c)] or as the gas O_2 content is increased [Fig. 4(a)–4(d)].

Phase transitions of the stable, bulk, room-temperature components of the Nb–O system are as follows:^{22–26} Nb (bcc)–NbO (cubic, NaCl structure)–NbO₂ (tetragonal)–Nb₂O_{5–x} with $0 < x < 0.2$ (many related forms, collectively called “niobia” here). The Nb₂O_{5–x} series, which terminates in Nb₂O₅ and whose precise crystal structure is still under investigation, is based on building blocks of the ReO₃-type lattice separated by planes along which crystallographic shear produces defects; nonstoichiometry is accommodated by crystallographic shear.

Nb, NbO, and NbO₂ phases present in bulk material are also formed in the sputter deposited films. Films 1, 8, and 15, grown in Ar discharges operated at -1.6 to -2.2

TABLE II. Crystallography of Nb-O films sputter deposited on fused silica: the diffraction angle (2θ), full width at one-half maximum intensity (FWHM), peak assignment, and relative intensity.

Film	V_r (-kV)	Rare gas	% O ₂	2θ (deg)	FWHM ^a (deg)	Plane	Rel. I
1.	2.2	Ar	0	38.16 69.31	0.77 1.64	110 Nb 211 Nb	100 10
2.	2.2	Ar	2	38.00 ^b 69.14	0.81 1.44	110 Nb 211 Nb	100 4
3.	2.2	Ar	4	38.14	1.70	110 Nb + 111 NbO	100
4.	2.2	Ar	6	35.98 ^c ~37 41.43	0.84 ... 0.47	501,431 NbO ₂ 111 NbO 620 NbO ₂	24 ... 100
5.	2.2	Ar	8	no diffraction peaks			
6.	2.2	Ar	10	no diffraction peaks			
7.	2.2	Ar	50	~27.33,49 ^d		Nb ₂ O ₅	
8.	1.9	Ar	0	38.36		110 Nb	100
9.	1.9	Ar	2	38.11 ~37.2 ^e 69.32	1.49 ... 1.23	110 Nb + 111 NbO 211 Nb + ?	77 ... 100
10.	1.9	Ar	4	37.2-38.4 67.5-70.5 104-110	111 NbO + 5 NbO ₂ planes ? 420,331 NbO	42 100 30
11.	1.9	Ar	6	no diffraction peaks			
12.	1.9	Ar	8	no diffraction peaks			
13.	1.9	Ar	10	no diffraction peaks			
14.	1.9	Ar	50	no diffraction peaks			
15.	1.6	Ar	0	38.19 69.30	0.76 1.59	110 Nb 211 Nb	100 31
16.	1.6	Ar	2	35.68 ^f ~36.2-40 40.92 0.91	222 NbO ₂ 111 NbO + 4 NbO ₂ planes 620 NbO ₂	100 ... 40
17.	1.6	Ar	4	no diffraction peaks			
18.	1.6	Ar	6	no diffraction peaks			
19.	1.3	Ar	0	37.31 67.51	1.06 1.93	110 Nb + ? 211 Nb + ?	100 59
20.	1.3	Ar	2	no diffraction peaks			
21.	1.3	Ar	4	no diffraction peaks			
22.	1.9	Ne	0	37.83	0.95	110 Nb	100
23.	1.9	Ne	2	no diffraction peaks			
24.	1.9	Ne	4	no diffraction peaks			
25.	1.9	Ne	6	no diffraction peaks			
26.	1.9	Ne	8	no diffraction peaks			
27.	1.9	Ne	10	no diffraction peaks			
28.	1.9	Ne	50	27.37 ~33 49.29	0.40 ... 0.70	Nb ₂ O ₅ Nb ₂ O ₅ Nb ₂ O ₅	100 ... 70
29.	1.6	Ne	0	37.21	1.3	110 Nb + ?	100
30.	1.6	Ne	2	no diffraction peaks			
31.	1.6	Ne	4	no diffraction peaks			
32.	1.6	Ne	50	no diffraction peaks			
33.	1.3	Ne	0	~32-39		110 Nb + ?	
34.	1.3	Ne	2	no diffraction peaks			
35.	1.3	Ne	4	no diffraction peaks			
36.	1.3	Ne	50	no diffraction peaks			

^aFWHM of the (01.1) diffraction peak of a quartz standard at $2\theta = 26.66 \pm 0.02^\circ$ is 0.18° .

^bFigure 4(a).

^cFigure 4(d).

^dThe precise structure of Nb₂O₅ has yet to be determined. Therefore, plane assignment is not possible.

^eAppears as a shoulder on {110} Nb peak. Figure 4(b).

^fA question mark throughout this table indicates a broad peak or shoulder whose assignment is ambiguous; therefore none is made.

^gFigure 4(c).

kV, film 2 grown in a -2.2 kV, Ar discharge [Fig. 4(a)], and film 22, grown in a -1.9 kV, Ne discharge, are bcc Nb with a strong preferred or sole {110} orientation.

Broad peaks and 2θ values shifted to lower angle than expected for {110} bcc Nb planes are observed in the diffraction patterns of film 19, grown in a -1.3 kV, Ar

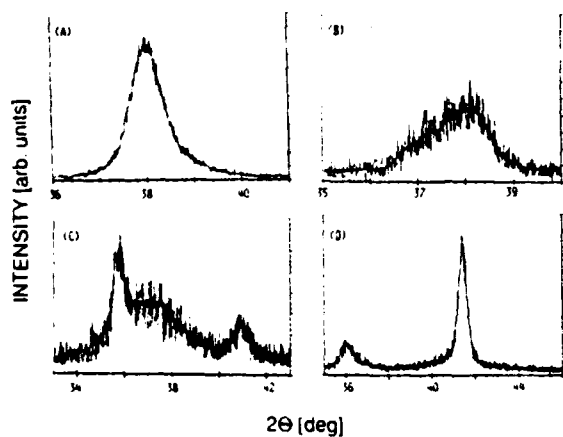


FIG. 4. X-ray diffraction intensity vs 2θ for (a) film 2, Nb, (b) film 9, Nb + NbO, (c) film 16, NbO + NbO₂, and (d) film 4, NbO + NbO₂.

discharge, and films 29 and 33, grown in Ne discharges operated at -1.3 and -1.6 kV, suggesting that another, yet-to-be identified, structure may be present in these films in addition to bcc Nb.

NbO and NbO₂ exist as components of mixed-phase structures formed when using Ar/O₂ discharges (films 3, 4, 9, 10, and 16). Crystalline niobia was formed only when a -1.9 kV, Ne/50% O₂ discharge was used (film 28). Film 7, grown in an -2.2 kV, Ar/50% O₂ discharge, is identified as microcrystalline niobia on the basis of three broad, low intensity peaks. In general, however, films produced in discharges with gas O₂ content $>O_2^*$ have no long-range crystallographic order. We shall refer to these films as "amorphous", but in fact they may contain microcrystallites whose size is beyond the detection limit of the XRD experiment.

Resistivity: The resistivity of films grown on fused silica are recorded in Table I. Relating resistivity to crystallography, Nb metal films have values of electrical resistivity ranging from 11 to 53 $\mu\Omega$ cm. These values are in reasonable agreement with bulk Nb metal, 12.7 $\mu\Omega$ cm, considering the interfacial sources for electron wave scattering within a thin film.

Bulk NbO is a metallic conductor and NbO₂ is a semiconductor with a band gap of 0.88 eV (Refs. 27 and 28). Nb + NbO films 3 and 9 have values of $\rho = 66$ –130 $\mu\Omega$ cm. NbO + NbO₂ films 4, 10, and 16 have values of $\rho = 180$ –440 $\mu\Omega$ cm, an order of magnitude larger than Nb metal films. Microcrystalline niobia film 7 and crystalline film 28 are insulating, as are all of the amorphous films with the exception of film 23 which has a resistivity of $4.5 \times 10^3 \mu\Omega$ cm.

Visual appearance: The visual appearance of films grown on fused silica is recorded in Table I. Nb, Nb + NbO, and NbO + NbO₂ films are reflecting and gray in color. Crystalline and microcrystalline niobia films are transparent and colorless. Films with no long-range crystallographic order are transparent and colorless, with the exception of film 23, which is transparent and gray.

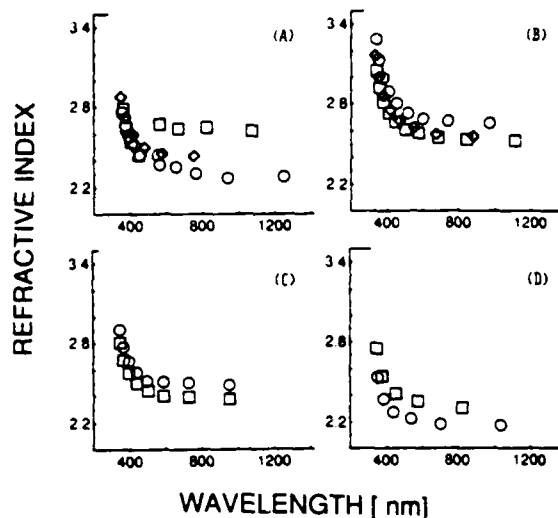


FIG. 5. Refractive index for niobia films grown in Ar/O₂ discharges operated at (a) -2.2 kV and 8% (circles), 10% (squares), and 50% (diamonds) O₂; (b) -1.9 kV and 6% (circles), 8% (squares), 10% (diamonds), and 50% (triangles) O₂; (c) -1.6 kV and 4% (circles), 6% (squares) O₂; and (d) -1.3 kV and 2% (circles) and 4% (squares) O₂.

Identification of transparent amorphous/microcrystalline films: In order to identify the transparent, colorless, insulating amorphous/microcrystalline films, we probed their chemistry, optical refractive index, and short-range order. RBS measurements showed that the Nb:O atomic ratio of films grown on carbon ribbon included in the same sputtering run as films 5–7, 11–14, 17, 18, 20, and 21 ranged from 0.39 to 0.43. These values are in good agreement with stoichiometric niobia, in which Nb:O = 0.38–0.42 after taking into account the $\pm 10\%$ error inherent in the RBS measurement.

The refractive index of films 5–7, 11–14, 17, 18, 20, and 21, determined in the 0.4–1.6 μm spectral region using Eq. (1), is shown in Figs. 5(a)–5(d). [Films grown in Ne/O₂ discharges were too thin to generate a set of interference fringes from which to calculate $n(\lambda)$.] The refractive index was found to equal 2.4–2.7 at 0.5 μm and ~ 2.5 at 1 μm for films grown in Ar/O₂ discharges operated -1.6 , -1.9 , and -2.2 kV. The refractive index is slightly lower for films grown in -1.3 kV, Ar/O₂ discharges, with $n = 2.5$ at 0.5 μm . These values are in excellent agreement with measurements on anodic Nb₂O₅ coatings²⁹ and larger than reported for sputter deposited films, $n = 2.24$ –2.28 at 0.63 μm .³⁰ For all films, the onset of the fundamental optical absorption edge occurred at $\sim 0.35 \mu\text{m}$ (3.5 eV), and $n(\lambda)$ rose rapidly there.

The infrared transmission spectrum from a film grown on Si during the same sputtering run as film 5 is shown in Fig. 6, curve A. (Duplicate films on Si are denoted by a "prime" hereafter in the text). This spectra is representative of all transparent, colorless, amorphous films. The IR transmission spectrum of microcrystalline film 7' is shown in curve B. For comparison, data obtained from crystalline

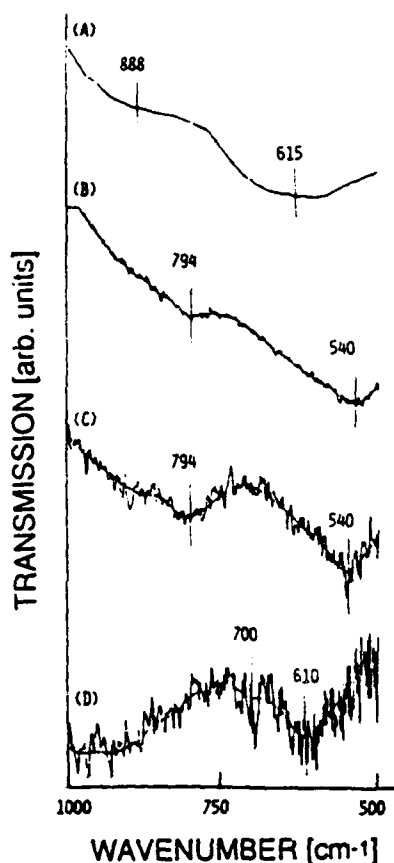


FIG. 6. Infrared transmission as a function of wave number for (A) film 5', amorphous niobia, (B) film 7', microcrystalline niobia, (C) film 28', crystalline niobia, and (D) film 23', amorphous x-niobia.

niobia film 28' is shown in curve C. From Fig. 6, it can be seen that a major double-peaked, IR absorption band occurs between 500 and 900 cm^{-1} for all transparent, colorless, insulating films. The width of the band and its general shape are characteristic of bulk niobia.³¹ There is a difference, however, between the spectra of films that have no long-range order (curve A) compared to that of microcrystalline (curve B) and crystalline (curve C) films; in the former there is a shift in the maxima of both absorption peaks to higher wave number. The correlation between IR absorption and normal modes of vibration of groups of atoms in niobia is as yet unknown. Therefore, the significance of the shift in the maxima, in terms of specific Nb—O bonding configurations cannot be determined at present.

Based on the above RBS, refractive index, and IR transmission measurements, the transparent, colorless, amorphous/microcrystalline, insulating films produced here are identified as niobia. Film 23, grown in a -1.9 kV, Ne/O₂ discharge, is also transparent and amorphous, although it is gray in color and has a finite resistivity, $4.3 \times 10^3 \mu\Omega \text{ cm}$. Its optical transmission spectrum, which is shown Fig. 7, curve A, has a short-wavelength cut-off identical to the transparent, colorless, insulating films, rep-

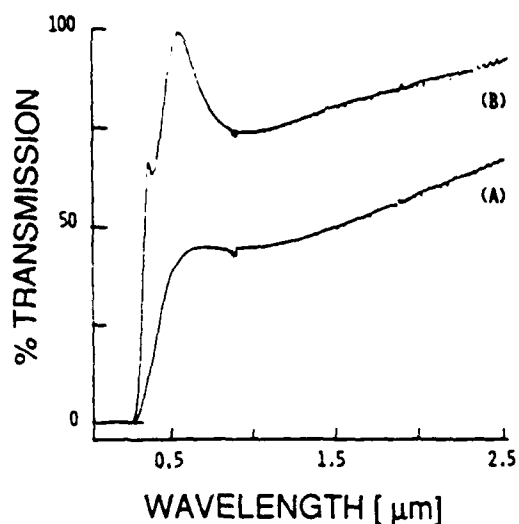


FIG. 7. Percent optical transmission through (a) film 23, 1.1-nm-thick x-niobia, and (b) film 35, 1.2-nm-thick, amorphous niobia.

resented by curve B taken from film 35, which is of comparable thickness to film 23. This result indicates that there is a niobia constituent in film 23. The IR absorption spectrum of film 23 is shown in Fig. 6, curve D. A comparison with curves A–C for amorphous niobia shows both similarities and differences. The low wave number peak, at 610 cm^{-1} is also present in the niobia spectra, at 540 and 615 cm^{-1} . However, this peak has a shoulder at 700 cm^{-1} in film 23. Furthermore, there is still considerable absorption in film 23 at 1000 cm^{-1} . The question to be answered at a later time is this: what bonding structure of Nb and O in film 23, present either as a second phase³² or in a random bonding configuration,³³ causes both optical absorption in the visible spectrum and electrical conductivity? Film 23 is denoted here "x-niobia".

C. A phase map for the sputter deposited Nb-O system

The phases and structures present in the sputter deposited Nb-O films studied here are graphed onto cathode voltage-gas O₂ content space in Fig. 8 for (a) Ar/O₂ and (b) Ne/O₂ discharges. It can be seen that niobia is formed over most of the process parameter space investigated here. When films were grown in Ar/O₂ discharges, the transition from Nb to niobia growth was accomplished through intermediate structures (Nb + NbO and NbO + NbO₂) in which phase mixing³² occurred, as though the system were in thermodynamic equilibrium. Decreasing the cathode voltage shifts the onset of the formation of the intermediate structures, as well as niobia, to lower gas O₂ content. The intermediate structures, Nb + NbO, NbO + NbO₂, are absent from the films when Ne/O₂ discharges are used. Niobia is formed in Ne/O₂ discharge at gas O₂ content $>2\%$, although x-niobia contains an additional yet-to-be-identified component responsible for its electrical conductivity and gray color.

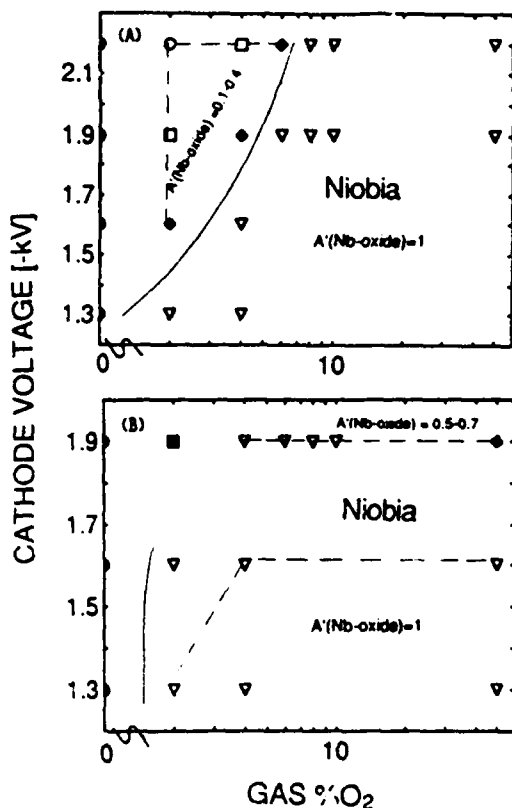


FIG. 8. Phase map for the Nb—O system showing the phases present (bcc Nb (circles), Nb + NbO (squares), NbO + NbO₂ (diamonds), x-niobia (dark square), amorphous and microcrystalline niobia (triangles), and crystalline niobia (diamond)) as a function of gas O₂ content and cathode voltage for (a) Ar/O₂ and (b) Ne/O₂ discharges. The solid lines indicate the boundaries of the niobia phase field. The dashed lines indicate regions of specific values of A'(Nb-oxide), determined from Eq. (7).

Changes in the film structure will next be related to the fractional flux of gaseous Nb and Nb-oxide species incident on the growth interface. We will use the following formalism^{9,34} to estimate this flux, written here for the general case of a metal (*M*) target sputtered in an O₂-bearing discharge. Let *A* = total flux of metal, *M*, in all forms arriving at the substrate relative to its value in a pure rare gas discharge operated at the same cathode voltage. Metal can arrive in atomic form or bonded to O as an oxide molecule, so that the total flux of *M* is equal to

$$A = A(M) + A(M\text{-oxide}). \quad (2)$$

Assuming unity sticking coefficient,

$$A = G'[\rho(M\text{-oxide})/\rho(M)_s], \quad (3)$$

where *G'* is growth rate relative to its value in rare gas and $\rho(M\text{-oxide})_s$ and $\rho(M)_s$ are the bulk atomic densities of the solid phases condensed on the substrate. For an optically thin plasma in local thermal equilibrium

$$I(\lambda) = hc\mathcal{A}_{ki}N_k/4\pi\lambda, \quad (4)$$

where \mathcal{A}_{ki} is the Einstein coefficient of the optical transition, *h* is Planck's constant, *c* is the speed of light in vacuum, and *N_k* is the number of atoms in the upper state.¹⁷ Therefore,

$$\text{Rel. } I(\lambda) = \text{Rel. } N_k = \text{Rel. } N_i = A(M), \quad (5)$$

where Rel. *I*(λ) is the intensity and Rel. *N_k*, Rel. *N_i* are the number of upper state, ground state atoms relative to their values in a pure rare gas discharge operated at the same cathode voltage. Using Eq. (2)

$$A(M\text{-oxide}) = A - A(M) \\ = [G'\rho(M\text{-oxide})/\rho(M)_s] - \text{Rel. } I(\lambda). \quad (6)$$

Dividing Eq. (6) by the total flux of target atom-bearing species to the substrate, yields the fraction of the flux that is *M*-oxide,

$$A'(M\text{-oxide}) = \frac{[G'\rho(M\text{-oxide})/\rho(M)_s] - \text{Rel. } I(\lambda)}{[G'\rho(M\text{-oxide})/\rho(M)_s]} \\ = 1 - \left[\text{Rel. } I(\lambda) / \frac{[G'\rho(M\text{-oxide})_s]}{\rho(M)_s} \right]. \quad (7)$$

The fraction of the flux that is atomic *M*: A'(M) = {Rel. *I*(λ)/[G'ρ(*M*-oxide)_s]}.

A'(Nb-oxide) was determined from Eq. (7) by calculating *G'* from growth-rate data (Fig. 2), and using data for Rel. *I*(λ) (Fig. 3) and the bulk densities for Nb (8.6 g/cm³), NbO (7.3 g/cm³), NbO₂ (5.9 g/cm³), and Nb₂O₅ (4.5 g/cm³). Applying Eq. (7) to mixed-phase films posed a challenge because overlapping XRD peaks prevented the volume fraction of each phase to be meaningfully determined. Therefore, we used the limits of possible density to calculate two separate data points for each set of [G', I(λ)] values for mixed-phase films, that is, using Nb and NbO density for films 3 and 9, and NbO and NbO₂ density for films 4, 10, and 16.

Figure 9 shows A'(Nb-oxide) for the two most complicated sets of data, obtained from Ar/O₂ discharges operated at -2.2 and -1.9 kV. A'(Nb-oxide) = 1 for -1.3 kV, Ar/>2% O₂ discharges, and is not shown here. The range of values for A'(Nb-oxide) for each phase region are included in Fig. 8(a).

It can be seen from Fig. 8(a) that niobia formation in films grown in -1.3 to -2.2 kV, Ar/O₂ discharges is concurrent with A'(Nb-oxide) = 1; niobia is formed in the film when Nb arrives from the plasma bonded to O. The gas O₂ content corresponding to both the onset of niobia formation in the film and a vanishing atomic Nb flux to the substrate is equal to O₂¹, as can be seen by comparing Fig. 8(a) with Figs. 1(a) and 2(a). Intermediate phases are formed when A'(Nb-oxide) = 0.1-0.4, that is, most, but not all, of the Nb flux arriving at the substrate is atomic.

A more complicated situation arises when correlating A'(Nb-oxide) with structure in films grown in Ne/O₂ discharges. A'(Nb-oxide) = 1 for -1.3 kV, Ne/>2% O₂ discharges and niobia formation is associated with a vanishing atomic Nb flux. Likewise, niobia formation in films grown

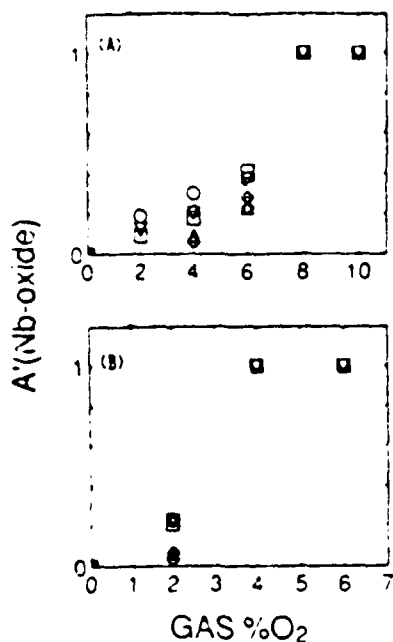


FIG. 4. A' (Nb-oxide), the fractional flux of Nb bonded to O in an unspecified molecular form incident on the substrate, determined from Eq. (7), as a function of gas O_2 content for Ar/ O_2 discharges operated at (a) -2.2 kV and (b) -1.6 kV ($I = 5344$ A) (circles, diamonds), ($I = 5079$ A) (inverted triangles, triangles), ($I = 4059$ A) (squares, slashed diamonds). [Note: The fractional flux of atomic Nb = $1 - A'$ (Nb-oxide).]

in -1.6 kV, Ne/ $4-50\%$ O_2 discharges is associated with A' (Nb-oxide) = 1. However, in the case of -1.9 kV, Ne/ $4-50\%$ O_2 discharges, A' (Nb-oxide) = $\sim 0.5-0.7$, indicating that niobia formed in the film even though the atomic Nb flux to the substrate did not vanish. As mentioned in Sec. IIIA, we concluded from growth rate [Fig. 2(b)] and Rel. $I(\lambda)$ [Fig. 3(d)] data that the target surface was oxidized by -1.9 kV, Ne/ $4-50\%$ O_2 discharges, and so the atomic Nb flux observed here must result from either dissociation of the sputtered oxide at the Nb target surface by sputtering action or in the plasma volume by collisional processes. Values for A' (Nb-oxide) for Ne/ O_2 discharges are included in Fig. 8(b).

The assumption of an optically thin plasma in local thermal equilibrium cannot be applied to data obtained from -1.6 and -1.9 kV, Ne/ 2% O_2 discharges. This is unfortunate because these conditions correspond to O_2 and in the case of a -1.9 kV, Ne/ 2% O_2 discharge, the condition at which α -niobia is produced. However, a difference in Rel. $I(\lambda)$ among the three wavelengths by as much as 40% [Figs. 3(d) and 3(e)] indicates that either selective enhancement of a transition, perhaps by a resonant process,⁹ or selective suppression of $I(\lambda)$ due to impurified radiation¹⁰ is occurring.

IV. SUMMARY

An Nb target was sputtered in rf Ar/ O_2 and Ne/ O_2 discharges, and films were grown on unheated fused silica, (111)-cut Si, and carbon ribbon. The transition from Nb

metal to niobia film growth was studied as a function of three independent process parameters: cathode voltage, gas O_2 content, and rare gas type. On the basis of x-ray diffraction results, resistivity, optical transmission, refractive index, Nb/O ratio, and infrared absorption characteristics, the following phases were identified in the films: bcc Nb, NbO, NbO₂, α -niobia, amorphous niobia, microcrystalline niobia, and crystalline niobia.

In situ optical spectrometry of the discharge was used to monitor the emission intensity $I(\lambda)$ of four radiative electronic transitions of the neutral excited Nb atom to ground state ($\lambda = 5344, 5079, 4101,$ and 4059 Å). Changes in $I(\lambda)$ and the growth rate were used to (1) determine the set of process parameters at which target surface oxidation occurred, and (2) estimate the fractional flux of atomic Nb and Nb bonded to O in an unspecified molecular form (Nb-oxide) incident on the substrate. Film structure was found to depend to some extent upon this fractional flux. In general, niobia was formed when Nb arrived from the plasma bonded to O, which occurred when the target surface was completely oxidized. Intermediate mixed-phase structures, Nb + NbO and NbO + NbO₂, were formed when most but not all, of the Nb flux from the plasma was atomic.

A phase map was constructed in which film structure and the fractional flux of Nb and Nb-oxide incident on the substrate were graphed onto process parameter space, demonstrating the equivalent effect of different sets of process parameters.

ACKNOWLEDGMENTS

The authors thank Dr. E. A. Kolawa and Dr. C.-K. Kwok for carrying out RBS measurements, and Professor M.-A. Nicolet, for making his RBS facility at Caltech available for our use, and for his helpful comments and generous and enduring encouragement. We acknowledge Dr. S. Mukherjee for suggesting the term "phase map" to describe "phase diagrams" for nonequilibrium systems. This work was supported under USARO grant No. DAAL-03-89-K-0022 and by a gift from Johnson Controls, Inc., to the Wisconsin Distinguished Professorship of CRA.

- C. R. Aita and M. E. Marha, *J. Appl. Phys.* **52**, 6536 (1981).
- C. R. Aita and M. E. Marha, *J. Vac. Sci. Technol. A* **1**, 69 (1983).
- C. R. Aita, *J. Vac. Sci. Technol. A* **3**, 625 (1985).
- C. K. Kwok and C. R. Aita, *J. Vac. Sci. Technol. A* **7**, 2215 (1989).
- C. K. Kwok and C. R. Aita, *J. Appl. Phys.* **66**, 2756 (1989).
- C. K. Kwok and C. R. Aita, *J. Vac. Sci. Technol. A* **8**, 1345 (1990).
- C. R. Aita and C. K. Kwok, *J. Am. Ceram. Soc.* **73**, 3294 (1990).
- C. K. Kwok, C. R. Aita, and F. Kusawa, *J. Vac. Sci. Technol. A* **8**, 1350 (1990).
- C. K. Kwok, C. R. Aita, and F. Kusawa, *J. Appl. Phys.* **68**, 2945 (1990).
- S. D. Hamen and C. R. Aita, *J. Vac. Sci. Technol. A* **1**, 661 (1983).
- C. R. Aita, Y. L. Liu, M. L. Kao, and S. D. Hamen, *J. Appl. Phys.* **66**, 749 (1990).
- C. R. Aita and M. L. Kao, *J. Vac. Sci. Technol. A* **5**, 2714 (1987).
- C. R. Aita, C. K. Kwok, and M. L. Kao, *Prog. Mater. Res. Soc.* **82**, 415 (1987).
- C. R. Aita, Y. L. Liu, C. K. Kwok, R. C. Lee, and F. Kusawa, *Thin Solid Films* **193-4**, 1 (1991).

- ¹⁵J. Lulisch and C. R. Aita, *J. Vac. Sci. Technol. A* 9, 542 (1991).
- ¹⁶C. Candler, *Atomic Spectra and the Vector Model* (Van Nostrand, Princeton, NJ, 1964), p. 373.
- ¹⁷H. G. Kuhn, *Atomic Spectra* (Academic, New York, 1963), pp. 79-83.
- ¹⁸J. E. Greene, *J. Vac. Sci. Technol.* 15, 1718 (1978).
- ¹⁹J. C. Manificier, J. Gasot, and J. P. Fillard, *J. Phys. E* 9, 1002 (1975).
- ²⁰A. M. Klumb, C. R. Aita, and N. C. Tran, *J. Vac. Sci. Technol. A* 7, 1697 (1989).
- ²¹ASTM Joint Committee on Powder Diffraction Standards, File Nos. 9-235, 12-104, 15-535, 16-1, 17-717, 1974.
- ²²S. Andersson and A. D. Wadsley, *Nature* 211, 581 (1966).
- ²³A. D. Wadsley and S. Andersson, *Perspect. Struct. Chem.* 3, 1 (1970).
- ²⁴R. Gruehn, *J. Less-Common Met.* 11, 119 (1966).
- ²⁵L. Eyring, in *Nonstoichiometric Oxides*, edited by O. T. Sorensen (Academic, New York, 1981) pp. 366-372.
- ²⁶A. F. Wells, *Structural Inorganic Chemistry* (Clarendon, Oxford, 1950), p. 376.
- ²⁷J. M. Gallego and C. B. Thomas, *Thin Solid Films* 98, 11 (1982).
- ²⁸M. Yousuf, B. Kulyev, and B. Lalevic, *J. Appl. Phys.* 53, 8647 (1982).
- ²⁹G. J. Sayag and A. Sepser, *Thin Solid Films* 55, 191 (1978).
- ³⁰S. Forouhar, R.-X. Lu, W. S. C. Chang, R. L. Davis, and S.-K. Yao, *Appl. Opt.* 22, 3128 (1983).
- ³¹R. A. Nyquist and R. O. Kagel, *Infrared Spectra of Inorganic Compounds* (Academic, New York, 1971), pp. 222-223.
- ³²R. J. Temkin, *J. Non-Cryst. Solids* 17, 215 (1975).
- ³³H. R. Philipp, *J. Non-Cryst. Solids* 8-10, 627 (1972).
- ³⁴The quantity $[p(M\text{-oxide})/p(M)]$ used below was inverted (a typographical error) in a similar formalism, published in Ref. 9 specifically for the Y-O system.

Growth conditions for sputter deposited niobium oxides

R. C. Lee and C. R. Aita⁴¹

Materials Department, University of Wisconsin-Milwaukee, P.O. Box 784, Milwaukee, Wisconsin 53201

(Received 28 October 1991; accepted 16 December 1991)

A Nb target was sputtered in radio-frequency-excited, Kr/O₂ discharges and films were deposited on unheated fused silica and (111)-cut Si substrates. Two independent process parameters, cathode voltage and gas O₂ content, were varied. Optical emission spectrometry was used for *in situ* discharge diagnostics. From this data, we determined: (1) the values of the process parameters at which a complete target surface oxide layer was formed, and (2) the fractional flux of gaseous atomic Nb and molecular Nb-oxide incident on the substrate over the entire range of process parameters. Post-deposition film characterization for metallurgical phase identification included x-ray diffraction, infrared absorption, and electrical resistivity measurements. A "phase map" was constructed, interrelating the independent process parameters, the growth environment, and the metallurgical phases in the films. Comparison with phase maps previously developed for the Nb-O system grown in Ar/O₂ and Ne/O₂ discharges allowed generalizations to be made regarding the growth environment (in terms of Nb, Nb oxide, and oxygen flux to the substrate) under which different Nb-oxide phases were formed in the film.

I. INTRODUCTION

We construct here a "phase map" for the Nb-O system sputter deposited in Kr-O₂ discharges on unheated substrates. The map interrelates independent process parameters, the growth environment, and the metallurgical phases present in the films. It is not a "phase diagram" since growth by sputter deposition cannot be assumed to be under conditions of thermodynamic equilibrium. The process parameters onto which phase regions and growth environment characteristics are mapped are not analogous to the thermodynamic variables used to describe overlayers.¹ The scientific motivation for constructing a phase map is to understand the phase formation sequence in terms of a changing growth environment—a first step toward modeling metal oxide growth by reactive sputter deposition. An important technological outcome is that another investigator, using the information about the equivalence of process parameters shown on the phase map, can make educated decisions when designing an experiment to obtain specific film properties, even when no means of *in situ* discharge diagnostics is available.

Phase transitions of the stable, bulk, room-temperature components of the Nb-O system are as follows:²⁻⁴ Nb (body-centered-cubic—bcc)—NbO (NaCl-type—cubic)—NbO₂ (0.4x±0.01—two stoichiometric forms—tetragonal NbO₂)—Nb₂O₅ (0.4x±0.2 (many related forms, collectively called "niobia")) The Nb₂O₅ series, which terminates in Nb₂O₅, and whose precise crystal structure is still under investigation, is based on building blocks of the ReO₄-type lattice separated by planes along which crystallographic shear produces defects; non-stoichiometry is accommodated by shear.

We had previously published phase maps for Nb-oxides sputter deposited in Ar/O₂ and Ne/O₂ discharges.⁵ As will be discussed in Sec. V both equilibrium and metastable phases formed in the sputter deposited films. The phase boundaries were found to depend upon two important as-

pects of the growth environment: (1) the fractional flux of gaseous Nb atoms and Nb-oxide molecules arriving at the substrate from the discharge, and (2) the formation of a target surface oxide layer that prevented the target from getting all oxygen from the discharge, thereby making oxygen available for reaction at the substrate. The phase map developed here for films grown in Kr/O₂ is compared to those obtained for Ar/O₂ and Ne/O₂ discharges, with an eye toward finding similarities and understanding differences in terms of these two aspects of the growth environment.

II. EXPERIMENTAL PROCEDURE

A. Film growth

Films were grown in a radio-frequency (rf) diode apparatus operated at 13.56 MHz by sputtering a 13 cm diam. Nb target bonded to a water-cooled Cu cathode. Suprasil fused silica and (111)-cut Si substrates were placed on a water-cooled Nb-coated Cu pallet covering the anode. The anode-cathode spacing was 6 cm. The chamber was evacuated to $<5 \times 10^{-7}$ Torr with a liquid N₂ trapped, hot Si-base oil diffusion pump and backfilled with the sputtering gas to a total pressure of 1×10^{-5} Torr. The sputtering gas consisted of Kr (99.997%) containing from 0%–50% O₂ (99.99%).

The total gas pressure was measured with a capacitance manometer. Each component of the sputtering gas was introduced separately into the chamber. Kr/O₂ ratios were established using an MKS Baratron Series 260 control system, model 258 flow transducers, and model 248A solenoid control valves. The instrument error in the O₂ partial pressure introduced into the experiment by the accuracy of the flow was 2.5×10^{-4} Torr.

Two presputters preceded each deposition. The presputter process was monitored by optical emission spectrometry, as described in Sec. II B. The first presputter was car-

TABLE I. Cathode voltage (V_c) and nominal gas O_2 content used to grow Nb-O films, and the resulting rf forward power in the discharge (P), film thickness (d), and growth rate (G), film resistivity (ρ), and visual appearance.

Film	V_c (-kV)	% O_2	P (W)	d (kÅ)	G (Å/min)	ρ^b ($\mu\Omega$ cm)	Appearance ^c
1	1.9	0	480	4.06±0.01	188±3	42±5	g,r
2	1.9	2	480	2.73±0.11	161±6	90±6	g,r
3	1.9	4	480	2.72±0.13	170±8	43±3	g,r
4	1.9	6	480	0.63±0.01	29±1	nc	c,t
5	1.9	8	480	2.02±0.09	25±1	nc	c,t
6	1.9	50	530	4.25±0.15	43±2	nc	c,t
7	1.6	0	330	2.15±0.18	108±9	42±7	g,r
8	1.6	2	360	1.90±0.05	105±3	13±1	g,r
9a	1.6	4	360	1.97±0.08	89±4	15±1	b,st
9b	1.6	4	360	1.30±0.06	57±2	734 ^d	y,st
10	1.6	5	350	0.96±0.25	34±1	nc	c,t
11	1.6	6	330	0.75±0.02	30±1	nc	c,t
12	1.6	8	330	2.42±0.12	25±1	nc	c,t
13	1.6	50	380±10	2.50±0.14	25±1	nc	c,t
14	1.3	0	220	1.50±0.05	77±2	...	g,r
15	1.3	2	230	1.80±0.04	80±2	65±3	g,r
16	1.3	3	230	1.27±0.02	21±1	nc	c,t
17	1.3	4	220	1.20±0.04	19±1	nc	c,t
18	1.3	50	240±10	1.20±0.06	14±1	nc	c,t

^aMeasured by profilometer from a step on films grown on fused silica. Each value represents a set of measurements. The standard deviation is not shown in the table. However, it is used to calculate the error in G tabulated here.

^b ρ for bulk Nb metal = 12.7 $\mu\Omega$ cm; nc = nonconductor, exceeds probe limits of 10^{10} $\mu\Omega$ cm.

^cg = gray, b = blue, y = dark yellow, c = colorless, r = reflecting, st = semitransparent, t = transparent.

ried out in Kr for ~60 min, and its purpose was to remove the oxide layer that had formed on the target surface upon exposure to air. The second presputter was carried out for ~20 min in the Kr/ O_2 mixture used for the actual deposition, and its purpose was to allow time for discharge and target surface reactions to reach dynamic equilibrium. The movable shutter that covered the substrates was then removed and the films were deposited. The process parameters that were varied in this study were the sputtering gas O_2 content and the cathode voltage, measured peak-to-peak during a 13.56 MHz rf cycle. Specific process parameters used for each deposition are recorded in Table I.

B. *In situ* discharge diagnostics

Optical emission spectrometry was used for *in situ* discharge diagnostics.⁹ An optical spectrometer with 1200 and 2400 groove/mm holographic gratings capable of 0.5 Å resolution in the near ultraviolet to near infrared spectrum was used to sample radiation of wavelength λ emitted between the anode and cathode through an optical window.

The optical emission intensity $I(\lambda)$ of radiative electronic transitions of excited neutral Nb atoms to ground state⁹ were monitored at $\lambda = 4059, 4101, \text{ and } 5079$ Å. Assuming the condition of an optically thin plasma in local thermal equilibrium, $I(\lambda)$ is proportional to the number of ground state Nb atoms in the discharge.¹⁰ Changes in $I(\lambda)$ were used to directly determine (1) when each step of the presputter process had been completed, and (2) the set of process parameters at which an oxide layer was formed at the target surface. Furthermore, assuming a unity sticking coefficient, an estimate of the fractional flux of Nb atoms

$f(\text{Nb})$ and Nb-oxide molecules, $f(\text{Nb oxide})$, incident on the substrate during deposition was made using the following equations⁷

$$f(\text{Nb}) = \{ \text{Rel. } I(\lambda) / [G\rho(\text{Nb oxide})/\rho(\text{Nb})_i] \}, \quad (1)$$

$$f(\text{Nb oxide})$$

$$= 1 - \{ \text{Rel. } I(\lambda) / [G\rho(\text{Nb oxide})/\rho(\text{Nb})_i] \}. \quad (2)$$

Here, Rel. $I(\lambda)$ is the emission intensity relative to its value in a pure rare gas discharge operated at the same cathode voltage, G is the growth rate relative to its value in a rare gas discharge operated at the same cathode voltage, $\rho(\text{Nb oxide})$ is the atomic density of the oxide phase condensed on the substrate, and $\rho(\text{Nb})_i$ is the atomic density of Nb metal. The exact form of the gas phase Nb-oxide(s) species incident on the substrate is not known, but mass spectrometry data show that for many oxide systems, the prevalent form is the neutral monoxide, MO.¹¹

C. Post-deposition film characterization

Film thickness was measured with a profilometer from a step made by masking part of the fused silica substrate during deposition. Growth rate was determined by dividing the value of thickness by the deposition time. A four-point probe was used to measure the electrical sheet resistance of films on fused silica, from which resistivity was calculated.

The crystallography of films on fused silica was determined by double-angle x-ray diffraction (XRD) using unresolved Cu $K\alpha$ radiation ($\lambda = 1.5418$ Å). XRD peak position ($2\theta \pm 0.02^\circ$), maximum peak intensity (I), and full width at half-maximum intensity (FWHM) were mea-

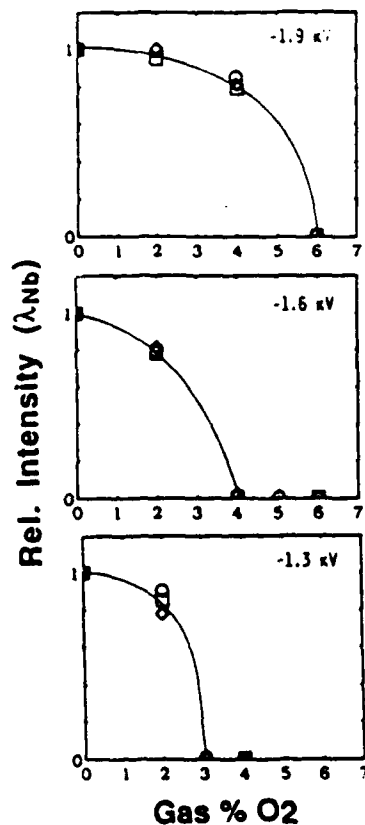


FIG. 1. The relative optical emission intensity from excited Nb atoms in the discharge, where $\lambda = 4059 \text{ \AA}$ (circles), 3079 \AA (diamonds), and 4101 \AA (squares).

sured. The diffractometer was calibrated using the $\{01.1\}$ diffraction peak of an α -quartz standard at $2\Theta = 26.66 \pm 0.02^\circ$ whose FWHM is 0.18° .

Fast-Fourier transform infrared spectrometry was used to determine absorption: due to lattice vibrations in films on infrared (IR)-transparent (111)-Si. This measurement enabled phase identification based on short range order when no long range crystallographic order was present.

III. DISCHARGE CHARACTERISTICS

$I(\lambda)_{\text{Nb}}$ relative to its value in a pure rare gas discharge operated at the same cathode voltage is shown in Fig. 1 as a function gas O_2 content. It can be seen that Rel. $I(\lambda)$ vanishes after a small amount of O_2 has been added to the discharge. This result indicates that atomic Nb is either no longer present in the plasma or its concentration has been reduced to below detection; Nb bonded to O in some form of molecule is being sputtered from the oxidized target surface layer. This molecule is denoted "Nb oxide" here.

The gas O_2 content at which Rel. $I(\lambda)$ vanishes is denoted " O_2^* ". O_2^* is equal to 3% O_2 for discharges operated at -1.3 , 4% for -1.6 kV discharges, and 6% for discharges operated at -1.9 kV discharges. A similar increase in O_2^* with increasing V_c has been reported for both Nb and other target materials sputtered in Ar/ O_2

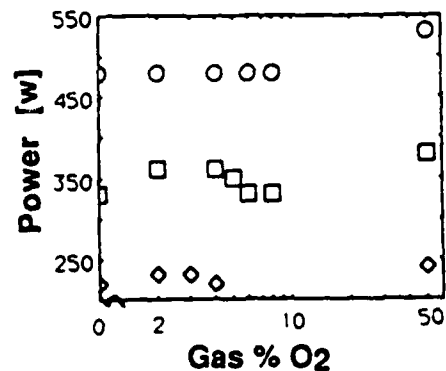


FIG. 2. The rf forward power in the discharge as a function of gas O_2 content in Kr/ O_2 discharges. Diamonds, $V_c = -1.3$ kV; squares, $V_c = -1.6$ kV; circles, $V_c = -1.9$ kV.

discharges.^{7,12-13} This effect is attributed to increased dissociation of the target surface oxide under bombardment by more energetic Ar^+ ions as V_c is increased.

Values of rf forward power and growth rate are recorded in Table I, and shown as a function of gas O_2 content for constant values of cathode voltage in Figs. 2 and 3. It can be seen from Fig. 2 that the rf forward power does not change abruptly at O_2^* . This result indicates that the electrical impedance of the deposition setup does not change significantly upon target surface oxidation. Similar behavior was found when Nb,⁷ V,^{13,14} and Au (Ref. 16) targets were sputtered in Ar/ O_2 and Ne/ O_2 discharges. It was hypothesized that an oxide, or a series of oxides, with secondary electron emission characteristics similar to Nb, V, or Au metal were formed at the target surface. The Y-O system offers a contrast to this behavior. The formation of a target surface layer of yttria, which is a more efficient secondary electron emitter than yttrium metal, caused the discharge power to double at O_2^* .^{12,17}

It can be seen from Fig. 3 that after a small amount of O_2 is added to the discharge, the growth rate decreases to

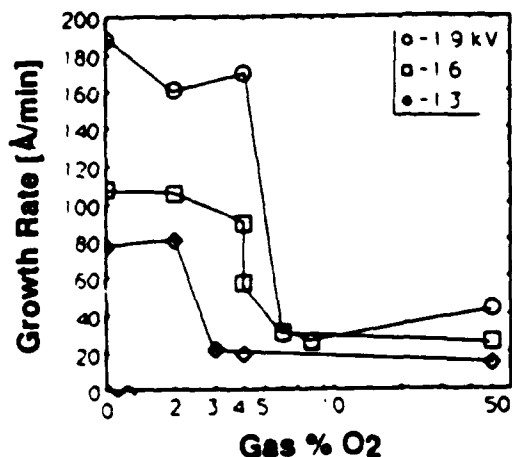


FIG. 3. The film growth rate as a function of gas O_2 content in Kr/ O_2 discharges.

< 30% of its value in a pure Kr discharge operated at the same cathode voltage. This phenomenon is well documented in the sputter deposition literature. In other metal-oxygen systems that we have studied¹²⁻¹⁹ (Y-, Zr-, V-, Al-, Zn-, Ge-, Pt-, Au-O), the formation of a complete target surface oxide layer (at O_2^+ for a given cathode voltage) is a requirement for a large, abrupt decrease in growth rate (if one occurs). However, if the oxide that is formed at the target surface does not offer a barrier to sputtering greater than that offered by the metal, the growth rate will not drop, as is the case of initial target oxidation in the form of ZrO in the Zr-O system¹⁵ and GeO in the Ge-O system.¹⁹

In the case of Nb-O films deposited in Ar/O₂ and Ne/O₂ discharges over a range of V_c from -1.3 to -2.2 kV, we previously reported that O_2^+ and a large growth rate drop were coincident.⁷ The data for Kr/O₂ discharges operated at -1.9 and -1.3 kV presented above also show this coincidence. However, in the case of Kr/O₂, -1.6 kV discharges, O_2^+ occurs at 4% O₂, before the drop in deposition rate has stabilized at 5% O₂. This result will be discussed further in Sec. IV in relation to the properties of films grown in Kr/4% O₂, -1.6 kV discharges.

IV. FILM PROPERTIES

A. Crystallography

The crystallography of films grown on fused silica is discussed next. Films on (111)-Si using the same growth conditions yielded similar results. Films grown in pure Kr discharges are bcc Nb. Film 14, grown at -1.3 kV has a completely {110} orientation, with diffraction at $2\Theta = 27.93^\circ$, corresponding to $d_{110} = 2.37 \text{ \AA}$.²⁰ Films 1 and 7, grown at -1.9 and 1.6 kV have a strong preferred {110} orientation, with $2\Theta = 38.19^\circ$, corresponding to $d_{110} = 2.35 \text{ \AA}$. Additional diffraction from Nb {211} planes occurs in films 1 and 7, at $2\Theta = 69.23^\circ$ corresponding to $d_{211} = 1.36 \text{ \AA}$, and from Nb {222} planes in film 1, at $2\Theta = 107.23^\circ$, corresponding to $d_{222} = 0.96 \text{ \AA}$. Calculation of the lattice parameter using $a = d_{hkl} (h^2 + k^2 + l^2)^{1/2}$ yields $a = 3.35 \text{ \AA}$ for film 14 and $a = 3.32 \text{ \AA}$ using all sets of {hkl} for films 1 and 7. These values are in good agreement (within 0.7% for films 1 and 7, and 1.6% for film 14) with $a = 3.30 \text{ \AA}$ for bulk, unstressed Nb.

Films 2, 3, 8, and 15 grown in Kr-O₂ discharges show multiple, overlapping, broad, low intensity diffraction peaks in two 2Θ ranges: from $\sim 35^\circ$ to 39° and from $\sim 65^\circ$ to 75° . It is possible to attribute these unresolvable peaks to diffraction from Nb, NbO, and/or NbO₂ planes, indicating a structural confusion within the films. These films will be referred to here as "Nb suboxide."

Films 4-6, 9a, 9b, 10-13, and 16-18 have no long range crystallographic order detectable by XRD. These films are called "amorphous," but in fact they may contain nanocrystallites whose size is below the coherence limit of the XRD experiment.

B. Resistivity

The resistivity of films grown on fused silica is recorded in Table I. Relating resistivity to crystallography, Nb metal films 1, 7, and 14 have resistivity ~ 3 times larger than bulk Nb metal, $12.7 \mu\Omega \text{ cm}$, which is not surprising considering the interfacial sources for electron wave scattering within a thin film. Nb-suboxide films 2, 3, and 15, have resistivity ranging from 43 to $90 \mu\Omega \text{ cm}$, comparable to that previously reported for mixed Nb + NbO films grown in Ar/O₂ discharges.⁷ However, Nb-suboxide film 8 has a low resistivity, $13 \mu\Omega \text{ cm}$, compared to the other Nb-suboxide films. NbO is a metallic oxide, and although we could not find a bulk resistivity value for this material in the literature, its presence in an appreciable amount is possibly responsible for the low resistivity of film 8.

Amorphous film 9a also has a low resistivity, $15 \mu\Omega \text{ cm}$. However, amorphous film 9b, grown under the same conditions as film 9a, has much higher resistivity, $7340 \mu\Omega \text{ cm}$. As mentioned in Sec. II A, the instrumental uncertainty in gas O₂ content is $\pm 0.25 \mu\text{m}$. Apparently, this set of discharge conditions, a cathode voltage of -1.6 kV and a sputtering gas composition of 60 mTorr Kr/40 ± 0.25 mTorr O₂, sits directly atop a narrow transition region between conductor and insulator growth, such that a small change in O₂ content (introduced by experimental uncertainty cited in Sec. II A) produces a large change in film properties. Amorphous films 4-6, 10-13, and 16-18 are insulators.

C. Visual appearance

Table I records the visual appearance in normal incidence light of films grown on fused silica. All Nb and Nb-suboxide films are reflecting and gray in color, with the exception of film 9a, which is semitransparent and blue, and film 9b, which is semitransparent and dark yellow. Insulating films with no long range crystallographic order are transparent and colorless.

D. Infrared transmission

Infrared transmission spectra were obtained from films on (111)-Si substrates included in the same sputtering runs as fused silica. These films are labeled with a "prime." Nb films 1', 7', and 14' and Nb-suboxide films 2', 3', and 8' do not transmit IR radiation. Insulating, transparent, colorless films 4'-6', 10'-13', and 16'-18' have IR spectra identical to that previously reported for amorphous (α -) niobia⁷ and these films are identified as such. A typical spectrum, taken from film 12' in the $400\text{-}1300 \text{ cm}^{-1}$ range ($25.0\text{-}7.7 \mu\text{m}$) is shown in Fig. 4(a). This spectrum consists of a broad absorption band with local minima at 600, 900, and 1080 cm^{-1} , and $> 90\%$ transmission at 1200 cm^{-1} .

Amorphous high resistivity film 9b yields the absorption spectrum shown in Fig. 4(b). The common features of film 9b and α -niobia are local minima at 900, and 1080 cm^{-1} , $> 90\%$ transmission at 1200 cm^{-1} , and low transmission at 600 cm^{-1} . However, at low frequency, between 400 and 600 cm^{-1} , film 9b does not recover transmission and the

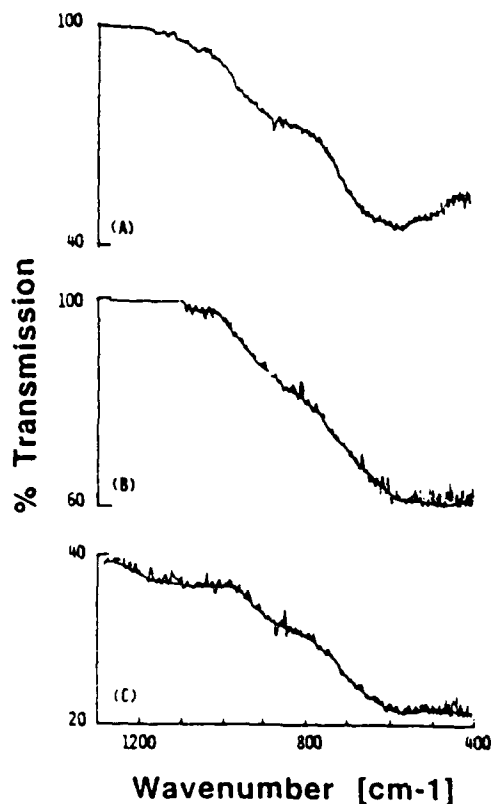


FIG. 4. The infrared transmission as a function of wave number for (a) film 12, α -niobia, (b) film 9b, high resistivity x -niobia, and (c) film 9a, low resistivity x -niobia.

absorption remains high. The spectrum of amorphous low resistivity film 9a [Fig. 4(c)] shows similar characteristics to that of film 9b, although the overall level of absorption is greater (due to free-carrier absorption) and the high frequency absorption peak at 1080 cm^{-1} in film 9b is shifted and considerably broadened in film 9a, extending from 1000 to 1270 cm^{-1} . We previously observed similar absorption behavior in a film, denoted " x -niobia," that was deposited using a Ne-O_2 discharge and a set of process parameters which were at the boundary between Nb-suboxide and α -niobia growth.⁷ Films 9a and 9b will hereafter also be called x -niobia.

V. A PHASE MAP FOR Nb-OXIDES SPUTTER DEPOSITED IN Kr/O_2 DISCHARGES

Based on the film characterization data presented in Sec. IV, metallurgical phases in the films were identified as Nb, Nb suboxide, x -niobia, and α -niobia. To construct a phase map, first metallurgical phase regions were graphed onto process parameter space. The process parameter-metallurgical phase diagram was then overlaid with the growth environment parameters of interest here: (1) the value of the fractional atomic Nb or molecular Nb-oxide flux to the substrate determined from Eqs. (1) and (2), keeping in mind that $f(\text{Nb}) + f(\text{Nb oxide}) = 1$, and (2) the process parameters at which formation of a complete

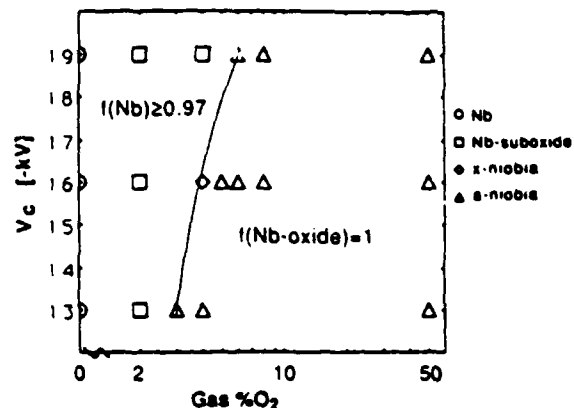


FIG. 5. A phase map for the Nb-O system sputter deposited in Kr/O_2 discharges showing the phases present as a function of gas O_2 content and cathode voltage. $f(\text{Nb})$ and $f(\text{Nb oxide})$ were calculated from Eqs. (1) and (2). The solid line indicates O_2^* , the gas O_2 content for a given V_c at which atomic Nb can no longer be detected in the discharge.

target surface oxide layer occurred. The phase map for Nb oxides sputter deposited in Kr/O_2 discharges is shown in Fig. 5.

Determination of the fractional flux of sputtered target species using Eqs. (1) and (2) depends upon two experimentally measured quantities $\text{Rel. } I(\lambda)$ shown in Fig. 1, and the growth rate G shown in Fig. 3, from which G' , the relative growth rate, is obtained. The film density relative to Nb is also a factor in Eqs. (1) and (2). We used bulk densities for this calculation. The bulk densities for Nb and the Nb oxides are as follows: Nb (8.6 g/cm^3), NbO (7.3 g/cm^3), NbO_2 (5.9 g/cm^3), and Nb_2O_5 (4.5 g/cm^3). Choosing a value for the density of the Nb-suboxide films posed a challenge because overlapping XRD peaks prevented the volume fraction of each phase to be meaningfully determined, as discussed in Sec. IV A. We therefore used an average value of the densities of all possible components in the suboxides, $[\rho_{\text{Nb}} + \rho_{\text{NbO}} + \rho_{\text{NbO}_2}]/3 = 7.25\text{ g/cm}^3$. This averaging introduces a maximum error of 19% into the calculation for relative density, that is, if the film under consideration is either pure Nb or NbO_2 .

VI. GROWTH CONDITIONS FOR Nb OXIDES

Optical spectrometry data (Fig. 1) showed that at a critical value of gas O_2 content, O_2^* , for a given target voltage, the emission intensity from Nb atoms in the discharge disappeared. In fact, for most of the process parameter space probed here, Nb was delivered to the substrate, not in atomic form, but bonded to O in some type of molecule. The change in the nature of the arriving flux of target-bearing species from atomic Nb to molecular Nb oxide had a profound effect on the type of phase formed in the film. The following general observations relating the phase formation sequence to this changing flux and the state of target oxidation were made by considering the phase map shown in Fig. 5.

(1) α -niobia was formed when the fractional flux of molecular Nb oxide to the substrate was large (here unity)

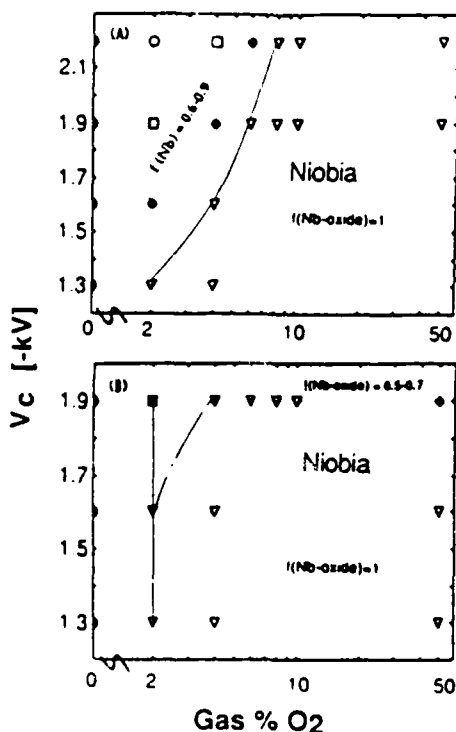


FIG. 6. A phase map for the Nb-O system showing the phases present [bcc Nb (circles), Nb + NbO (squares), NbO + NbO₂ (diamonds), x-niobia (dark square), amorphous and microcrystalline niobia (triangles), and crystalline niobia (dark diamond)] as a function of gas O₂ content and cathode voltage for (a) Ar/O₂ and (b) Ne/O₂ discharges. $f(\text{Nb})$ and $f(\text{Nb oxide})$ were calculated from Eqs. (1) and (2). The solid line indicates O₂ the gas O₂ content for a given V_c at which atomic Nb can no longer be detected in the discharge or its level has been greatly reduced.

and the target surface was oxidized, thereby unable to get-
ter all oxygen from the discharge and making it available
for reaction at the substrate.

(2) Nb suboxides were formed when the fractional flux
of atomic Nb to the substrate was large and the target
surface was not fully oxidized, thereby able to get-
ter oxygen from the discharge and making it unavailable for re-
action at the substrate.

(3) An amorphous, semitransparent transition phase,
x-niobia, was sometimes formed at the boundary of the
Nb-suboxide/niobia phase regions, under conditions of a
large Nb-oxide fractional flux and an oxidized target sur-
face, evidenced by the disappearance of Nb optical emis-
sion (Fig. 1). However, analogous to the Zr-O system
mentioned in Sec. III,¹⁵ the nature of the initial oxide (in
the limit of small gas O₂ content for a given value of V_c)
was possibly different than that formed at greater gas O₂
content. As in the case of ZrO, this initial target surface Nb
oxide (for example, NbO) may get-ter oxygen from the
discharge. The result will be a deficit in the amount of
oxygen required to complete oxidation at the substrate to
form α -niobia.

Phase maps for Nb oxides deposited using Ar/O₂ and
Ne/O₂ discharges are shown in Fig. 6, taken from Ref. 7.
As in the present study, the regime used to obtain these

phase maps was growth on a near-room temperature sub-
strate, low surface diffusion, and unity sticking coefficient.
A comparison of Figs. 5 and 6 reinforces the three gener-
alizations made above describing the growth conditions
under which Nb oxides were formed. The fact that the Nb-
suboxide phase field was absent when Ne was used as the
rare gas component of the discharge is consistent with the
absence of a growth environment in which there is a large
atomic Nb fractional flux to the substrate and an unoxi-
dized (or partially oxidized) target surface.

A comparison of the phase maps for Ar/O₂ and Kr/O₂
discharges shows an interesting difference in structure
within the Nb-suboxide phase field. Nb-suboxides grown in
Ar/O₂ were biphasic Nb + NbO or NbO + NbO₂, the type
of growth expected under conditions of thermodynamic
equilibrium. However, phase separation on a scale resolv-
able by XRD was absent in Nb-suboxide films grown in
Kr/O₂ discharges. Although the reason for this difference
is as yet unknown, possible contributing factors are as fol-
lows. Within the Nb-suboxide phase region, the atomic Nb
fractional flux is larger when Kr, rather than Ar, is used.
To form a well-ordered suboxide (NbO or NbO₂), these
free Nb atoms must react with oxygen before their surface
mobility is quenched by the subsequent arriving flux. There
is always an overpressure of neutral rare gas atoms on the
substrate, characteristic of the sputter deposition environ-
ment. Kr, with an atomic diameter of 2.06 Å, compared to
Ar, with an atomic diameter of 1.76 Å, may be more ef-
fective in blocking the diffusion of a Nb or oxygen species
along the substrate. In other words, more Nb atoms must
react at the substrate and more severe limitations on their
surface mobility may make it more difficult for these atoms
to find a reaction partner when Kr, rather than Ar, is used.
The deposition rate in Kr/O₂ and Ar/O₂ was approxi-
mately the same for a given set of process parameters,
hence the rate of arriving flux capable of quenching a re-
action, was not a factor.

ACKNOWLEDGMENTS

This work was supported under USARO Grant No.
DAAL-O3-89-K-0022 and by a gift from Johnson Con-
trols, Inc., to the Wisconsin Distinguished Professorship of
C.P.A.

¹¹ Author to whom all correspondence should be addressed.
¹² See, for example: M. G. Lagally, Y.-W. Mo, R. Karnots, B. S. Swartz-
entruber, and M. B. Webb, in *Kinetics of Ordering and Growth at*
Surfaces, edited by M. G. Lagally (Plenum, New York, 1990), pp.
145-150.
¹³ S. Anderson and A. D. Wadsley, *Nature* 211, 581 (1966).
¹⁴ A. D. Wadsley and S. Anderson, *Perspect. Struct. Chem.* 3, 1 (1970).
¹⁵ R. Gruehn, *J. Less-Common Met.* 11, 119 (1966).
¹⁶ L. Eyring, in *Nonstoichiometric Oxides*, edited by O. T. Sorenson (Ac-
ademic, New York, 1981), pp. 366-372.
¹⁷ A. F. Wells, *Structural Inorganic Chemistry* (Clarendon, Oxford,
1950), p. 376.
¹⁸ R. C. Lee and C. R. Aita, *J. Appl. Phys.* 70, 2094 (1991).
¹⁹ J. E. Greene, *J. Vac. Sci. Technol.* 15, 1718 (1978).
²⁰ C. Candler, *Atomic Spectra and the Vector Model* (Van Nostrand,
Princeton, 1964), p. 373.
²¹ H. G. Kuhn, *Atomic Spectra* (Academic, New York, 1963), pp. 79-83.
²² C. R. Aita, *J. Vac. Sci. Technol. A* 3, 625 (1985)

- ¹²C.-K. Kwok, C. R. Aita, and E. Kolawa, *J. Vac. Sci. Technol. A* 8, 1330 (1990).
- ¹³S. D. Hansen and C. R. Aita, *J. Vac. Sci. Technol. A* 3, 660 (1985).
- ¹⁴C. R. Aita, L.-J. Liou, C.-K. Kwok, R. C. Lee, and E. Kolawa, *Thin Solid Films* 193-4, 18 (1991).
- ¹⁵C.-K. Kwok and C. R. Aita, *J. Vac. Sci. Technol. A* 7, 1235 (1989).
- ¹⁶A. M. Klumb, C. R. Aita, and N. C. Tran, *J. Vac. Sci. Technol. A* 7, 1697.
- ¹⁷C.-K. Kwok, C. R. Aita, and E. Kolawa, *J. Appl. Phys.* 68, 2945 (1990).
- ¹⁸N. Abuhadba and C. R. Aita, *J. Non-Cryst. Solids* 122, 305 (1990).
- ¹⁹C. R. Aita and N. C. Tran, *J. Appl. Phys.* 56, 958 (1984).
- ²⁰For all XRD peak assignments in the following text are from American Society for Testing and Materials (ASTM) Joint Committee on Powder Diffraction Standards, File Nos. 9-235, 12-104, 15-335, 16-1, 17-717 (1974).

APPENDIX V

"The relationship of phase formation in sputter deposited metal-oxygen systems to metal, metal-oxygen, and oxygen flux." C.R. Aita, J. Vac. Sci. Technol. A, 11 1540-7 (1993). INVITED

Phase formation in sputter deposited metal (V, Nb, Zr, Y) oxides: Relationship to metal, metal-oxygen, and oxygen flux

Carolyn Rubin Aita

Materials Department and Laboratory for Surface Studies, University of Wisconsin-Milwaukee, P.O. Box 784, Milwaukee, Wisconsin 53201

(Received 20 November 1992; accepted 12 April 1993)

It is well documented that an oxide is formed on the surface of a metal target sputtered in an O_2 -bearing discharge. The sputtered flux will, in general, consist of metal atoms (M) and metal-oxygen molecules ($M-O$). In this study, a series of metal ($M = V, Nb, Y, Zr$) targets were sputtered in rare gas- O_2 discharges. Films were grown on substrates at low temperatures (70–325 °C). Optical emission spectrometry was used to index the growth environment in terms of (a) the fractional flux of M and $M-O$ species to the growth interface, and (b) the availability of oxygen for reaction at the growth interface. The interrelation of process parameters, phase formation, and the growth environment indices was presented in the form of phase maps. Common features in the phase maps of all systems were identified.

I. INTRODUCTION

Reactive sputter deposition, widely used for growing metal oxide films, involves nonequilibrium growth at a solid surface in contact with a low pressure glow discharge. The growth environment is complex, does not easily lend itself to even rudimentary *in situ* discharge diagnostics, and has not been a topic of active study. Historically, research was geared to developing process parameter-film property relations with an eye towards making a film with desired behavior. However, even the most detailed parametric study is phenomenological and machine-specific unless it contains growth environment information. The present paper reviews a program that interrelates deposition process parameters, phase formation in the film, and several important features of the growth environment for a series of metal-oxygen systems.

The experiment was carried out in a radio frequency diode apparatus, the simplest possible configuration for reactive sputter deposition. The discharge contained a rare gas + O_2 . The targets were vanadium, niobium, zirconium, and yttrium. These metals form a sequence down column VB of the periodic table and across the second long period. As a group, they have a broad range of oxidation and bulk phase formation behavior. The independent process parameters that were varied were nominal sputtering gas O_2 content, rare gas type (R), and cathode voltage (V_c). Discharge power, growth interface temperature, and growth rate are dependent upon all of these parameters.

A metal target surface sputtered in a rare gas contains a small nominal amount of O_2 getters oxygen (all types) from the discharge. As the nominal gas O_2 content is increased, an oxide forms on the target surface, gettering reaches a steady state, and excess oxygen appears in the discharge available for reaction at the growth interface. The sputtered flux from an oxidized target surface in general consists of metal atoms, M , and metal bonded to oxygen in molecular form(s), collectively denoted $M-O$.¹ Earlier studies suggested that the fraction of total flux sputtered as molecules was proportional to the $M-O$ bond

strength.²⁻⁴ However, recent data show that even molecules with a positive free energy of formation, such as AuO and AuO_2 , are sputtered intact.⁵

In light of the above, we asked the following questions about the growth environment for the metal-oxygen systems studied here: (1) what is the fractional gaseous flux of M and $M-O$, denoted f^M and f^{M-O} , where $f^M + f^{M-O} = 1$, as a function of process parameters; (2) for what process parameter sets, denoted $Q(O_2, R, V_c)$, does excess oxygen initially appear in the discharge, available for reaction at the growth interface? f^M and $Q(O_2, R, V_c)$ were used to index the growth environment. A phase map was developed for each metal-oxygen system, combining these indices with the relevant process parameter-metallurgical phase relations. Common features in the phase maps of all systems were identified.

We know that the growth environment indices chosen here give an incomplete picture. There are other factors, including indigenous "activated" oxygen species carrying internal and/or kinetic energy whose bombardment of the growth interface potentially has a strong influence on phase formation. However, we feel that these species are more likely to influence long range structural order, especially in the high valence oxides, rather than controlling stoichiometry. Thermodynamics drives each of these metal-oxygen systems towards forming the high valency oxide, using whatever form of oxygen is available.

II. EXPERIMENT

A. Film growth and characterization

Films were grown in an rf diode apparatus operated at 13.56 MHz by sputtering a 13-cm diam. metal ($M = Nb, V, Y, Zr$) target bonded to a water-cooled ($\sim 15^\circ C$) Cu cathode. Suprasil fused silica, (111)-cut Si, and carbon foil substrates were used, each required for a specific post-deposition analytical technique. The target-substrate spacing was 6 cm, the base pressure was $< 5 \times 10^{-7}$ torr, and the working gas pressure was 1×10^{-2} torr.

In this experiment, the sputtering gas O_2 content was varied over a range that included a metal to high valency oxide growth sequence in the films. The rare gas (Ar or Ne) ion, not O_2^+ , was the majority sputterer throughout this range. Several values of cathode voltage, measured peak to peak during a 13.56 MHz rf cycle, were investigated for each gas composition. Changing these process parameters has an anticipated influence on the growth environment indices. A higher V_c and more massive R cause a greater extent of target surface oxide dissociation upon sputtering,^{6,7} resulting in a larger f^M and a shift of $Q(O_2, R, V_c)$ to higher gas O_2 content. In addition, R atoms in low-lying metastable energy states (R^m) engage in plasma volume reactions with ground state O_2 . Two plasma volume reactions, Penning ionization,⁸ and dissociative transfer of excitation⁹ produce oxygen that is more reactive with metal or suboxide at both electrodes when Ne, rather than Ar, is used,¹⁰ with the effect of decreasing f^M and shifting $Q(O_2, R, V_c)$ to lower gas O_2 content.

The rf forward power as a function of gas composition and V_c for the metal-oxygen systems studied here is reported in Refs. 11–15. Contact with the plasma heated the growth interface, with most of the temperature rise occurring within the first 5 min of exposure. In a separate experiment, films were deposited on Si for 30 min and the discharge was extinguished. A movable thermocouple was then immediately placed in contact with the film surface, the rate of temperature decay was measured, and the temperature at the time of discharge extinction was estimated.¹⁶ For our setup, temperature (T) in degrees kelvin (K) was found to be strongly dependent upon rf forward power (P) in watts (W) according to the empirical relationship $P = (3.5 \times 10^{-9} \text{ W/K}) T^4 + 50 \text{ W}$. The working temperature ranged from 73 °C for a 100-W discharge to 375 °C for a 670-W discharge.

Specific details of post-deposition film analysis are referenced in Secs. III–VI. In summary, thickness was measured with a profilometer. Films were from 1 to 10 kÅ thick, with high valency oxides in the 1–5-kÅ range. The growth rate was determined by dividing thickness by growth time. The crystallography of films on silicon and silica was determined using double-angle x-ray diffraction. Rutherford backscattering spectrometry was used to obtain the M:O atomic concentration ($\pm 10\%$) of films on carbon ribbon. Fast Fourier transform infrared spectrometry was used to measure optical absorption due to lattice vibrations in films on silicon, giving information about metal-oxygen short range order. Resistivity $< 10^{10} \mu\Omega \text{ cm}$ was determined from four-point probe measurements of films on silica. Near ultraviolet-visible-near infrared optical transmission and reflection were measured by double-beam spectrophotometry for films on silica, from which the optical absorption coefficient was calculated.

B. *In situ* discharge diagnostics

Optical emission spectrometry was used for *in situ* discharge diagnostics.¹⁷ A spectrometer with 1200 and 2400 groove/mm holographic gratings capable of 0.5 Å resolu-

tion was used to detect radiation of wavelength λ emitted from the plasma volume through an optical window with a transmission cutoff at 3200 Å.

Emission data from excited M, O, and O_2^+ species only were used to develop the formalisms in Secs. II B 2 and II C relating to phase mapping. However, VO, ZrO, and YO bands were also observed but their intensities were difficult to quantify due to the mixed-gas nature of the plasma.

1. Emission from metal atoms

The intensity of radiative electronic transitions of excited neutral metal atoms to the ground state was monitored at $\lambda = 4112, 4379, 6150, \text{Å}$ for V; 4059, 4101, 5079, 5344 Å for Nb; 3520, 3548, 3601 Å for Zr; and 3621, 4128, 4143, 4236, 6191, 6793 Å for Y.¹⁸

The intensity detected at λ due to a transition from upper state j to lower state i is¹⁹ $I_{ij} = [(hc/4\pi\lambda)A_{ji}n_jg(\lambda)]$, where A_{ji} is the Einstein coefficient for spontaneous emission, n_j is the upper level population density, h is Planck's constant, c is the speed of light in vacuum, and $g(\lambda)$ is the detected fraction of emitted radiation. $n_j = P_{ij}n_i$, where n_i is the lower level density and P_{ij} is the probability of exciting an atom to the upper level. $P_{ij} = \int n_e(v)\sigma(v)dv$, where $n_e(v)$ is the free electron density in the plasma, and $\sigma(v)$ is the scattering cross section for excitation of an atom from i to j by impact with a free electron with velocity v . In terms of the ground state population density, $I_{ij} \propto n_i P_{ij} g(\lambda)/\lambda$.

With respect to metal atom emission intensity, I_{ij}^M , in an optically thin plasma in local thermal equilibrium,²⁰ $g(\lambda)$ is independent of V_c and gas composition. n_i^M , the ground-state metal atom density, is derived from the sputter yield, and therefore varies with V_c and gas composition. P_{ij} is also a function of V_c and gas composition, since these parameters potentially affect $n_e(v)$ and $\sigma(v)$. However, the gas composition range of primary interest here coincides with a large change in I_{ij}^M occurring over a small range of O_2 content. P_{ij} is therefore considered to be a function of R and V_c only. Therefore:

$$I_{ij}^M|_{R, V_c} \propto n_i^M|_{R, V_c} \quad (1)$$

That is, for a given rare gas type and fixed cathode voltage but varying gas O_2 content, the detected emission intensity due to excited metal atoms returning to the ground state is proportional to the density of ground state metal atoms in the discharge.

Using Eq. (1), the relative intensity (I_{ij}^M in an R:O₂ discharge operated at V_c relative to its value in a pure R discharge operated at the same V_c) is $I' = n_i^M|_{R, O_2} / n_i^M|_{R, O_2}$. The detection limit of n_i^M using our experimental setup, obtained from the rms noise limit on the I_{ij}^M signal, is $\sim 10^8$ atoms/cm³. This limit corresponds to a partial pressure of $\sim 10^{-6}$ torr, six orders of magnitude lower than the working gas pressure

2. Fractional flux of M and M-O to the growth interface

Unity sticking coefficient of the sputtered flux at the growth interface (negligible desorption into the vapor) is assumed. For any film composition, the total arrival flux of M atoms plus M-O molecules is $F = G \cdot V \rho / W$. W is the molecular weight/mole of film, V is the number of M atoms/mole of film, and ρ is the film density. The total flux of all sputtered M-bearing species for any $\{O_2, R, V_c\}$ set, relative to its value in a pure R discharge at the same V_c , is

$$F' = (G \cdot V \rho / W)_{R, V_c} / (G \cdot V \rho / W)_{R, V_c, O_2 = 0} = G' N' \rho' / W' \quad (2)$$

Writing F' as the sum of contributions from M and M-O species, and identifying F'^M with I'

$$F' = I' + F'^{M-O} \quad (3)$$

Combining Eqs. (2) and (3), and normalizing to a total flux of unity, the fractional flux of M atoms to the growth interface is

$$f^M = I' / (G' N' \rho' / W'), \quad (4)$$

and the fractional flux of M-O molecules to the growth interface is $f^{M-O} = 1 - f^M$. Equation (4) expresses f^M in quantities that can be experimentally determined.

3. Emission from oxygen species

Excited O_2 molecules do not produce an easily detectable emission spectrum in low pressure glow discharges.²¹ Emission from O atoms, at $\lambda = 3947, 5331, 6157,$ and $7772-5 \text{ \AA}$,²² and from the first negative system of O_2^+ ions,²³ which produced bands throughout the visible spectrum, was monitored. The initial appearance or rapid increase in O and O_2^+ emission was used as evidence of the target's inability to getter all O_2 from the discharge.

C. Phase mapping

Phase maps were constructed by graphing phase fields onto process parameter space and overlaying with the growth environment indices, which are as follows: (1) The fractional atomic metal flux to the growth interface, f^M , calculated using Eq. (4).

(2) The initial appearance or rapid increase of oxygen in the discharge available for reaction at the growth interface, at the coordinates $Q(O_2, R, V_c)$. This set of coordinates is shown on the phase maps that follow for each rare gas type as " $Q(O_2, V_c)$ ".

III. VANADIUM-OXYGEN SYSTEM

There are single and mixed valency bulk vanadium oxides at STP.²⁴ The phase sequence of single valency oxides is $VO - V_2O_3 - VO_2 - V_2O_5$. A homologous series, V_nO_{2n-1} with $3 < n < 9$ in which V takes on +3 and +4 valency lies between V_2O_3 and VO_2 . A second series, V_nO_{2n+1} with $3 < n < 6$, in which V takes on +4 and +5 valency, lies between VO_2 and V_2O_5 . The mixed higher

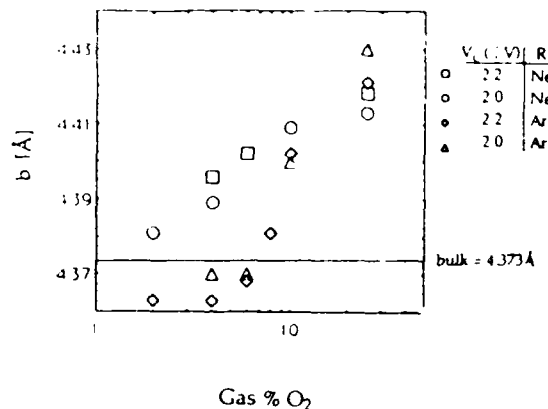


FIG. 1 The interlayer spacing of sputter deposited vanadia as a function of gas % O_2 .

valency vanadium oxides and V_2O_5 (vanadia) are based on ReO_3 -archetype blocks.^{25,26} Changes in stoichiometry are accommodated by extended defects linking these blocks.

In spite of the multitude of bulk vanadium oxides, only two structures occur in the films studied here:^{11,12,27,28} crystalline (*c*-) vanadia and a material that yielded no diffraction pattern, temporarily denoted "V-oxide." All films were transparent, colored insulators with a V:O atomic ratio of 0.4 ($\pm 10\%$).

Bulk vanadia has an orthorhombic lattice.²⁹ Its extended structure consists of alternating layers of V + O atoms and O atoms alone (vanadyl O) oriented parallel to the *b* axis or $\langle 010 \rangle$ crystallographic direction. In this study, *c*-vanadia grew with the *b* axis in all crystallites oriented normal, i.e., layers parallel, to the substrate. The interlayer spacing, *b*, shown in Fig. 1 as a function of gas O_2 content, varied from less to greater than the bulk constant $b_0 = 4.373 \text{ \AA}$ in films grown in Ar- O_2 ,^{11,27,28} and was always greater than b_0 in films grown in Ne- O_2 discharges.¹²

An intriguing feature of vanadium oxide films, and actually a clue to understanding their short range order, is their green or yellow color in transmitted light. Each structure can have either color, so that there were four possible combinations: green V-oxide, yellow V-oxide, green *c*-vanadia, and yellow *c*-vanadia. Bulk single crystal vanadia is yellow. Spectrophotometry studies^{26,30,31} of as-grown and air-annealed films showed that the green color results from an intragap absorption band near the fundamental optical absorption edge, produced by a V^{+4} -vanadyl O vacancy defect. In films, these defects are associated with $b < b_0$, and if present in sufficient number, cause local order in adjacent V + O planes to collapse, resulting in a stacking V_6O_{13} fault.^{32,33} The relationship between interlayer spacing, color, and intragap absorption can be seen from Fig. 2, which shows the optical absorption coefficient versus incident photon energy for a sequence of films with *b* ranging from 4.363 to 4.381 \AA .

The fact that V-oxide can be either green or yellow indicates that short range, not long range, order determines

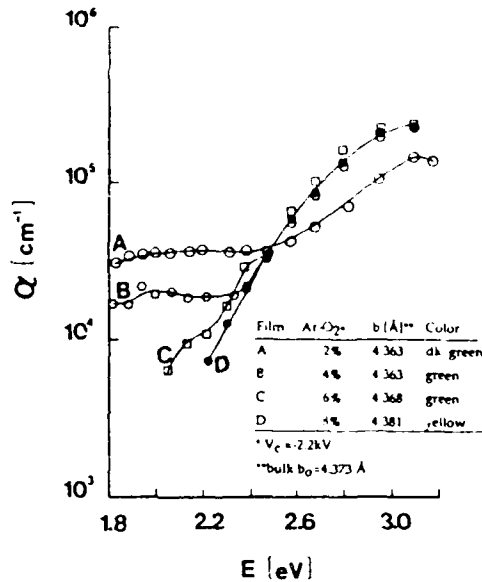


FIG 2 The optical absorption coefficient as a function of incident photon energy for four c-vanadia films.

color; yellow films satisfy the condition of five O coordinated with a central V whereas green films do not. Yellow V-oxide films lack the intragap absorption band associated with green color in c-vanadia with $b < b_0$, and have infra-

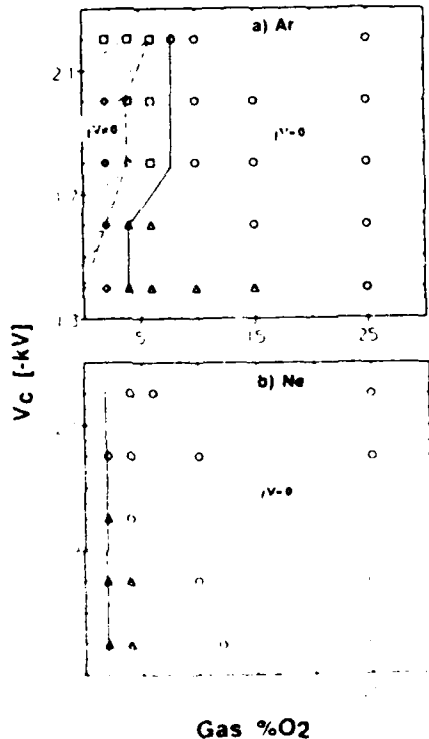


FIG 3 A phase map for the vanadium-oxygen system. \circ c-vanadia with $b < b_0$, \square V-oxide, \triangle c-vanadia with $b > b_0$, Δ a-vanadia; solid line = $Q(T, E)$

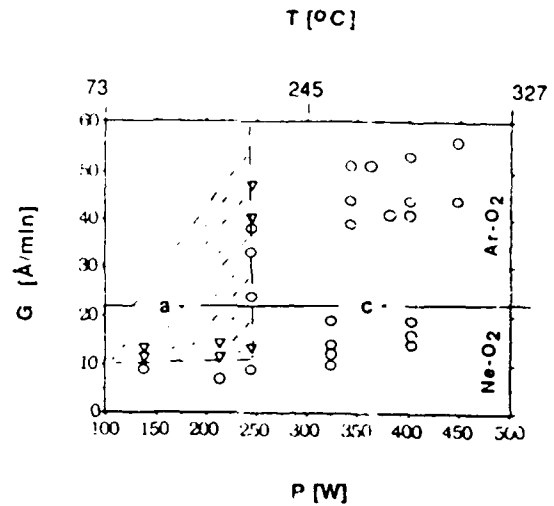


FIG 4 c-vanadia with $b > b_0$ and a-vanadia phase fields graphed onto power-growth rate space. Data for Ne-O₂ and Ar-O₂ discharges are separated by the heavy solid line. The dashed line represents the boundary between the a- and c-phase fields (± 15 W). The growth interface temperature (T) in degrees kelvin (K) is shown on an auxiliary axis, with values calculated according to the relationship $P = (3.5 \times 10^{-9} \text{ W/K}^4) T^4 + 50 \text{ W}$, where the power (P) is in watts (W)

red transmission spectra similar to that of yellow c-vanadia. Yellow V-oxides are hereafter denoted "a-vanadia." All phase fields are shown in Fig. 3.

With respect to calculating f^V for the a- and c-vanadia phase fields, I' and G' were taken from Refs. 11 and 12, and the bulk V₂O₅ density was used in Eq. (4). The unknown density of the V-oxides allowed only the semiquantitative estimate of $f^V \neq 0$ to be made in that phase field. f^V and $Q(O_2, V_c)$ are shown in Fig. 3.

It can be seen that the growth of a-vanadia and c-vanadia with $b > b_0$ growth, i.e., all yellow films, was coincident with (a) a vanishingly small f^V ; V-O arrived at the growth interface, and (b) oxygen available for reaction at the growth interface. V-oxides and c-vanadia with $b < b_0$, i.e., all green films, were grown when f^V was non-vanishing and there was insufficient oxygen for reaction at the growth interface.

Figure 3 shows that both a- and c-vanadia grew under conditions of a vanishing f^V and oxygen available for reaction at the growth interface. c-vanadia replaced a-vanadia as the gas O₂ content and V_c increased. Figure 4 shows the phase fields for a- and c-vanadia mapped onto power-growth rate coordinates, with growth temperature indicated on the abscissa. Lower rate and higher power (higher temperature) promote c-vanadia growth, a general trend that is in agreement with the classic results of Krakorian and Sneed⁴ on the elemental Ge system. The a- to c-vanadia transition appears to be independent of gas composition within the experimental uncertainty of power (± 15 W), supporting the idea of a thermally induced structure change. However, these data show that the transition temperature for a- to c-vanadia growth is so low,

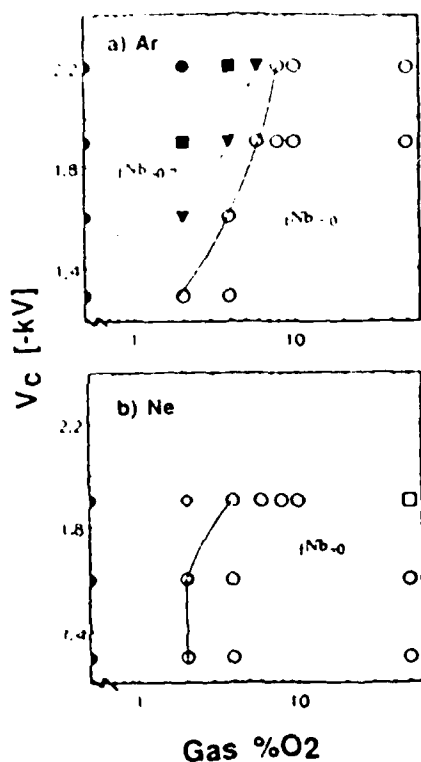


FIG. 5 A phase map for the niobium-oxygen system. ●, Nb; ■, Nb + NbO; ▼, Nb + NbO₂; ○, *a*-niobia; ◇, *x*-niobia; □, crystalline niobia; solid line, $Q(O_2, V_c)$

~220 °C, that the role of active oxygen in athermally assisted crystallization³⁵⁻³⁷ needs to be considered.

IV. NIOBIUM-OXYGEN SYSTEM

The phase sequence of bulk niobium oxides at STP is³⁸ NbO (fcc, NaCl structure) → NbO₂ (tetragonal) → Nb₂O₅ (several related rhombohedral forms collectively called niobia). In addition, there is a mixed valency homologous series between NbO₂ and Nb₂O₅ with the general formula Nb_{2n+1}O_{8n-2}.³⁹ As in the case of mixed valency V-oxides, this series as well as the niobia polymorphs are based on ReO₃ archetype blocks.

With respect to sputter deposited films,¹³ Fig. 5 shows that Ar-NO₂ discharges [Fig. 4(a)] produced Nb + NbO and NbO + NbO₂ biphasic structures, whereas Ne-O₂ discharges [Fig. 5(b)] produced no suboxides. Crystalline (*c*-) niobia grew only when a high voltage Ne-50% O₂ discharge was used. *a*-niobia with no long range crystallographic order grew over a large region of process parameter space. All *a*- and *c*-niobia films were transparent, colorless insulators with Nb:O atomic ratios from 0.39 to 0.44 (±10%). In addition, a semitransparent, grey material denoted "*x*-niobia" which had no long range order, a finite resistivity, and an IR absorption spectrum with a strong *a*-niobia component, was formed at the Nb-suboxide/*a*-niobia phase boundary.

With respect to calculating f^{Nb} , I' and G' were taken from Ref. 13. The bulk rhombohedral Nb₂O₅ density was

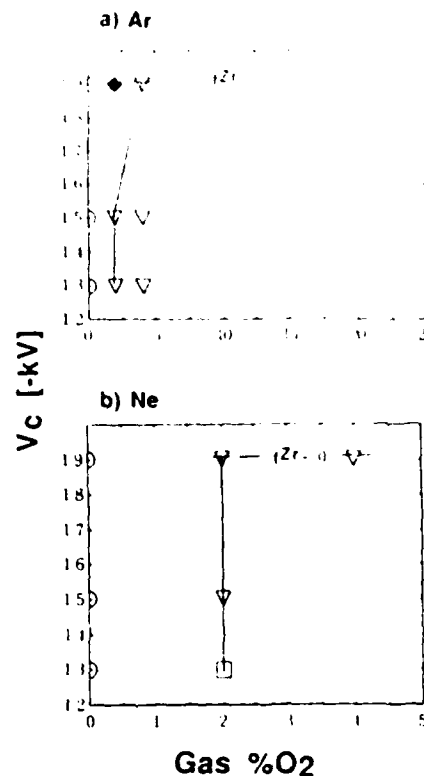


FIG. 6 A phase map for the zirconium-oxygen system. ○, Zr; ◆, ZrO; ▼, *m*-ZrO₂; □, *m*-ZrO₂; solid line, $Q(O_2, V_c)$; f^{Zr} data only for $V_c = -1.9$ kV, shown as dashed line.

used in Eq. (4) for *a*- and *c*-niobia films. Deciding the correct density for biphasic films was a challenge because overlapping diffraction peaks prevented the volume fraction of each phase to be precisely determined. We therefore used the limits of possible density to calculate two separate data points for each set of $\{G', I'\}$ for mixed Nb + NbO and NbO + NbO₂ films. f^{Nb} and $Q(O_2, V_c)$ are shown in Fig. 5.

It can be seen that *a*- and *c*-niobia growth was coincident with (a) a small f^{Nb} , > 80% of the sputtered flux that arrived at the growth interface was Nb-O, and (b) oxygen available for reaction at the growth interface. *x*-niobia also formed when f^{Nb-O} was large, but in this case, there was insufficient oxygen at the growth interface to complete oxidation. Biphasic metal and suboxide films grew when f^{Nb} was large; > 70% of the Nb sputtered from the target arrived at the growth interface as atoms, and there was insufficient oxygen for reaction at the growth interface.

V. ZIRCONIUM-OXYGEN SYSTEM

Monoclinic (*m*-) ZrO₂ is the only bulk zirconium oxide at STP.⁴⁰ However, Fig. 6 shows that ZrO, a metastable phase, and *t*-ZrO₂, a high temperature polymorph, were formed in addition to *m*-ZrO₂ in sputter deposited films.⁴¹⁻⁴³

ZrO was identified on the basis of three orders of diffraction from {111} planes of its NaCl-type fcc structure.

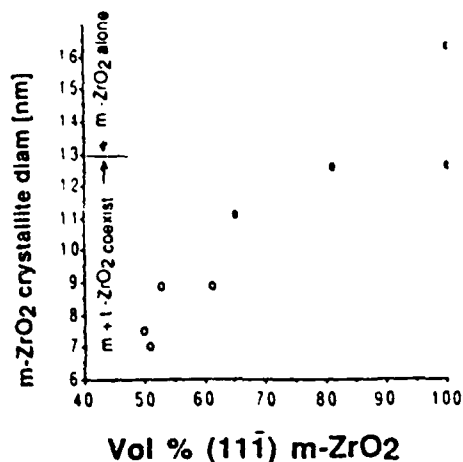


FIG. 7. The crystalline diameter calculated from the Scherrer x-ray diffraction relation as function of volume % $\{11\bar{1}\}$ -orientation m - ZrO_2 .

ZrO grew with solely $\{11\bar{1}\}$ planes parallel to the substrate, with a 2.65-Å interplanar spacing. t - ZrO_2 formed in a mixture with m -zirconia. In bulk material, $m + t$ - ZrO_2 coexist when the crystallite diameter is small.^{40,44} In sputter deposited films, the amount of t - ZrO_2 was also related to the crystallite diameter,⁴² as shown in Fig. 7. t - ZrO_2 was not stabilized in crystallites with diameter > 13 nm. The reason(s) for t - ZrO_2 stabilization at room temperature is still under debate. An early but challenged explanation is that t - ZrO_2 is the stable phase for small crystallites, due to the dominance of the surface energy contribution to the Gibbs free energy of formation when the surface area/volume ratio is large. Another explanation is that t - ZrO_2 is indeed formed as a metastable phase, but there is an insufficient driving force to overcome the kinetic barrier to transform it to m - ZrO_2 . m - ZrO_2 films formed with either solely $\{11\bar{1}\}$ planes (closest-packed planes in the structure) or the twin $\{11\bar{1}-11\bar{1}\}$ planes parallel to the substrate.

With respect to electrical and optical behavior, the resistivity of ZrO films was $272 \pm 14 \mu\Omega$ cm, compared to $40 \mu\Omega$ cm for Zr. ZrO films were metallic in appearance with a reflectance of 0.52 at $0.5 \mu\text{m}$ radiation, compared to 0.67 for Zr. All ZrO_2 films were transparent, colorless insulators. The fundamental optical absorption edge of m - ZrO_2 and $m + t$ - ZrO_2 films was studied and related to band structure calculations for each polymorph.^{42,43,45} The fact that single- $\{11\bar{1}\}$ orientation m - ZrO_2 could be produced allowed easy spectrophotometric analysis of this material without internal scattering from $\{11\bar{1}-11\bar{1}\}$ twin boundaries that are prevalent in bulk material. An initial indirect transition across the energy band gap of m - ZrO_2 at 4.70 eV and two direct transitions at 5.17 and 5.93 eV were identified.

With respect to calculating f^{Zr} , I' data were known only for -1.9-kV discharges. Combining this data with G' (Ref. 43) and the relevant bulk densities, f^{Zr} was calculated to be <0.3 for Ar discharges containing 2-20% O_2 . I' , hence f^{Zr} , vanished for Ne (>2%) $-O_2$ discharges, i.e.,

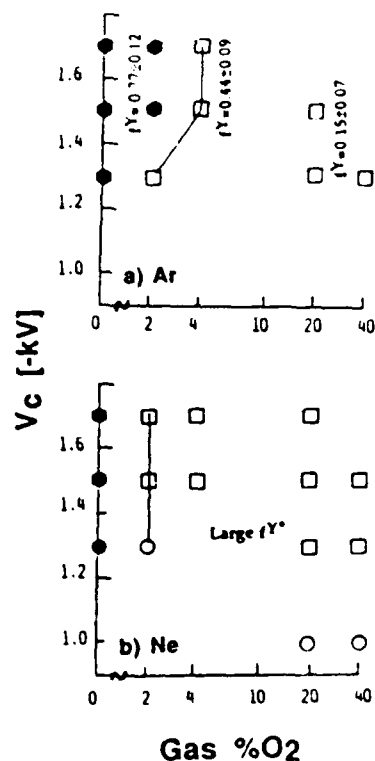


FIG. 8. A phase map for the yttrium-oxygen system ●, c-Y, closed ●, a-Y; □, multiorientation c-yttria; □, $\{11\bar{1}\}$ -c-yttria; ○, a-yttria; solid line, $Q(O_2, V_c)$.

$f^{Zr-O} \approx 1$, f^{Zr} at -1.9 kV, as well as $Q(O_2, V_c)$ for Ar- O_2 and Ne- O_2 discharges operated at all values of V_c , is shown in Fig. 6.

It can be seen that a large f^{Zr-O} is associated with zirconia formation if there is sufficient oxidation available for reaction at the growth interface. A large f^{Zr-O} is also associated with ZrO growth if there is insufficient oxygen at the growth interface to complete oxidation. Similar conditions produced x-niobia, as described in Sec. IV. Based on these results, we proposed⁴¹ that ZrO was the first oxide to be formed at the target and sputtered intact. Only when ZrO_2 was formed at the target at $Q(O_2, R, V_c)$ and the target ceased to get all oxygen from the discharge was ZrO_2 formed in the film.

VI. YTTRIUM-OXYGEN SYSTEM

Y_2O_3 (yttria) with a bcc bixbyite structure is the only bulk yttrium oxide at STP.⁴⁶ The 80-atom unit cell has a distorted fluorite structure with vacancies on $\frac{1}{2}$ of the anionic sites. Y occupies two structurally nonequivalent but chemically equivalent sites within the unit cell.

Figure 8 shows the crystalline (c-) yttria films grew in Ar- O_2 discharges, with a sole $\{11\bar{1}\}$ orientation over much of the phase field. In addition, a phase with no long range crystallographic order (a-yttria) formed in films grown in Ne- O_2 discharges operated at low V_c . All a- and c-yttria films had a Y:O atomic ratio of 3:2 ($\pm 10\%$) and were transparent, colorless insulators.

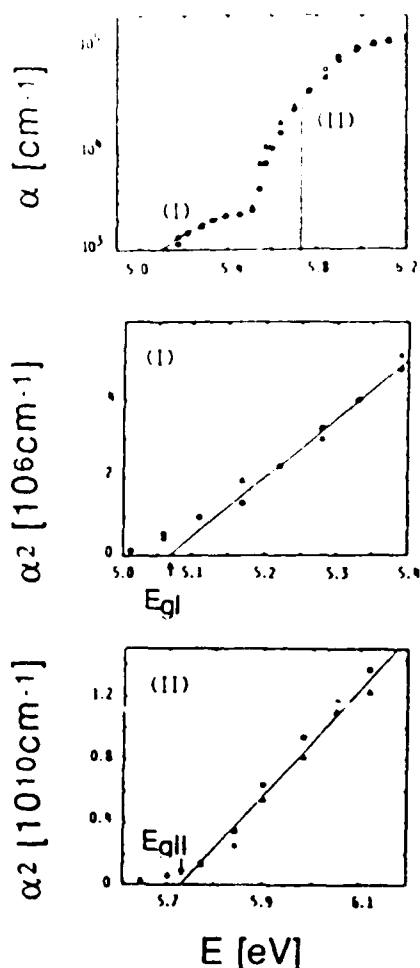


FIG. 9 The optical absorption coefficient as a function of incident photon energy for *c*-yttria with a sharp optical edge and the decomposition of this edge into two direct transitions across the band gap. The data for each transition were fitted to a curve of the form: $\alpha^2 = C(E - E_g)$, where $C_I = 1.5 \times 10^7 \text{ (cm}^2 \text{ eV)}^{-1}$, $E_{gI} = 5.07 \text{ eV}$, $C_{II} = 3.5 \times 10^{10} \text{ (cm}^2 \text{ eV)}^{-1}$, $E_{gII} = 5.73 \text{ eV}$.

The fundamental optical absorption edge of *c*-yttria grown under certain conditions described below consists of two direct interband transitions, at 5.07 and 5.73 eV, as shown in Figs. 9(a)–9(c).⁴⁵ This edge is denoted "sharp" and its structure is derived from two split-off Y 4*d* subbands at the bottom of the yttria conduction band. *c*-yttria grown under other conditions, also described below, has an optical absorption edge in which the distinction between the subbands is obscured, as shown in Fig. 10. This edge is denoted "smeared" and is similar to that of *a*-yttria, also shown in Fig. 10.

Infrared vibrational absorption spectra data for *a*- and *c*-yttria are recorded in Table I. A single, large peak dominates all spectra. The vibrational frequency ν , although lower for *c*- than *a*-yttria, lies within the range reported for bulk crystalline yttria.^{47,48} However, the distribution about this frequency, $\Delta\nu$, is smaller in *c*- than in *a*-yttria, indicating a smaller distribution about an average Y—O bond

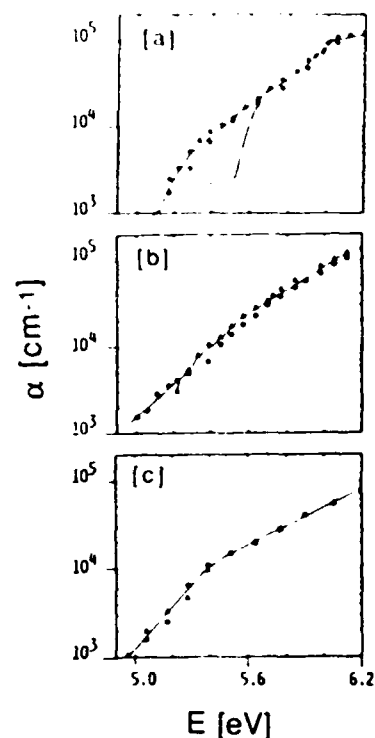


FIG. 10. The optical absorption coefficient as a function of incident photon energy for yttria with a smeared optical edge. *c*-yttria grown with oxygen available for reaction at (a) $f^Y = 0.44 \pm 0.09$; (b) large f^Y ; (c) *a*-yttria grown with oxygen available for reaction at large f^Y . The dashed line in (a) is a fit through the data for *c*-yttria with a sharp edge from Fig. 9.

length (or strength). IR absorption does not distinguish between *c*-yttria with a sharp versus smeared optical absorption edge, suggesting that disruption of crystal field symmetry (long range order that depends upon the correct distribution of Y in the two structurally nonequivalent sites within the unit cell), rather than short range order, is responsible for edge smearing.

With respect to calculating f^Y , I' and G' for Ar–O₂ discharges were taken from Ref. 14 and used with the bulk yttria density in Eq. (4). f^Y and $Q(\text{O}_2, V_c)$ are shown in Fig. 8(a). f^Y could not be calculated for Ne–O₂ discharges because there was a selective enhancement of two of the optical transitions monitored here, by a yet-to-be identified broadband source. (One possibility is dissociative transfer

TABLE I. Infrared absorption characteristic of yttria films sputter deposited on (111)-Si.

Film	Edge type	$\nu \text{ (cm}^{-1}\text{)}^a$	$\Delta\nu \text{ (cm}^{-1}\text{)}$
1. <i>c</i> -yttria	Sharp	561	22
2. <i>c</i> -yttria	Smeared	559	20
3. <i>a</i> -yttria	Smeared	571	32

Single crystal (Ref. 43): $\nu = 561 \text{ cm}^{-1}$, bulk powder (Ref. 44): $\nu = 580 \text{ cm}^{-1}$

^a ± 4 cm⁻¹

of excitation from Ne^m to a sputtered YO molecule.) Equation (4) was therefore not valid. However, it is qualitatively argued^{15,45} that there was a large excited atomic Y flux incident on the growth interface, denoted f^{Y*} in Fig. 8(b), when Ne-O_2 discharges were used.

It can be seen that growth of c-yttria with a sharp optical edge was coincident with (a) a small f^Y ; ~85% of the sputtered flux that arrived at the growth interface was Y-O, and (b) oxygen available for reaction at the growth interface. c-yttria with a smeared optical edge and a-yttria formed when f^Y increased, and in fact, a large flux of excited Y atoms was present. Even though there was sufficient oxygen at the growth interface to complete oxidation, there may not have been time to form an ordered structure before the arriving flux quenched surface diffusion. Yttrium metal films grew when f^Y was large and oxygen was not available for reaction at the growth interface.

VII. SUMMARY

In this study, a series of metal ($M = \text{V, Nb, Y, Zr}$) targets were sputtered in O_2 -bearing discharges. Films were grown on substrates at low temperature (70–325 °C). Optical emission spectrometry was used to index the growth environment in terms of (a) the fractional flux of M and M-O species to the growth interface, and (b) the availability of oxygen for reaction at the growth interface. The interrelation of process parameters, phase formation, and the growth environment indices was presented in the form of phase maps.

Three common features were observed in the phase maps:

(1) A small or vanishing f^M (large f^{M-O}) and oxygen available for reaction at the growth interface resulted in high valency oxide growth, e.g., a- and c-niobia, c-yttria, m + t- and m-zirconia, and a- and c-vanadia.

(2) A small or vanishing f^M (large f^{M-O}) but insufficient oxygen at the growth interface resulted in suboxide growth, e.g., ZrO , x-niobia, and possibly V-oxides.

(3) A large f^M and insufficient oxygen at the growth interface resulted in metal and suboxide growth, e.g., Y, Nb, NbO , NbO_2 , and possibly V-oxides.

These results show that f^{M-O} as well as f^M must be taken into account when modeling reactive sputter deposition. Highest valency oxide films are in general grown by a reaction between M-O and oxygen at the growth interface. However, the growth environment indices used here do not explain differences in the structure of the highest valency oxides in the same system, e.g., crystalline versus vitreous vanadia, monoclinic versus tetragonal zirconia. The examination of additional growth environment features is underway, including consideration of the kinetic energy and electronic excitation of oxygen species.

ACKNOWLEDGMENTS

The author wishes to thank Professor G. S. Baker for helpful discussions regarding the preparation of this manuscript. This work was supported under U.S. ARO Grant

No. DAAL03-89-K-0022 and by a gift from Johnson Controls, Inc.

¹C. R. Aita, *J. Vac. Sci. Technol. A* 3, 625 (1985), and references therein

²J. W. Coburn, E. Tagliauer, and E. Kay, *J. Appl. Phys.* 45, 1779 (1974)

³J. W. Coburn, E. Tagliauer, and E. Kay, *J. Vac. Sci. Technol.* 12, 151 (1975)

⁴Y. Okajima, *J. Appl. Phys.* 55, 230 (1984).

⁵C. R. Aita, *J. Appl. Phys.* 61, 5182 (1987).

⁶C. R. Aita, R. J. Lad, and T. C. Tison, *J. Appl. Phys.* 51, 6405 (1980).

⁷N. M. Abuhadba and C. R. Aita, *J. Appl. Phys.* 71, 3054 (1992).

⁸F. M. Penning, *Z. Phys.* 46, 225 (1925); 57, 723 (1929).

⁹W. R. Bennett, Jr., *Appl. Opt. Suppl.* 1, 1 (1962).

¹⁰C. R. Aita and M. E. Marhic, *J. Vac. Sci. Technol. A* 1, 69 (1983).

¹¹C. R. Aita, J.-L. Liou, C.-K. Kwok, R. C. Lee, and E. Kolawa, *Thin Solid Films* 193/194, 18 (1990).

¹²N. M. Abuhadba and C. R. Aita, in *Surface Modification Technologies V*, edited by T. S. Sudharshan and J. F. Braza (Institute of Metals, London, 1992), pp. 517–526.

¹³R. C. Lee and C. R. Aita, *J. Appl. Phys.* 70, 2094 (1991).

¹⁴C.-K. Kwok, C. R. Aita, and E. A. Kolawa, *J. Vac. Sci. Technol. A* 8, 1330 (1990).

¹⁵C.-K. Kwok, C. R. Aita, and E. A. Kolawa, *J. Appl. Phys.* 68, 2945 (1990).

¹⁶C. R. Aita, *Proc. IEEE Ultrasonics Symp.* 1, 795 (1980).

¹⁷J. E. Greene, *J. Vac. Sci. Technol.* 15, 1718 (1978).

¹⁸C. Candler, *Atomic Spectra and the Vector Model* (Van Nostrand, Princeton, 1964), pp. 373, 389–392.

¹⁹See, for example, M. Garbuny, *Optical Physics* (Academic, New York, 1965), pp. 87–119.

²⁰H. G. Kuhn, *Atomic Spectra* (Academic, New York, 1961), pp. 79–84

²¹R. W. B. Pearse and A. G. Gaydon, *The Identification of Molecular Spectra* (Chapman and Hall, London, 1963), p. 239.

²²C. Candler, in Ref. 18, p. 375.

²³R. W. B. Pearse and A. G. Gaydon, in Ref. 21, pp. 243–245.

²⁴C. H. Griffiths and H. K. Eastwood, *J. Appl. Phys.* 45, 2201 (1974), and references therein.

²⁵A. Magneli, *Acta Crystallogr.* 6, 495 (1953).

²⁶A. K. Cheetham, in *Nonstoichiometric Oxides*, edited by O. T. Sorenson (Academic, New York, 1981), pp. 418–421.

²⁷C. R. Aita, Y.-I. Liu, M. L. Kao, and S. D. Hansen, *J. Appl. Phys.* 60, 749 (1986).

²⁸C. R. Aita, C.-K. Kowk, and M. L. Kao, *Mater. Res. Soc. Symp. Proc.* 82, 435 (1986).

²⁹ASTM Joint Commission on Powder Diffraction Standards File No. 9-387 (1974).

³⁰S. D. Hansen and C. R. Aita, *J. Vac. Sci. Technol. A* 3, 660 (1985)

³¹C. R. Aita and M. L. Kao, *J. Vac. Sci. Technol. A* 5, 2714 (1987)

³²E. Gillis and E. Boesman, *Phys. Status Solidi* 14, 337 (1966)

³³L. Fiermans and J. Vennik, *Surf. Sci.* 9, 187 (1968).

³⁴E. Krikorian and R. J. Sneed, *J. Appl. Phys.* 37, 3665 (1966)

³⁵J. E. Greene, in *The Handbook of Crystal Growth, Vol. 1. Fundamentals*, edited by D. T. J. Hurle (Elsevier, Amsterdam, in press)

³⁶S. Nikzad and H. A. Atwater, *Mater. Res. Soc. Symp. Proc.* 223, 53 (1991).

³⁷N. Herbots, O. C. Hellman, and O. Vancauwenberghe, *Mater. Res. Soc. Symp. Proc.* (in press)

³⁸A. D. Wadsley and S. Anderson, *Prospect Struct. Chem.* 3, 1 (1970)

³⁹L. Eyring, in Ref. 26, pp. 366–372

⁴⁰R. C. Garvie, in *High Temperature Oxides, Part II*, edited by A. M. Alper (Academic, New York, 1970), pp. 122–132

⁴¹C.-K. Kwok and C. R. Aita, *J. Vac. Sci. Technol. A* 7, 1235 (1989)

⁴²C.-K. Kwok and C. R. Aita, *J. Appl. Phys.* 66, 2756 (1989)

⁴³C.-K. Kwok and C. R. Aita, *J. Vac. Sci. Technol. A* 8, 3345 (1990)

⁴⁴M. Ruhle, *J. Vac. Sci. Technol. A* 3, 749 (1985), and references therein

⁴⁵C. R. Aita and C. K. Kwok, *J. Am. Ceram. Soc.* 73, 3209 (1990)

⁴⁶R. C. Anderson, in Ref. 40, pp. 1–40

⁴⁷Y. Nigara, *Jpn. J. Appl. Phys.* 7, 404 (1968)

⁴⁸N. T. McDevitt and W. L. Baun, *Spectrochim. Acta* 20, 799 (1964)

APPENDIX VI

"Core level and valence band x-ray photoelectron spectroscopy of gold oxide."

C.R. Aita and N. C. Tran, J. Vac. Sci. Technol. A 9, 1498-1500 (1991).

Core level and valence band x-ray photoelectron spectroscopy of gold oxide

Carolyn Rubin Aita^{a)} and Ngoc C. Tran^{b)}

Materials Department, University of Wisconsin, Milwaukee, Milwaukee, Wisconsin 53201

(Received 19 September 1990, accepted 5 November 1990)

Reactive sputter deposition was used to grow a phase-separated 0.40 Au/0.56 Au₂O₃/0.04 Au-hydroxide cermet film and x-ray photoelectron spectroscopy was used to examine the Au 4f and O 1s core electron binding energy of each phase. The valence band structure of Au₂O₃ is reported here for the first time, and consists of an O 2p electron-derived peak centered at 5.5 eV and a density of states that approaches zero at the Fermi energy, characteristic of a semiconductor. The results are compared to other third long period conducting and semiconducting oxides.

I. INTRODUCTION

Auric oxide (Au₂O₃), with a volume free-energy of formation of +39 kcal/mol,¹ cannot be synthesized in bulk under conditions of equilibrium thermodynamics. We have, however, used reactive sputter deposition to produce ceramic-metal composite (cermet) films in which one of the components is Au₂O₃,² and used x-ray photoelectron spectroscopy to determine the chemical shift in Au 4f core electron binding energy in this compound. Here, a corresponding shift in the O 1s electron binding energy is reported. Furthermore, the valence band structure of Au₂O₃ is reported for the first time, and discussed in relationship to the oxides of other third long period metals.³⁻⁶

II. EXPERIMENTAL

An Au/Au-oxide cermet film was grown on a Si-(111) substrate by sputtering a 99.99%, 76 mm diam Au target in a radio-frequency (rf)-excited 50% Ne-50% O₂ discharge.² The substrate was chemically cleaned using a chelating procedure before being placed in the chamber and sputter cleaned in an Ar discharge before deposition. The sputtering chamber base pressure was $< 5 \times 10^{-7}$ Torr. The sputtering gases, 99.996% pure Ne and 99.99% pure O₂, were admitted separately into the chamber using mass flow controllers. The total gas pressure was 1×10^{-2} Torr. The deposition was carried out at -1 kV peak-to-peak cathode voltage with a grounded anode. With a shutter covering the substrate, the target was sputtered for 10 min in Ne and then for 10 min in 50% Ne-50% O₂. When an Au target is sputtered in an O-bearing discharge, Au-O molecular complexes are formed at and sputtered from the target surface.⁷⁻⁹ The delivery of these complexes to the substrate is essential for Au-O bonding in the film.^{2,9} The purpose of the presputters, therefore, is to allow target surface reactions that produce these species to reach dynamic equilibrium. The shutter was then opened and a 70-nm thick film was deposited at the rate of 1.2 nm/min.

A Perkin-Elmer PHI Model 5400 electron spectroscopy for chemical analysis (ESCA) system equipped with a 15 keV Mg K α radiation source was used for core level and valence band x-ray photoelectron spectrometry. The instrument was calibrated using the Au 4f_{7/2} electron binding energy of a gold foil standard at 84.0 ± 0.2 eV.

With respect to other film properties, the crystallography, resistivity, and optical reflectivity at 500 nm incident photon wavelength were reported in Ref. 2. To summarize here, the film showed a single broad x-ray diffraction (XRD) peak attributable to (111) planes of the Au lattice. The integrated intensity of the peak was 1/100th of its value for an Au film of the same thickness. The electrical resistivity of the film was $7.5 \pm 1.1 \times 10^3 \mu\Omega$ cm, ~3 orders of magnitude greater than that of a pure Au film of the same thickness. The optical reflectivity at 500 nm is $26 \pm 4\%$, ~1/2 of its value for an Au film of the same thickness, and of the bulk material. The cermet film had a bronze color in reflected light.

III. Au 4f AND O 1s CORE ELECTRON BINDING ENERGY

The Au 4f electron spectrum of the cermet, shown in Fig. 1, is more complicated than for a pure Au film, shown in the insert, and is resolved into five Gaussian peaks with binding energy and relative integrated intensity recorded in Table I. These peaks can be related to contributions from metallic Au and Au bonded to O in two different oxidation states using the following information: (1) the Au 4f_{7/2} and 4f_{5/2} electron binding energy for metallic Au is 84.0 and 87.7 eV, respectively, (2) the energy splitting between the Au 4f_{7/2} and 4f_{5/2} total angular momentum (*J*) states corresponding to the same Au oxidation state is 3.7 eV, and (3) the integrated intensity ratio of the 7/2:5/2 states is equal to the ratio their multiplicities $(2J + 1)$, $\{ [2(7/2) + 1] : [2(5/2) + 1] \} = 4:3$.

With respect to Fig. 1, peak A is attributed to the 4f_{7/2} state in metallic Au. Peaks B and D, whose integrated intensities *I*(B) and *I*(D) are in the ratio of 4:3, are attributed to the 4f_{7/2} and 4f_{5/2} states of Au bonded to O in a phase denoted here "Au-oxide 1." Peak E is attributed to the 4f_{5/2} state of Au bonded O in a phase denoted here "Au-oxide 2." Peak C is the sum of contributions from the 4f_{5/2} state in metallic Au, of intensity is $3I(A)/4$, and the 4f_{7/2} state in Au-oxide 2, of intensity $4I(E)/3$. The fact that the measured intensity of peak C equals the calculated intensity $[3I(A)/4] + [4I(E)/3]$ supports the correctness of its assignment.

Based on the chemical shift observed for the anodic oxidation products of Au,¹⁰ Au-oxide 1 was identified as auric

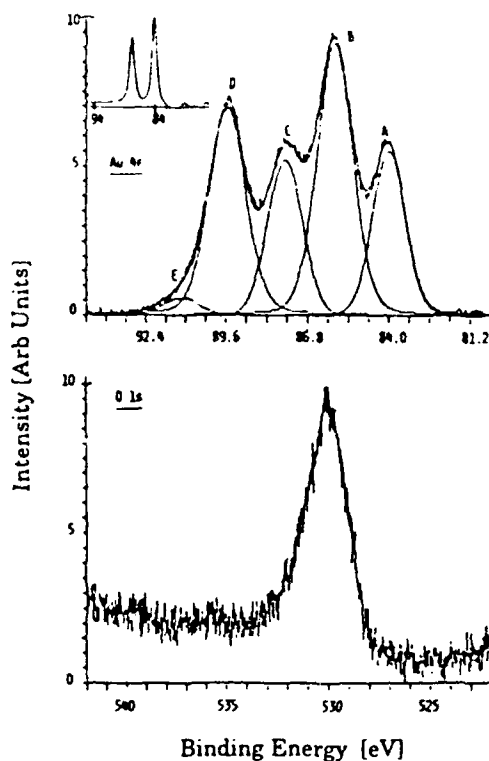


FIG. 1 The Au 4f and O 1s electron binding energy spectra of a 0.40 Au/0.56 Au₂O₃/0.04 Au-hydroxide cermet film. The intensity scale factor of the Au 4f spectrum is 3X that of the O 1s spectrum. The Au 4f electron spectrum of an Au film is shown in the insert.

oxide, Au₂O₃, and Au-oxide 2, as a hydrated form, possibly Au(OH)₃. In addition to the electrochemical study cited above, Au 4f electron spectra of the form shown in Fig. 1 have been obtained from an Au surface that had been sputtered in O₂,¹¹ and from an Au surface that had been etched in CF₄ and subsequently hydrolyzed in air.¹² The atom fraction of Au in each phase of the cermet was calculated from a ratio of the Au 4f_{7/2} electron peak intensities, and the phase composition of the cermet was determined to be 0.40 Au/0.56 Au₂O₃/0.04 Au-hydroxide.

The O 1s electron binding energy peak of the cermet, shown in Fig. 1, is centered at 530.1 eV, and based on electrochemical data¹⁰ is attributed to O bonded to Au in Au₂O₃.

TABLE I. XPS Au 4f electron binding energy in a 0.40 Au/0.56 Au₂O₃/0.04 Au-hydroxide cermet film

Peak	Binding energy (eV)	Rel intensity	J _i assignment
A	84.0	60	7/2 Au
B	85.9	100	7/2 Au ₂ O ₃
C	87.7	53	5/2 Au + 7/2 Au-hydroxide
D	89.6	75	5/2 Au ₂ O ₃
E	91.4	6	5/2 Au-hydroxide

The small shoulder at ~532.5 eV is attributed to O in water and/or hydroxyl groups.^{10,12} The ratio of Au/O atoms in the Au₂O₃ phase of the cermet was calculated from the ratio of the integrated intensities of the Au 4f_{7/2} peak in Au₂O₃ (peak B) to the O 1s peak, adjusted to the same scale and divided by their sensitivity factors,¹¹ and found to be 0.6, in good agreement with stoichiometry.

On the basis of XRD and x-ray photoelectron spectroscopy (XPS) data, the proposed structure of the film is that of a phase-separated material consisting of a mixture of Au and Au₂O₃, with a small amount of Au hydroxide. The O-bearing phases have no long range order detectable by XRD, and the Au phase is microcrystalline.

IV. Au₂O₃ VALENCE BAND STRUCTURE

Figure 2 shows the upper part of the valence band of the cermet, from the Fermi level (E_F) at zero binding energy to 10 eV below E_F . The valence band spectrum obtained from a metallic Au film is shown for comparison in the insert in Fig. 2. The Au 5d states dominate the metallic Au spectrum from 1.5–8 eV, with Au 6s states at the Fermi edge.¹⁴ The cermet valence band spectrum is a composite of contributions from metallic Au and the O-bearing phases. The metallic Au component was separated out, assuming the same atomic density for Au in the pure metal film and in the metallic component of the cermet. The difference spectrum, shown in Fig. 3, represents the valence band of Au₂O₃, "contaminated" with ~7% Au hydroxide. This spectrum consists of a single peak centered at ~5.5 eV below E_F , with shoulders at ~2 and 8 eV, and is similar in form to the valence band of α -PtO₂,³ ReO₃,⁴ and Na_xWO₃ (sodium-tungsten bronzes)⁵ valence band spectra have similar structures centered at 5.5–7 eV below E_F which are attributed to O 2p-derived states. The high energy binding shoulder is possibly due to the 3d orbital of OH⁻, keeping in mind that the fine structure in the cermet-minus-gold valence band difference spectrum shown in Fig. 3 is somewhat speculative because the cross section for

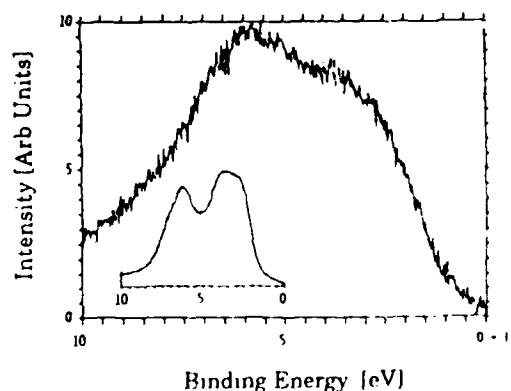


FIG. 2 The valence band of a 0.40 Au/0.56 Au₂O₃/0.04 Au hydroxide cermet film. The valence band of an Au film is shown in the insert.

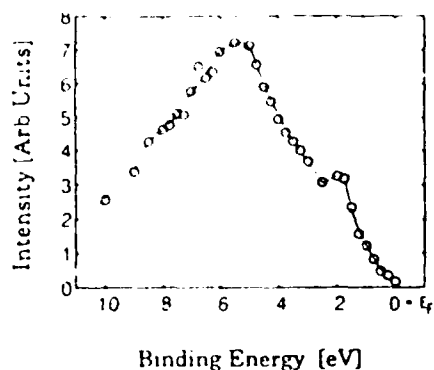


FIG. 3 The valence band of the Au_2O_3 phase of the cermet, including 7% Au hydroxide. The intensity scale factor is the same in Figs. 2 and 3.

Au $5d$ electrons is much larger than for O $2p$ electrons. However, unlike ReO_3 , Na_2WO_4 , and other third long period conducting oxides, IrO_2 and OsO_2 , which have filled metal d -O $2p_{\pi}$ states that form a split-off band centered just below E_F with a significant number of states at E_F ,⁶ it can be seen from Fig. 3 that the number of valence band states in Au_2O_3 , like PtO_2 ,⁷ approaches zero at E_F , characteristic of a semiconductor.

ACKNOWLEDGMENTS

The authors thank Professor M. G. Lagally, University of Wisconsin-Madison, for use of the XPS facility. We also

thank the referee of this paper for pertinent comments which have been incorporated into the text. This work was supported under USARO Grant No. DAAL-03-89-K-0022 and through a gift from Johnson Controls, Inc. to the Wisconsin Distinguished Professorship of CRA.

¹ Author to whom correspondence should be addressed.

² Permanent address: Auger/ESCA Laboratory, University of Wisconsin-Madison, 1500 Johnson Drive, Madison, WI 53706.

³ D. M. Mattox, *J. Appl. Phys.* **37**, 3613 (1966).

⁴ A. M. Klumb, C. R. Aita, and N. C. Tran, *J. Vac. Sci. Technol. A* **7**, 1701 (1989).

⁵ G. K. Wertheim, L. F. Mattheiss, and M. Campagna, *Phys. Rev. Lett.* **32**, 997 (1974).

⁶ M. Campagna and G. K. Wertheim, *Phys. Rev. Lett.* **34**, 738 (1975).

⁷ D. Cahen, J. A. Ibers, and J. B. Wagner, *Inorg. Chem.* **13**, 1377 (1974).

⁸ J. B. Goodenough, in *Progress in Solid State Chemistry*, edited by H. Reiss (Pergamon, Oxford, London, 1971), Vol. 5, pp. 362-263.

⁹ A. Hecq, M. Vandy, and M. Hecq, *J. Chem. Phys.* **72**, 2876 (1980).

¹⁰ B. L. Bentz and W. W. Harrison, *Int. J. Mass Spectrom. Ion Phys.* **37**, 167 (1981).

¹¹ C. R. Aita, *J. Appl. Phys.* **61**, 5182 (1987).

¹² T. Dickinson, A. F. Povey, and P. M. A. Sherwood, *J. Chem. Soc. Faraday Trans. 1* **71**, 298 (1975).

¹³ J. J. Pireaux, M. Liehr, P. A. Thiry, J. P. Delrue, and R. Caudano, *Surf. Sci.* **141**, 221 (1984).

¹⁴ J. H. Linn and W. E. Swartz, *Appl. Spectrosc.* **39**, 755 (1985).

¹⁵ D. Briggs and M. P. Seah, *Practical Surface Analysis by Auger and X-Ray Photoelectron Spectroscopy* (Wiley, New York, 1983), pp. 511-514.

¹⁶ P. H. Citrin, G. K. Wertheim, and Y. Baer, *Phys. Rev. B* **27**, 3160 (1983).



APPENDIX VII

"Sputter deposition of highly $\langle 100+001 \rangle$ textured tetragonal barium titanate grown on unheated silica using a neon discharge." C.R. Aita and N.M. Abuhadba, J. Appl. Phys. 71, 3054-3046 (1992).

Sputter deposition of highly (100+001)-textured tetragonal barium titanate on unheated silica using a neon discharge

N. M. Abuhadba and C. R. Aita

Materials Department, University of Wisconsin-Milwaukee, P.O. Box 784, Milwaukee, Wisconsin 53201

(Received 5 June 1991; accepted for publication 10 December 1991)

The sputter deposition of highly (100 + 001)-textured tetragonal BaTiO₃ on unheated substrates using a pressed powder BaTiO₃ target and a radio frequency-excited Ne discharge is reported. For comparison, amorphous BaTiO₃ was also produced, using an Ar discharge operated at the same value of all other independent process parameters. *In situ* discharge diagnostics using optical emission spectrometry was used to study the plasma volume. Data show that there was atomic Ti but no atomic Ba in the Ne discharge used to produce *t*-BaTiO₃. However, both atomic Ba and Ti were identified in the Ar discharge used to produce *a*-BaTiO₃. A probable source of free Ba atoms in the plasma is the reduction of BaTiO₃ at the target surface due to the sputtering action of Ar⁺ ions. By comparison with other sputter-deposited metal oxide systems, the effect on film crystallinity of atomic metal versus molecular metal oxide flux incident on the substrate is discussed.

At room temperature, barium titanate (BaTiO₃) is a wide band gap ferroelectric material with a high dielectric constant and high optical index of refraction. The bulk material has a tetragonal crystal structure (*t*-BaTiO₃) at room temperature that is derived by a displacive phase transition from a high temperature (> 120 °C), nonpolarizable, paraelectric state with the cubic, perovskite-type lattice structure.¹ The polarization axis of *t*-BaTiO₃ is along the [001] or *c* direction.

Recent interest in BaTiO₃ thin films for use in nonvolatile ferroelectric memory devices requires fabricating the material in the tetragonal phase. Deposition by sputtering a pressed powder BaTiO₃ target in Ar or Ar/O₂ discharges had previously been attempted for this purpose,²⁻⁸ but *t*-BaTiO₃ grew consistently only on substrates heated to > 500 °C, with one exception: Mansingh and Kumar recently produced *t*-BaTiO₃ on a 200 °C substrate using an Ar-20% O₂ discharge.⁹ In general, however, an amorphous or poorly crystallized structure was produced on unheated substrates, or even on heated substrates after the target had been sputtered for a period of time. Changes in target chemistry due to aging, in particular reduction, were suspected. Here, we report the growth of *t*-BaTiO₃ on unheated substrates from a pressed powder BaTiO₃ target and an rf-excited Ne discharge. For comparison, amorphous BaTiO₃ was also produced, using an Ar discharge.

Films were grown in a planar diode sputter deposition system. The target was a 12.7-cm-diam, hot-pressed BaTiO₃ ceramic disk of 99.9% purity bonded to a water-cooled stainless-steel cathode. Depositions were made at -1.0 kV peak-to-peak cathode voltage, with a grounded anode and a 5 cm anode-cathode spacing. Films (denoted by an unprimed letter) were grown on uv-visible transparent Suprasil II fused silica flats, and (denoted by a primed letter) on IR-transparent, high resistivity (111)-cut silicon rounds. After a triple solvent clean,⁹ the substrates were placed on a water-cooled Cu pallet that had been previously coated with ~10 nm of BaTiO₃ to prevent backsputtering of Cu and its incorporation into the growing film.

The chamber was evacuated to a base pressure of 6.66×10^{-5} Pa (5×10^{-7} Torr), throttled, and backfilled to an operating pressure of 1.33 Pa (1×10^{-2} Torr). 99.996% Ne or 99.999% Ar was used as the sputtering gas. The total gas pressure was measured with a capacitance manometer. Gas was introduced into the chamber at a flow rate of 20 sccm. With a shutter covering the anode, the target was presputtered for 20 min with the rare gas used for the deposition, to allow the target surface chemistry to equilibrate. Films A and A' were deposited in Ne at a power level of 325 W. Films B and B' were deposited in Ar at a power level of 200 W.

Optical emission spectrometry¹⁰ was used for *in situ* sputter deposition discharge diagnostics, in order to examine the extent of BaTiO₃ target dissociation due to the sputtering process. An optical spectrometer with 1200 and 2400 groove/mm holographic gratings capable of 0.5 Å resolution in the near ultraviolet to near infrared spectrum was used to sample radiation of wavelength λ emitted between the anode and cathode through an optical window. The optical emission intensity $I(\lambda)$ of radiative electronic transitions of excited neutral metal atoms to ground state were monitored at the following wavelengths: for Ba, $\lambda = 3501$ Å in Ar and 5535 Å in Ne; for Ti, $\lambda = 3956$ Å in Ar and 3642 Å in Ne.¹¹ In addition, for the purposes of calibration an Ar line at 4702 Å and a Ne line at 3472 Å were monitored. Assuming the condition of an optically thin plasma in local thermal equilibrium, $I(\lambda)$ is proportional to the number of ground state metal atoms in the discharge.¹²

Film thickness was determined using a Tencor Alpha Step model 200 profilometer to measure the height of a step produced by masking a region of the substrate during deposition. Growth rate was determined by dividing thickness by deposition time. Film A was 580 nm thick and deposited at a rate of 3 nm/min. Film B was 662 nm thick and deposited at a rate of 11 nm/min. The crystallography of films A and B was determined by double-angle x-ray diffraction (XRD) using CuK α radiation ($\lambda = 1.5418$ Å).

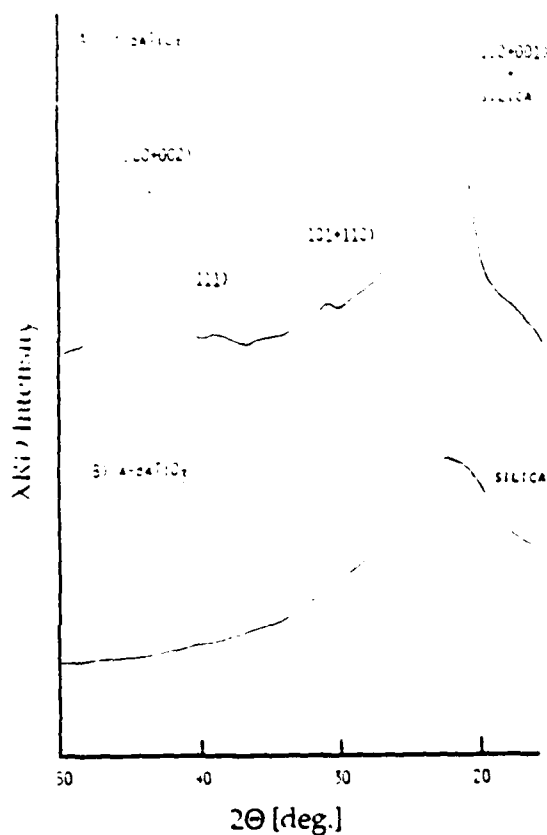


FIG. 1 X-ray diffraction patterns for (a) *r*-BaTiO₃ film A and (b) *a*-BaTiO₃ film B.

The diffractometer was calibrated using the {01.1} peak of a quartz standard at $2\theta = 26.66 \pm 0.02^\circ$ whose width was 0.25° . A Nicolet model MX-1 FT IR spectrometer was used to obtain the infrared transmission spectra of films A and B. The instrument was calibrated using a polystyrene standard to an accuracy of $\pm 4 \text{ cm}^{-1}$ in the wave number region of interest, $400\text{--}4000 \text{ cm}^{-1}$ ($2.5\text{--}25 \mu\text{m}$).

Figure 1 shows XRD patterns taken from films A and B. Film A is *r*-BaTiO₃. Its XRD pattern consists of a major peak at $2\theta = 43.5^\circ$ attributed to {200 + 002} planes. Minor peaks with relative intensity < 4% at 38.5° and 31.0° are attributed to {111} and {110 + 101} planes, respectively. The wide peak centered at $\sim 22^\circ$ is due to diffraction from {100 + 001} planes and fused silica substrate microcrystallites. The relative {110 + 101}: {111}: {200 + 002}: {100 + 001} intensity in bulk *r*-BaTiO₃ is 100:46:35:12. Film A, therefore, has a strong preferred {100 + 001} texture. The XRD pattern of film B is identical to that of the bare silica substrate, not shown in Fig. 1. Film B, therefore, has no long range crystallographic order and is identified as *a*-BaTiO₃.

Films A and B are transparent and colorless in transmitted visible light. The infrared transmission spectra of both films A and B show a major, featureless absorption band centered at $\sim 510 \text{ cm}^{-1}$ and extending from $450\text{--}620 \text{ cm}^{-1}$, characteristic of short-range order in bulk *r*-BaTiO₃.¹³⁻¹⁵

$I(\lambda)$ data show that there was atomic Ti but no atomic Ba sputtered from the target surface by the Ne discharge used to produce *r*-BaTiO₃ film A. However, both atomic Ba and Ti were sputtered from the target surface by the Ar discharge used to produce *a*-BaTiO₃ film B. A probable source of free Ba atoms in the plasma is the reduction of BaTiO₃ at the target surface due to the sputtering action of Ar⁺ ions. Ne, because of its lower momentum transfer function to either Ba or Ti, would not be expected to be as effective at dissociating BaTiO₃ at the target surface. The arrival to the substrate of metal atoms, as opposed to metal bonded to O in molecular form during growth of other oxides (yttria, zirconia, vanadia, niobia, zinc oxide), has been found to produce films with increased structural disorder,¹⁶⁻²⁰ as we conclude to be the case here.

This work was supported under USARO Grant No. DAAL-03-89-K-0022 and by a gift from Johnson Controls, Inc., to the Wisconsin Distinguished Professorship of C.R.A.

¹ See, for example, M. E. Lines and A. M. Glass, *Principles and Applications of Ferroelectrics and Related Materials* (Clarendon, Oxford, 1977).

² V. S. Dharmadhikan and W. W. Grannemann, *J. Appl. Phys.* **53**, 8988 (1982).

³ J. H. Pratt and S. Firestone, *J. Vac. Sci. Technol.* **8**, 256 (1970).

⁴ C. A. T. Salama and E. Sicinuas, *J. Vac. Sci. Technol.* **9**, 91 (1971).

⁵ A. Mansingh, *Ferroelectrics* **102**, 69 (1990).

⁶ A. Mansingh and C. V. R. Vasant Kumar, *J. Mater. Sci. Lett.* **7**, 1104 (1988).

⁷ K. Sreenivas, A. Mansingh, and M. Sayer, *J. Appl. Phys.* **62**, 4475 (1987).

⁸ D. J. McClure and J. R. Crowe, *J. Vac. Sci. Technol.* **16**, 331 (1979).

⁹ These were ultrasonic rinses in trichlorethylene, acetone, and ethyl alcohol, each for 10 min, successively, and dried in hot, dry air.

¹⁰ J. E. Greene, *J. Vac. Sci. Technol.* **15**, 1718 (1978).

¹¹ C. Candler, *Atomic Spectra and the Vector Model* (Van Nostrand, Princeton, NJ, 1964), p. 373.

¹² H. G. Kuhn, *Atomic Spectra* (Academic, New York, 1963), pp. 79-83.

¹³ R. A. Nyquist and R. O. Kagel, *Infrared Spectra of Inorganic Compounds* (Academic, New York, 1971), pp. 98-99.

¹⁴ W. G. Spitzer, R. C. Miller, D. A. Klienman, and L. E. Howarth, *Phys. Rev.* **126**, 1710 (1962).

¹⁵ M. I. Diaz-Guemes, T. Gonzales Carreno, and C. J. Serna, *Spectrochim. Acta A* **45**, 589 (1989).

¹⁶ C. R. Aita, L.-J. Liou, C.-K. Kwok, R. C. Lee, and E. Kolawa, *Thin Solid Films* **193-194**, 18 (1991).

¹⁷ C.-K. Kwok and C. R. Aita, *J. Vac. Sci. Technol. A* **7**, 1235 (1989).

¹⁸ C.-K. Kwok, C. R. Aita, and E. Kolawa, *J. Vac. Sci. Technol. A* **8**, 1330 (1990).

¹⁹ C. R. Aita, A. J. Purdes, R. J. Lad, and P. D. Funkenbush, *J. Appl. Phys.* **51**, 5533 (1980).

²⁰ C. R. Aita, R. J. Lad, and T. C. Tison, *J. Appl. Phys.* **51**, 6405 (1980).

APPENDIX VIII

"Nanocrystalline aluminum nitride: growth by sputter deposition, optical absorption, and corrosion protection behavior." C.R. Aita and W.S. Tait, Nanostructured Mater. 1, 269-80 (1992). REVIEW

NANOCRYSTALLINE ALUMINUM NITRIDE: GROWTH BY SPUTTER DEPOSITION, OPTICAL ABSORPTION, AND CORROSION PROTECTION BEHAVIOR

C. R. Aita and W.S. Tait

Materials Department and the Laboratory for Surface Studies
University of Wisconsin-Milwaukee
P.O. Box 784, Milwaukee, Wisconsin 53201

(Accepted August 1992)

Abstract—This paper reviews our work with low pressure reactive sputter deposition as a viable method for producing nanocrystalline AlN. An aluminum target and rare gas-N₂ discharges were used to grow films on water-cooled <111>-Si, fused SiO₂, carbon ribbon, and 1008 steel substrates. In situ optical emission spectrometry was used for real-time process monitoring. A relationship between N₂⁺/Al flux to the substrate and nanocrystallite formation is presented. With respect to film behavior, optical absorption was studied, and the near-ultraviolet fundamental absorption edge was modeled using the coherent potential approximation. The optical band gap was determined to be 5.50–5.64 eV, compared to 6.18 eV for a "perfect, infinite-size" AlN crystal. We also demonstrate the use of this material as an excellent self-sealing corrosion protection coating for steel.

I. INTRODUCTION

Physical sputter deposition at high pressure (~100 mtorr) is used to produce nanocrystalline metals and metallic composite films (1). A metal target is sputtered in a rare gas discharge. The mean free path of sputtered species at this pressure is <0.5 mm, two orders of magnitude smaller than a typical target-substrate spacing of 5 cm. Collisions that produce nanosize clusters of sputtered atoms in the discharge are therefore possible. The clusters condense intact on a cold substrate (2), forming a nanocrystalline film.

High pressure physical sputter deposition from a ceramic target has also been used to produce nanocrystalline ceramic films (3). As in the case of low pressure sputter deposition, some degree of dissociation of the ceramic target surface will in general occur (4), and the material collected at the substrate will be metal-rich (3). Subsequent annealing, an additional process step with the risk of crystallite growth, must then be undertaken to produce stoichiometry.

By judicious choice of process parameters, reactive sputter deposition from a metal target at low pressure (~10 mtorr), a process that is normally used to grow films with larger crystallite size, will produce nanocrystalline high valency ceramics, as well. The mechanism, however, is not cluster formation in the discharge and subsequent "freezing" of these clusters on the substrate. The mean free path of sputtered species is 5 mm at 10 mtorr, too long to produce the required number of collisions for cluster formation. Instead, nanocrystallinity occurs by clustering on the substrate.

as a part of the phase formation sequence from metal to ceramic as the reactive gas content of the discharge is increased.

When a metal (M) target is sputtered in a rare gas discharge containing increasing amounts of reactive gas, e.g. O₂ or N₂, the generalized phase formation sequence at the substrate is as follows: M doped with O or N (M:O or M:N) → M-suboxide(s) or M-subnitride(s) → high valency M-oxide or M-nitride. In some metal-oxide and metal-nitride systems, the first *structural* form of the high valency phase in the above sequence is nanocrystalline. This effect has been observed for several sputter deposited ceramics including ZrO₂, where nanocrystallinity is accompanied by stabilization of a high temperature polymorph (5) to be discussed in a future paper, and AlN (6-10), surveyed here.

The outline of this paper is as follows. The experimental details of nanocrystalline AlN film growth are presented in Sec. II. Film characteristics including optical behavior are given in Sec. III. A practical application for nanocrystalline AlN, as a "self-sealing" corrosion protection film (11-13) on steel, is demonstrated in Sec. IV, followed by a brief conclusion in Sec. V.

II. FILM GROWTH

A radio frequency diode apparatus was used for film growth. A 99.9995% pure aluminum target was thermally bonded to the water-cooled stainless steel cathode and sputtered in rare gas-N₂ discharges, as detailed in Refs 6, 7, and 9. Films were grown on <111>-Si, suprasil fused SiO₂, carbon foil, and polished 1008 steel substrates. The substrates were placed in thermal contact with the water-cooled (15 °C) copper anode. The target-substrate spacing was 5 cm. The chamber pressure before backfilling with the sputtering gas was $\sim 10^{-7}$ torr and the total working discharge pressure was 10 mtorr.

Two presputters preceded each deposition, during which time the substrates were shuttered from the sputtered flux. The first presputter was carried out in Ar and its purpose was to remove the oxide layer formed on the target surface upon air-exposure (6). If this step is omitted, the film that is ultimately deposited will be an aluminum oxynitride with unreproducible chemistry (8). The second presputter, carried out in the gas composition used to deposit the film, allows time for discharge and target reactions to reach dynamic equilibrium. Both presputters were monitored *in situ* using either optical emission spectrometry (9) or glow discharge mass spectrometry (4,6). The time required for each presputter was determined from these measurements, and was typically < 1 hr. After the presputters were completed, the shutter was opened and a film was deposited.

The diagram shown in Fig. 1 was obtained by varying the nominal chemistry of Ar-Ne-N₂ discharges at a fixed cathode voltage of -1.7 kV. Similar "phase maps" indicating the region of process parameter space in which a particular structure prevails were constructed for other values of cathode voltage as well. These maps apply to growth on all of the substrate types used here. In the regime of low surface diffusion and near unity sticking coefficient, the effect of different nucleating surfaces is apparently minimal.

The general phase formation sequence for sputter deposited aluminum-nitrogen films grown near room temperature, mapped in Fig. 1, is as follows: <111>-orientation fcc Al → multiorientation fcc Al:N → phase-separated (Al:N)_{1-x}(AlN)_x → nanocrystalline hcp AlN → multiorientation hcp AlN → <0001>-orientation hcp AlN. There are two equilibrium phases in the aluminum-nitrogen system at standard temperature and pressure, fcc Al and hcp wurtzite-type AlN. Sputter deposition

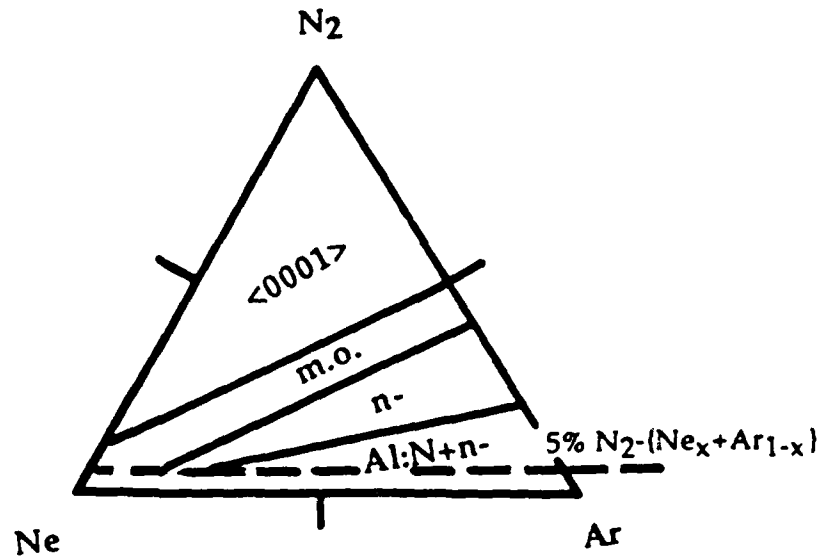


Figure 1. A phase map for the aluminum-nitrogen system sputter deposited on water-cooled substrates using up to three components in the sputtering gas, Ar, Ne, and N_2 . Cathode voltage = -1.7 kV, total pressure = 10 mtorr., $\langle 0001 \rangle$ = basal orientation AlN, mo = multiorientation AlN, n- = nanocrystalline AlN. (After Ref. 9)

is a nonequilibrium process, which could produce phases and structures not predictable from thermodynamic considerations. However, the above data does not support metastable phase formation in the aluminum-nitrogen system.

Nanocrystalline AlN films were grown here using Ar- N_2 and Ar-Ne- N_2 discharges. Although gas dynamics is beyond the scope of the present paper, it is important to understand the effects of Ar and Ne on phase formation. Aluminum cannot be nitrided by ground state N_2 . N_2^+ in the discharge, however, dissociates upon impact with a solid surface to produce N (14) which can nitride aluminum. One way in which N_2^+ is created in the discharge is by Penning ionization (15), i.e. the gas phase collision of a ground state N_2 molecule with a rare gas atom in a low-lying metastable energy level. The energy requirement is that the metastable level of the rare gas atom be greater than 15.58 eV, the ionization potential of N_2 . A metastable Ne atom is able to Penning ionize N_2 whereas metastable Ar cannot (4). The addition of Ne to an Ar plasma containing a small amount of N_2 vastly increases the N_2^+ ion flux to the substrate (16).

But how does the N_2^+ flux influence phase formation in the film? To answer, we used *in situ* optical spectrometry (17) to monitor the emission intensity from electronically excited (*) N_2^+ and neutral aluminum atoms in the negative glow region of the discharge. The emission intensity ratio $I(N_2^{+*}(3914 \text{ \AA}))/I(Al^*(3961 \text{ \AA}))$ is shown in Fig. 2 (9) as a function of the nominal sputtering gas N_2 content. Stoichiometric AlN (nanocrystalline, multiorientation, or $\langle 0001 \rangle$ -orientation) is

formed when $I(N_2^+(3914 \text{ \AA}))/I(Al^+(3961 \text{ \AA})) \geq 0.9$. This ratio is machine-specific, but correlation with dual ion beam deposition data for the aluminum-nitrogen system (18) allows us to equate it with an arrival flux of one N_2^+ molecule for every two Al atoms, i.e., a unity ratio of N/Al. N/Al

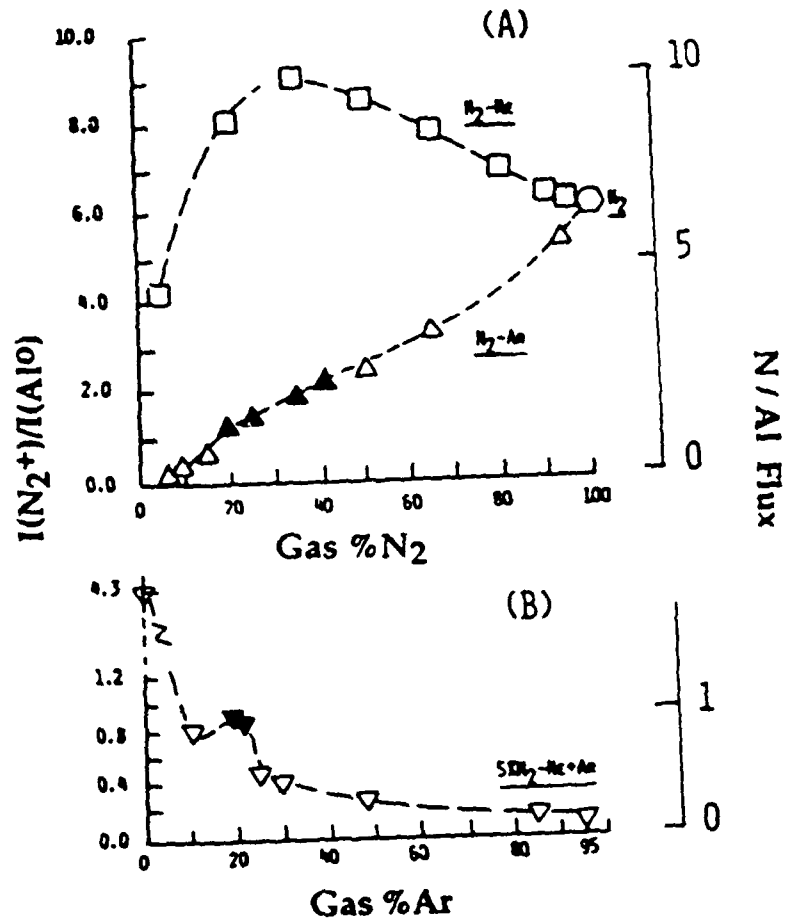


Fig. 2. The ratio of optical emission intensities from the v₀₀ band head of the N₂⁺ [B→X] transition at 3914 Å and the Al¹⁰ [4s→3p] transition at 3961 Å as a function of a) gas N₂ content in Ar-N₂ and Ne-N₂ discharges, and b) gas Ar content in 5% N₂-Ne-Ar discharges. Cathode voltage = -1.7 kV, total pressure = 10 mtorr. Blackened symbols represent nanocrystalline AlN (After Ref. 9). Right side ordinate scale marks N/Al atomic flux.

ratio is shown on a second ordinate scale in Fig. 2. From these data, it can be seen that nanocrystalline AlN is formed when the N/Al ratio at the substrate is close to unity, i.e. all arriving N_2^+ is consumed by the growing film. Increasing the N/Al ratio shifts the phase formation sequence towards $\langle 0001 \rangle$ -AlN. Based on this data, it can be seen that it is not practical to try to grow nanocrystalline AlN using Ne- N_2 discharges. The window for its production, Ne discharges containing greater than 0 and less than 5% N_2 , is too small for good process control.

III. FILM CHARACTERISTICS

Structural and chemical

The double-angle x-ray diffraction (XRD) pattern of a ~1 μ m-thick film grown on $\langle 111 \rangle$ -Si in 70% Ar-30% N_2 gas is shown in Fig. 3a (7). Broad, weak peaks corresponding to diffraction from (1010), (0002), and (1011) AlN planes are present. In addition, there is a featureless background that rises at lower angle. A long time exposure, cylindrical camera pattern of the same film (Fig. 3b) shows arcs corresponding to weak reflections from the above-mentioned AlN lattice planes. These XRD patterns are representative of all of the nanocrystalline AlN films studied here, and are characteristic of a material with small crystallites + regions of poorly-defined crystal structure. For comparison, the XRD patterns of a $\langle 0001 \rangle$ -AlN film of the same thickness is shown in Figs. 3c and d.

Figure 4 is a transmission electron micrograph showing the nanoscale structure and boundary network of a film grown on carbon ribbon using a 95%(Ne_{0.8}+Ar_{0.2})-5% N_2 discharge.

The films were examined (as a matter of routine without regard for their nanocrystallinity) by traditional spectroscopic techniques that yield information about *average* chemistry and aluminum-nitrogen coordination. X-ray photoelectron (XPS) and Auger electron spectroscopy (AES) of films on $\langle 111 \rangle$ -Si, and Rutherford backscattering spectroscopy of films on carbon ribbon, showed that nanocrystalline AlN is stoichiometric within the accuracy of the measurement. XPS core electron binding energy and AES kinetic energy spectra showed that aluminum-nitrogen coordination was characteristic of the tetrahedral bonding in wurtzite-type hcp AlN. However, these techniques are not useful for probing bonding in the crystallite boundary region. Future work will involve specific spectroscopies for this purpose.

Optical

Optical behavior near the fundamental absorption edge of a disordered wide band gap semiconductor, such as nanocrystalline AlN, can differ from its ordered counterpart (the perfect, infinite-size or "virtual" crystal) in several ways, including edge broadening and the formation of discrete intraband absorption states (19). Nanocrystalline AlN films are visually transparent and colorless in transmitted light. Near UV-visible-near IR optical transmittance and reflectance of films grown on fused silica was measured by spectrophotometry. The absorption coefficient, α , was calculated from these data and is shown in Fig. 5a as a function of incident photon energy, E (10).

The onset of the fundamental optical absorption edge is at ~4 eV. The shape of the edge was modeled using the coherent potential approximation with Gaussian site disorder (20) introduced in the valence and conduction bands of a virtual crystal with parabolic band edges and an energy

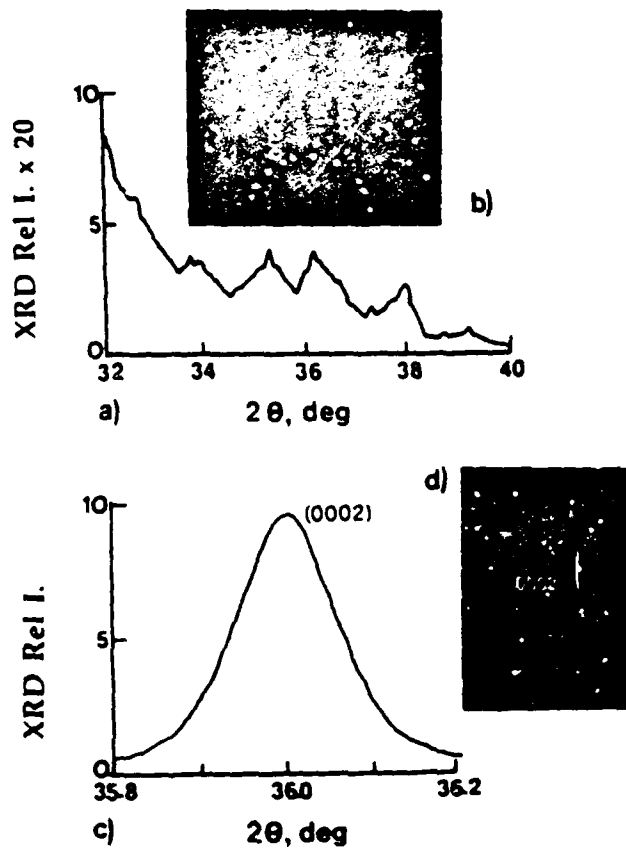


Figure 3. A double-angle XRD pattern of a) nanocrystalline AlN and c) $\langle 0001 \rangle$ -AlN on $\langle 111 \rangle$ Si; a cylindrical camera pattern of b) nanocrystalline AlN and d) $\langle 0001 \rangle$ -AlN on $\langle 111 \rangle$ -Si. (From Ref. 7)

band gap, E_g . The value of E_g was determined graphically as shown in Fig. 5b and found equal to 6.18 eV, in agreement with data for epitaxial $\langle 0001 \rangle$ -AlN grown at high temperature on sapphire (21).

A general expression (applicable to *all* AlN) relating the inverse slope of the absorption edge, E_0 , and the *optical* band gap, E_x , of the material was derived:

$$E_x = 6.18 \text{ eV} - 2.3 E_0. \quad (1)$$

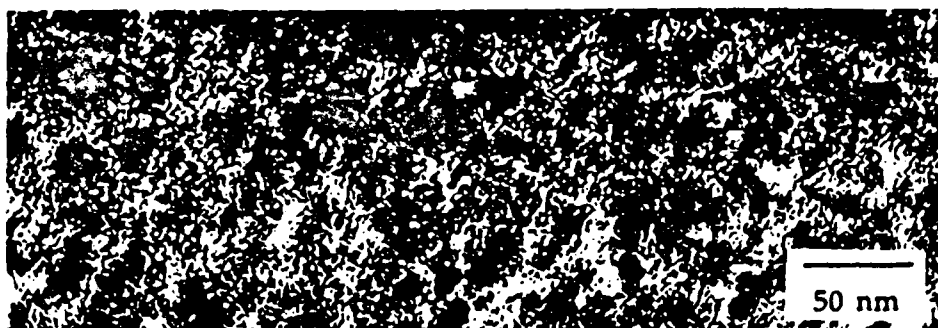


Figure 4. A transmission electron micrograph showing the nanoscale structure and boundary network of a nanocrystalline film grown on carbon ribbon.

E_x was found to range from 5.50 to 5.64 eV. A relative disorder parameter, defined as $(E_0)^{1/2}$ (22), enabled comparison of films grown under different conditions. Equation (1) was recently used by other investigators (23) working with nanocrystalline AlN.

In addition to edge broadening, discrete intragap states associated with nanocrystallinity were identified. These states were responsible for the low energy shoulder that occurs between 4-5 eV, as seen in Fig. 5a. What remains to be done is to correlate these states, as well as optical edge broadening, with specific electronic defects that are a consequence of structural disorder at crystallite boundaries.

IV. CORROSION PROTECTION BEHAVIOR

We will next summarize experiments to determine the corrosion protection behavior of nanocrystalline films on 1008 steel (11-13). Data for other types of films will also be presented for comparison, including Al:N and composite Al:N+nanocrystalline (n-)AlN with different values of electrical resistivity. The films were grown using 95%(Ar_x+Ne_{1-x})-5% N₂ discharges, with values of x given in Table I.

TABLE I
Growth Parameters Thickness [d] Resistivity [ρ], and Structure

Film	x [Ar _x +Ne _{1-x}]	d [μm]	ρ [$\mu\Omega\text{-cm}$]	Structure ^a
A	0.20	1.4	b	n-AlN
B	0.25	1.1	219	Al:N+n-AlN
C	0.30	1.1	84	Al:N+n-AlN
D	0.50	1.4	7	Al:N

a) n = nanocrystalline, b) nonconductor $\rho \geq \mu\Omega\text{-cm}$, ρ of Al = 2.8 $\mu\Omega\text{-cm}$.

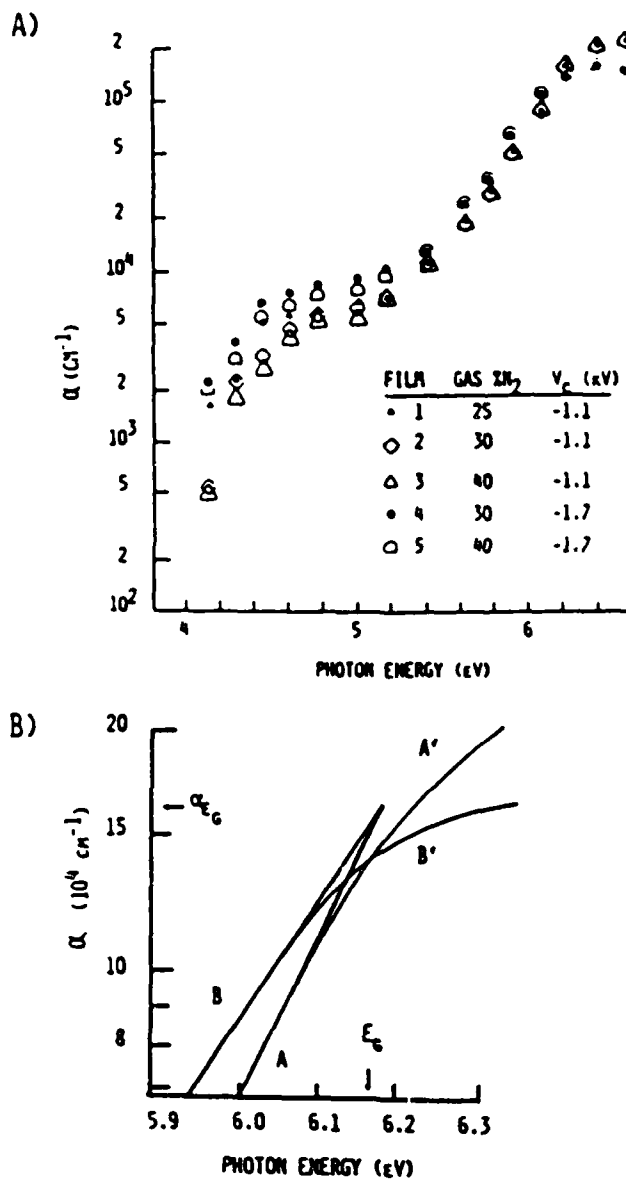


Figure 5. a) The optical absorption coefficient, α , as a function of the incident photon energy, E , for sputter deposited nanocrystalline AlN on fused silica; b) Curves AA' and BB' are the best fit to the data shown in Fig. 5a for films grown at -1.1 and -1.7 kV, respectively. The band gap of the virtual crystal is determined by the value of E at which Curves A and B intersect, $E_g = 6.18$ eV. (From Ref. 10)

Electrochemical measurements were made by using the film+steel sample as the test electrode in a Model K47 EG&G Princeton Applied Research corrosion cell. The electrolytic solution was O₂-purged 0.2M KCl. Test electrodes were equilibrated in solution for 24h prior to cathodic polarization, described next.

The overall corrosion reaction of interest here is,



and the cathodic (half-cell) electrode reaction is the reduction of H⁺ ions that are formed by the dissociation of water in the electrolyte,



The open circuit potential of the cell is V_0 . For reference, V_0 for Fe and Al is equal to -660 and -1882 mV respectively (26), therefore galvanic action between these metals is possible. The relationship between reaction current, I , and overpotential, $V - V_0$, is given by the Butler-Volmer equation (25). Cathodic polarization curves were obtained by applying an increasingly negative overpotential to the test electrode until -250 mV from V_0 was reached. The cathodic polarization curves were extrapolated to V_0 to obtain the steady state corrosion current I_0 , as detailed in Ref. (11).

I_0 is a measure of the steady state corrosion rate for the test electrode, and is used here as the parameter with which to compare the corrosion rate of the coated steel. I_0 for an uncoated steel electrode is equal to values between 4.1 and 5.5 $\mu\text{A}/\text{cm}^2$. I_0 for an uncoated commercial grade 1100 Al electrode is equal to 3.0 $\mu\text{A}/\text{cm}^2$.

Table 2 records values of V_0 and I_0 obtained for the n-AlN, AlN and composite films. Comparing the values of I_0 , it can be seen that the four films represent a wide range of corrosion behavior. I_0 is lowest for n-AlN (film A), increases more than an order of magnitude for AlN+n-AlN (films B and C), and over two orders of magnitude for AlN (film D). Figure 6 shows I_0 as a function of resistivity, ρ , for conducting films B, C, and D. It can be seen that I_0 increases linearly with decreasing ρ .

We wanted to study the chemistry of the corrosion process for n-AlN-coated steel as a function of time so that a model could be developed. Electrolyte pH values were determined as a function of exposure time of film A to KCl, using a Beckman Altex model pH 43 pH meter. pH

TABLE 2
The Open Circuit Potential [V_0] and the Exchange Current Density [I_0] of Aluminum-Nitrogen Films on Steel

Film	V_0 (mV)	I_0 ($\mu\text{A}/\text{cm}^2$)
A	-723	0.09
B	-750	2.10
C	-675	6.30
D	-666	9.90

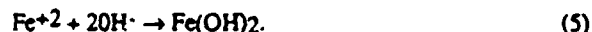
measurements were made at daily intervals for 7 days. Surface hydroxide formed at the electrolyte-film interface, increasing the OH^- concentration in the electrolyte by the following reaction (12):



The electrolyte OH^- concentration increased by an order of magnitude from its initial value after containing film A for 2 days, after which the OH^- concentration remained constant.

XPS was used to determine changes in film surface chemistry that accompanied corrosion. Table 3 lists the binding energy of N 1s, Al 2p, O 1s and Fe 2p_{1/2-3/2} core photoelectron peaks from films A (n-AlN) and D (Al:N) before and after exposure to electrolyte for 7 days. A comparison shows that after KCl exposure:

1) Fe was present on the surface of film D and bonded to O in some form, probably as a hydroxide (27), and absent from the surface of film A. Fe-hydroxide is produced from Fe^{+2} , a corrosion reaction product, as follows:



2) The amount of N on the surface of film A was greatly reduced, and the amount of O was increased, indicating that oxidizing changes occurred in the outermost layer of the n-AlN film after exposure to the electrolyte.

The physical aspects of the corrosion process of bare steel in contact with an electrolytic solution can be summarized in five steps:

1. H^+ arrives from solution and is adsorbed on the steel surface.
2. H^+ _{ad} combines with an electron from the steel to form a neutral adsorbed hydrogen atom, H_{ad} .
3. Two H_{ad} atoms combine to form a H_{2ad} molecule.
4. Many, n, H_{2ad} molecules combine to form a $n\text{H}_{2ad}$ bubble.
5. The $n\text{H}_{2ad}$ bubble desorbs from the steel surface.

The fact that Fe was not present on the surface of n-AlN-coated steel (film A) and was present on the surface of Al:N-coated steel (film D) supports I_0 data showing the capability of n-AlN to inhibit the basic corrosion reaction given by Eq. (2). We propose that the n-AlN film specifically inhibits Step 2 by being a barrier to H^+ _{ad} diffusion to the underlying steel. It is also likely that the

TABLE 3
X-ray Photoelectron Spectroscopy Data for Nanocrystalline AlN and Al:N
Before and After Exposure to Electrolyte

Film	Condition	Al2p	N 1s	Binding Energy (± 0.2 eV)		
				O 1s	Fe2p _{3/2}	Fe2p _{1/2}
A. n-AlN	as-grown	73.4	396.2	531.4	no peaks	
A. n-AlN	KCl	73.9	.	531.5	no peaks	
D. Al:N	as-grown	73.3	396.9	531.1	no peak:	
D. Al:N	KCl	73.9	396.3	531.5	710.4	723.7

amount of H^+ adsorbed on the surface of n-AlN will be less than H^+ adsorbed on bare steel (8, 28, 29).

The question now arises as to whether n-AlN is inert or is itself changed by exposure to electrolyte. Solution pH measurements show an initial increase in the amount of OH^- in the electrolyte as a result of contact with n-AlN, suggesting that AlN reacts with water in the electrolyte via Eq. (4). The Al-hydroxide that forms "seals" the n-AlN film, and consequently protects the underlying steel from corrosion, after which no further change in solution pH is observed.

XPS data show an increase in the amount of Al bonded to O and a decrease in the amount of Al bonded to N at the surface of the film after exposure to electrolyte, consistent with the conversion of AlN to $Al(OH)_3$. According to the above model, any internal surface in the film such as a pore, fissure, or pin-hole or *nanocrystallite boundary* that is exposed to electrolyte will also self-seal. This phenomenon, schematically drawn in Fig. 7, was observed to occur (12).

Aluminum, a material that is traditionally used as a protective coating for steel, or for that matter, another metal, might also self-seal by forming a hydroxide. However, if internal surfaces exist in the film such that the electrolyte comes into contact with the steel substrate, a galvanic action will be established before self-sealing occurs provided that V_0 values for the metal and steel are different (30).

In addition to differences in V_0 , another criterion for galvanic corrosion is that electromigration from the film to the steel must be possible. Electromigration is not possible in insulating n-AlN. Figure 6, which shows the linear decrease of i_0 with increasing electrical resistivity for the conducting films B, C, and D, gives additional supporting evidence of the superior behavior of an electrically insulating material for corrosion protection.

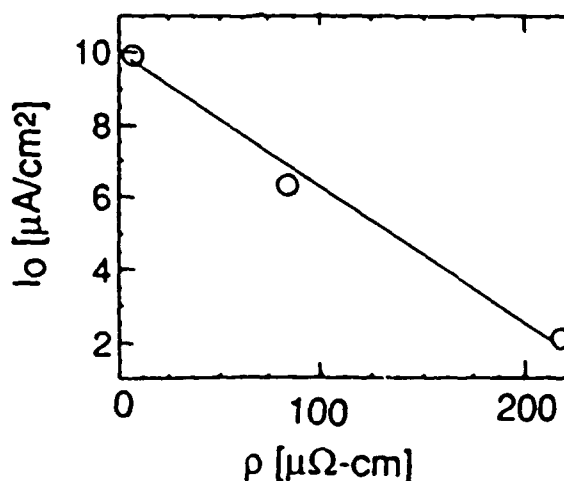


Figure 6. The exchange current density, i_0 , as a function of resistivity, ρ , for Al:N and Al:N+n-AlN films on steel. (From Ref. 12)

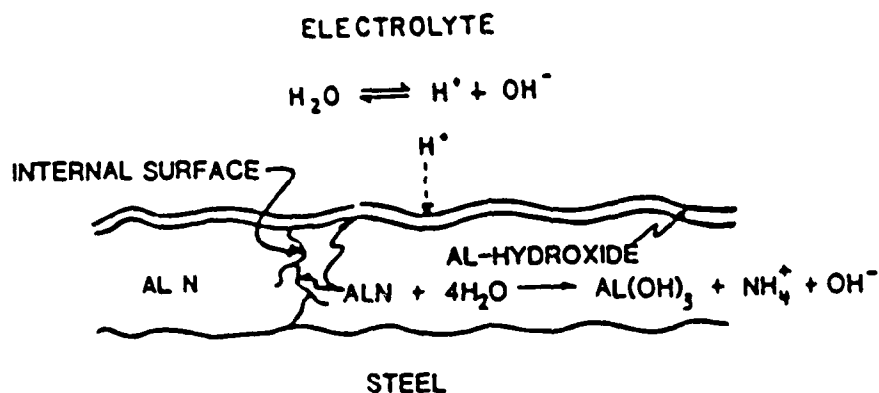


Figure 7. The n-AlN film as a self-sealing porous electrode. (From Ref. 12)

V. SUMMARY

We reviewed the growth of nanocrystalline AlN by low pressure reactive sputter deposition using an Al target and Ar-Ne-N₂ and Ar-N₂ discharges and presented a phase map showing the gas composition range over which this material was formed. *In situ* optical emission spectrometry was used for discharge monitoring and enabled us to relate the ratio of the N₂⁺/Al flux to the substrate to nanocrystalline AlN growth.

With respect to optical behavior, the position and shape of the near-ultraviolet fundamental absorption edge of nanocrystalline AlN on fused silica was determined from transmission and reflection measurements. The onset of the edge was at -4 eV. The absorption coefficient as a function of energy was modeled using the coherent potential approximation with Gaussian site disorder in the valence and conduction bands. The optical band gap was calculated from this data and found to range from 5.50-5.64 eV, compared to 6.18 eV for a perfect "infinite-size" AlN crystal.

The corrosion behavior of nanocrystalline AlN-coated steel was also reviewed. The corrosion rate for nanocrystalline AlN-coated steel was several orders of magnitude lower than for uncoated steel. A self-sealing porous electrode model of corrosion protection was proposed to explain this result. This model applies to any film material that fulfills two requirements: 1) there must be a (thermodynamic) driving force for the film to react with H₂O to form a self-sealing hydroxide; 2) there must be no electromigration from the film to the steel, so that no galvanic action precedes self-sealing. Nanocrystalline ceramics are especially attractive for corrosion protection applications because of the amount of active internal surface area available for hydroxide formation.

ACKNOWLEDGEMENTS

The authors acknowledge fruitful discussions with Prof. G.S. Baker. This work was supported under US ARO Grant Nos. DAAG29-84-K-0126 and DAAL03-89-K-0022, and by gifts from Johnson Controls, Inc. and Schunk Graphite Technology. WST was supported in part by S.C. Johnson and Son.

REFERENCES

1. G.M. Chow and A.S. Edelstein, *Nanostruct. Mater.* 1, 107 (1992).
2. D.M. Cox, B. Kessler, P. Fayet, W. Eberhardt, Z. Fu, D. Sondemcher, R. Sherwood, and A. Kaidor, *Nanostruct. Mater.* 1, 161 (1992).
3. R.S. Averback, H.J. Hofter, H. Hahn, and J.C. Logas, *Nanostruct. Mater.* 1, 173 (1992).
4. C.R. Aita, *J. Vac. Sci. Technol. A* 3, 625 (1985).
5. C.-K. Kwok and C.R. Aita, *J. Vac. Sci. Technol. A* 7, 1235 (1989); *J. Appl. Phys.* 66, 2756 (1989); C.R. Aita and C.-K. Kwok, *J. Amer. Ceram. Soc.* 73, 3209 (1990).
6. C.R. Aita, *J. Appl. Phys.* 53, 1807-1808 (1982).
7. C.R. Aita and C.J. Gawlak, *J. Vac. Sci. Technol. A* 1, 403 (1983).
8. J.A. Kovacich, J. Kasperkiewicz, D. Lichtman, and C.R. Aita, *J. Appl. Phys.* 55, 2935 (1984).
9. J.R. Siettmann and C.R. Aita, *J. Vac. Sci. Technol. A* 6, 1712 (1988).
10. C.R. Aita, C.J.G. Kubiak, and F.Y.H. Shih, *J. Appl. Phys.* 66, 4360 (1989).
11. W.S. Tait, C.O. Huber, B.C. Begnoche, J.R. Siettmann, and C.R. Aita, *J. Vac. Sci. Technol. A* 6, 924 (1988).
12. W.S. Tait and C.R. Aita, *Corrosion* 46, 115 (1990).
13. W.S. Tait and C.R. Aita, *Surface Eng.* 7, 327 (1991).
14. H.F. Winters, D.E. Horne, and E.E. Donaldson, *J. Chem. Phys.* 41, 2733 (1966); H.F. Winters and Eric Kay, *J. Appl. Phys.* 38, 3928 (1967); H.F. Winters, *J. Chem. Phys.* 44, 1472 (1969); H.F. Winters and D.E. Horne, *Surf. Sci.* 24, 587 (1971).
15. See for example: C.R. Aita and M.E. Marhic, *J. Vac. Sci. Technol. A*, 1, 69 (1982), and references within.
16. J.R. Siettmann, MS Thesis, U. Wisconsin-Milwaukee, 1987.
17. J.E. Greene, *J. Vac. Sci. Technol.* 15, 1718 (1978).
18. J.M.E. Harper, J.J. Cuomo, and H.T.G. Hentzell, *Appl. Phys. Lett.* 43, 547 (1983).
19. I. Hamberg and C.G. Granqvist, *J. Appl. Phys.* 60, R123 (1986).
20. G.D. Cody, in *Semiconductors and Semimetals Volume 21, Hydrogenated Amorphous Silicon, Part B, Optical Properties*, edited by J.I. Pankove (Academic, Orlando, FL, 1984) pp. 11-79.
21. W.M. Yim, E.J. Stofko, P.J. Zanzucchi, J.I. Pankove, M. Ettenberg, and S.L. Gilbert, *J. Appl. Phys.* 44, 292 (1973).
22. S. Abe and Y. Toyozawa, *J. Phy. Soc. Jpn.* 50, 2185 (1981).
23. R. Zarwasch, E. Rille, and H.K. Pulker, *J. Appl. Phys.* 71, 5275 (1992).
24. A. J. Bard and L. R. Faulkner, *Electrochemical Methods: Fundamentals and Applications*, (Wiley and Sons, New York, NY, 1980) p. 103.
25. K.E. Heusler and W.J. Lorentz, in *Standard Potentials in Aqueous Solution*, (edited by A.J. Bard, R. Parsons, and J. Jordon, Dekker, New York, NY, 1985) p. 407.
26. C.D. Wagner, W.M. Riggs, L.E. Davis, J.F. Moulder, and G.E. Muilenberg, *Handbook of X-ray Photoelectron Spectroscopy*, (Perkin-Elmer, Eden Prairie, MN, 1978) pp. 76-77.
27. C.J.G. Kubiak, C.R. Aita, F.S. Hickernell, and S.J. Joseph, *Proc. Mater. Res. Soc.* 47, 75 (1985).

29. C.J.G. Kubiak, C.R. Aja, N.C. Tran, and T.L. Barr, Proc. Mater. Res. Soc. 60, 379 (1986).
30. R.A. Anderson, E.A. Dobisz, J.H. Perepezko, R.E. Thomas, and J.D. Wiley, in The Chemistry and Physics of Rapidly Solidified Materials, (edited by B.J. Berkowitz and R.O. Scattergood, ADME, Warrendale, PA, 1983) p. 111.